MAGNETIC STUDIES OF RARE AND HIGHLY SYMMETRIC GEOMETRIES IN 3D AND LANTHANIDE METAL SINGLE MOLECULE MAGNETS

A Dissertation

by

KELSEY ANNE SCHULTE

Submitted to the Office of Graduate and Professional Studies of
Texas A&M University
in partial fulfillment of the requirements for the degree of

DOCTOR OF PHILOSOPHY

Chair of Committee,	Kim Dunbar
Committee Members,	Timothy Hughbanks
	Michael Nippe
	Donald Naugle
Head of Department,	Simon North

May 2019

Major Subject: Chemistry

ABSTRACT

In 1993, the first report of a single molecule magnet (SMM) appeared in the literature, namely $[Mn_{12}(CH_3COO)_{16}(H_2O)_4O_{12}]\bullet 2CH_3COOH\bullet 2H_2O$ ($Mn_{12}OAc$). This molecule was remarkable in that it exhibits hysteresis similar to that of a bulk magnetic material. In this case, however, rather than an extended structure property with long range ordering as in solid state magnetic materials, each $Mn_{12}OAc$ molecule behaves as a tiny magnet with a thermal barrier to the reversal of the magnetization. This discovery led to the realization that such materials are promising for the study for applications such as data storage and spintronics. In $Mn_{12}OAc$, hysteretic behavior was only be observed up to 4 K, making practical applications impossible. Since this time, the field has focused on increasing the blocking temperature for SMMs, and much progress has been made.

Recently, the field has focused on low spin, highly symmetric molecules, some with only one paramagnetic metal center responsible for the magnetic behavior. The work in this dissertation is involved in this pursuit, with the goal of testing predictions and lending credence to future synthetic pathways for better SMMs. The first part of the work focuses on trigonally symmetric 3d SMMs using highly bulky ligands. Chapter II focuses on a direct comparison of two geometries, namely trigonal monopyramidal and bipyramidal. A series of divalent iron, cobalt, and nickel complexes were synthesized in both geometries through use of a tris-anionic, tetradentate ligand, and in the case of the bipyramidal structures, a water molecule. Additionally, the effect of electron donating and withdrawing substituents on the Co(II) trigonal bipyramidal structures was investigated.

The third chapter is a study of the differences in magnetic behavior between partial and complete metal encapsulation through neutral, tetradentate based ligands which coordinate one or two Co(II) metal centers. The fourth chapter describes a series of octahedral 3d metal molecules that employ Ti(IV) as a new diamagnetic capping ligand. The fifth chapter focuses on lanthanide based SMMs in a geometry never before observed for SMM behavior, namely cubic. The goal was to observe how this highly symmetric geometry would affect the magnetic behavior of trivalent Dy, Er, and Tb complexes.

DEDICATION

To my parents. Thank you.

ACKNOWLEDGEMENTS

I would like to thank my advisor, Professor Kim Dunbar, for her support and dedication though out my time at Texas A&M. I am grateful for her guidance through all of my projects, as well as her support of personal growth both inside and outside of the laboratory.

Thank you to my committee members: Dr. Hughbanks, Dr. Nippe, and Dr. Naugle. Your support and assistance throughout my Ph.D. studies is much appreciated.

Thank you to all the members, past and present, in the Dunbar group. I would not have been able to finish this without all your help and support over the years. I enjoyed working with you all, and wish you the best in your future endeavors, wherever they may be.

I would also like to thank a few extra mentors throughout my scientific career so far. To Dr. Yu-Sheng Chen at Argonne National Lab, who taught me many things about crystallography, especially how synchrotron radiation can be used in single crystal diffraction experiments. To my undergraduate advisor Prof. Matthew Shores, thank you for starting me on my magnetism career. Working in your group was the reason I pursed my graduate degree, and my successes here would not have been possible without that experience.

Finally, thank you to my friends and family. Graduate school would not have been the same without the wonderful group of people I met here. Your support certainly ensured my successes. To my family, thank you for always being there as I rode the crazy roller

coaster that is graduate school. Your support and faith was invaluable. Finally, thank you to my soon to be husband, Carl. Your unending patience and unwavering support throughout means more than I can express. Thank you for always reminding me what is truly important.

CONTRIBUTORS AND FUNDING SOURCES

This work was supervised by a dissertation committee consisting of my advisor Professor Kim Dunbar, and my committee members, Professor Timothy Hughbanks and Professor Michael Nippe of the Department of Chemistry, and Professor Donald Naugle of the Department of Physics.

Computational studies throughout the dissertation were performed by Dr. Kuduva R. Vignesh, of the Department of Chemistry. Dr. Dimitris I. Alexandropoulos, of the Department of Chemistry, contributed equally to the work in Chapter V.

All other work for the dissertation was completed by the student, under the advisement of Professor Kim Dunbar of the Department of Chemistry.

This work was made possible in part by the Department of Energy under Grant Numbers DE-SC0012582 and DE-FG02-02ER45999 and the Welch Foundation under Grant Number A-1449.

Its contents are solely the responsibility of the authors and do not necessarily represent the official views of the Department of Energy or the Welch Foundation.

NOMENCLATURE

AC	Alternating Current
DBM	1,3-diphenyl-1,3-propanedionate
DC	Direct Current
DCM	Dichloromethane
DMA	Dimethylacetamide
EPR	Electron Paramagnetic Resonance
FST	N,N',N''-(nitrilotris(ethane-2,1-diyl))tris(4-(trifluoromethyl) benzene-sulfonamide)
L^1	6,16,2,5-tribenzena(1,4)-1,4,8,11,14,18,23,27-octaazabicyclo [9.9.9]nonacosaphane
MST	N,N',N''-(nitrilotris(ethane-2,1-diyl))tris(2,4,6-trimethylbenzene-sulfonamide)
PST	N,N',N''-(nitrilotris(ethane-2,1-diyl))tribenzenesulfonamide
SMM	Single molecule magnet
SOC	Spin-orbit coupling
TBP	Trigonal Bipyramidal
TMP	Trigonal Monopyramidal
Tp	tri(1H-pyrazol-1-yl)hydroborate
Tp*	tris(3,5-dimethyl-1H-pyrazol-1-yl)hydroborate
Tren	tris(2-aminoethyl)amine

TST	N,N',N''-(nitrilotris(ethane-2,1-diyl))tris(4-methylbenzene-sulfonamide)
ZFS	Zero field splitting

TABLE OF CONTENTS

Page

LIST OF FIGURES

Page

LIST OF TABLES

Page

CHAPTER I

INTRODUCTION

I.1 Magnetic Behavior and the Problem with the Top-Down Approach

Paramagnetic materials which exhibit the ability to behave as magnets are essential in our daily lives. The capability of retaining magnetization once a magnetic field has been removed is the defining characteristic of a magnet. One of the major methods of characterization of magnetic materials is the observation hysteresis curves, Figure I.1.[1] In this case, a magnetic field is applied to the material and the spins align with the field until they reach a saturation point. Once the field is removed, the magnetization that remains is known as the remnant magnetization. The magnetic field can then be applied in the opposite direction, and a coercive field is observed upon return to zero magnetization. Upon continued application of the field, saturation is reached in the opposite direction. One-half of the difference between the two coercive fields, known as coercivity, is a way to measure the resistance a magnetic material exhibits to changes in magnetization. The magnetic materials which we use in technology, for example in data storage, must exhibit high coercivity to retain magnetic memory without relaxation for extended periods of time.

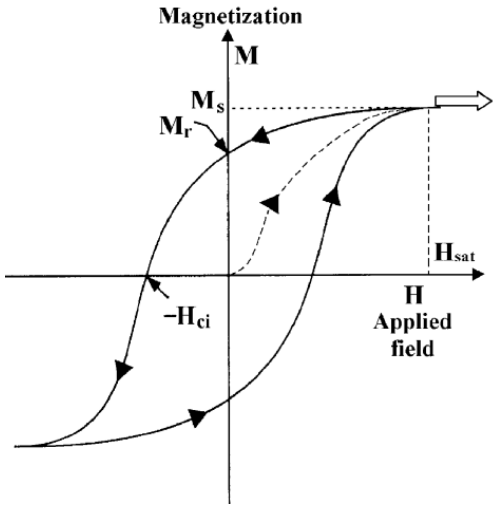

Figure I.1 Sample hysteresis curve for magnetic materials. M_s, M_r, and H_{ci} stand for the saturation magnetization, remnant magnetization, and coercive field respectively. Reproduced by permission from Elsevier: Journal of Magnetism and Magnetic Materials from reference 1, copyright 2003.

Technology is essential to our society, and its advancement is an ever pressing issue. In particular, the ability to store and process larger volumes of information on smaller and smaller magnetic particles is a big challenge. One method to do this can be thought of as taking a magnetic material and cutting it into smaller and smaller pieces. This continual decrease in the size of materials can be defined as a top-down approach.

Once the material becomes small enough, it becomes a superparamagnet, in which it is defined by a single domain where all of the spins align with the applied magnetic field. A problem with this size is that the coercivity decreases, and thermal energy begins to compete with the preferred spin orientation, or anisotropy, of these particles. As a result, coercivity decreases and magnetic memory is no longer possible at room temperature, Figure I.2.[2]

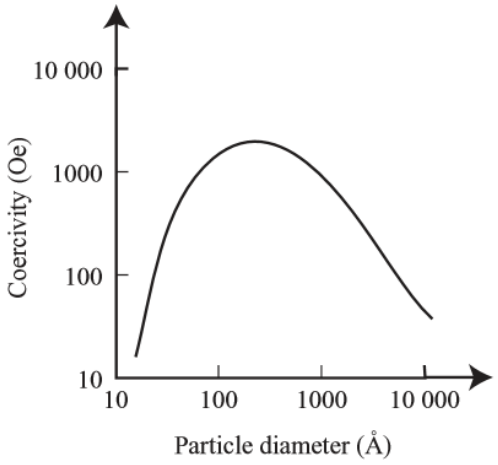

Figure I.2 Coercivity as a function of particle diameter, exhibiting the sharp decline in coercivity as magnetic materials get small and smaller in size. Reproduced with permission by Cambridge Press: Magnetic Materials, Fundamentals and Applications, 2nd Edition from Reference 2, copyright 2010.

This competition between the anisotropy of a system and thermal energy is restricting to the success of the top-down approach. When such a method is no longer viable, it is perhaps better to start with a bottom up approach. In this case, materials are designed starting with the smallest particle, an atom, and building up around it to form a strongly anisotropic magnetic material. One field which takes distinct advantage of this method is that of single molecule magnets. Strong anisotropy is engendered in single molecules, where each molecule can be thought of as a tiny bar magnet. These materials have the ability to overcome the thermal energy competition and retain magnetization at temperatures closer to room temperature.

I.2 Discovery of Single Molecule Magnets

The saga of single molecule magnets began in 1980 when Lis postulated that his newly reported molecule, $[Mn_{12}(CH_3COO)_{16}(H_2O)_4O_{12}]\bullet 2CH_3COOH\bullet 2H_2O$ ($Mn_{12}OAc$)

should exhibit interesting magnetic properties (Figure I.3).[3] The core structure of $Mn_{12}Ac$ is defined by four Mn^{IV} metal centers bridged via μ_3-oxo bridges, forming a cube. Surrounding this cube is a ring of eight Mn^{III} metal centers connected to each other and the cubane core via μ_3-oxo and acetate bridges.

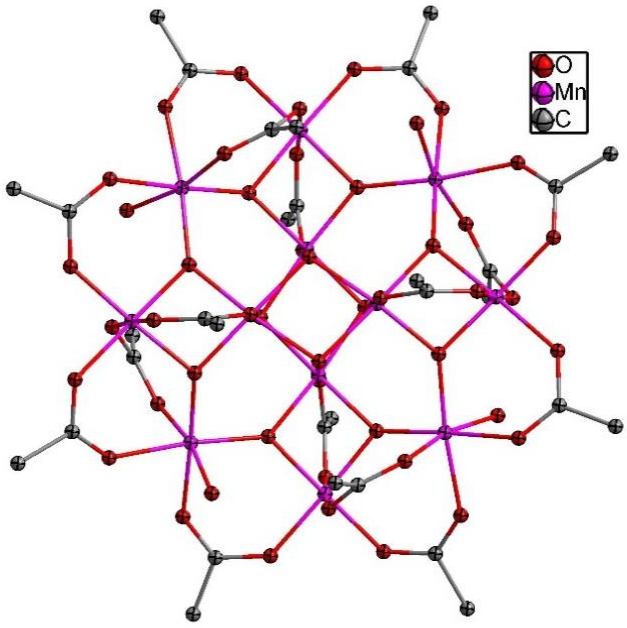

Figure I.3 Structure of $[Mn_{12}(CH_3COO)_{16}(H_2O)_4O_{12}]\bullet 2CH_3COOH\bullet 2H_2O$. Hydrogen atoms are omitted for clarity. Colors are as follows: purple, Mn; red, O; grey, C.[3]

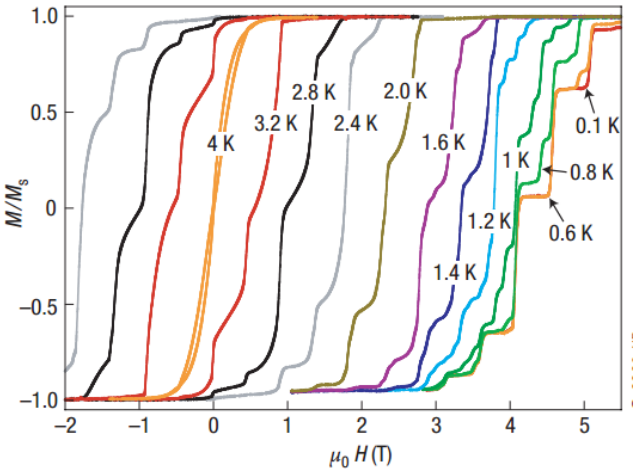

Figure I.4 Hysteresis loops of single crystals of $Mn_{12}OAc$ at temperatures from 0.1 K to 4 K under a constant field sweep rate of 2 mT s^{-1}. The loops exhibit steps due to quantum tunneling between M_S energy levels. The hysteresis loops become temperature independent below 0.6 K, demonstrating quantum tunneling at the lowest energy levels. Reproduced with permission by Elsevier: Nature Materials from reference 6, copyright 2008.

Although Lis was certainly correct about interesting magnetic properties due to exchange between each of the Mn metal centers via the oxo bridges, it was not until 1991 that the magnetic properties started to be investigated by Gatteschi, Sessoli, Caneschi, et al.[4] They confirmed an S=10 ground state for the molecule via magnetization data, and verified that the M_s = -10 state is lowest in energy via magnetization and high field EPR studies. Interestingly, they also observed that the in-phase component of the susceptibility (χ') began to decrease to zero around 8 K. Correspondingly, the out-of-phase susceptibility (χ") exhibited a signal that was frequency dependent. This behavior was previously only observed in superparamagnets and spin glasses, and suggested that bistable behavior on the molecular scale was possible.

The origin of this behavior remained elusive until 1993, when Gatteschi, Sessoli,

Caneschi, and Novak built upon their previous studies when they reported the first example of hysteresis observed in a molecular system, Figure I.4.[5,6] The molecular origin of this bistability was confirmed due to the "steps" observed in the hysteresis loop. These are due to quantum tunneling of the spins, a phenomenon that is molecular in origin. Around the same time, the Hendrickson group published a paper confirming the origin of the out-of-phase susceptibility which agreed with the work by the Novak group.[7] Friedman and Sarachik confirmed that the steps observed in the hysteresis loop originated from thermally assisted quantum tunneling.[8]

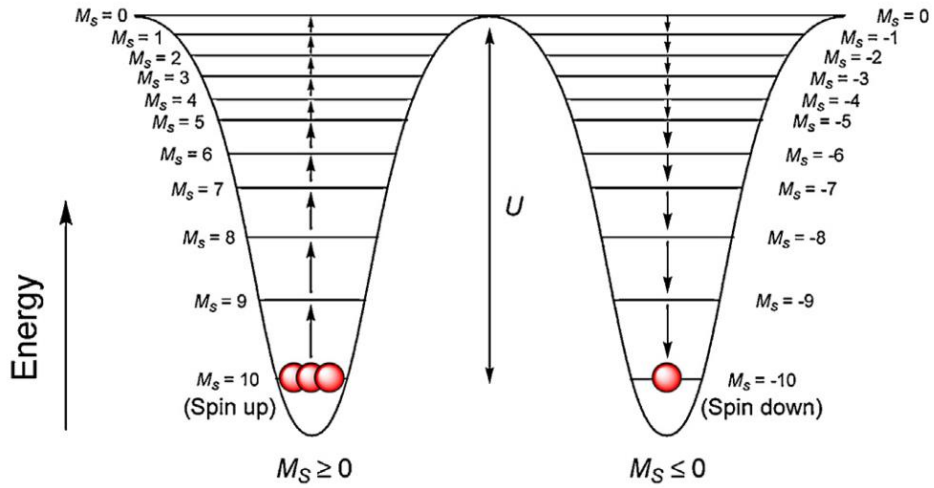

Figure I.5 Barrier to spin reversal for the $Mn_{12}OAc$ molecule. The thermal barrier results in bistability and subsequent hysteresis. Reproduced with permission by Elsevier: Coordination Chemistry Reviews from reference 7, copyright 2008.

The origin of this barrier comes from a breaking of the degeneracy of the M_S states in 21 sublevels due to zero field splitting that lifts the degeneracy resulting in the $\pm M_S = 10$ state being lowest in energy while the $\pm M_S = 1$ state is highest in energy. A thermal barrier

between the $+M_S$ and $-M_S$ states exists as a result, leading to a thermal spin reversal, Figure I.5.[9] The effective height of this barrier is defined by two equations for integer and non-integer spins, respectively:

$$U_{eff} = |D|S^2$$

$$U_{eff} = |D|\left(S^2 - {}^1/_4\right)$$

Where U_{eff} is the effective barrier height, D is the zero field splitting parameter, and S is the total spin of the system. These equations formed the basis for the field by providing a template for the operating temperature at which bistability is observed.

The work of the Christou group delved into the exploration of manganese SMMs with higher and lower nuclearity, alternative carboxylate derivatives, and alternative metal complexes such as a V_4 complex.[10-13] Pursuits then began to focus on increasing the spin of the system, given its quadratic relation to the barrier. To this end, a number of complexes of note appeared in the literature. The first is another manganese based SMM, $[Mn^{III}_{12}Mn^{II}_7(\mu_4\text{-}O)_8(\mu_3,\eta^1\text{-}N_3)_8(HL)_{12}(MeCN)_6]^{2+}$ which exhibits a record bearing ground spin state of 83/2.[14] However, the effective barrier for this compound is only 5.75 K. Another prominent example is the record cyanide compound which exhibits a ground spin state of 31, but only exhibits glassy magnet behavior.[15] In this case the spins are locked into random orientations at low temperatures, and some barrier exists to changing those orientations. It cannot be attributed to SMM behavior due to this difference in origin.

Around this time, theory was published in the literature by Waldmann, noting that, while the current equations to describe the barrier are correct, D is also inversely proportional to S^2.[16] The realization of these countervailing trends led to the focus in the

field being turned towards increasing the zero field splitting parameters. The spin Hamiltonian which describes the ZFS can described by the following:

$$\hat{H} = D(\hat{S}_z^2 - {}^1/_3\,\hat{S}^2) + E\left(\hat{S}_x^2 + \hat{S}_y^2\right)$$

Where D and E are the axial and rhombic zero field splitting parameters, respectively, $\hat{S}$ is the total spin operator, and $\hat{S}_i$ is the spin operator projected along an axis. Spin-orbit coupling (SOC) is key to increasing the splitting between M_S states, and subsequently increasing the barrier height, as given by the equation:[17]

$$\lambda = \frac{\zeta}{2S}$$

Where λ is spin-orbit coupling parameter, ζ is the single electron spin orbit coupling parameter, and S is the spin of the system. Spin-orbit coupling can largely be classified into two different categories, first-order and second-order. The former is direct mixing of the spin and orbital momentum components in the ground state of a given system, commonly observed in lanthanide and heavier transition metal spin centers. The latter type of SOC requires the mixing of an excited state which possesses orbital angular momentum with the ground state that does not exhibit spin-orbit coupling, commonly observed in 3d metals. Maximizing the anisotropy via spin-orbit coupling has subsequently become the focus for increasing the barrier height and operating temperatures of SMMs.

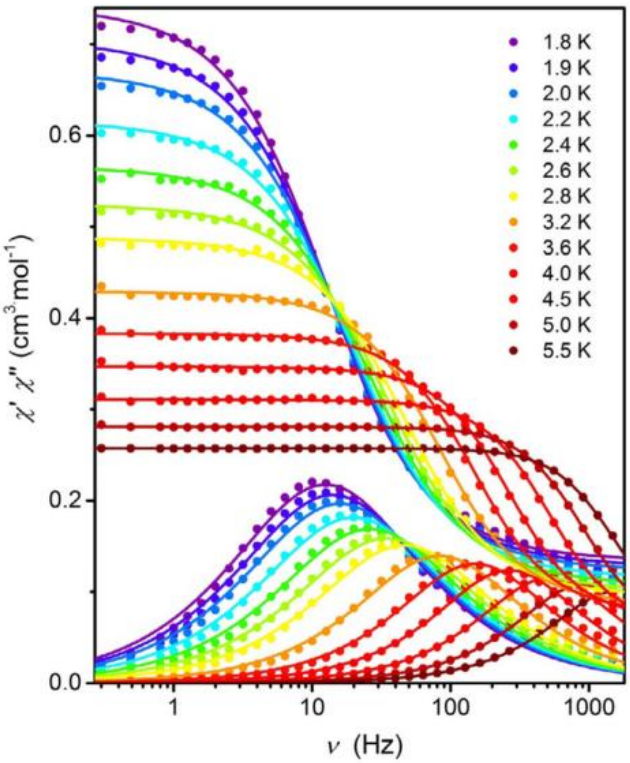

Figure I.6 In-phase (χ') and out-of-phase (χ") components of the susceptibility for the compound [Li(THF)Co(N_3N)]. Reproduced with permission by John Wiley and Sons: Chemistry – A European Journal from reference 12, copyright 2017.

At this stage, it is important to explore the methods that are used to measure the magnetic properties of these complexes. Measurements under both a static DC field and a dynamic AC field are performed inside a Superconducting Quantum Interference Device (SQUID). The most definitive way to observed SMM behavior is through the observation of hysteresis. In this case, the highest temperature at which hysteresis is observed is known as the blocking temperature (T_B). As a cautionary note, while more definite proof of SMM behavior, hysteresis parameters from one experiment to another can often be hard to compare. If different sweep rates are used, no direct comparison can be made as the faster the sweep rate, the wider the hysteresis loop will be.

Often hysteresis is measured on too slow of a time scale, and no signal is observed for potential SMMs. In this case, it is possible to use an AC field, which operates on a much faster time scale, to measure the SMM behavior. To observe the in-phase (χ') and out-of-phase (χ") components of the magnetic susceptibility, an AC field is applied in which the field oscillates at a particular frequency, υ. The ability of the spins to follow the fluctuating field is then measured. The magnitude of χ' can be thought of as a measure of the number of spins which are able to keep up with that oscillating field. If the thermal barrier exists for the compound being measured, some of the spins will get trapped on one side of the barrier and will not be able to keep up with the field as a result. This is observed in χ' as a steep drop off in the susceptibility. The value of χ" represents a measure of the number of spins which are not able to keep up with the oscillating field. When a barrier is present, a frequency dependent maximum in χ" will be observed. The observed peak in this plot is the point at which the frequency of the oscillating field is equivalent to the rate of spin reversal (τ) according to the following equation:

$$\tau = \frac{1}{2\pi\upsilon}$$

A combined plot of χ' and χ" are given in Figure I.6 as a representative example of these concepts.[18] Given that these experiments are a measure of a kinetic process, an Arrhenius plot may be constructed based on thermal relaxation over the barrier. This plot should be linear according to the equation, where τ_o is the relaxation rate:

$$\left(\frac{1}{\tau}\right) = \left(\frac{1}{\tau_0}\right) e^{\left(\frac{-U_{eff}}{k_b T}\right)}$$

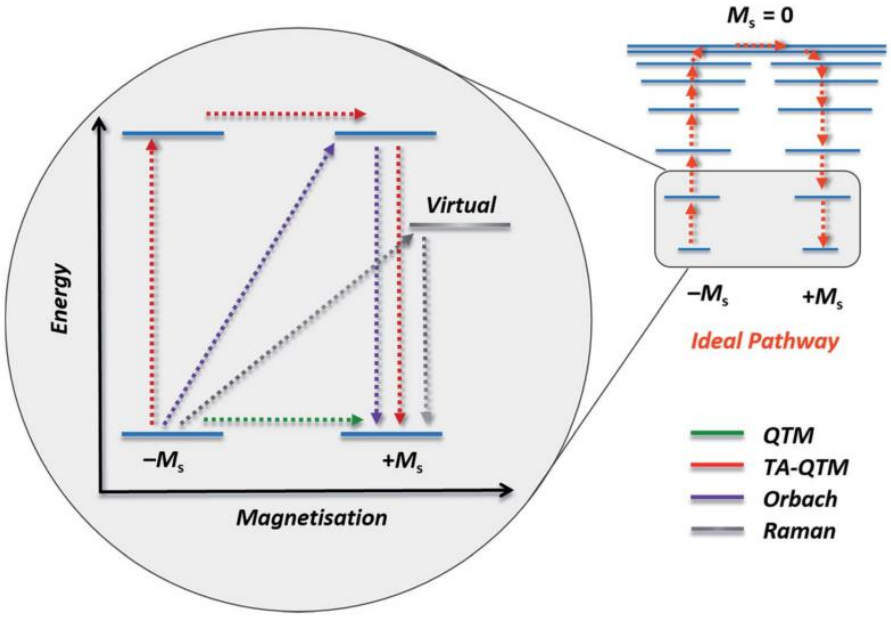

Figure I.7 Possible pathways for spin relaxation in SMMs. Blue lines represent spin states. The grey line represents a virtual state by which Raman relaxation process. Color code is as follows: green, ground state quantum tunneling of magnetization; red, thermally assisted quantum tunneling of magnetization; purple, Orbach relaxation; grey, Raman relaxation. Reproduced with permission by Royal Society of Chemistry: Chemical Science from reference 11, Copyright 2015.

Non-linearity is often observed in these Arrhenius plots due to the presence of alternate relaxations wherein the spins are relaxing without all the way over the barrier, Figure I.7.[17] The ideal relaxation for SMMs, Orbach relaxation, takes place via thermal relaxation of the spins up and over the total barrier height, but, in most cases, this is not the only relaxation that takes place. A number of other dominant relaxations have been identified and explored. A prominent one is quantum tunneling, in which the spins relax via tunneling through the barrier. Quantum tunneling often dominates at lower temperatures until thermal relaxation becomes energetically more favorable at higher temperatures. Alternative pathways include thermally assisted quantum tunneling and

Raman relaxations. The former type is where the spins relax after excitation to a higher M_S state via quantum tunneling to the other side of the barrier, and subsequent relaxation down to the lowest M_S state. Raman relaxation is similar to Orbach relaxation, but the excitation is into a virtual state rather than a real M_S state. Given these components, the original equation for the Arrhenius plot can now be modified in the following way to account for the alternate relaxation pathways.

$$\frac{1}{\tau} = \tau_{QTM}^{-1} + AT + CT^n + \left(\frac{1}{\tau_0}\right) e^{\left(\frac{-U_{eff}}{k_b T}\right)}$$

The first term describe the relaxation rate due to quantum tunneling. The second describes the direct relaxation process. The third, Raman relaxation process. The last part still corresponds to the Orbach relaxation process.

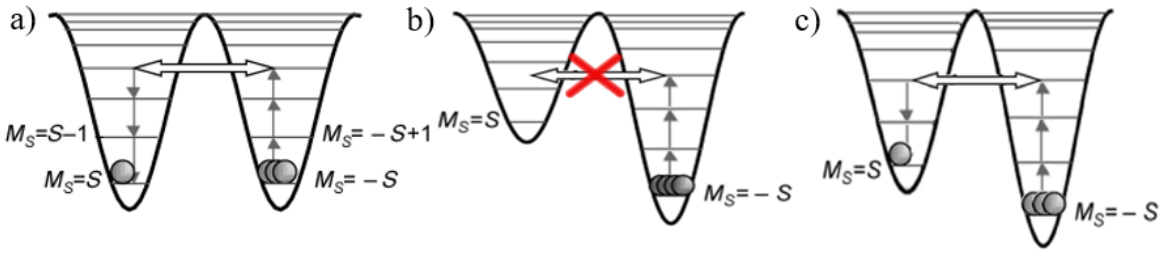

Figure I.8 a) Schematic representing thermally assisted quantum tunneling. b) Effect on energy wells under the application of a DC field. Degeneracy of the M_S states is broken, and quantum tunneling is suppressed. c) Further application of a DC field which can result in aligning of M_S microstates of differing M_S values, resulting in the potential for quantum tunneling to once again be allowed. Adapted with permission by John Wiley and Sons: Angewandte Chemie International Edition from reference 15, copyright 2003.

One of the biggest problems in this field is the suppression of quantum tunneling in these molecules. A main approach is to impose certain geometries on the metal center

via ligand coordination. Purely axial symmetry that is trigonally symmetric or higher completely suppresses quantum tunneling as the process is forbidden.[19-20] Even small deviations from perfect symmetry, however, allow for quantum tunneling to become operative. Perfect geometries are difficult to achieve, so this method is not always sufficient. An alternate method is to apply a DC field to the compound while taking AC measurements. Such a field results in a breaking of the degeneracy of the sublevels, suppressing quantum tunneling.[21] However, the distortion of the two wells can become so much that two different sublevels become degenerate, and quantum tunneling is once again promoted, Figure I.8. For this reason, a test of the DC fields is required to ascertain at which field the best SMM behavior can be observed. Admittedly, for true magnetic bistability to be observed, a field should not be necessary, and those that do require one are often referred to as field-induced SMMs. Another method to minimize quantum tunneling is to use Kramer's doublets, or systems with half-integer spin. In this case, the doublet degeneracy can help suppress quantum tunneling.[17, 22]

With the goals of increasing spin-orbit coupling, and subsequently the ZFS parameter, the field of mononuclear SMMs, also known as single ion magnets, began to flourish. In this case, one metal center is responsible for the interesting magnetic behavior rather than a collection of coupled metal spin centers. Research in this area has rapidly expanded to include metals across the transition metal block, as well as with key examples in the lanthanides and actinides. To date, mononuclear SMMs have been reported for the following metal ions: Cr^{II}, Mn^{III}, Fe^{III}, Fe^{II}, Fe^{I}, Co^{II}, Co^{I}, Ni^{II}, Ni^{I}, Cu^{III}, Re^{IV}, Ce^{III}, Nd^{III}, Tb^{III}, Dy^{III}, Ho^{III}, Er^{III}, Tm^{III}, Yb^{III}, U^{III}, U^{V}, Np^{III}, and Pu^{III}.[23] The majority of mononuclear

SMMs are based on 3d metals and the lanthanide metals.

SMMs have applications in quantum computing and spintronics, and progress towards these goals is contingent on identifying molecules that could be useful for devices in the future. Namely, the possibility of these applications is contingent upon increasing the operating temperature of single molecule magnets to, at least, liquid nitrogen temperatures and long relaxation times without quantum tunneling of the magnetization. The true "holy grail" of magnetism is the isolation of an SMM that operates at room temperature. In the following sections, the design basis and records for 3d and lanthanide metal based categories of SMMs are discussed in reference to this goal of designing higher operating temperature SMMs.

I.3 3d Metal Single Molecule Magnets

The field of 3d metal, mononuclear SMMs began in 2010 with the discovery by Long *et al.* of slow magnetic relaxation in a high spin Fe(II) trigonal monopyramidal complex: K[(tpa^{Mes})Fe] (tpa = tris(pyrrolyl-α-methyl)amine), Figure I.9.[24] The geometry around the metal center is enforced by an N_4 coordination sphere. For the first time, slow magnetic relaxation was observed in a mononuclear, 3d metal based system, a remarkable advance in the field. The authors report a barrier of U_{eff} = 42 cm^{-1} under an applied DC field of 1500 Oe. No χ" signal was observed under zero applied DC field, which was attributed to the small rhombic ZFS parameter caused by distortions from trigonal symmetry, as well as the low spin state due which increases the probability for quantum tunneling. The D value is a remarkable -39.6 cm^{-1}, resulting in a maximum possible barrier height (U) of 158 cm^{-1}. The E value is a small -0.4 cm^{-1}. Although the actual thermal

barrier is much lower due to alternate relaxation methods, the large, negative D value and observable slow magnetic relaxation confirmed the plausibility of designing molecules with inherently large ZFS parameters in mind. Quickly thereafter, a series of these trigonal monopyramidal complexes was published, also by the Long group, with various electron donating and withdrawing groups decorating the end of the tpa ligands.[25] Interestingly, the only compound in the series with crystallographically imposed trigonal symmetry about the metal center exhibits the highest barrier of the entire series. Theoretical analysis of these compounds revealed a direct correlation between the sigma donor ability (e_σ^e) and the magnitude of the ZFS parameter.[26]

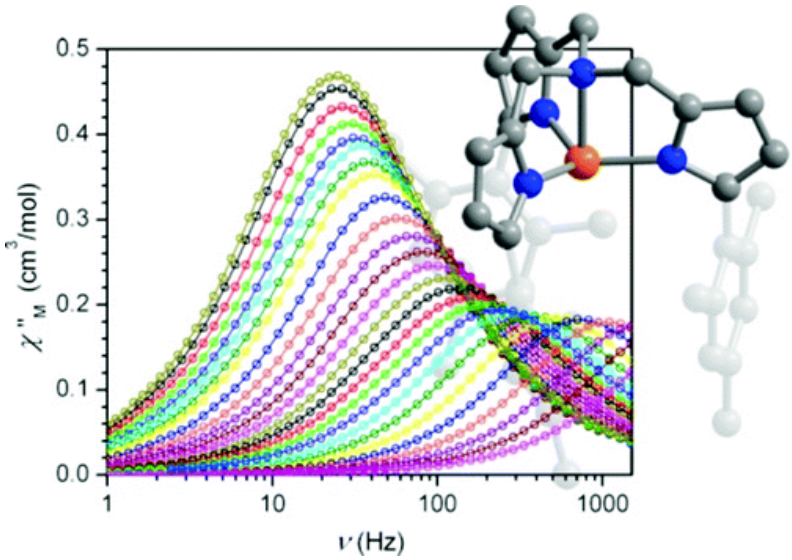

Figure I.9 Simplified structure and slow magnetic relaxation for the compound. Hydrogen atoms are omitted for clarity. Colors are as follows: orange, Fe; grey, C; blue, N. Reproduced with permission by American Chemical Society: Journal of the American Chemical Society from reference 18, copyright 2010.

As the research continued, it was discovered in 2011 that the sign of D does not have to be negative to observe SMM behavior. The compound [(3G)CoCl](CF_3SO_3) (3G = 1,1,1-tris-[2N-(1,1,3,3-tetramethylguanidino)methyl]ethane) was probed by high-field EPR spectroscopy which revealed a positive D value of 12.7 cm^{-1}.[27] In this case, the M_S = ±1/2 sublevel is lower in energy than the M_S = ±3/2 sublevel. AC magnetic studies resulted in slow magnetic relaxation with a U_{eff} = 24 cm^{-1} and τ_o = 1.9 x 10^{-10} s. In the case that D is positive, the molecule has easy plane, rather than easy axis, anisotropy. This means that the magnetization preferentially lies in a plane rather than along an axis. Given that a positive D value is the result of smaller M_S sublevels lying lower in energy than higher M_S sublevels, this has the effect of turning the double well potential diagram on its head, Figure I.10.

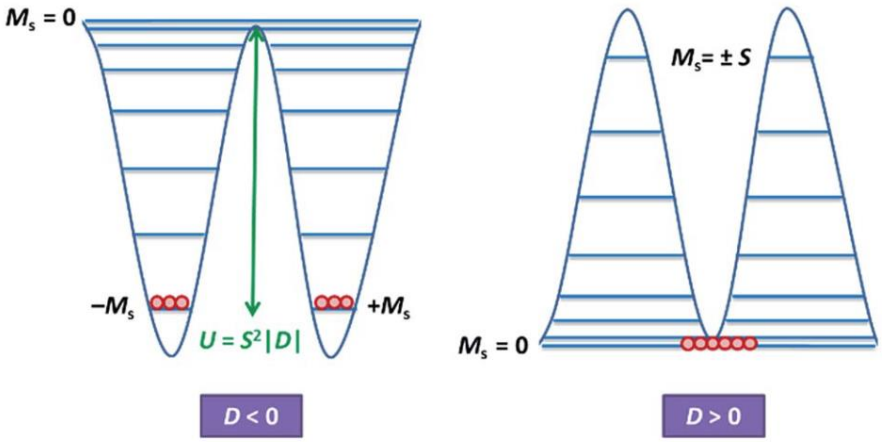

Figure I.10 Effect of positive D compared to negative D on the double well energy diagram for SMMs. Reproduced with permission by Royal Society of Chemistry: Chemical Science from reference 11, Copyright 2015.

Many examples of this phenomenon have been reported to date, but in each case an applied field is required to observe any slow magnetic relaxation.[27-36] The reasoning behind the observation is a topic that continues to be debated within the magnetism community. Some potential theories that have been presented include a phonon bottle neck which traps the relaxing spins by reducing the number of vibrational modes that the spins can use to relax,[27] spin flip controlled by, and the effective barrier defined by, the E (rhombic) zero-field splitting parameter,[28] and acoustic and optical Raman processes.[33] The majority of complexes exhibiting a positive D value are Co^{II} ions, though recently a few Re^{IV} species have been shown to exhibit positive D values as well.[37-39] Remarkably, it is possible for these complexes to exhibit waist-restricted hysteresis, wherein the curve is open at each end of the highest fields, but not in the middle, Figure I.11.[28]

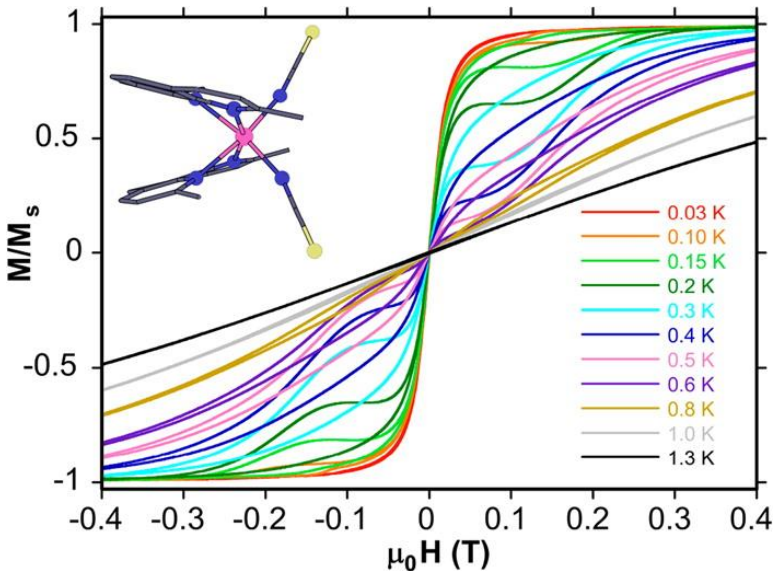

Figure I.11 Waist-restricted hysteresis observed in the shown molecule which exhibits a positive D value of 98 cm^{-1}. Reproduced with permission by American Chemical Society: Journal of the American Chemical Society from reference 22, copyright 2012.

At this stage, it became obvious that there is a need to predict which metals, oxidation states, and geometries would be most promising to pursue out of the wide myriad of possibilities available. In an attempt to tackle this problem, Ruiz *et al.* published a paper in 2013 describing a theoretical investigation of numerous possible combinations.[40] The base model for their calculations was a $Fe^{II}(NH_3)_x$ complex, from which they varied electron configurations from d^1 to d^9 in combination with 31 different geometries, Table I-1. The Jahn-Teller distortions of the complexes were calculated, and the resulting orbital energies and the orbitals involved in the first excitation were subsequently calculated. The main results are predictions of the sign and magnitude of the D values. Complexes with large positive or negative D values should be promising to pursue as potential SMMs. The origin of the sign of D comes from the orbitals that are involved in the first excitation. If that excitation takes place between two orbitals with the same $|m_l|$ values, d_{xy} and $d_{x^2-y^2}$ ($m_l = \pm 2$) or d_{xz} and d_{yz} ($m_l = \pm 1$), then the sign of D will be negative. If the excitation occurs between two orbitals with different m_l values, then the sign of D will be positive. The magnitude of D is determined by the excitation energy of the first excitation. The smaller that energy, the larger |D| becomes, Figure I.12. Upon comparison to published examples, the predictions appear to generally be correct. For example, the first 3d SMM, which is d^6 trigonal monopyramidal, is predicted to lead to a large, negative D value.

Table I-1 Estimation of the D values for high spin mononuclear transition metal complexes with different electronic configurations and coordination modes using ammonia ligands (using the molecular orbitals of $Fe^{II}(NH_3)_x$ models)[a]. Reproduced with permission by American Chemical Society: Journal of the American Chemical Society from reference 34, copyright 2012.

[a]Green and blue squares indicate large and small negative values, in that order, while red and orange represent large and small positive values, respectively. Cases with more than one color indicate that the nondistorted structure has a zero D value, and different options are possible depending on the symmetry of the Jahn-Teller distortion.

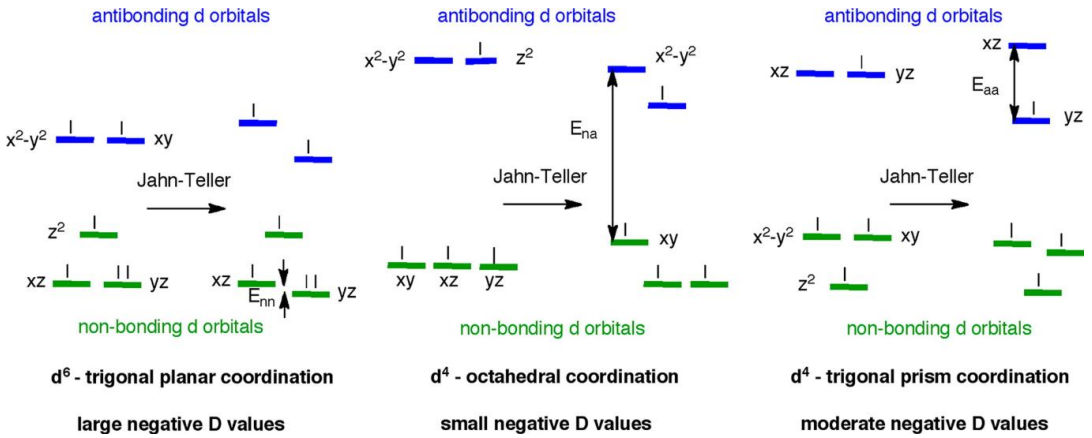

Figure I.12 Splitting of the d orbitals due to the Jahn−Teller effect for three cases with negative D values: d^6-trigonal planar coordination (left), d^4-octahedral coordination (middle), and d4-prism trigonal coordination (right). The energy difference indicated by the arrow in each case corresponds to the first excitation that leads to the main contribution to D_{zz}. The smaller the excitation energy, the larger |D| becomes. Reproduced with permission by American Chemical Society: Journal of the American Chemical Society from reference 34, copyright 2012.

Based on literature predictions such as the previous example, as well as experimental evidence, the field quickly began to focus on unusual geometries that are promising for SMM behavior. With the publication of a tetrahedral Co^{II} compound in 2011, $(Ph_4P)_2Co(SPh)_4$, slow magnetic relaxation was observed in a 3d metal mononuclear SMM in the absence an applied DC field.[41] This was a big step forward as it verified that 3d metal based SMMs could indeed exhibit SMM behavior. New records for various 3d metals began to appear in literature. The most notable examples to date are [K(crypt-222)][$Fe^{I}(C(TMS)_3)_2$] with a U_{eff} barrier of 226 cm^{-1},[42] [(sIPr)Co^{II}NDmp] with a U_{eff} barrier of 413 cm^{-1},[43] and most recently, $Co^{II}(C(SiMe_2ONaphthyl)_3)_2$ with a U_{eff} barrier of 450 cm^{-1}.[44] Both cobalt complexes exhibit magnetic hysteresis.

I.4 Lanthanide Metal Single Molecule Magnets

The first mononuclear SMM in the literature was the report of [TBA][Pc_2Tb] in 2003.[45] This molecule exhibited a remarkable barrier of 260 cm^{-1}, significantly surpassing the barriers of any polynuclear SMMs that had been reported at the time. However, the description of the barrier height as $S^2|D|$ is not applicable to such a highly anisotropic system owing to the fact that lanthanide and actinide molecules exhibit strong first order spin-orbit coupling. The spin value S is longer a valid quantum number to describe the sublevels causing the thermal barrier.

When considering 3d metal systems, the energy of the sublevels is usually primarily determined by the ligand field, and secondly by spin orbit coupling. However, in lanthanides, the opposite is true, Figure I.13.[9] Electron interactions still establish the ground state term. However, next the Russel Saunders term must be used to describe the splitting of the orbitals due to spin orbit coupling, formatted as $^{2S+1}L_J$. S is the total spin of the system and J is the total angular momentum quantum number which takes on the values of |L+S| to |L-S|. The degeneracy of the $^{2S+1}L_J$ states is broken by the spin-orbit coupling according to the equation:

$$E_{S.O.} = \left(\frac{\lambda}{2}\right)[J(J+1) - L(L+1) - S(S+1)]$$

where λ is the spin-orbit coupling constant.[46] The ordering of these states is determined by the maximum S allowed given the Pauli Exclusion Principle and Hund's rule. L is determined by applying the maximum value, and going down from there. If the f orbitals in lanthanides are less than half filled, then the smallest J value is lowest in energy. If the f orbitals are greater than half filled, then the largest J value is lowest in energy.[47]

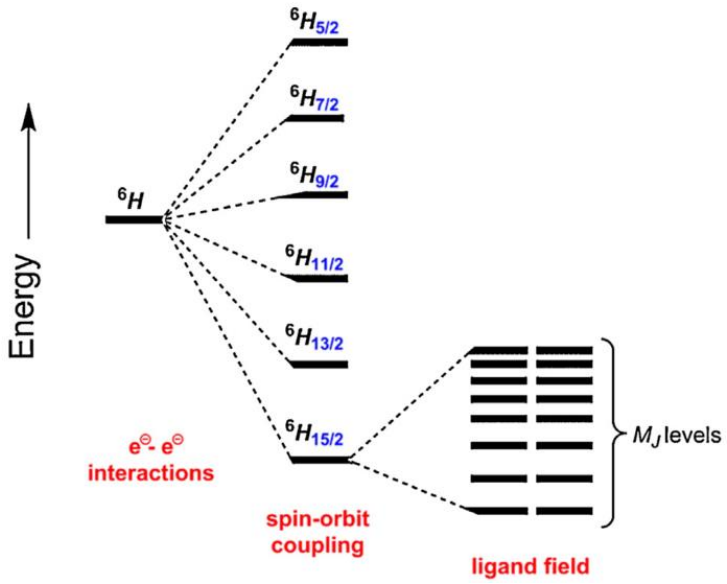

Figure I.13 The 2J+1 sublevels with quantum number M_J created by the effect of a ligand field on the $^6H_{15/2}$ ground state of a Dysprosium(III) ion. Not all ^6H_J states of the Dysprosium(III) ion are shown. The sixteen M_J sublevels of $^6H_{15/2}$ are arranged in eight Kramers doublets. Reproduced with permission by Elsevier: Coordination Chemistry Reviews from reference 7, copyright 2008.

The lowest energy $^{2S+1}L_J$ state is subsequently split into M_J sublevels from +J to –J due to interactions with the ligand field. The ordering of these microstates is determined by interactions between the electrons from the ligand with the electron cloud of the lanthanide metal center. In this case, the largest M_J state can be stabilized by minimizing these interactions. These M_J states are the basis for the thermals barrier that allow lanthanide complexes to behave as SMMs. In summary, rather than the M_S microstates which define the barrier for transition metal based SMMs, M_J microstates define the barrier for lanthanide metal based SMMs, Figure I.14.[48] In the ideal scenario, the highest M_J state will be lowest in energy, and there will be no mixing between M_J states.

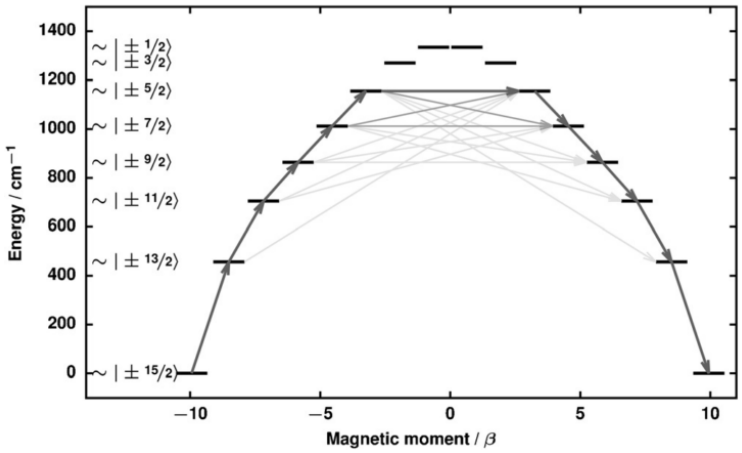

Figure I.14 Energy barrier for a dysprosium(III) SMM, which is defined by the M_J sublevels. Reproduced with permission by John Wiley and Sons: Angewandte Chemie International Edition from reference 42, Copyright 2017.

Since the discovery of the first lanthanide mononuclear SMM in 2004, the field has evolved to make predictions about how to synthesize improved magnets. The theoretical basis for this improvement was first proposed in 2011 by Rinehart and Long who described two classifications of lanthanide metals based on the shape of their electron clouds: oblate and prolate, Figure I.15.[49] The oblate lanthanides are defined by 4f electron clouds that are compressed in the axial direction, resulting in short and wide electron clouds. The prolate lanthanides are defined by compression in the equatorial direction, resulting in tall and thin electron clouds. The oblate lanthanide metals include trivalent Ce, Pr, Nd, Tb, Dy, and Ho ions. The prolate lanthanide metals include trivalent Pm, Sm, Er, Tm, and Yb ions. Eu is neither due to a J=0 ground state, and Gd and Lu are isotropic due to half and fully filled 4f electron counts, respectively.

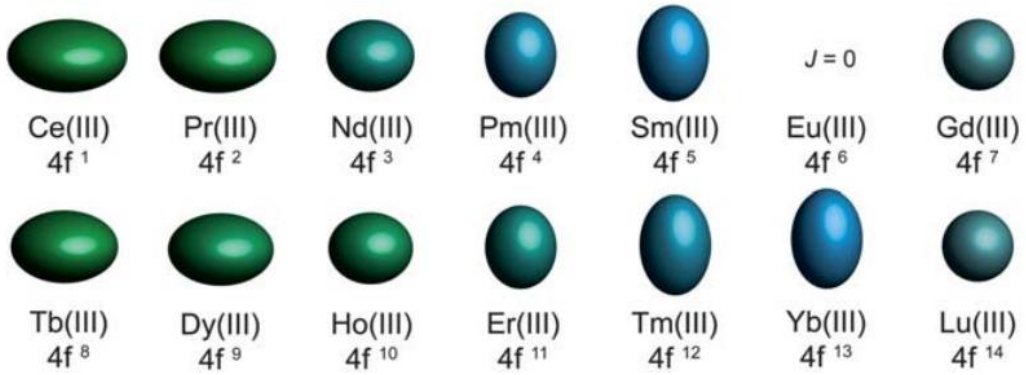

Figure I.15 Quadrupole approximations of the 4f-shell electron distribution for the tripositive lanthanides. Values are calculated using the total angular momentum quantum number (J), the Stevens coefficient of second order (α) and the radius of the 4f shell squared ‹r^2›. Europium is not depicted due to a J = 0 ground state. Reproduced with permission by the Royal Society of Chemistry: Chemical Science from reference 43, Copyright 2011.

As previously mentioned, a way to lower the energy of the ground M_J state is through minimal interaction between the electron clouds of the ligand and the metal center. As demonstrated by Rinehart and Long, for oblate lanthanide ions, this is in the form of axial coordination. For prolate lanthanide ions, this is in the form of equatorial coordination, Figure I.16. This simple basis is the foundation upon which great strides have been made in the field, with lanthanide based SMMs continually holding and breaking the current records for T_b in all SMMs.

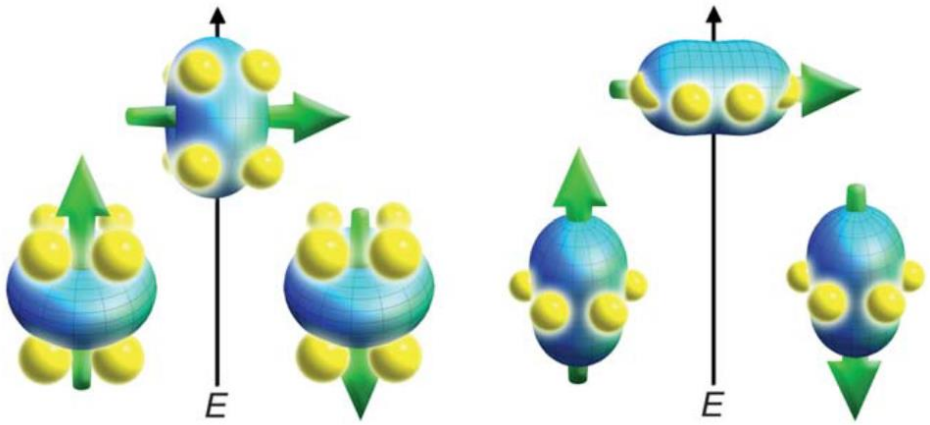

Figure I.16 Depictions of low- and high-energy configurations of the f-orbital electron density with respect to the crystal field environment for a 4f ion of oblate (left) and prolate (right) electron density. The green arrow represents the orientation of the spin angular momentum coupled to the orbital moment. For the oblate electron density, an axial ‘‘sandwich’’ type crystal field minimizes the energy of the $M_J = J$ (high moment) state, making it a desirable target for single-molecule magnet design. In the prolate electron density case, an equatorial electron configuration minimizes the energy of the $M_J = J$ state. Reproduced with permission by the Royal Society of Chemistry: Chemical Science from reference 43, Copyright 2011.

Due to the reliance of the energy barrier on interactions with the crystal field, geometric control is just as important for lanthanide based SMMs as it is for transition metal based SMMs. A major breakthrough for mononuclear SMMs came in 2011 with the publication of $[K(18\text{-crown-}6)(THF)_2]$ $[([(Me_3Si)_2N]_2(THF)Tb)_2(\mu\text{-}\eta^2\text{:}\eta^2\text{-}N_2)]$ which exhibits hysteresis up to 14 K.[50] In 2013, a new record for mononuclear SMMs appeared in the literature with $(Zn_2Dy(L^{12})_2(MeOH)]NO_3\cdot 3MeOH\cdot H_2O$ (L^{12}=2,2’,2’’-(((nitrilo-tris(ethane-2,1-diyl))tris(azanediyl))tris(methylene))tris-(4-bromo-phenol)) which exhibits hysteresis up to 11 K.[51] In 2016, the T_b record jumped to 20 K with the report of a mononuclear Dy SMM in D_{5h} symmetry: $[Dy(Cy_3PO)_2(H_2O)_5]Br_3\cdot 2(Cy_3PO)\cdot 2H_2O\cdot 2EtOH$.[52] The record U_{eff} barrier also increased to unprecedented

temperatures in 2016 with the report of [Dy(bbpen)Br] (bbpen = N,N′-bis(2-hydroxybenzyl)-N,N′-bis(2-methylpyridyl)ethylenediamine) which exhibits a U_{eff} barrier of 1,025 K and hysteresis up to 14 K.[53] These records held until 2017 when the barrier jumped to an incredible 60 K with the simultaneous reporting of $[Dy(Cp^{ttt})_2][B(C_6F_5)_4]$ ($Cp^{ttt} = C_5H_2{}^tBu_3$-1,2,4) by the Chilton and Layfield groups.[48, 54] This was very exciting as 60 is getting close to the goal of 77 K, which is liquid nitrogen temperature. The goal of 77 K was met and exceeded very recently in 2018 with the report of $[(\eta^5\text{-}Cp^*)Dy(\eta^5\text{-}Cp^{iPr5})][B(C_6F_5)_4]$, which exhibits hysteresis up to 80 K, Figure I.17.[55] These records are exemplary examples of how careful control over the coordination geometry in lanthanide ion based SMMs can result in exceptional performance in SMMs. The current focus is not only to further improve these records, but to explore new geometries and modes of relaxation in lanthanide based SMMs. Also of great importance is the air stability of the compounds, which is typically not the case for the record holders.

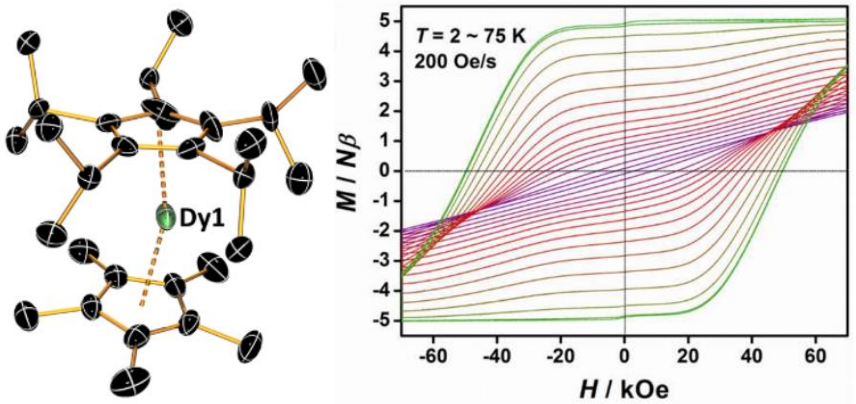

Figure I.17 Left: Crystal structure of $[(\eta^5\text{-}Cp^*)Dy(\eta^5\text{-}Cp^{iPr5})][B(C_6F_5)_4]$. Hydrogen atoms and counter-anion are omitted for clarity. Colors are as follows: black, C; Green, Dy. Right: Magnetization vs. field hysteresis loops in the temperature ranges of 2 to 75 K using a field sweep rate of 200 Oe s^{-1}. Reproduced with permission by The American Association for the Advancement of Science: Science from reference 49, copyright 2018.

I.5 Summary of Work

The preceding summary of the origin and history of single molecule magnets, while not comprehensive, serves as the backdrop and foundation for the research presented in the following chapters. Where appropriate, more specific details and history of SMMs will be discussed in each of the chapters. Chapter II describes two different series: the first comprises of six divalent Fe, Co, and Ni complexes in trigonal mono- and bi-pyramidal geometries. The effect of this small, but significant geometry change on SMM behavior is explored. The second series is that of four divalent Co^{II} trigonal bipyramidal complexes in which the electron donating and withdrawing properties of the ligand are varied with the resulting magnetic properties being compared. Chapter III details the synthesis and magnetic behavior of a series of Co^{II} molecules that are partially or fully encapsulated by cage-like structures. The differences in magnetic behavior due to these ligand enclosures and accompanying halide coordination is described. Chapter IV explores Ti^{IV} as a new inorganic metal ligand, and describes the magnetic properties of a series of divalent Mn, Fe, Co, and Ni complexes. This research is a continuation of work started by Andrew Brown at the end of his Ph.D. studies. Chapter V involves the chemistry of an extremely rare geometry for lanthanide based SMMs, namely cubic. Structural and magnetic characterization data were collected on a series of four complexes and are described.

CHAPTER II

EFFECTS OF COORDINATION SPHERE AND LIGAND DONOR STRENGTH ON THE MAGNETISM OF TRIGONALLY SYMMETRIC MOLECULES*

II.1 Introduction

In the presence of axial magnetic anisotropy, the total spin, S, of a system will split into a bistable ground state of the microstates $+m_s$ and $-m_s$. A thermal barrier exists between these levels which must be overcome to reverse the orientation of the spins (U or ΔE), which is defined as $U = |D|S^2$ for integer spins, or $U = |D|(S^2-1/4)$ for non-integer spin systems in the case of second order or quenched spin-orbit coupling effects. After application and subsequent removal of a DC field, this barrier results in magnetic memory and hysteresis reminiscent of bulk magnetic materials. Single Molecule Magnets (SMMs) have applications in quantum computing, spin transistors, and data storage.[6, 56-57] While the Orbach relaxation process over the barrier is the ideal pathway, relaxation also occurs via Raman and quantum tunneling processes which undercut the barrier resulting in a lower blocking temperature.[17] The effective barrier, or U_{eff}, is the experimentally observed barrier described only by the Orbach relaxation process.

After the first recognition in 1993 of a Singe Molecule Magnet (SMM) in the case of $[Mn_{12}O_{12}(OAc)_{16}(H_2O)_4]$[5], known as $Mn_{12}OAc$, attention quickly turned towards

* Reproduced with permission from "Effects of coordination sphere on unusually large zero field splitting and slow magnetic relaxation in trigonally symmetric molecules" Schulte, K. A.; Vignesh, K. R.; Dunbar, K. R. *Chemical Science*, **2018**, *9*, 9018. Reproduced by permission of the Royal Society of Chemistry.

increasing the barrier by increasing the spin of the system. It has largely been the case, however, that even significant increases in the ground spin state do not result in the expected increase in barrier height, with a prominent example being an S = 83/2 system that exhibits a barrier of U_{eff} = 4 cm^{-1}.[14] Relying on exchange interactions in polynuclear systems has led to the successful increase in S values but with a concomitant decrease in *D*,[16, 58] resulting in lower barriers. Clearly increasing the axial anisotropy is vital to increasing the operating temperature of SMMs.

In this vein, recent focus has been on the single molecule magnet behavior of mononuclear complexes for which spin orbit coupling can be maximized.[23] Mononuclear complexes hold the recent hysteresis records of 20 K[52] and 60 K.[48, 54] While rare-earth SMMs exhibit the highest barriers, several 3d metal complexes have been found to exhibit barriers similar to their lanthanide counterparts. Complexes of d-block elements have the distinct advantage of being highly tunable, such that strict control over magnetic anisotropy is feasible, making them highly promising targets as well.

The first reported mononuclear 3d SMM is the trigonal monopyramidal Fe(II) complex K[(tpa^{Mes})Fe] (tpa = tris(pyrrolyl-α-methyl)amine).[24] Since this finding and the subsequent exploration of a family with various tpa^{R} ligands[25], many more 3d SMMs have been reported. To date, first row transition metal SMM behavior has been observed in complexes of Cr^{II}, Mn^{III}, $Fe^{I,II,III}$, $Co^{I,II}$, $Ni^{I,II}$, and Cu^{III}.[23] The U_{eff} barriers above 100 cm^{-1} have been found in complexes with coordination numbers of 2-4,[43, 59-63] a clear indication that low coordinate and highly symmetric 3d SMMs are worth pursuing. The current records for Fe, Co, and Ni are [K(crypt-222)][$Fe^{I}(C(TMS)_3)_2$],[60] [(sIPr)Co^{II}NDmp] (Dmp

= 2,6-dimesitylphenyl),[43] and $[Ni^{II}(MDABCO)_2Cl_3]ClO_4$ (MDABCO = 1-methyl-4-aza-1-azo-niabicyclo[2.2.2]octanium)[64] with barriers of 226, 413, 48 cm^{-1} respectively. Although the barrier of $[Ni^{II}(MDABCO)_2Cl_3]ClO_4$ is not particularly large, the zero field splitting parameter (D) is a record holding -535 cm^{-1}. The iron and cobalt complexes are both linear molecules, and the nickel complex is in a trigonal bipyramidal geometry.

In line with these trends in literature as well as theoretical predictions by Ruiz et al.,[40] the work described in this chapter involves the pursuit of complexes containing $3d^6$, $3d^7$, and $3d^8$ metal centers in trigonal monopyramidal or bipyramidal geometries. These complexes are expected to lead to large negative D values for $d^{6,8}$ and large positive D values for d^7 complexes. Previously, the Dunbar group has demonstrated that both trigonal monopyramidal[18] (TMP) and bipyramidal[65] (TBP) geometries can indeed lead to slow magnetic relaxation. These studies also unearthed the fact that very small perturbations in symmetry and metal to metal distances have a distinct effect on magnetic behavior for compounds in the same geometry.[65]

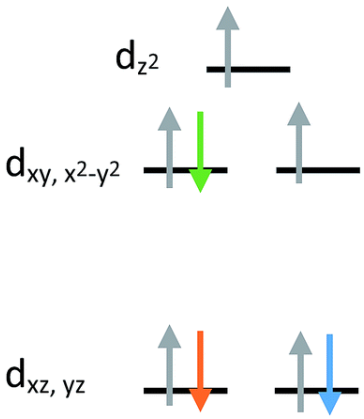

Figure II.1 Crystal field splitting diagram for divalent iron, cobalt and nickel in ideal trigonal mono and bipyramidal geometries, as indicated by the orange, blue, and green electron arrows. Reprinted by permission from reference 98.

The current aim is to further explore the effect of specific coordination changes across a series. To this end, a comparison of TMP and TBP complexes was pursued. The crystal field splitting diagram for these geometries can be found in Figure II.1, for which divalent iron, cobalt, and nickel complexes have total spins, S, of 2, 3/2, and 1 respectively. The energies of the orbitals differ between the two geometries due to additional coordination in the second axial position, but the relative order remains the same with the $d_{xz,yz}$ orbitals being the lowest in energy, followed by the d_{xy},$d_{x^2-y^2}$ orbitals, and finally by the d_{z^2} orbital at the highest energy. Ideally, this geometry will lead to first order spin-orbit coupling in the iron and nickel complexes, generating large axial anisotropies, but the reality is that Jahn-teller distortions will result in a breaking of the degeneracy of these orbitals and subsequent quenching of first order spin orbit coupling. A strategy for minimizing the effects of these distortions is to use rigid, bulky ligands in an effort to isolate a near perfect geometry. To this end, it is prudent to choose a polydentate ligand that binds to all four of the positions of the TMP geometry. In this case, one can also prepare five-coordinate TBP adducts with the second axial position being occupied.

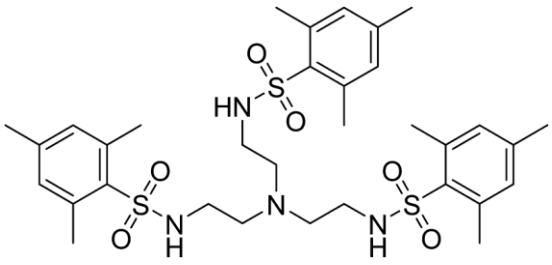

Figure II.2 Structural formula of the neutral ligand N,N',N''-[nitrilotris(ethane-2,1-diyl)]tris(2,4,6-trimethylbenzenesulfonamide) [H_3MST]. Reprinted by permission from reference 98.

The tetradentate ligand N,N′,N″-[2,2′,2″-nitrilotris-(ethane-2,1-diyl)]tris(2,4,6-trimethylbenzenesulfonamide) [H_3MST], first reported by the Borovik group in research with iron and cobalt metal ions, nicely fits these requirements, Figure II.2.[66-67] They focused on using these to mimic active sites in biologically relevant proteins and enzymes such as nonheme iron-containing monooxygenases and secondary coordination spheres in metalloproteins.[66, 68-69] In the present work with 3d metals, the steric bulk of the mesityl substituents enforces trigonal monopyramidal geometry with an open axial position. Subsequent coordination of a water molecule in the second axial position results in the trigonal bipyramidal geometry. Herein, experimental and computational studies are reported in order to understand the magnetic behavior of six compounds, *viz.*, (Me_4N)[Co(MST)], (Me_4N)[Co(MST)(OH_2)], (Me_4N)[Fe(MST)], (Me_4N)[Fe(MST)(OH_2)], (Me_4N)[Ni(MST)], and (Me_4N)[Ni(MST)(OH_2)].

II.2 MST Complexes Experimental Details

II.2.1 Complex Synthesis

All syntheses were conducted under a N_2 atmosphere. Anhydrous complexes were synthesized in an MBRAUN glovebox under rigorous anhydrous conditions. The synthesis of the water complexes took place in a Vacuum Atmosphere glovebox with the catalyst turned off so that it was not a totally dry atmosphere. Commercial anhydrous dimethylacetamide (DMA) was dried over BaO, and stored in the drybox over molecular sieves. Diethyl ether was purified using an MBRAUN purification system and stored over 3Å molecular sieves. Dichloromethane (DCM) was dried over P_2O_5 and stored over 3Å molecular sieves. Diethyl ether and dichloromethane in the purge box were degassed with

an Argon stream. $Co(OAc)_2$, $Fe(OAc)_2$ and NaH were purchased from VWR and used as received. $Ni(OAc)_2 \cdot 4H_2O$ and Me_4NOAc were dried under vacuum at 100°C overnight. Dryness was confirmed for each of these starting materials using infrared spectroscopy. The ligand H_3[MST] was synthesized according to literature procedures.[66] Syntheses of the $(Me_4N)[M^{II}(MST)]$ and $(Me_4N)[M^{II}(MST)(OH_2)]$ complexes were performed with modified procedures from literature;[66-68] the details are provided in the following sections.

(Me_4N)[Co(MST)] (**1**). A 20 mL vial was charged with H_3[MST] (300 mg, 0.43 mmol), NaH (31.2 mg, 1.30 mmol), Me_4NOAc (86.4 mg, 0.65 mmol), and DMA (5 mL). The reaction was stirred until all of the NaH had reacted. $Co(OAc)_2$ (76.5 mg, 0.43 mmol) was added to the reaction and the mixture was stirred for overnight to give a dark pink solution which was subsequently filtered over a fine frit. Crystals were obtained via diethyl ether diffusion into the DMA solution. The crystals were further purified by dissolution in dichloromethane and filtration over a fine frit. Slow diffusion of diethyl ether resulted in sky blue crystals (181 mg, 51% yield). Analysis calculated for (Me_4N)[Co(MST)] ($C_{37}H_{57}CoN_5O_6S_3$): C: 54.00%, H: 6.98%, N: 8.51%. Found: C: 53.77%, H: 7.25%, N: 8.31%.

(Me_4N)[Co(MST)(OH_2)]•DCM (**2**). Crystals of **1** were dissolved in dichloromethane and water was added dropwise to the rapidly stirring solution until it turned bright pink. Slow diffusion of diethyl ether resulted in the isolation of pink crystals (166 mg, 90% yield). Analysis calculated for (Me_4N)[Co(MST)(OH_2)]•DCM ($C_{38}H_{61}Cl_2CoN_5O_7S_3$): C: 49.29%, H: 6.64%, N: 7.56%. Found: C: 49.53%, H: 6.64%, N: 7.64%.

(Me_4N)[Fe(MST)] (**3**). **3** was synthesized in a manner akin to **1** using $Fe(OAc)_2$ (74.8 mg, 0.43 mmol), H_3[MST] (300 mg, 0.43 mmol), NaH (31.2 mg, 1.30 mmol), Me_4NOAc (86.4 mg, 0.65 mmol), and DMA (5 mL). Pale yellow-to-colorless crystals suitable for x-ray analysis were obtained via slow diffusion of diethyl ether into the original DMA solution (194 mg, 55% yield). Analysis calculated for (Me_4N)[Fe(MST)] ($C_{37}H_{57}FeN_5O_6S_3$): C: 54.20%, H: 7.01%, N: 8.54%. Found: C: 54.38%, H: 7.28%, N: 8.03%.

(Me_4N)[Fe(MST)(OH_2)] (**4**). To a solution of **3** in DMA was added 10 µL of water. Pale yellow crystals suitable for x-ray analysis were obtained via slow diffusion of diethyl ether into the DMA solution (172 mg, 87% yield). Analysis calculated for (Me_4N)[Fe(MST)(OH_2)] ($C_{37}H_{57}FeN_5O_6S_3$): C: 52.04%, H: 7.10%, N: 6.66%. Found: C: 52.85%, H: 7.32%, N: 8.09%.

(Me_4N)[Ni(MST)] (**5**). **5** was synthesized in a manner analagous to **1** using $Ni(OAc)_2$ (76.0 mg, 0.43 mmol), H_3[MST] (300 mg, 0.43 mmol), NaH (31.2 mg, 1.30 mmol), Me_4NOAc (86.4 mg, 0.65 mmol), and DMA (5 mL). Salmon colored crystals suitable for x-ray analysis were obtained via slow diffusion of diethyl ether into the original DMA solution (134 mg, 38% yield). Analysis calculated for (Me_4N)[Ni(MST)] ($C_{37}H_{57}NiN_5O_6S_3$): C: 54.01%, H: 6.98%, N: 8.51%. Found: C: 54.24%, H: 6.75%, N: 8.21%. Yield can be increased by adding DCM to the solid which was collected by filtration and re-filtering the orange solution. Crystals were grown via slow diffusion of diethyl ether into the DCM solution (184mg, 52% total yield).

(Me_4N)[Ni(MST)(OH_2)] (**6**). To a stirred solution of **5** in DMA, water was added dropwise until the solution turned green. Green crystals suitable for x-ray analysis were

obtained via slow diffusion of diethyl ether into the DMA solution (175 mg, 93% yield). Analysis calculated for $(Me_4N)[Ni(MST)(OH_2)]\bullet H_2O$ ($C_{37}H_{57}NiN_5O_6S_3$): C: 51.75%, H: 7.16%, N: 8.16%. Found: C:51.38%, H: 7.54%, N: 7.77%.

II.2.2 Crystallography

Structural characterization was performed with single crystals on Bruker QUEST and VENTURE instruments with Mo Kα and microfocus Cu Kα sources respectively. Compounds **1**, **2**, and **6** were collected on the VENTURE instrument equipped with a CMOS detector and **3**, **4**, and **5** were collected on the QUEST instrument equipped with a CCD detector. Suitable crystals were mounted on MiTeGen microloops using ®Paratone oil and placed in a cold stream of N_2 for collection at 100 K. The collected data was integrated within the APEX 2 software suite, as well as SADABS for absorbance corrections.[70] The structures were solved and refined using SHELXT[71] and SHELXL[72] respectively within the OLEX program.[73] Hydrogen atoms were added in calculated positions. In some cases, reorientations of hydrogen atoms were performed to match visible electron density as well as due to obvious hydrogen bonding interactions.

All non-hydrogen atoms were refined anisotropically, with the exception of disordered solvent in **2**. The structure of **2** exhibits disordered dichloromethane over two positions in a ratio of 85:15. The major component of the disorder could be modelled anisotropically, whereas the minor component could only be refined isotropically. The SIMU and SADI restraints were necessary in order to achieve a reasonable model of the disorder. Structures **4** and **6** exhibit disorder in the $[Me_4N]^+$ cation. For **4**, three of the methyl groups rotate around an axis between the central carbon and remaining methyl

group. The two parts exist in a 51:49 ratio. The same type of disorder exists in **6**, but with one orientation being preferred 77% of the time. Further crystallographic details can be found in Table II-1.

Table II-1 Crystal structure data and refinement parameters for $(Me^4N)[M^{II}(MST)]$ and $(Me^4N)[M^{II}(MST)(OH_2)]$ complexes. Reprinted by permission from reference 98.

Identification code	$(Me_4N)[Co(MST)]$	$(Me_4N)[Co(MST)(OH_2)]$
Empirical formula	$C_{37}H_{57}CoN_5O_6S_3$	$C_{38}H_{63}Cl_2CoN_5O_8S_3$
Formula weight	822.98	943.94
Temperature/K	100	100
Crystal system	monoclinic	triclinic
Space group	$P2_1/n$	P-1
a/Å	21.1512(8)	8.8767(7)
b/Å	9.0244(4)	14.5893(11)
c/Å	21.2686(9)	19.0022(14)
α/°	90	107.139(2)
β/°	95.072(2)	97.232(2)
γ/°	90	101.356(2)
Volume/Å^3	4043.8(3)	2260.7(3)
Z	4	2
ρ_{calc}g/cm^3	1.352	1.387
μ/mm^{-1}	5.18	5.799
F(000)	1748	998
Crystal size/mm^3	0.693 × 0.079 × 0.036	0.548 × 0.103 × 0.088
Radiation	CuKα (λ = 1.54178)	CuKα (λ = 1.54178)
2Θ range for data collection/°	5.648 to 130.166	4.962 to 136.062
Index ranges	$-24 \le h \le 24$, $-10 \le k \le 10$, $-24 \le l \le 24$	$-10 \le h \le 10$, $-17 \le k \le 17$, $-22 \le l \le 22$
Reflections collected	44132	26923
Independent reflections	6898 [R_{int} = 0.0598, R_{sigma} = 0.0375]	7962 [R_{int} = 0.0391, R_{sigma} = 0.0366]
Data/restraints/parameters	6898/0/482	7962/50/544
Goodness-of-fit on $F^{2\,c}$	1.044	1.057
Final R indexes [I>=2σ (I)] ^{a,b}	R_1 = 0.0413, wR_2 = 0.0912	R_1 = 0.0477, wR_2 = 0.1232
Final R indexes [all data] ^{a,b}	R_1 = 0.0566, wR_2 = 0.0984	R_1 = 0.0499, wR_2 = 0.1246
Largest diff. peak/hole / e Å^{-3}	0.64/-0.52	0.45/-0.90

Table II-1 Continued.

Identification code	$(Me_4N)[Fe(MST)]$	$(Me_4N)[Fe(MST)(OH2)]$
Empirical formula	$C_{37}H_{57}FeN_5O_6S_3$	$C_{37}H_{59}FeN_5O_7S_3$
Formula weight	819.9	837.92
Temperature/K	100	100
Crystal system	monoclinic	monoclinic
Space group	$P2_1/n$	C2/c
a/Å	21.1950(6)	26.6560(8)
b/Å	9.0313(3)	9.6645(3)
c/Å	21.2797(6)	31.5226(9)
α/°	90	90
β/°	94.9100(10)	90.4400(10)
γ/°	90	90
Volume/$Å^3$	4058.4(2)	8120.5(4)
Z	4	8
$\rho_{calc}g/cm^3$	1.342	1.371
μ/mm^{-1}	0.576	0.579
F(000)	1744	3568
Crystal size/mm^3	0.21 × 0.209 × 0.121	0.584 × 0.134 × 0.129
Radiation	Mo Kα (λ = 0.71073)	MoKα (λ = 0.71073)
2Θ range for data collection/°	4.902 to 51.482	4.484 to 56.73
Index ranges	$-24 \le h \le 24$, $-10 \le k \le 10$, $-25 \le l \le 25$	$-35 \le h \le 35$, $-12 \le k \le 12$, $-41 \le l \le 41$
Reflections collected	85488	132799
Independent reflections	7470 [R_{int} = 0.0482, R_{sigma} = 0.0274]	9986 [R_{int} = 0.0581, R_{sigma} = 0.0339]
Data/restraints/parameters	7470/0/482	9986/0/523
Goodness-of-fit on $F^{2\,c}$	1.118	1.081
Final R indexes [I>=2σ (I)] ^{a,b}	R_1 = 0.0412, wR_2 = 0.0904	R_1 = 0.0388, wR_2 = 0.0902
Final R indexes [all data] ^{a,b}	R_1 = 0.0550, wR_2 = 0.0947	R_1 = 0.0553, wR_2 = 0.0965
Largest diff. peak/hole / e $Å^{-3}$	0.44/-0.44	0.49/-0.49

Table II-1 Continued.

Identification code	(Me4N)[Ni(MST)]	(Me4N)[Ni(MST)(OH2)]
Empirical formula	$C_{37}H_{57}N_5NiO_6S_3$	$C_{39}H_{66}N_5NiO_{8.5}S_3$
Formula weight	822.76	895.85
Temperature/K	100	100
Crystal system	monoclinic	triclinic
Space group	$P2_1/n$	P-1
a/Å	21.0944(17)	8.9571(7)
b/Å	8.9422(8)	14.5969(11)
c/Å	21.3506(17)	18.6587(14)
α/°	90	107.6400(10)
β/°	94.977(2)	99.2520(10)
γ/°	90	103.1570(10)
Volume/Å^3	4012.2(6)	2193.3(3)
Z	4	2
ρ_{calc}g/cm^3	1.362	1.356
μ/mm^{-1}	0.69	2.432
F(000)	1752	958
Crystal size/mm^3	0.207 × 0.096 × 0.027	0.322 × 0.213 × 0.163
Radiation	Mo Kα (λ = 0.71073)	CuKα (λ = 1.54178)
2Θ range for data collection/°	4.942 to 50.974	5.13 to 144.956
Index ranges	-24 ≤ h ≤ 25, -10 ≤ k ≤ 10, -25 ≤ l ≤ 25	-11 ≤ h ≤ 11, -18 ≤ k ≤ 17, -23 ≤ l ≤ 22
Reflections collected	65547	33214
Independent reflections	7410 [R_{int} = 0.1191, R_{sigma} = 0.0572]	8550 [R_{int} = 0.0206, R_{sigma} = 0.0170]
Data/restraints/parameters	7410/0/482	8550/75/582
Goodness-of-fit on F$^{2\,c}$	1.156	1.056
Final R indexes [I>=2σ (I)]^{a,b}	R_1 = 0.0904, wR_2 = 0.2314	R_1 = 0.0295, wR_2 = 0.0787
Final R indexes [all data] ^{a,b}	R_1 = 0.1162, wR_2 = 0.2436	R_1 = 0.0309, wR_2 = 0.0818
Largest diff. peak/hole / e Å^{-3}	1.35/-0.95	0.35/-0.42

$^a R_1 = \Sigma(||F_o| - |F_c||)/\Sigma|F_o|$. $^b wR_2 = [\Sigma[w(F_o^2 - F_c^2)^2]/\Sigma[w(F_o^2)^2]]^{1/2}$ ^{c}Goodness-of-fit = $[\Sigma[w(F_o^2 - F_c^2)^2]/(n - p)]^{1/2}$, where *n* is the number of reflections and p is the total number of parameters refined.

(Me_4N)[Co(MST)]. The coordination of this molecule involves the four nitrogen atoms contained in the MST ligand. Tetramethylammonium co-crystallizes with the Co^{II} anionic moiety. This confirms both the divalent state of the cobalt center, as well as full deprotonation of the ligand. The compound crystallizes in the monoclinic space group $P2_1/n$. The crystal structure of the anion can be found in Figure II.3. The three arms of the ligand coordinate to the cobalt cation with bond angles that vary between 117.56(10)° and 120.34(10)°. These deviations away from 120° are indicative of a break in ideal trigonal geometry about the metal center. The bond lengths vary between 1.959(2) Å and 1.972(2) Å, further emphasizing this distortion from ideal geometry. The metal center is also above the plane generated by these three equatorial nitrogen atoms by 0.207 Å. The closest intermolecular distance between two of the cobalt centers is 8.508 Å.

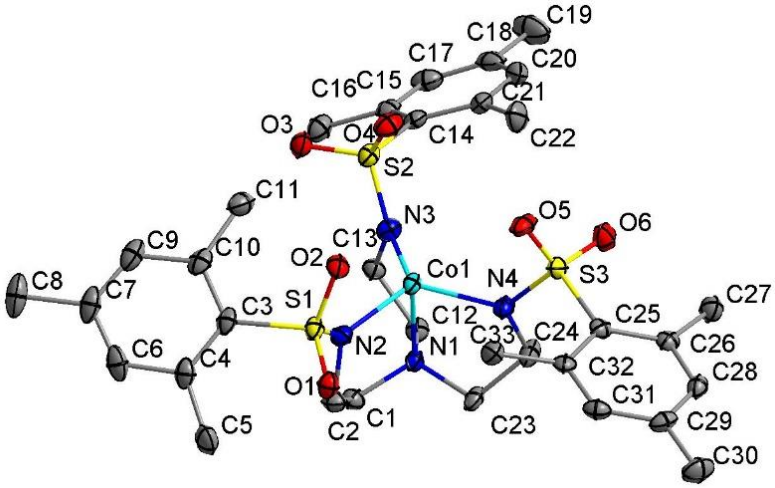

Figure II.3 Crystal structure and atom numbering scheme of the $[Co(MST)]^-$ anionic moiety. The Me_4N^+ cation and hydrogen atoms were omitted for clarity. Thermal ellipsoids were drawn at the 50% probability level. Colors are as follows: turquoise, Co; blue, N; yellow, S; red, O; grey, C.

$(Me_4N)[Co(MST)(OH_2)]$. The molecule consists of the metal ion being bound to four nitrogen atoms of the MST ligand and one water molecule in the axial position. Tetramethylammonium co-crystallizes with the Co^{II} anionic moiety, as well as DCM and water. The compound crystallizes in the triclinic space group $P\bar{1}$. The crystal structure of the anion is depicted in Figure II.4. The three arms of the ligand coordinate about the cobalt cation with bond angles that vary between 114.81(10)° and 120.04(10)°. These deviations away from 120° are indicative of a non-ideal trigonal geometry about the metal center. The bond lengths vary between 2.022(2) Å and 2.033(3) Å, further emphasizing this distortion. The bond angle between the axial nitrogen atom, cobalt ion, and axial oxygen atom is 176.72(9)°. The metal center is also above the plane generated by these three equatorial nitrogen atoms by 0.295 Å. The closest intermolecular distance between two of the cobalt centers is 8.479 Å.

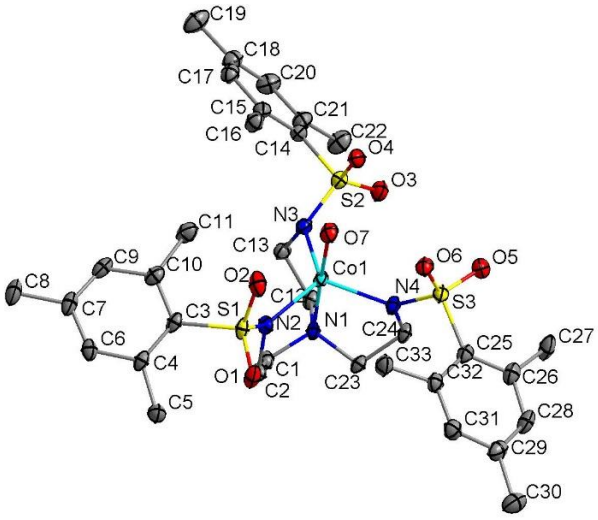

Figure II.4 Crystal structure and atom numbering scheme of the $[Co(MST)(OH_2)]^-$ anionic moiety. The Me_4N^+ cation, hydrogen atoms, and solvent were omitted for clarity. Thermal ellipsoids were drawn at the 50% probability level. Colors are as follows: turquoise, Co; blue, N; yellow, S; red, O; grey, C.

(Me_4N)[Fe(MST)]. Coordination and crystallization of this molecule is identical to **1**, with divalent iron substituting for cobalt. The crystal structure of the anion is depicted in Figure II.5. The three arms of the ligand coordinate about the iron cation with bond angles that vary between 116.71(9)° and 119.99(9)°. The bond lengths vary between 2.002(2) Å and 2.018(2) Å. The metal center is also above the plane generated by these three equatorial nitrogen atoms by 0.261 Å. The closest intermolecular distance between two of the iron centers is 8.588 Å.

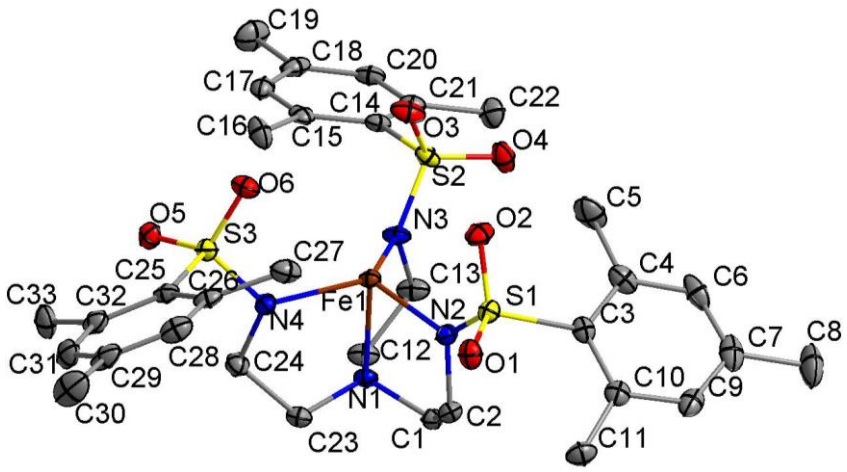

Figure II.5 Crystal structure and atom numbering scheme of the $[Fe(MST)]^-$ anionic moiety. The Me_4N^+ cation and hydrogen atoms were omitted for clarity. Thermal ellipsoids were drawn at the 50% probability level. Colors are as follows: brown, Fe; blue, N; yellow, S; red, O; grey, C.

(Me_4N)[Fe(MST)(OH_2)]. Coordination of this molecule is identical to **2**, with divalent iron substituting for cobalt. The compound crystallizes in the monoclinic space group C2/c. The crystal structure of the anion is depicted in Figure II.6. The three arms of the ligand coordinate about the iron cation with bond angles that vary between 113.74(6)° and

120.84(6)°. The bond lengths vary between 2.0564(15) Å and 2.0981(15) Å. The bond angle between the axial nitrogen atom, iron ion, and axial oxygen atom is 171.74(5)°. The metal center is also above the plane generated by these three equatorial nitrogen atoms by 0.358 Å. The closest intermolecular distance between the iron centers is 8.427 Å.

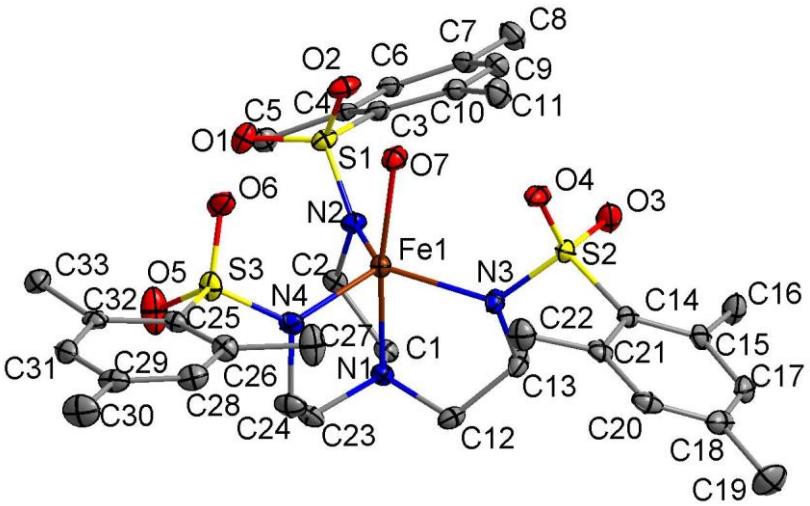

Figure II.6 Crystal structure and atom numbering scheme of the $[Fe(MST)(OH_2)]^-$ anionic moiety. The Me_4N^+ cation and hydrogen atoms were omitted for clarity. Thermal ellipsoids were drawn at the 50% probability level. Colors are as follows: brown, Fe; blue, N; yellow, S; red, O; grey, C.

(Me_4N)[Ni(MST)]. Coordination and crystallization of this molecule is identical to **1**, with divalent nickel substituting for cobalt. The crystal structure of the anion is depicted in Figure II.7. The three arms of the ligand coordinate about the nickel cation with bond angles that vary between 116.2(3)° and 122.5(3)°. The bond lengths vary between 1.965(6) Å and 1.998(6) Å. The metal center is also above the plane generated by these three equatorial nitrogen atoms by 0.159 Å. The closest intermolecular distance between two of the nickel centers is 8.423 Å.

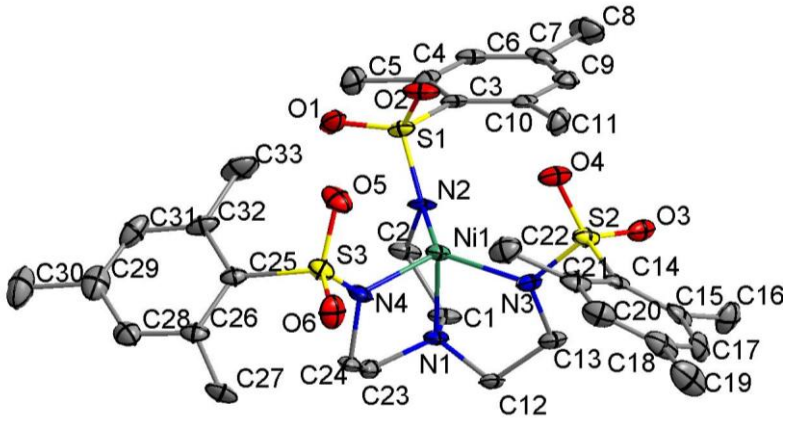

Figure II.7 Crystal structure and atom numbering scheme of the $[Ni(MST)]^-$ anionic moiety. The Me_4N^+ cation and hydrogen atoms were omitted for clarity. Thermal ellipsoids were drawn at the 50% probability level. Colors are as follows: green, Ni; blue, N; yellow, S; red, O; grey, C.

$(Me_4N)[Ni(MST)(OH_2)]$. Coordination of this molecule is identical to **2**, with divalent iron substituting for cobalt. Water and diethyl ether co-crystallize with the Ni^{II} anionic moiety. The compound crystallizes in the triclinic space group $P\bar{1}$. The crystal structure of the anion is depicted in Figure II.8. The three arms of the ligand coordinate about the nickel cation with bond angles that vary between 108.42(5)° and 128.98(5)°. The bond lengths vary between 2.0254(12) and 2.0383(12). The bond angle between the axial nitrogen atom, nickel ion, and axial oxygen atom is 178.44(4)°. The metal center is also above the plane generated by these three equatorial nitrogen atoms by 0.222 Å. The closest intermolecular distance between two of the cobalt centers is 8.356 Å.

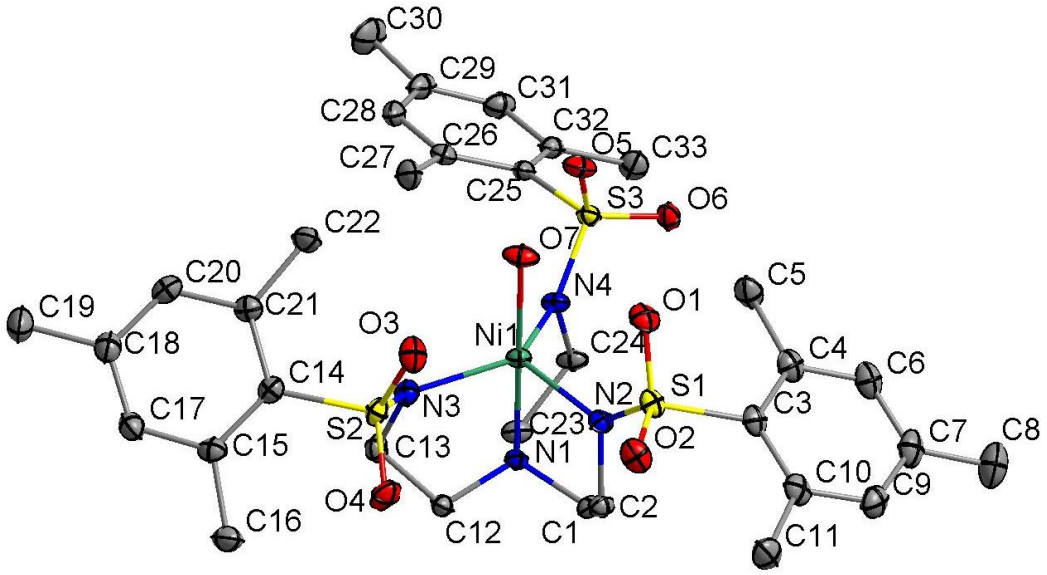

Figure II.8 Crystal structure and atom numbering scheme of the $[Ni(MST)(OH_2)]^-$ anionic moiety. The Me_4N^+ cation, water, diethyl ether, and hydrogen atoms were omitted for clarity. Thermal ellipsoids were drawn at the 50% probability level. Colors are as follows: green, Ni; blue, N; yellow, S; red, O; grey, C.

II.2.3 Magnetic Measurements

Magnetic data were collected on a Quantum Design MPMS-3 SQUID from 1.8-300 K with DC fields from 0-7 T. Compounds **1-4, 6** were collected in plastic bags and compound **5** was collected in an NMR tube under a coating of eicosaine. Diamagnetic corrections were applied for the bags, NMR tube, and eicosaine. The diamagnetic contribution from the compounds were calculated based on Pascal's constants.[74]

II.2.4 Computational Methods

Ab initio calculations were performed by Dr. Kuduva R. Vignesh, a postdoctoral researcher in our laboratories. These calculations were based on the wave function theory approach were used to compute the ZFS of Co^{II}, Fe^{II}, and Ni^{II} ions in **1**−**6** using ORCA 3.0 suite of programs.[75] The BP86 functional was employed, along with scalar relativistic

ZORA Hamiltonians and def2-TZVP basis sets for the metal ions and the first coordination sphere and def2-SVP for the rest of the atoms. The RI approximation with secondary TZV/J Columbic fitting basis sets were used along with increased integration grids (Grid 5 in ORCA convention). The tight SCF convergence was used throughout the calculations ($1x10^{-8}$ Eh). The spin-orbit coupling (SOC) contributions in the *ab initio* framework were obtained using second-order perturbation theory as well as by employing the effective Hamiltonian approach, which enables calculations of all matrix elements to be made of the anisotropic spin Hamiltonian from the *ab initio* energies and wave functions numerically. Here we have employed the state average-CASSCF (Complete Active Space Self-Consistent Field) method to compute the ZFS. The active space involves seven active electrons in five active d-orbitals (d^7 system; CAS (7,5)) for the Co^{II} ion, six active electrons in five active d-orbitals (d^6 system; CAS (6,5)) for the Fe^{II} ion, and eight active electrons in five active d-orbitals (d^8 system; CAS (8,5)) for the Ni^{II} ion. With this active space, all of the 10 quartet and 40 doublet states for the Co^{II} ion, 5 quintet and 45 triplet states for the Fe^{II} ion, and 10 triplet and 15 singlet states for the Ni^{II} ion were calculated in the configuration interaction procedure.[76] In addition to the converged CASSCF wave function, NEVPT2 (n-electron valence state perturbation theory) calculations were performed to treat the dynamical correlations.[77-78]

$$\widehat{H}_{so} = \sum_{i} \xi_i \left(\hat{l}_{Zi}.\hat{s}_{Zi} + \frac{1}{2} \left(\hat{l}_{+i}.\hat{s}_{-i} + \hat{l}_{-i}.\hat{s}_{+i} \right) \right)$$

The sign and the magnitude of *D* values are rationalized using the spin−orbit operator, see above equation. When a spin-allowed excitation of a β-electron between

orbitals with same $|\pm m_l|$ levels occurs, the $\sum_i \hat{l}_{Zi}.\hat{s}_{Zi}$ operator couples those orbitals and leads to a negative *D* value. Conversely, when such an excitation occurs between orbitals with different $|\pm m_l|$ levels, the $\frac{1}{2}\sum_i (\hat{l}_{+i}.\hat{s}_{-i} + \hat{l}_{-i}.\hat{s}_{+i})$ operator couples those orbitals and leads to a positive *D* value.[40, 65]

II.3 Results and Discussion

II.3.1 Crystallographic Details

The six compounds, $(Me_4N)[Co(MST)]$ (**1**), $(Me_4N)[Co(MST)(OH_2)]$•DCM (**2**), $(Me_4N)[Fe(MST)]$ (**3**), $(Me_4N)[Fe(MST)(OH_2)]$ (**4**), $(Me_4N)[Ni(MST)]$ (**5**), $(Me_4N)[Ni(MST)(OH_2)]$ (**6**) were synthesized based on literature procedures[66] via a reaction between the deprotonated ligand using NaH, the appropriate metal(II) acetate salt, and tetramethylammonium acetate in dimethylacetamide (DMA) as the solvent. Crystals were obtained by slow diffusion of diethyl ether into either DMA or dichloromethane (DCM) solutions. The anhydrous salts crystallize in the monoclinic space group $P2_1/n$, whereas complexes **2** and **6** crystallize in triclinic $P\bar{1}$ and **4** in monoclinic C2/c. The structures of **1**, **2**, and **4** were previously reported.[66-67] Compound **2** was collected in an alternate space group of triclinic $P\bar{1}$ rather than the reported C2/c. The monoclinic space group was isolable by their reported synthesis method or via slow diffusion of diethyl ether directly into the DMA solution. The triclinic crystals form in a larger excess of water followed by slow diffusion of diethyl ether into the DCM solution. The triclinic phase was studied for ease of synthesis and consistency in crystallization methods.

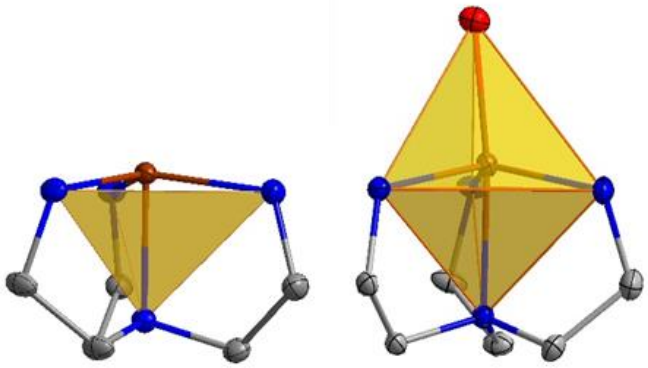

Figure II.9 Inner coordination spheres of complexes **3** (left) and **4** (right). Shaded polyhedron emphasize the trigonal monopyramidal and bipyramidal geometries. Atom colors: brown for iron, blue for nitrogen, and grey for carbon. All other atoms have been omitted for clarity. Reprinted by permission from reference 98.

The coordination environment for **1**, **3**, and **5** consists of nitrogen atoms from the tetradentate ligand MST. The three arms of the ligand coordinate in an equatorial plane around the metal center and the central nitrogen atom binds in one of the axial positions. The second axial position is unoccupied which generates TMP geometry. In addition to the MST ligand, complexes **2**, **4**, and **6** feature coordination of a water molecule resulting in TBP geometry. Figure II.9 highlights the trigonal monopyramidal and bipyramidal geometries of the inner coordination sphere in complexes **3** and **4**. The geometries of the complexes were confirmed using the SHAPE program[79-80] which compares the experimental metrical parameters to the perfect geometry, with 0 indicating a perfect match to that geometry. These results can be found in Table II-2, with the trigonal monopyramidal complexes being much closer to the ideal geometry than the trigonal bipyramidal complexes.

Table II-2 Shape measurements for compounds 1-6. Abbreviations are as follows: SP, square; T, tetrahedron; SS, seesaw; vTBPY, axially vacant trigonal bipyramid; PP, pentagon; vOC, vacant octahedron; TBPY, trigonal bipyramid; SPY, square pyramid; JTBPY, Johnson trigonal bipyramid. Reprinted by permission from reference 98.

	SP	**T**	**SS**	**vTBPY**	**PP**	**vOC**	**TBPY**	**SPY**	**JTBPY**
1	35.505	5.094	8.176	0.233					
3	35.555	5.675	8.338	0.350					
5	34.630	5.046	7.822	0.176					
2					35.541	7.083	0.695	5.309	2.498
4					34.330	7.205	1.050	5.154	2.770
6					33.794	5.213	0.669	3.966	3.135

In each structure, the metal center is above the equatorial plane generated by the 3 coordinating nitrogen atoms, with **5** exhibiting the least distortion at a Ni-N_{plane} distance of 0.159 Å. The M-N_{plane} distances in the aquo adducts are ~0.1 Å further out of plane than their anhydrous counterparts. See Table II-3 for a summary of these measurements for all compounds.

Table II-3 Selected intermolecular and intramolecular distances (Å) of **1**-**6**. Reprinted by permission from reference 98.

	1	**3**	**5**	**2**	**4**	**6**
N_3…M[a]	0.207	0.261	0.159	0.295	0.358	0.222
M…M[b]	8.508	8.588	8.423	8.479	8.427	8.356

[a] distance between the metal center and the plane generated by the three equatorially coordinated nitrogen atoms (N2-N4)
[b] closest intermolecular distance between two metal centers

In each case, there is deviation from the ideal trigonal angle of 120° in the equatorial plane and compounds **2**, **4**, and **6** have angles between the axial nitrogen and oxygen atoms that are <180°. This bend can be attributed to hydrogen bonding between

the water and the sulfonyl oxygen atoms. See Table II-4 for a summary of the relevant distances and angles. Coordination of water results in a lengthening of the M-N bonds in all of the complexes by at least 0.04 Å indicating a decrease in bond strength.

Table II-4 Selected bond lengths (Å) and angles (°) around the inner coordination sphere of **1-6.** Reprinted by permission from reference 98.

	1	**2**	**3**	**4**	**5**	**6**
N1	2.118(2)	2.180(2)	2.165(2)	2.2495(14)	2.035(6)	2.0885(11)
N2	1.972(2)	2.032(2)	2.018(2)	2.0692(15)	1.965(6)	2.0311(12)
N3	1.969(2)	2.033(3)	2.002(2)	2.0981(15)	1.984(6)	2.0254(12)
N4	1.959(2)	2.022(2)	2.018(2)	2.0564(15)	1.998(6)	2.0383(12)
N2-M-N3	117.56(10)	120.04(10)	118.34(9)	116.66(6)	122.5(3)	108.42(5)
N3-M-N4	118.83(10)	114.81(10)	119.99(9)	120.84(6)	116.2(3)	128.98(5)
N4-M-N2	120.34(10)	118.90(10)	116.71(9)	113.74(6)	119.4(3)	118.00(5)
N1-M-O7		176.72(9)		171.74(5)		178.44(4)

II.3.2 DC Magnetic Studies and Computational Studies

Static DC measurements were performed on complexes **1-6** from 1.8 – 300 K using a SQUID magnetometer, Figure II.10. The $\chi_m T$ values of 2.45 and 2.57 emu K mol^{-1} at 300 K for complexes **1** and **2** respectively are higher than 1.87 emu K mol^{-1}, the ideal value for an S=3/2 system with g=2. Complexes **3** and **4** exhibit $\chi_m T$ values of 3.19 and 3.92 emu K mol^{-1}, higher than the expected 3.0 emu K mol^{-1} for an S=2 system with g=2. Complexes **5** and **6** follow the same trend with $\chi_m T$ values of 1.55 and 2.19 emu K mol^{-1}, higher than the expected value of 1 emu K mol^{-1} for an S=1 system with g=2. These deviations from ideality reflect spin-orbit coupling. Compounds **1-5** exhibit Curie-like

behavior until ~30 K, after which $\chi_m T$ decreases as expected due to zero-field splitting. Compound **6** exhibits TIP, resulting in a linear increase in $\chi_m T$ at higher temperatures.

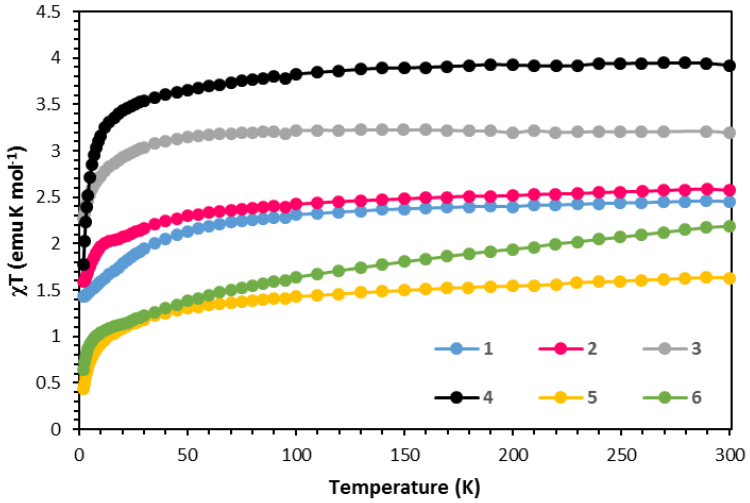

Figure II.10 χT vs T data for compounds **1**-**6**, as labelled, under a 1000 Oe DC field. Solid lines are guides for the eye. Reprinted by permission from reference 98.

The anisotropic nature of these complexes is also supported by the M versus H plots at 1.8 K that do not saturate even up to 7 T. The expected saturation point for compounds **1** and **2** is 3 μ_B. Neither compound reaches this value, with **1** reaching a maximum below 2 μ_B at 7 T and **2** reaching a maximum below 2.5 μ_B, Figure II.11. In both cases, the lack of saturation and values well below those expected are indicative of significant anisotropy.

a)

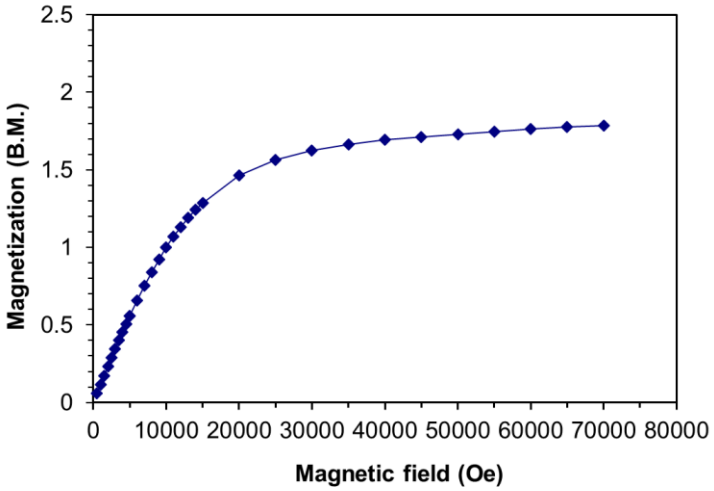

b)

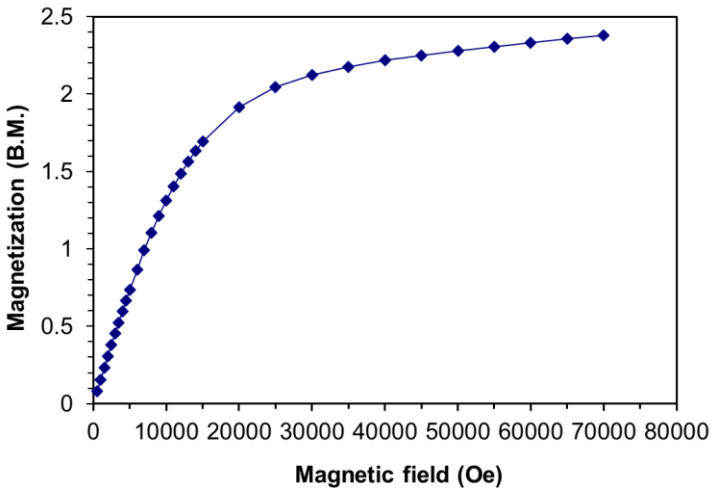

Figure II.11 Magnetization vs Field for a) compound **1** and b) compound **2**. Solid lines are guides for the eye. Reprinted by permission from reference 98.

The expected saturation point for compounds **3** and **4** is 4 μ_B. Neither compound reaches this value, with **3** reaching a maximum below 3.5 μ_B at 7 T and **2** also reaching a maximum below 3.5 μ_B, Figure II.12. In both cases, the lack of saturation and values well below those expected are indicative of significant anisotropy.

a)

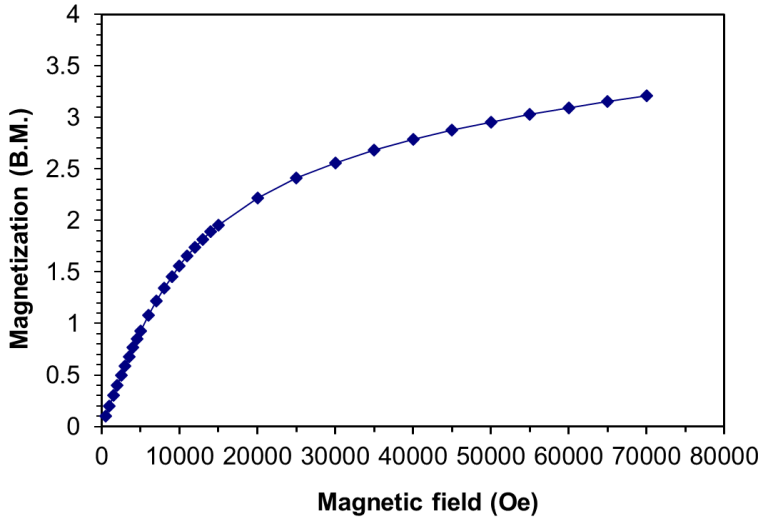

b)

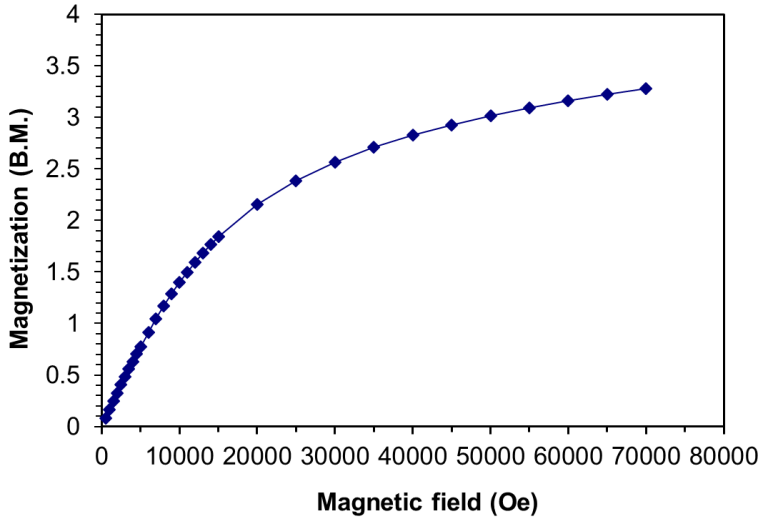

Figure II.12 Magnetization vs Field for a) compound **3** and b) compound **4**. Solid lines are guides for the eye. Reprinted by permission from reference 98.

The expected saturation point for compounds **5** and **6** is 2 μ_B. Neither compound reaches this value, with **5** reaching a maximum below 1.5 μ_B at 7 T and **6** also reaching a maximum below 1.5 μ_B, Figure II.13. In both cases, the lack of saturation and values well below those expected are indicative of significant anisotropy.

a)

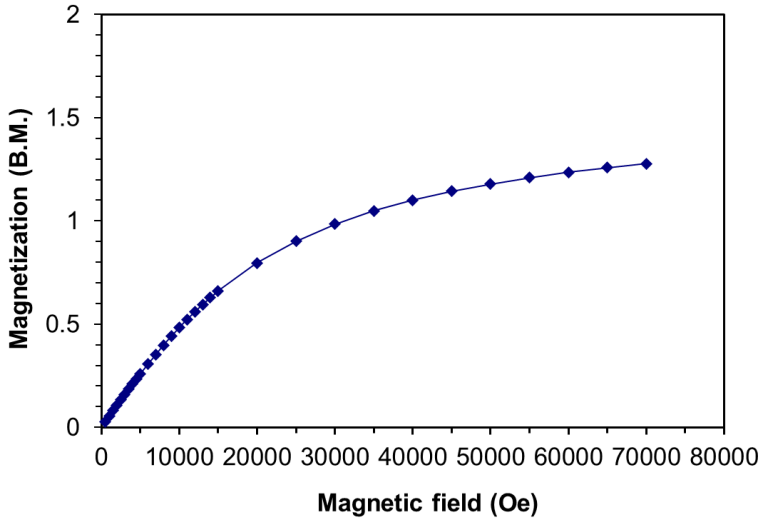

b)

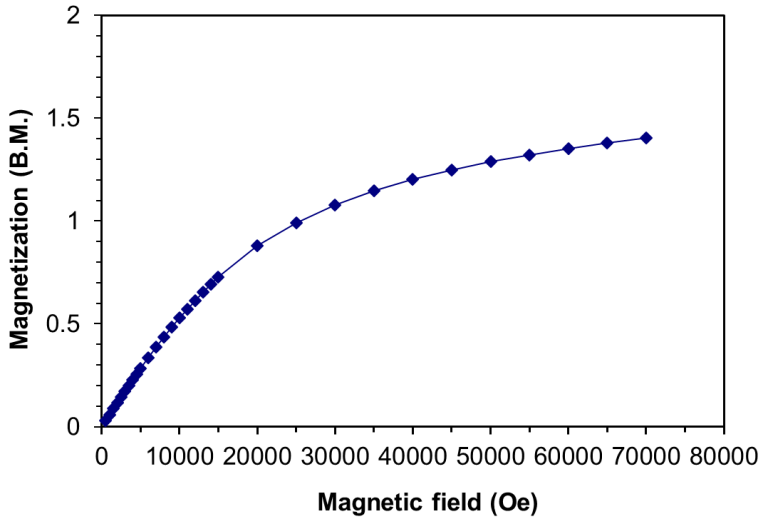

Figure II.13 Magnetization vs Field for a) compound **5** and b) compound **6**. Solid lines are guides for the eye. Reprinted by permission from reference 98.

Reduced magnetization was measured for **1**-**6** between 1.8 and 4 K and subsequently fit with the PHI program.[81] The reduced magnetization for Compound **1** shows a lack of superposition in the isofield lines, indicative of anisotropy. The data were fit with g, D, and E values equal to 2.24, 33 cm^{-1}, and 0.2 cm^{-1}, respectively, Figure II.14.

The reduced magnetization for Compound **2** also shows a lack of superposition in the isofield lines, indicative of anisotropy. The data were fit with g, D, and E values equal to 2.40, 24 cm^{-1}, and 0.001 cm^{-1}, respectively, Figure II.15.

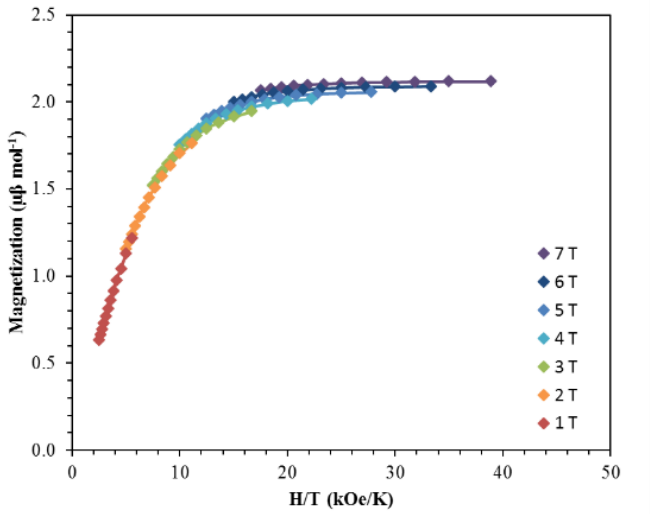

Figure II.14 Reduced magnetization for **1**. Solid lines are fits to the experimental data using the PHI program. Reprinted by permission from reference 98.

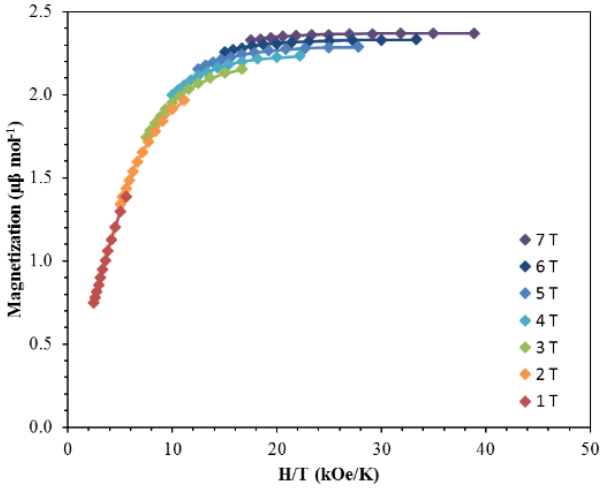

Figure II.15 Reduced magnetization for **2**. Solid lines are fits to the experimental data using the PHI program. Reprinted by permission from reference 98.

The reduced magnetization for Compound **3** shows a lack of superposition in the isofield lines, indicative of anisotropy. The data were fit with g, D, and E values equal to 2.19, -31 cm^{-1}, and 4.7 cm^{-1}, respectively, Figure II.16. The reduced magnetization for Compound **4** also shows a lack of superposition in the isofield lines, indicative of anisotropy. The data were fit with g, D, and E values equal to 2.37, 8.7 cm^{-1}, and 2.4 cm^{-1}, respectively, Figure II.17.

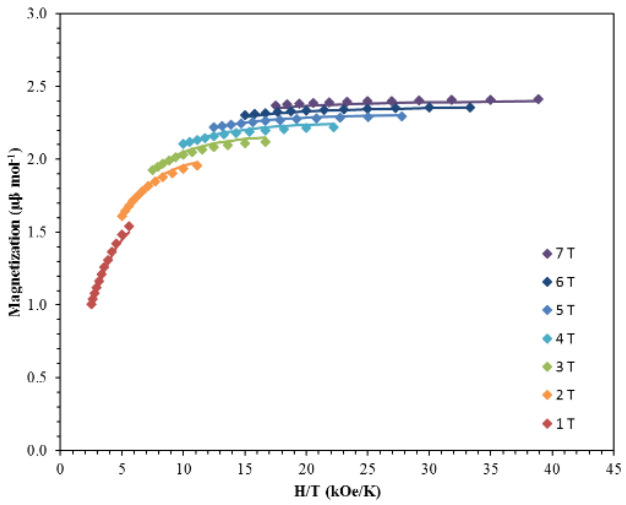

Figure II.16 Reduced magnetization for **3**. Solid lines are fits to the experimental data using the PHI program. Reprinted by permission from reference 98.

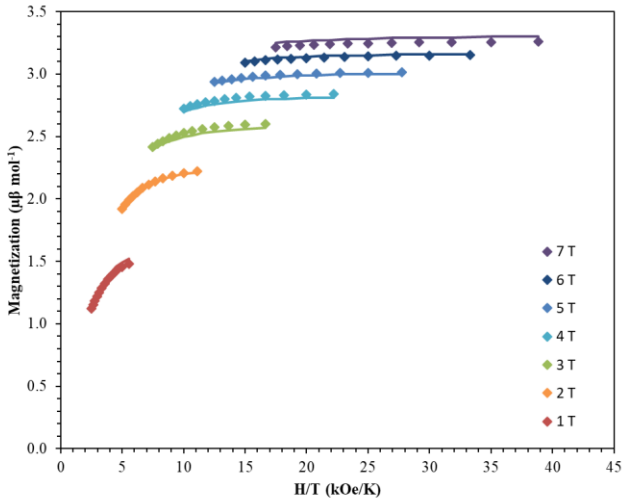

Figure II.17 Reduced magnetization for **4**. Solid lines are fits to the experimental data using the PHI program. Reprinted by permission from reference 98.

The reduced magnetization for Compound **5** shows a lack of superposition in the isofield lines, indicative of anisotropy. The data were fit with g, D, and E values equal to 2.67, -276 cm^{-1}, and 2.1 cm^{-1}, respectively, Figure II.18. The reduced magnetization for Compound **6** also shows a lack of superposition in the isofield lines, indicative of anisotropy. The data were fit with g, D, and E values equal to 2.81, -209 cm^{-1}, and 1.8 cm^{-1}, respectively, Figure II.19.

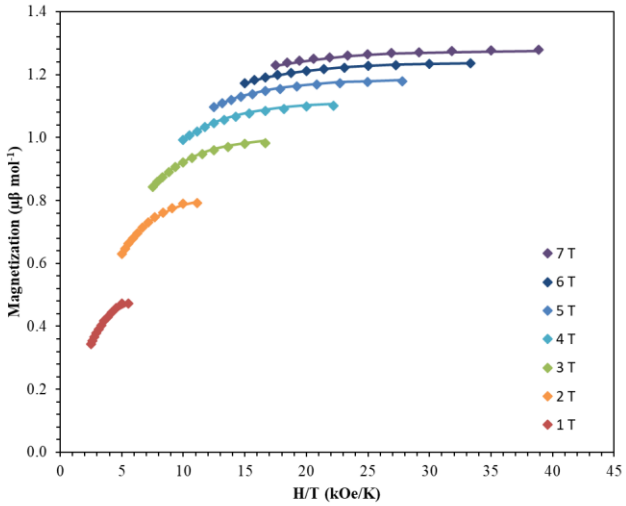

Figure II.18 Reduced magnetization for **5**. Solid lines are fits to the experimental data using the PHI program. Reprinted by permission from reference 98.

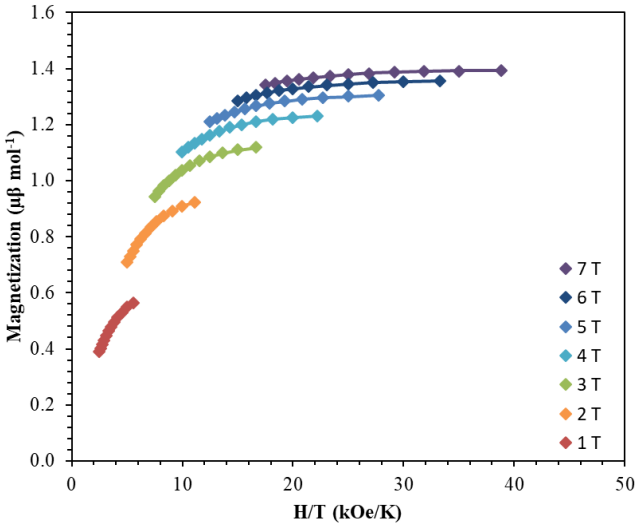

Figure II.19 Reduced magnetization for **6**. Solid lines are fits to the experimental data using the PHI program. Reprinted by permission from reference 98.

In each case, the experimental fittings lead to a smaller *D* value for the water containing complexes versus the anhydrous complexes. These findings are in accord with the longer M-N bond distances in the water complexes as well as the greater geometric distortion in the trigonal bipyramidal complexes. If one compares these results to the predictions in the paper of Ruiz et al.[40], they are in good agreement except for **4**. In this case, a negative *D* value was predicted on the basis of electron count and geometry, but a small, positive *D* value was observed.

In order to rationalize the observed zero field splitting parameters for complexes **1**−**6**, and to probe the change in *D* values among the two geometries, *ab initio* CASSCF and NEVPT2 calculations were performed. The first four excited state energies were calculated, along with g_x, g_y, and g_z values to find the resulting D and g values for each of compounds **1-6**, Table II-5.

Table II-5 CASSCF (NEVPT2) computed energies (cm-1) and contributions to D value from the first four excited states for **1** – **6** along with the g_x, g_y, and g_z values from the effective Hamiltonian. Reprinted by permission from reference 98.

Complex	g_x, g_y, g_z	Excited state	Energy	*D* Contribution
1	2.00, 2.35, 2.36	First	4811.3 (4731.5)	17.1 (12.0)
	(2.00, 2.25, 2.26)	Second	4972.8 (4894.5)	16.3(11.5)
		Third	5706.6 (5562.3)	-0.6 (-0.4)
		Fourth	5738.5 (5594.2)	-0.1(-0.1)
2	2.09, 2.31, 2.34	First	3384.0 (3381.9)	-3.7 (-2.6)
	(2.07, 2.23, 2.25)	Second	4054.2 (4105.6)	-0.1(-0.1)
		Third	4870.8 (4912.1)	13.1 (9.4)
		Fourth	5204.3 (5219.2)	12.6 (8.9)
3	1.83, 1.89, 2.56	First	874.9 (879.2)	-36.0 (-33.9)
	(1.85, 1.92, 2.54)	Second	5650.5 (5643.4)	2.5 (2.0)
		Third	6962.3 (6959.0)	0.7 (0.6)
		Fourth	7126.2 (7132.9)	0.6 (0.5)

Table II-5 Continued.

Complex	g_x, g_y, g_z	Excited state	Energy	*D* Contribution
4	2.03, 2.09, 2.19	First	1284.6 (1346.2)	4.1 (3.3)
	(2.02, 2.07, 2.15)	Second	4617.8 (4622.5)	-1.1 (-0.9)
		Third	5393.8 (5499.3)	1.2 (0.9)
		Fourth	8814.1 (8711.7)	1.6 (1.2)
5	1.85, 1.85, 3.75	First	77.6 (77.7)	-530.8 (-500.0)
	(1.79, 1.80, 3.73)	Second	5671.8 (5688.1)	34.3 (23.6)
		Third	5763.7 (5775.8)	13.1 (8.3)
		Fourth	5987.5 (6002.5)	15.4 (11.1)
6	2.13, 2.16, 3.25	First	244.3 (253.2)	-264.0 (-186.6)
	(2.13, 2.15, 2.96)	Second	6494.9 (6522.1)	24.6 (17.2)
		Third	7384.7 (7380.3)	21.6 (15.3)
		Fourth	9036.9 (9011.6)	7.1 (4.8)

From these calculations, the predicted g, D, and E values could be identified and compared to experimental results. This comparison is summarized in Table II-6, where the experimental, CASSCF, and NEVPT2 calculation results are reported. The CASSCF calculations follow the experimentally observed trend of the trigonal monopyramidal complexes **1**, **3**, and **5**, namely higher magnitudes for the *D* value compared to the water coordinated complexes **2**, **4**, and **6**. The transverse ZFS parameters (E) are close to zero, as expected for complexes with trigonal symmetry. The experimental g_{iso} and E values are universally higher than predicted by the computations, but still in agreement.

Table II-6 Top row: g, D, and E values for compounds 1-6 based on fittings of reduced magnetization data. Bottom rows: Calculated values for g, D (cm^{-1}), and E (cm^{-1}) based on CASSCF and NEVPT2 methods, as labelled. Reprinted by permission from reference 98.

		1	**2**	**3**	**4**	**5**	**6**
PHI	g	2.24	2.40	2.19	2.37	2.67	2.81
	D	33	24	-31	8.7	-276	-209
	|E|	0.2	0.001	4.7	2.4	2.1	1.8
CASSCF	g	2.24	2.25	2.09	2.10	2.48	2.51
	D	37.8	25.4	-30.1	6.6	-434.1	-185.7
	E	0.7	0.1	0.15	0.23	0.6	0.007
NEVPT2	g	2.17	2.18	2.10	2.08	2.44	2.41
	D	30.4	20.7	-28.6	6.0	-428.9	-131.3
	E	0.6	0.05	0.16	0.14	0.001	0.007

The reduced magnetization data were simulated based on these calculations. The deviation of the experimental data from computational data is expected given the increase in g_{iso} and transverse ZFS parameters. The simulated results for compound **1** can be found in Figure II.20. Visually, the CASSCF simulation more closely models the data than the NEVPT2 simulation.

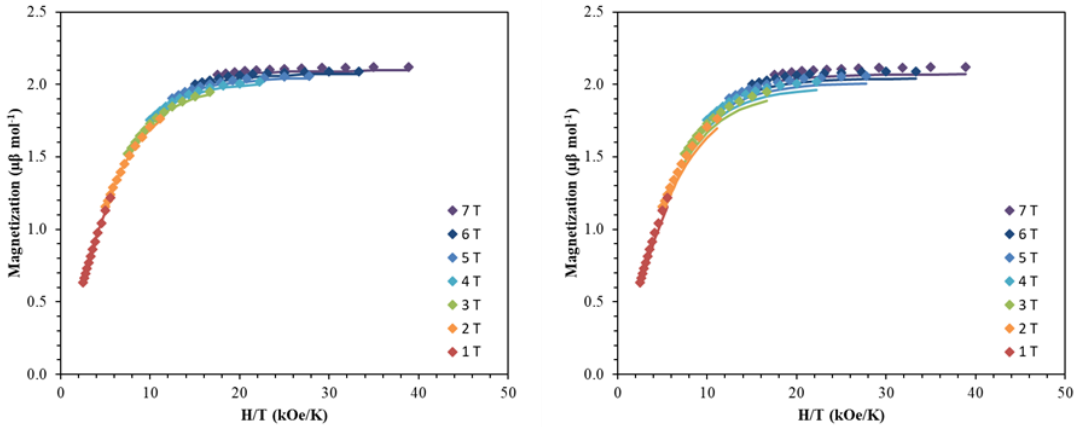

Figure II.20 Reduced magnetization for **1**. Solid lines are simulations of CASSCF (left) and NEVPT2 (right) computational results. Reprinted by permission from reference 98.

The simulated results for compound **2** can be found in Figure II.21. Visually, the deviation from the experimental data is about equal between both the CASSCF and NEVPT2 simulated data sets. The simulations have very similar shapes and spacing, but overall lower magnetization values.

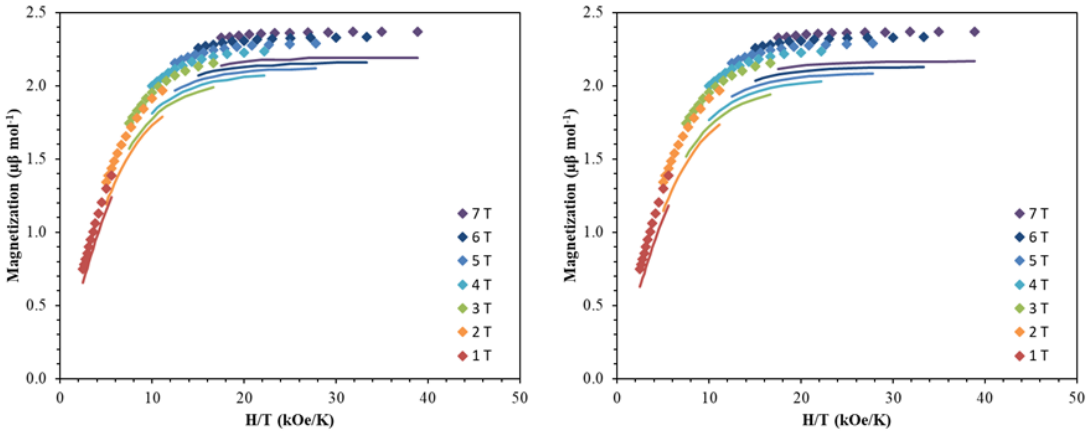

Figure II.21 Reduced magnetization for **2**. Solid lines are simulations of CASSCF (left) and NEVPT2 (right) computational results. Reprinted by permission from reference 98.

The simulated results for compound **3** can be found in Figure II.22. Visually, the deviation from the experimental data is about equal between both the CASSCF and NEVPT2 simulated data sets. The simulations have very similar shapes and spacing, but overall lower magnetization values.

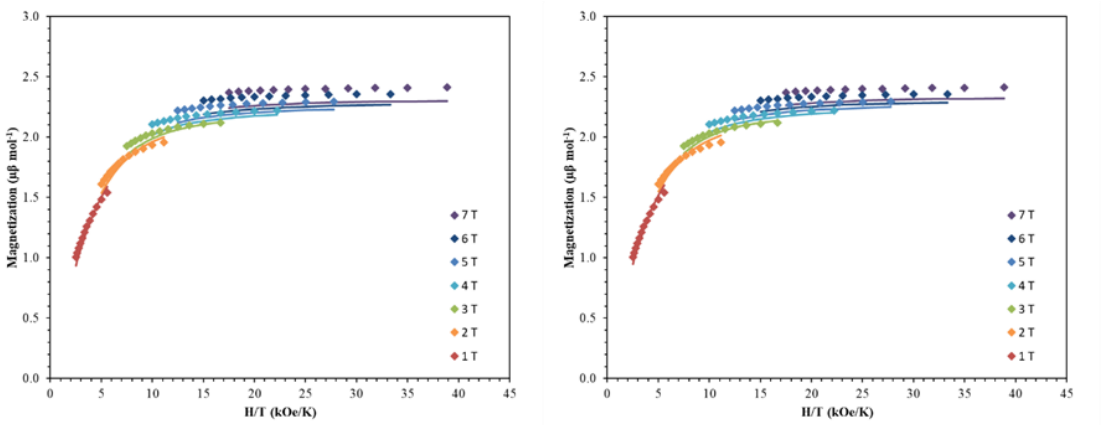

Figure II.22 Reduced magnetization for **3**. Solid lines are simulations of CASSCF (left) and NEVPT2 (right) computational results. Reprinted by permission from reference 98.

The simulated results for compound **4** can be found in Figure II.23. Visually, the NEVPT2 simulated data is closer to experimental than the CASSCF experimental, particularly at the highest fields. Overall, the predicted magnetization values are lower than those observed experimentally, especially at the lowest fields.

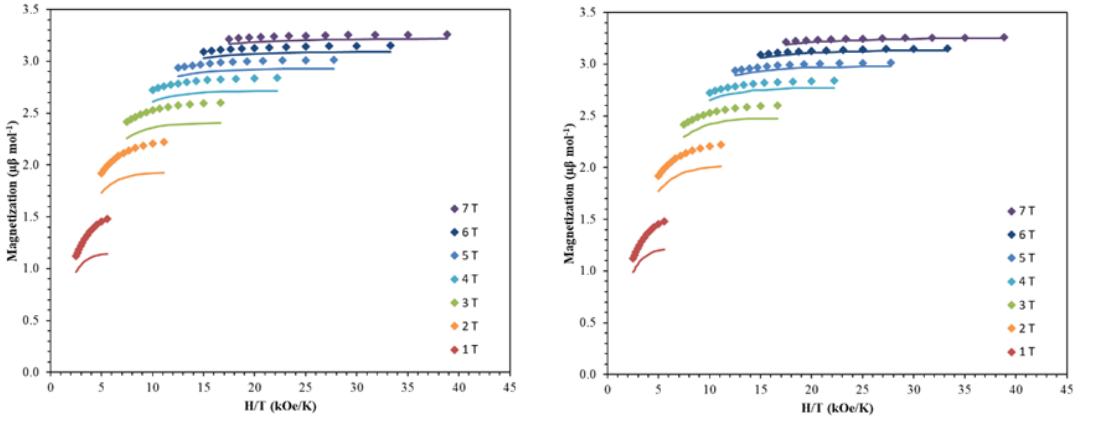

Figure II.23 Reduced magnetization for **4**. Solid lines are simulations of CASSCF (left) and NEVPT2 (right) computational results. Reprinted by permission from reference 98.

The simulated results for compound **5** can be found in Figure II.24. Visually, the simulated data is significantly different from the experimental, particularly in the superposition of the field lines. The can likely be attributed to the large difference in experimental and calculated D values which originates from the difficulty in isolating an anhydrous sample.

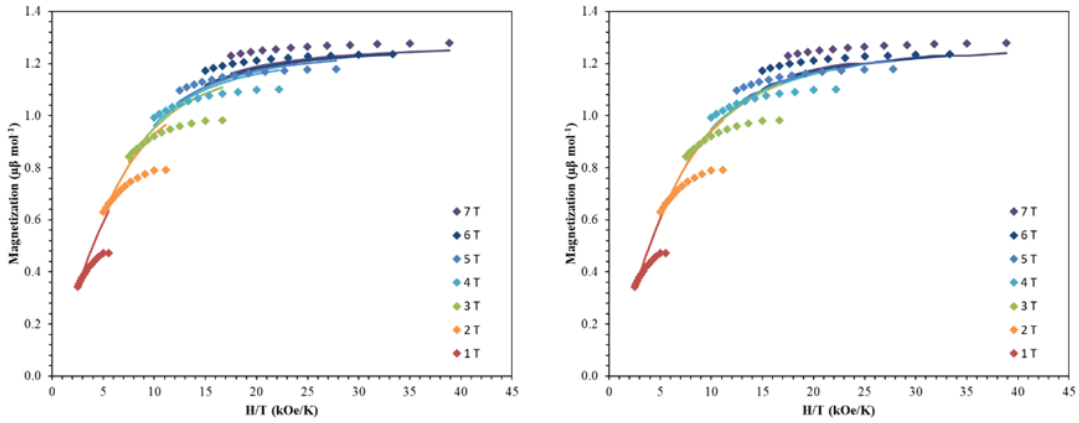

Figure II.24 Reduced magnetization for **5**. Solid lines are simulations of CASSCF (left) and NEVPT2 (right) computational results. Reprinted by permission from reference 98.

The simulated results for compound **6** can be found in Figure II.25. Visually, the simulated data is significantly different from the experimental, particularly in the superposition of the field lines. Similar to compound **5**, the can likely be attributed to the large difference in experimental and calculated D values, given extremely large D values can be difficult to fit.

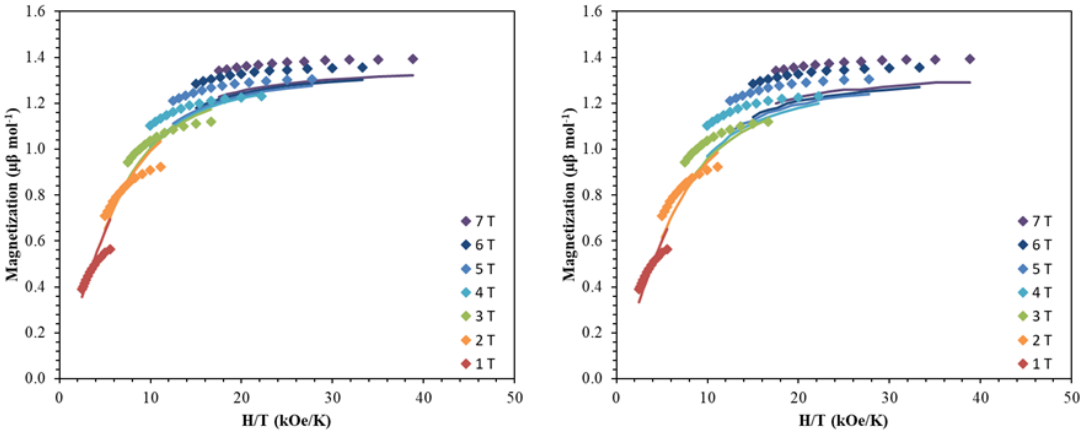

Figure II.25 Reduced magnetization for **6**. Solid lines are simulations of CASSCF (left) and NEVPT2 (right) computational results. Reprinted by permission from reference 98.

In order to further assess the effect of water coordination on the magnetic behavior, the orientation of the D_{xx}, D_{yy}, and D_{zz} axes were computed for complexes **1**–**6**, Figure II.26. In the trigonal monopyramidal complexes **1**, **3** and **5**, the D_{zz} axis passes through the C_3 axis of symmetry of the molecule along the M^{II}-N_{axial} bonds. When the water molecule is coordinated in the other axial position, the D_{zz} axis deviates from the C_3 axis of symmetry, explaining the significant reduction in the magnitude of the *D* values.

The CASSCF computed *D* values were validated by inclusion of dynamic correlations using the NEVPT2 method, which resulted in reduced *D* values. The dynamic correlation stabilizes the ground state, rather than the excited states, increasing the energy gap between orbitals resulting in lower *D* values. NEVPT2 computed *D*, E and *g* values follow the same trend as the CASSCF computed values, which offers additional support to the results.

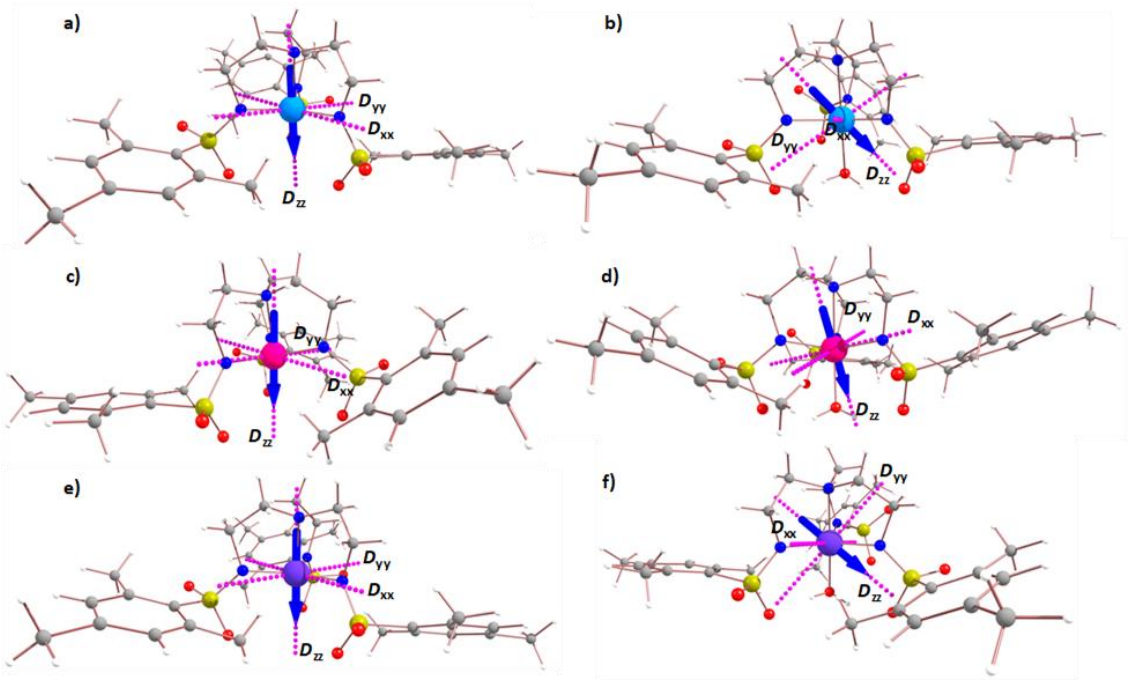

Figure II.26 CASSCF computed D_{xx}, D_{yy}, and D_{zz} axes (pink dotted lines) for a) **1** b) **2** c) **3** d) **4** e) **5** f) **6**. The blue arrow emphasizes the direction and orientation of the D_{zz} axis. Reprinted by permission from reference 98.

The computed crystal splitting of the d orbitals for complexes **1** and **2**, Figure II.27, indicate that the first excitation should involve the d_{yz} and $d_{x^2-y^2}/d_{xy}$ orbitals with different $|\pm m_l|$ levels, resulting in the observed positive *D* value. In the case of **1**, the energy gap between the ground and the first and second excited quartet states are relatively large (~4800 cm^{-1}), contributing the most to the total *D* value, whereas the other excited states only marginally affect the *D* value. In the case of **2**, the third and fourth excited states contribute the most to the positive *D* value. A small, negative contribution from the first excited state is due to a decrease in energy gap between the ground and first excited state (~3380 cm^{-1}), attributed to the presence of a water molecule in the axial position. This

small negative contribution is not sufficient to offset the total positive *D* value. The experimental *D* values of 33 cm^{-1} for **1** and 24 cm^{-1} for **2** are in agreement with the calculations, falling in between the CASSCF and NEVPT2 values of 37.8 and 30.4 cm^{-1}, and 25.4 and 20.7 cm^{-1} respectively. These results lend credence to the ability of the calculated orbitals and excitations to accurately model the magnetic behavior of these systems. Moreover, a positive rather than negative *D* value resulted in better fits of the experimental data and was in agreement with the calculations for **1** and **2**.

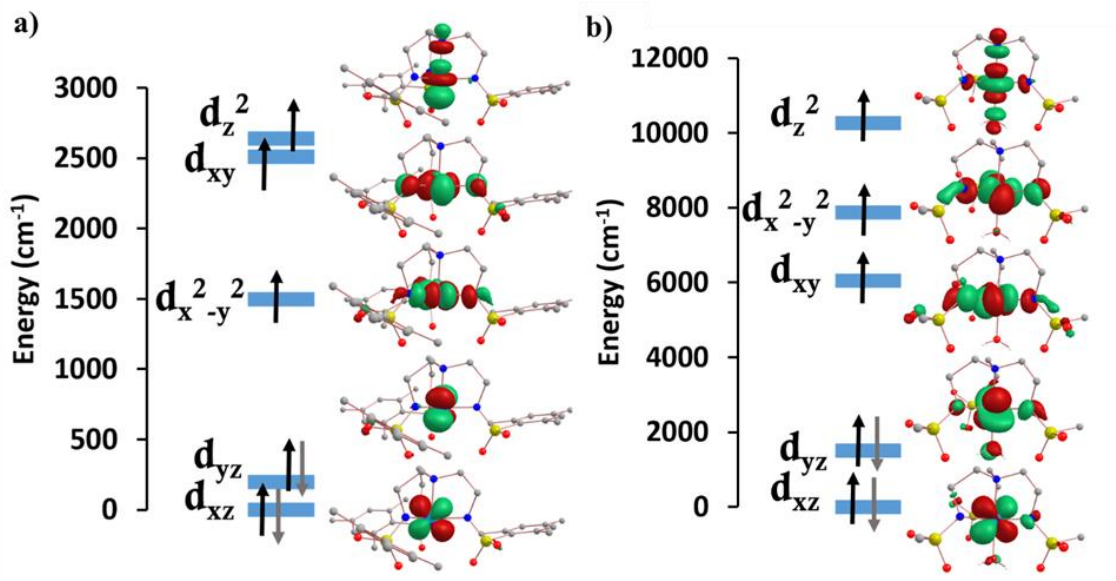

Figure II.27 CASSCF-computed d-orbital ordering for complex a) **1** and b) **2**. Reprinted by permission from reference 98.

The d-orbital splitting for the Fe^{II} ion in complexes **3** and **4** are shown in Figure II.28. In **3**, the first excitation between the d_{xz} and d_{yz} levels (same $|\pm m_l|$ value) causes the largest negative contribution to *D* (-36.0 cm^{-1}) due to the low-lying first excited state (~870 cm^{-1}). The other three excitations cause a small positive contribution on *D*, resulting in a

slightly smaller negative *D* value. For compound **4**, both CASSCF and NEVPT2 calculations predict that the first excitation occurs unusually between the d_{xz} and d_{xy} levels (different $|\pm m_l|$ values) rather than d_{xz} and d_{yz} levels (same $|\pm m_l|$ values) resulting in a positive contribution to *D*. The magnitude of *D* decreases due to an increase in the first excited state energy (~1300 cm^{-1}). A small negative contribution to *D* from the second excitation (between the d_{xz} and d_{yz} levels) and positive *D* contributions from the third and fourth excitations lead to the overall positive *D* value for this compound. The fitted *D* values of -31 cm^{-1} for 3 and 8.7 cm^{-1} for 4 are slightly higher than the CASSCF and NEVPT2 values of -30.1 and -28.6 cm^{-1}, and 6.6 and 6.0 cm^{-1} respectively. A positive *D* value results in a better fit of the experimental data for 4 which is in line with the calculations.

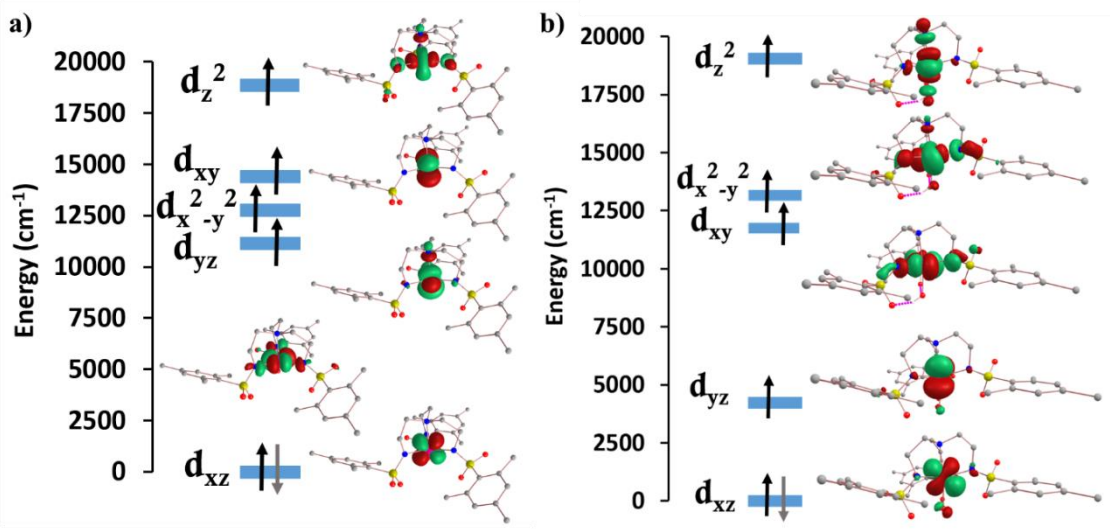

Figure II.28 CASSCF-computed d-orbital ordering for complexes a) **3** and b) **4**. Reprinted by permission from reference 98.

The d-orbital splitting for complexes **5** and **6** are depicted in Figure II.29. The enormous magnitude of *D* for both complexes arises from three predominant spin-conserved triplet excitations.[82] Both the CASSCF and NEVPT2 methods predict that the first spin-free excitation between the $d_{x^2-y^2}$ and d_{xy} orbitals is lowest in energy for Ni^{II} complexes **5** and **6**. A relatively large negative contribution to the *D* value from this excited state leads to a giant zero field splitting for these two complexes (Table 3). For **5**, a very low-lying first excited state (below 80 cm^{-1}) causes the largest negative contribution to *D* of -530 cm^{-1}. The other excited states are much higher in energy from the ground state (above 5500 cm^{-1}), resulting in a small positive contribution to *D*. Overall, this situation leads to a giant negative *D* value for compound **5**. In the case of complex **6**, the first excited state (~250 cm^{-1}) is approximately three times higher in energy than that of complex 5, thereby reducing the magnitude of *D*. As is the case for **5**, the next three excited states are much higher in energy (above 6,400 cm^{-1}) and result in relatively small positive contributions to the *D* value. Although smaller than the corresponding value for **5**, **6** still displays an unusually large axial ZFS parameter. The fitted value of *D* for 6 of -209 cm^{-1} is slightly higher than the calculated *D* values of -185.7 and -131.3 cm^{-1}.

The biggest discrepancy in all of these fits occurs with **5** which exhibits an experimentally fitted value of -276 cm^{-1} versus the calculated values of 434.1 and 428.9 cm^{-1}. A rigorously anhydrous atmosphere could not be maintained during handling, and, given that this complex is extraordinarily hygroscopic, a rigorously dehydrated sample could not be obtained. The differences in the experimental and calculated values is attributed to partial coordination of water, a hypothesis that is supported by an observed

visible change from salmon to orange/tan before the sample could be sealed under vacuum. Given the accuracy of the other five complexes in terms of the calculations, it is expected that the actual *D* value is much closer to the computed *D* values rather than the fitted *D* value.

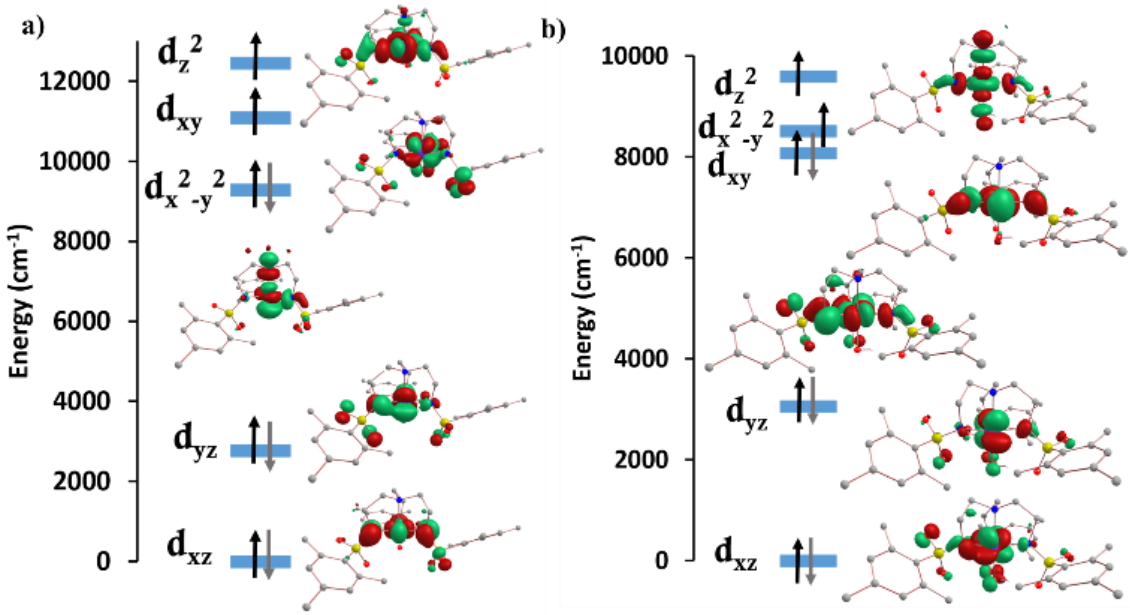

Figure II.29 Ab initio computed crystal field splitting for compounds a) **5** and b) **6**. Reprinted by permission from reference 98.

II.3.3 AC Magnetic Studies

Dynamic AC measurements under varying fields were performed on complexes **1**-**6**. No signal was observed for any of the complexes without an applied DC field. As a result, AC measurements under applied DC fields from 400-2000 Oe were measured, and complexes **1**-**3** were found to exhibit slow magnetic relaxation. The field used for further

studies was chosen as the one with the most obvious maximum in χ" signals at the lowest frequencies.

Compound **1** exhibits a maximum around 40 Hz, and its water counterpart exhibits a maximum at a higher frequency of approximately 100 Hz. Compound **3** displays the lowest frequency maximum at ~10 Hz. Interestingly, the coordination of water in **4** results in complete quenching of slow magnetic relaxation, with no signals up to 2000 Oe. Complexes **5** and **6** did not display slow relaxation at 1.8 K under applied fields up to 2000 Oe. Fittings of the Cole-Cole plots for **1-3** were performed to extract U_{eff}, τ, and α parameters based on a modified Debye Function. The resulting Arrhenius plot was fit using the following equation. To avoid over-parameterization, A was assumed to be 0.

$$\boldsymbol{\tau^{-1} = \tau_{QTM}^{-1} + AT + CT^{n} + \tau_{0}^{-1} exp\left(-\frac{U_{eff}}{k_B T}\right)}$$

Complex **1** was measured under an applied DC field of 1000 Oe. A maximum in χ" was observed up to 5.8 K, along with the corresponding decrease in χ'. The low temperature regime is dominated by frequency independent quantum tunneling up to approximately 3 K, after which temperature the thermal regime becomes more prevalent. The χ' and χ" plots can be found in Figure II.30.

a)

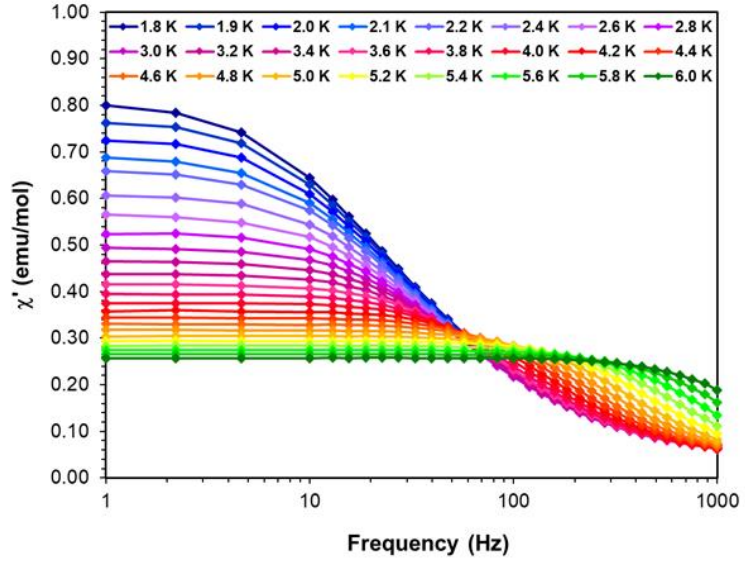

b)

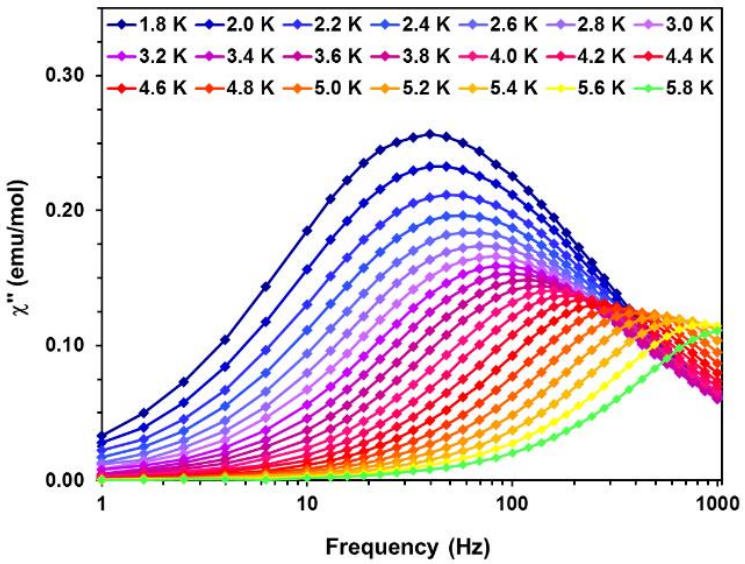

Figure II.30 a) In phase susceptibility (χ') vs Frequency and b) out of phase susceptibility (χ") for **1**. Solid lines are guides for the eye. Adapted by permission from reference 98.

The in-phase and out-of-phase susceptibility plots were subsequently converted into Cole-Cole plots. These were subsequently fit using CC-fit[83] which led to a maximum

α value of 0.27, indicating a moderately wide range of relaxations times. The fit of all temperatures in the Arrhenius plot resulted in a barrier of U_{eff}/k_b = 45 K and τ_o = 3.1 x 10^{-9} s, Figure II.31. Extracted Raman parameters of C = 0.014 s^{-1} and n = 7.3 are in agreement with the expected range for a Kramers ion.[84] The τ^{-1} value for quantum tunneling was fit to 0.003 s.

a)

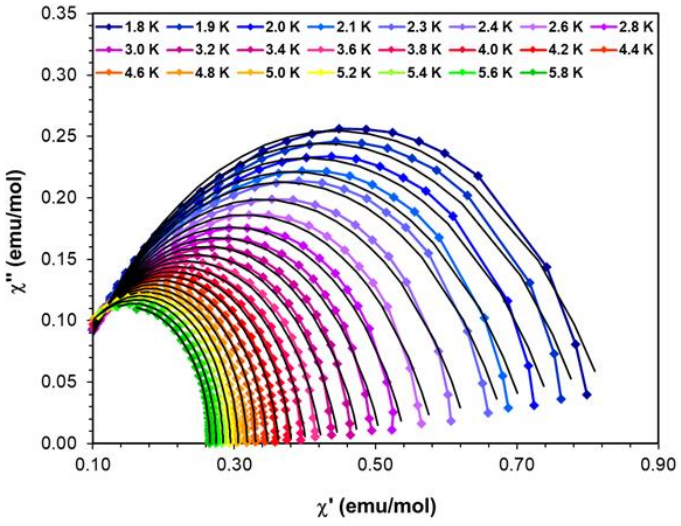

b)

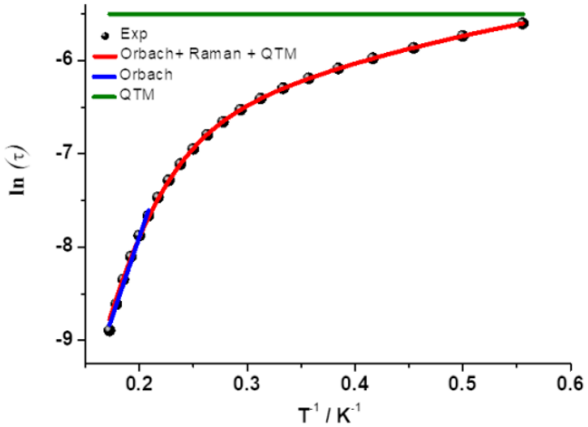

Figure II.31 a) Cole-Cole plot fit via CC-fit, black lines are fits to the data b) ln(τ) vs 1/T, black dots are experimental data and colored lines are fits as labelled. Adapted by permission from reference 98.

The water complex, **2**, was also measured under an applied DC field of 1000 Oe. A maximum of χ" could be observed up to 3.8 K. Interestingly, the low temperature range is no longer dominated by quantum tunneling, but rather by thermal relaxation. The χ' and χ" plots can be found in Figure II.32.

a)

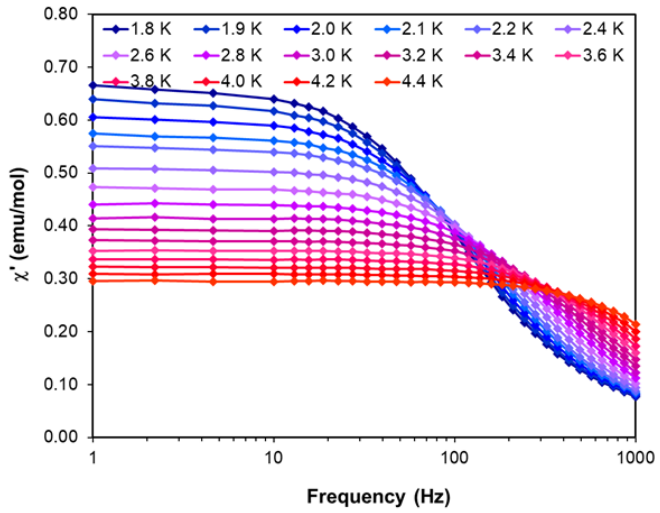

b)

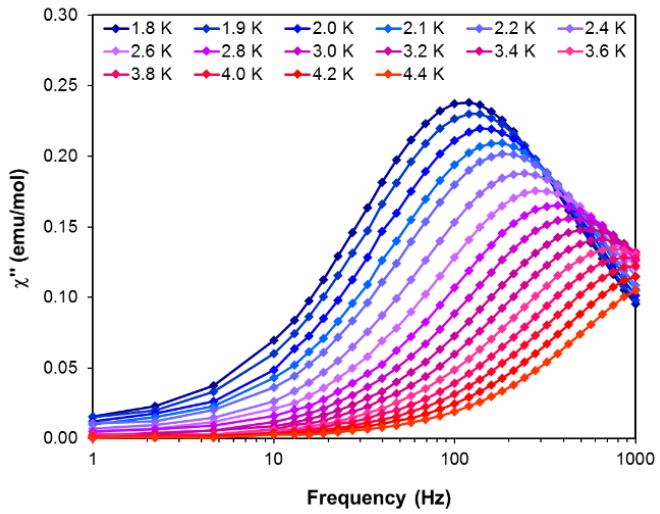

Figure II.32 a) In phase susceptibility (χ') vs Frequency and b) out of phase susceptibility (χ") for **2**. Solid lines are guides for the eye. Adapted by permission from reference 98.

The α values are less than 0.17, indicating a narrower range of relaxation times compared to **1**. A fit of all temperatures in the Arrhenius plot was conducted, Figure II.33, to give U_{eff}/k_b = 9.9 K and τ_o = 1.5 x 10^{-5} s. Extracted Raman parameters of C = 0.008 s^{-1} and n = 7.2 are in agreement with the expected range for a Kramers ion. The τ^{-1} value for quantum tunneling was fit to be 0.0014 s.

a)

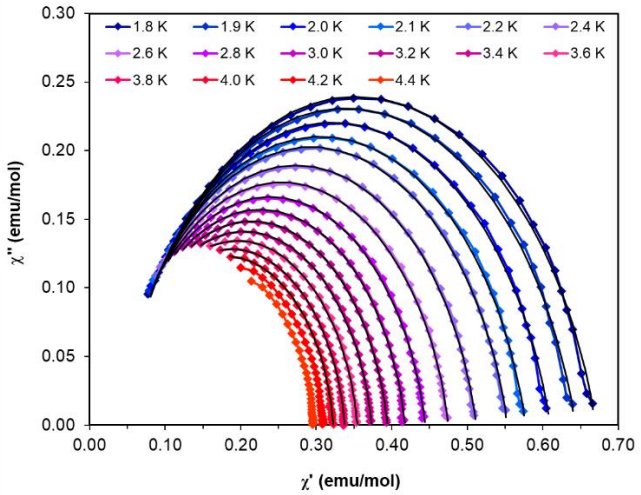

b)

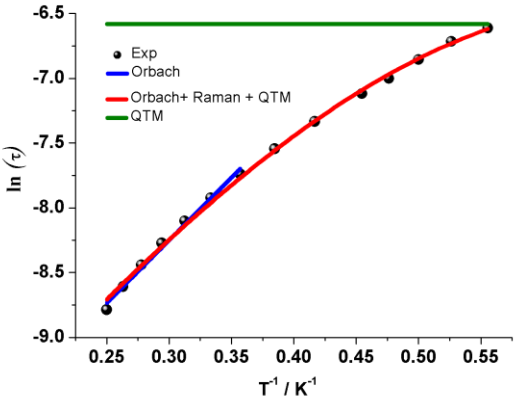

Figure II.33 a) Cole-Cole plot fit via CC-fit, black lines are fits to the data b) ln(τ) vs 1/T, black dots are experimental data and colored lines are fits as labelled. Adapted by permission from reference 98.

Complex **3** also displays SMM behavior under an applied DC field, with the optimum field being 1200 Oe. A maximum in χ" can be observed up to 5.6 K. The low temperature regime exhibits some quantum tunneling, after which temperature the thermal regime becomes more prevalent. The χ' and χ" plots can be found in Figure II.34.

a)

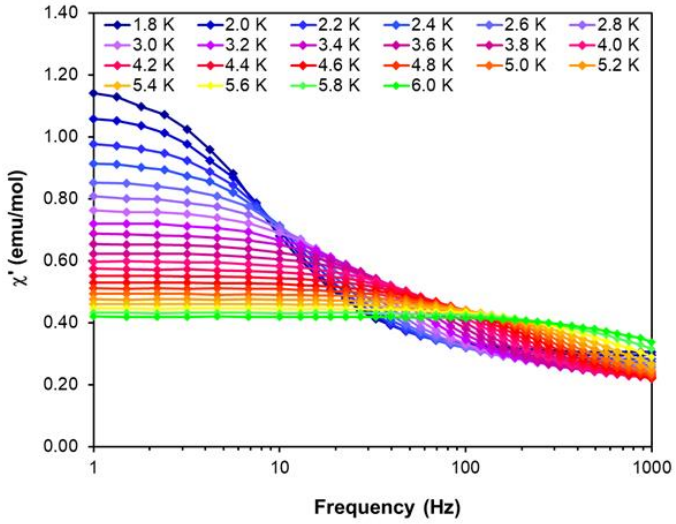

b)

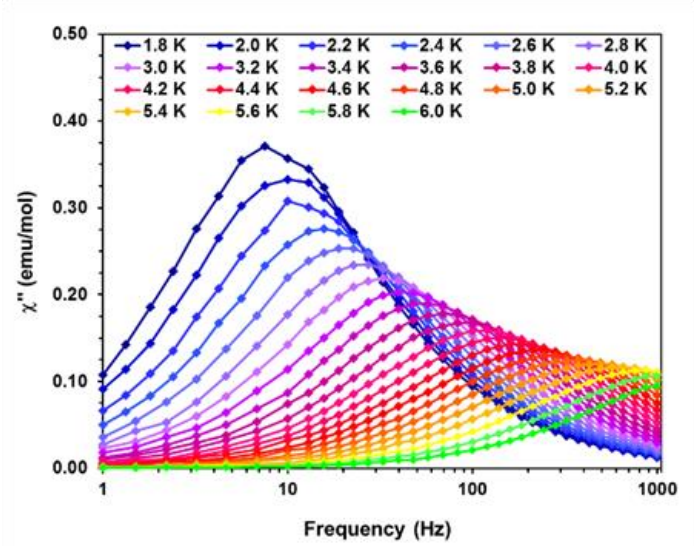

Figure II.34 a) In phase susceptibility (χ') vs Frequency and b) out of phase susceptibility (χ") for **3**. Solid lines are guides for the eye. Adapted by permission from reference 98.

The α values vary from 0.14 to 0.16, indicating a small range of relaxation times. A fit of all temperatures in the Arrhenius plot was conducted resulting in a barrier of U_{eff}/k_b = 63.9 K and τ_o = 1.98 x 10^{-8} s, Figure II.35. Extracted Raman parameters of C = 1.41 s^{-1} and n = 4.4 are in agreement with the expected range for a non-Kramers ion. The τ^{-1} for quantum tunneling is 0.0012 s.

a)

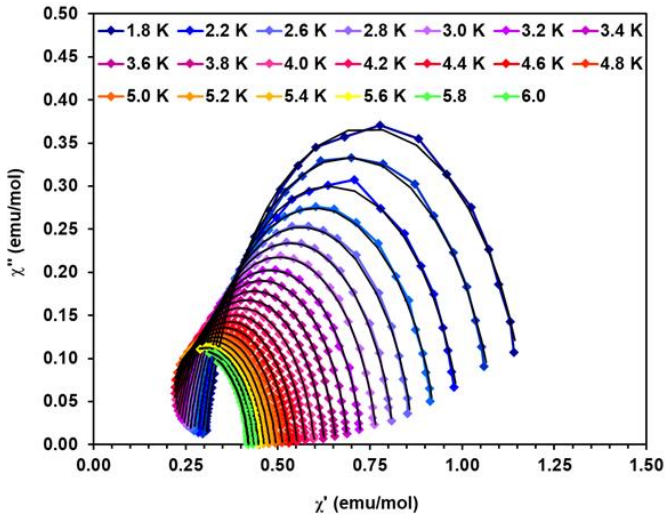

b)

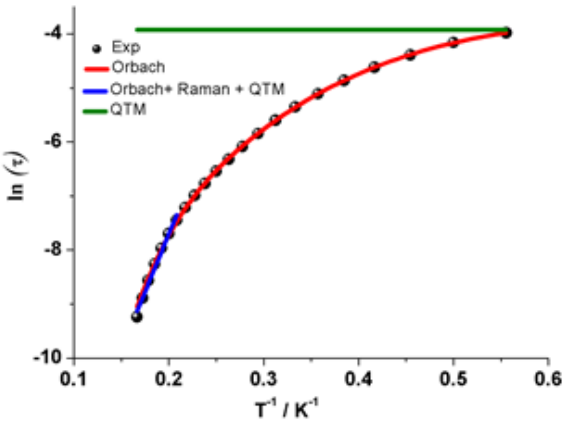

Figure II.35 a) Cole-Cole plot fit via CC-fit, black lines are fits to the data b) ln(τ) vs 1/T, black dots are experimental data and colored lines are fits as labelled. Adapted by permission from reference 98.

The barriers of both **1** and **2** are lower than expected given the 2|D| energy gaps between the m_S = 1/2 and m_S = 3/2 microstates, which are 66 and 48 cm^{-1}, respectively. This situation in **1** can be attributed to the quantum tunneling and Raman relaxations being larger contributors than the Orbach process. The same conclusion is reached for complexes **3** and **4**, for which the expected barrier height (U) would be 4|D|, or 124 and 34 cm^{-1} respectively. No slow magnetic relaxation is observed in **5** and **6** due to significant quantum tunneling, although the barrier could be as high as 434 cm^{-1}, given that the energy between the m_S=0 and m_S=1 microstates is |D|. This finding is not entirely unexpected as, to the best of our knowledge, only two divalent nickel complexes exhibiting slow magnetic relaxation have been reported, and a large applied field of 2000 Oe was necessary to observe that behavior.[64, 85]

II.3.4 Structural, Magnetic, and Computational Correlations

Detailed crystallographic, computational, and magnetic studies were undertaken in order to understand the strong variance in magnetic behavior that coordination of a single water molecule exerts on trigonal monopyramidal complexes. Generally, the original species all exhibit slow magnetic relaxation at higher temperatures with higher D values than their trigonal bipyramidal water adducts.

Comparisons of crystal structures revealed a few trends across the 3 pairs of compounds. The trigonal monopyramidal complexes are all much closer to ideal geometry than their trigonal bipyramidal counterparts. The results of our studies lend credence to the requirement of strict geometric control for superior magnetic behavior. Compounds **1**,

3, and **5** exhibit M···M separations that are larger than their partners **2**, **4**, and **6** respectively; the variation across the anhydrous versus water adduct pairs is 0.029, 0.161, and 0.067 Å for cobalt, iron, and nickel, respectively. These parameters are in accord with the magnetic behavior, but are unlikely to be a major contributing factor. For example, the distances observed for the cobalt complexes are larger than the ~8 Å at which dipolar relaxations are expected to be suppressed. Therefore, it appears that the geometric distortions have greater control over the observed magnetic properties.

The computational results support this hypothesis. In each case, the trigonal monopyramidal geometries exhibit lower excitations than their trigonal bipyramidal pair which follows the observed trend in the AC susceptibility studies. The increased distortion in **2** results in a larger energy gap between the d-orbitals, causing a smaller *D* value. Computations also explain why no slow relaxation is observed for **4** even under an applied field. In this case, rather than the expected excitation between the d_{xz} and d_{yz} orbitals, the excitation takes place between the d_{xz} and d_{xy} orbitals resulting in a positive *D* value. The decrease in magnitude and change in sign of *D* completely quenches slow relaxation.

It must be noted that this work does not imply that TMP geometry is inherently better for SMM behavior than TBP geometry. The TMP complexes are closer to ideal geometry than the TBP complexes across the series, which corresponds to improved magnetic properties. While **1** performs better, to the best of our knowledge, than any of the reported barriers for divalent cobalt trigonal monopyramidal and bipyramidal SMMs, with only 8 complexes available for

comparison (6 TBP and 2 TMP), a concrete conclusion cannot be drawn.[18, 40, 65, 86-87] $[Co(TPMA)(CH_3CN)](BF_4)_2$ (TPMA = tris(2-pyridylmethyl)amine) is the only other TBP compound reported to have a positive *D* value.[65] In both cases, the positive sign of *D* is largely due to contributions from the third and fourth excited states.

No reports of a divalent iron TBP complex exhibiting slow magnetic relaxation have appeared in literature and the only TMP complexes prior to this work is the tpa^R series by Long, *et al.*[24-25] Compound **3** exhibits a barrier only slightly smaller than these molecules which range from 36 to 93.5 K. In each case, an applied field is necessary to observe slow magnetic relaxation. The SHAPE values for these complexes are all similar to that of **3**, with no observable trend between the SHAPE value and barrier height. It is important to note, however, that the only complex with crystallographically imposed trigonal symmetry displays the highest barrier among the previously reported complexes as well as the one in this work. Theoretical analysis of the series by Long *et al.* emphasized the importance of σ-donating and withdrawing substituents on the magnetic behavior in that there is a correlation between increased σ donation and an increase in the *D* value.[26] These considerations must also be taken into account.

There is only one reported divalent nickel complex in trigonal bipyramidal geometry which exhibits slow relaxation, *viz.*, $[Ni(MDABCO)_2Cl_3]ClO_4$ with a *D* value of -535 cm^{-1}, which is close to the theoretical maximum of 668 cm^{-1}, given by the one electron spin-orbit coupling parameter for a Ni(II) free ion.[64, 88] The

SHAPE value of 0.13 is much closer to ideal TBP geometry than is **6**, which is in agreement with the magnetic behavior. The structure of **5** is much closer to ideal geometry with a shape value of 0.18, which more closely aligns with $[Ni(MDABCO)_2Cl_3]ClO_4$. Both **5** and **6** exhibit equatorial bond angles deviating from the ideal 120° more so than $[Ni(MDABCO)_2Cl_3]ClO_4$. The slightly lower *D* value of -434 cm^{-1} for **5** and absence of slow magnetic relaxation could possibly be attributed to this slightly greater deviation from ideal geometry. These results are consistent with theoretical calculations and high pressure studies on TBP Ni(II) complexes underscoring the importance of equatorial bond angles as close to 120° as possible for SMM behavior to be observed.[89-90]

II.4 Cobalt RST Complexes Experimental Details

II.4.1 Complex Synthesis

All syntheses were conducted under a N_2 atmosphere. The original syntheses were performed in a MBRAUN glovebox under rigorous anhydrous conditions. The conversion to the water complexes took place in a Vacuum Atmosphere glovebox with the catalyst turned off so that it was not a totally dry atmosphere. Commercial anhydrous dimethylacetamide (DMA) was dried over BaO, and stored in the drybox over molecular sieves. Diethyl ether and dichloromethane solvents in the purge box were degassed with an Argon stream. $Co(OAc)_2$ and NaH were purchased and used as received. Me_4NOAc was dried under vacuum at 100°C overnight. Dryness was confirmed for each of these starting materials using infrared spectroscopy. The ligands H_3[PST], H_3[TST], and H_3[FST] were synthesized according to literature procedures.[66, 69] Syntheses of

$(Me_4N)[Co^{II}(RST)(OH_2)]$ complexes were performed with modified procedures from literature;[66-69] details are below.

$(Me_4N)[Co(PST)(OH_2)]$ (**7**). A 20 mL vial was charged with H_3[PST] (100 mg, 0.17 mmol), NaH (13.1 mg, 0.55 mmol), Me_4NOAc (35 mg, 0.26 mmol), and DMA (5 mL). The reaction was stirred until all of the NaH had reacted. $Co(OAc)_2$ (31.2 mg, 0.17 mmol) was added to the reaction, and the mixture was stirred for overnight to give a dark pink solution which was subsequently filtered over a fine frit. This solution was transferred into the wet glovebox, and water was added until the solution turned light pink. Crystals were obtained via diethyl ether diffusion into the DMA solution (83 mg, 67% yield).

$(Me_4N)[Co(TST)(OH_2)]$ (**8**). Compound **8** was synthesized in a manner akin to **7** using $Co(OAc)_2$ (29.1 mg, 0.16 mmol), H_3[TST] (100 mg, 0.16 mmol), NaH (12 mg, 0.50 mmol), Me_4NOAc (32.8 mg, 0.25 mmol), and DMA (5 mL). Pink crystals suitable for x-ray analysis were obtained via slow diffusion of diethyl ether into the original DMA solution (71 mg, 59% yield).

$(Me_4N)[Co(FST)(OH_2)]$ (**9**). Compound **9** was synthesized in a manner akin to **7** using $Co(OAc)_2$ (23.0 mg, 0.13 mmol), H_3[FST] (100 mg, 0.13 mmol), NaH (9.7 mg, 0.40 mmol), Me_4NOAc (25.9 mg, 0.19 mmol), and DMA (5 mL). Pink crystals suitable for x-ray analysis were obtained via slow diffusion of diethyl ether into the original DMA solution (76 mg, 65% yield).

II.4.2 Crystallography

Structural characterization was performed with single crystals on a Bruker QUEST instrument with a Mo Kα source. Compounds **7**, **8**, and **9** were collected on the QUEST

instrument equipped with a CCD detector. Suitable crystals were mounted on MiTeGen microloops using ®Paratone oil and placed in a cold stream of N_2 for collection at 100 K. The collected data was integrated within the APEX 2 software suite, as well as SADABS for absorbance corrections.[70] The structures were solved and refined using SHELXT[71] and SHELXL[72] respectively within the OLEX program.[73] Hydrogen atoms were added in calculated positions. In some cases, reorientations of hydrogen atoms was performed to match visible electron density as well as due to obvious hydrogen bonding interactions.

All non-hydrogen atoms were refined anisotropically, with the exception of compound **9**. The best crystals diffracted to 1.2 Å on QUEST or with a synchrotron source, and so the structure was refined isotropically. SIMU and SADI restrains as well as EADP constraints were necessary to reasonably refine all atoms. There is disorder in the phenyl rings that could not be modelled due to the available data. Disorder can be observed in the $[Me_4N]^+$ cation of compound **8**, where three methyl groups rotate about an axis formed by the remaining methyl group and central carbon atom. The two orientations exist in a ratio of 65:35. Further disorder is present in the SO_2 linking group for one arm of one $[Co(TST)(OH_2)]^-$ anion. The rocking behavior is modelled with two parts which exist in a 60:40 ratio. SADI and SIMU restraints and EADP constraints were necessary to refine the disorder anisotropically. Further crystallographic details can be found in Table II-7.

Table II-7 Crystal structure data and refinement parameters for $(Me^4N)[M^{II}(RST)(OH_2)]$ complexes.

Identification code	(Me4N)[Co(PST)(OH2)]	(Me4N)[Co(TST)(OH2)]
Empirical formula	$C_{28}H_{41}CoN_5O_7S_3$	$C_{186}H_{278.88}Co_6N_{30}O_{41.08}S_{18}$
Formula weight	714.77	4523.16
Temperature/K	100	110
Crystal system	monoclinic	monoclinic
Space group	$P2_1/n$	$P2_1/c$
a/Å	8.8333(4)	27.6756(7)
b/Å	19.4522(9)	28.1247(8)
c/Å	18.8765(8)	27.3928(7)
α/°	90	90
β/°	98.9080(10)	98.7760(10)
γ/°	90	90
Volume/Å^3	3204.4(2)	21072.0(10)
Z	4	4
ρ_{calc}g/cm^3	1.482	1.426
μ/mm^{-1}	0.784	0.719
F(000)	1500.0	9534.0
Crystal size/mm^3	0.114 × 0.057 × 0.042	0.95 × 0.36 × 0.23
Radiation	MoKα (λ = 0.71073)	MoKα (λ = 0.71073)
2Θ range for data collection/°	4.188 to 50.15	4.154 to 45.972
Index ranges	$-10 \le h \le 10$, $-23 \le k \le 23$, $-22 \le l \le 21$	$-30 \le h \le 30$, $-30 \le k \le 30$, $-30 \le l \le 30$
Reflections collected	66775	305314
Independent reflections	5703 [R_{int} = 0.1211, R_{sigma} = 0.0623]	29257 [R_{int} = 0.0698, R_{sigma} = 0.0420]
Data/restraints/parameters	5703/0/402	29257/83/2637
Goodness-of-fit on F^2 [c]	1.087	1.121
Final R indexes [I>=2σ (I)] [a,b]	R_1 = 0.0449, wR_2 = 0.1040	R_1 = 0.0472, wR_2 = 0.0942
Final R indexes [all data] [a,b]	R_1 = 0.0806, wR_2 = 0.1259	R_1 = 0.0754, wR_2 = 0.1032
Largest diff. peak/hole / e Å^{-3}	0.38/-0.60	0.36/-0.49

Table II-7 Continued.

Identification code	(Me4N)[Co(FST)(OH2)]
Empirical formula	$C_{62}H_{76}Co_2F_{18}N_{10}O_{14}S_6$
Formula weight	1837.54
Temperature/K	120
Crystal system	monoclinic
Space group	$P2_1/c$
a/Å	29.724(4)
b/Å	9.1042(13)
c/Å	32.574(5)
α/°	90
β/°	114.795(4)
γ/°	90
Volume/Å^3	8002(2)
Z	4
ρ_{calc}g/cm^3	1.525
μ/mm^{-1}	0.677
F(000)	3768.0
Crystal size/mm^3	0.054 × 0.032 × 0.008
Radiation	MoK_α (λ = 0.71073)
2Θ range for data collection/°	4.2 to 34.888
Index ranges	$-24 \leq h \leq 24$, $-7 \leq k \leq 7$, $-27 \leq l \leq 27$
Reflections collected	78285
Independent reflections	4985 [R_{int} = 0.1423, R_{sigma} = 0.0540]
Data/restraints/parameters	4985/17/397
Goodness-of-fit on F^2 [c]	1.097
Final R indexes [I>=2σ (I)] [a,b]	R_1 = 0.2284, wR_2 = 0.4716
Final R indexes [all data] [a,b]	R_1 = 0.2385, wR_2 = 0.4777
Largest diff. peak/hole / e Å^{-3}	2.19/-1.95

[a]$R_1 = \Sigma(||F_o| - |F_c||)/\Sigma|F_o|$. [b]$wR_2 = [\Sigma[w(F_o^2 - F_c^2)^2]/\Sigma[w(F_o^2)^2]]^{1/2}$ [c]Goodness-of-fit = $[\Sigma[w(F_o^2 - F_c^2)^2]/(n - p)]^{1/2}$, where *n* is the number of reflections and p is the total number of parameters refined.

(Me$_4$N)[Co(PST)(OH$_2$)]. Similar to compound **2,** the coordination of this molecule takes place between the four nitrogen atoms of the PST ligand and one water molecule in the axial position. Tetramethylammonium co-crystallizes with the Co^{II} anionic moiety. This confirms both the divalent state of the cobalt center, as well as full deprotonation of the

ligand. The compound crystallizes in the monoclinic space group $P2_1/n$. The molecular structure of the anion is depicted in Figure II.36. The three arms of the ligand coordinate about the cobalt cation with bond angles that vary between 116.99(12)° and 118.91(12)°. These deviations away from 120° are indicative of deviation in ideal trigonal geometry. The bond lengths vary between 2.026(3) Å and 2.043(3) Å, and the bond angle between the axial nitrogen atom, cobalt ion, and axial oxygen atom is 174.57(10) which corroborates the distortion. The metal center is out of the plane generated by these three equatorial nitrogen atoms by 0.318 Å. The closest intermolecular distance between two of the cobalt centers is 8.833 Å.

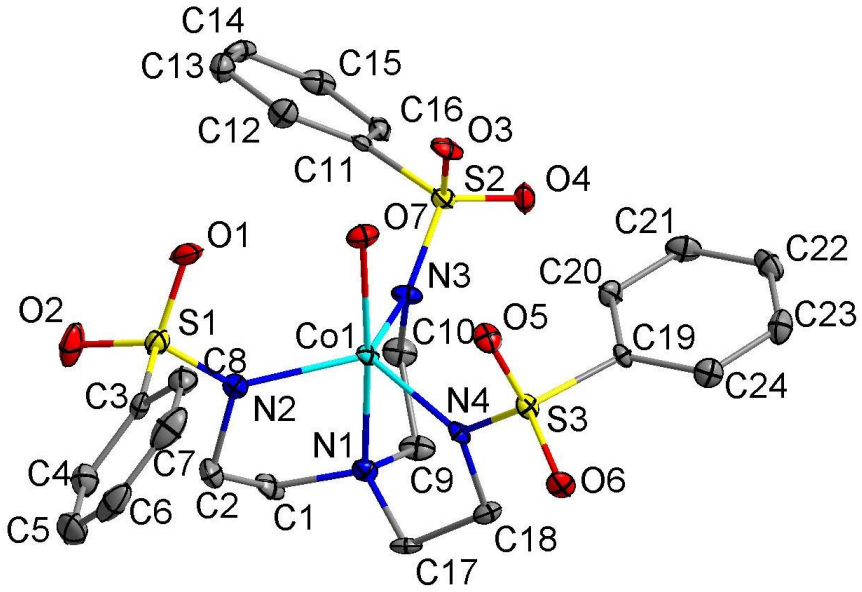

Figure II.36 Crystal structure and atom numbering scheme of the $[Co(PST)(OH_2)]^-$ anionic moiety. The Me_4N^+ cation and hydrogen atoms were omitted for clarity. Thermal ellipsoids were drawn at the 50% probability level. Colors are as follows: turquoise, Co; blue, N; yellow, S; red, O; grey, C.

$(Me_4N)[Co(TST)(OH_2)]$. Coordination of this molecule is identical to **7**. The compound crystallizes in the monoclinic space group $P2_1/c$. The asymmetric unit contains 6 $(Me_4N)[Co(TST)(OH_2)]$ molecules. The differences in these structures largely originates in the coordination of water, which varies from fully occupied to occupied 62% of the time. Three of the molecules are fully occupied, with the remaining molecules containing water with occupancies of 0.62, 0.64, and 0.81. SADI and SIMU restraints were placed on the disordered sulfur and oxygen atoms, as well as the bonded carbon and nitrogen atoms. SADI and EADP were applied to the disordered tetramethylammonium cation. These commands resulted in reasonable anisotropic refinement of the disorder. The crystal structure of one of the anionic molecules can be found in Figure II.37, representative of the coordination found in each of the 6 molecules in the asymmetric unit. The three arms of the ligand coordinate about the cobalt cation with bond angles that vary between 116.33(13)° and 119.38(13)°. The bond lengths vary between 2.002(3) Å and 2.040(3) Å. The bond angle between the axial nitrogen atom, cobalt ion, and axial oxygen atom is 177.20(11). The metal center is out of the plane generated by these three equatorial nitrogen atoms by 0.300 Å. The closest intermolecular distance between two of the cobalt centers is 9.116 Å.

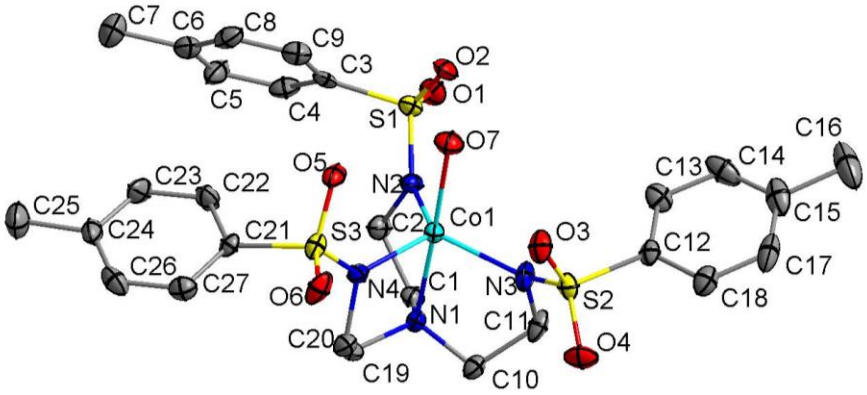

Figure II.37 Crystal structure and atom numbering scheme for one of the $[Co(TST)(OH_2)]^-$ anionic moieties. The Me_4N^+ cation, hydrogen atoms, and remaining $(Me_4N)[Co(TST)(OH_2)]$ molecules were omitted for clarity. Thermal ellipsoids were drawn at the 50% probability level. Colors are as follows: turquoise, Co; blue, N; yellow, S; red, O; grey, C.

$(Me_4N)[Co(FST)(OH_2)]$. Coordination of this molecule is identical to **7**. The compound crystallizes in the monoclinic space group $P2_1/c$. The asymmetric unit contains 2 $(Me_4N)[Co(FST)(OH_2)]$ molecules. The crystal structure of one of the anions can be found in Figure II.38. The three arms of the ligand coordinate about the cobalt cation with bond angles that vary between 114.1(12)° and 125.4(11)°. The bond lengths vary between 1.99(3) Å and 2.05(3) Å. The bond angle between the axial nitrogen atom, cobalt ion, and axial oxygen atom is 174.3(11)°. The metal center is out of the plane generated by these three equatorial nitrogen atoms by 0.334 Å. The closest intermolecular distance between two of the cobalt centers is 8.833 Å.

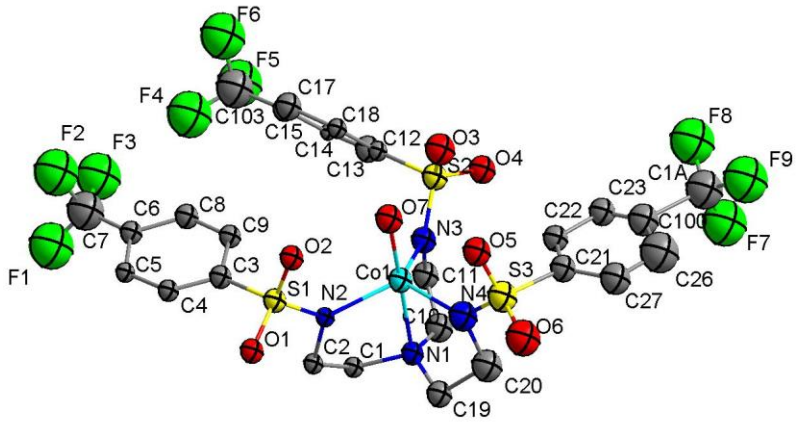

Figure II.38 Crystal structure and atom numbering scheme of the $[Co(FST)(OH_2)]^-$ anionic moiety. The Me_4N^+ cation, hydrogen atoms, and remaining $(Me_4N)[Co(TST)(OH_2)]$ molecules were omitted for clarity. Thermal ellipsoids were drawn at the 50% probability level. Colors are as follows: turquoise, Co; green, F; blue, N; yellow, S; red, O; grey, C.

II.4.3 Magnetic Measurements

Magnetic data were collected on a Quantum Design MPMS-3 SQUID from 1.8-300 K with DC fields from 0-7 T. Compounds **7-9** were collected in plastic bags. Diamagnetic corrections were applied for the bags. The diamagnetic contribution from the compounds were calculated based on Pascal's constants.[74]

II.5 Results and Discussion

II.5.1 Crystallographic Details

The three new compounds, $(Me_4N)[Co(PST)(OH_2)]$ (**7**), $(Me_4N)[Co(TST)(OH_2)]$ (**8**), and $(Me_4N)[Co(FST)(OH_2)]$ (**9**) were synthesized based on literature procedure[69] via a reaction between the deprotonated ligand using NaH, the appropriate metal(II) acetate salt, and tetramethylammonium acetate in

dimethylacetamide (DMA) as the solvent. A schematic of the ligand synthesis is provided in Figure II.39.

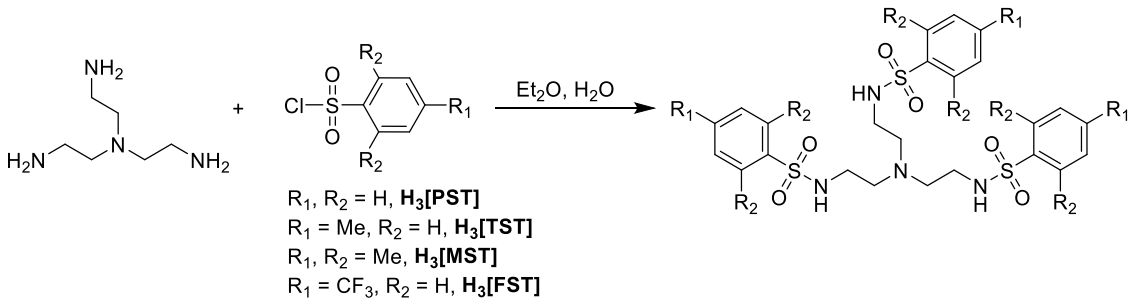

Figure II.39 Schematic of the synthetic procedure for the ligands H_3[PST], H_3[TST], H_3[MST], and H_3[FST].

Crystals were obtained by slow diffusion of diethyl ether into either DMA or dichloromethane (DCM) solutions. Complex **7** crystallizes in the space group monoclinic $P2_1/n$, and complexes **8** and **9** in monoclinic $P2_1/c$. These three compounds were compared to complex **2**, which crystallized in the triclinic space group $P\bar{1}$, as it fits in with the series as a whole.

The geometries of all four complexes were confirmed using the SHAPE program[79-80] which compares the experimental metrical parameters to the perfect geometry, with 0 indicating a perfect match to that geometry. These results are summarized in Table II-8, with the trigonal monopyramidal complexes being much closer to the ideal geometry than the trigonal bipyramidal complexes.

Table II-8 Shape measurements for compounds **2**,**7**-**9**. Abbreviations are as follows: PP, pentagon; vOC, vacant octahedron; TBPY, trigonal bipyramid; SPY, square pyramid; JTBPY, Johnson trigonal bipyramid.

	PP	**vOC**	**TBPY**	**SPY**	**JTBPY**
2	35.541	7.083	0.695	5.309	2.498
7	35.793	7.384	0.809	5.417	2.698
8	35.250	7.283	0.868	5.382	2.320
9	33.875	6.834	0.992	5.277	3.028

In each structure, the metal center is above the equatorial plane generated by the 3 coordinating nitrogen atoms, with **2** exhibiting the least distortion at a Co-N_{plane} distance of 0.295 Å. See Table II-9 for a summary of these measurements for all compounds.

Table II-9 Selected intermolecular and intramolecular distances (Å) of **2, 7-9**.

	2	**7**	**8**	**9**
$N_3…M^a$	0.295	0.318	0.300	0.334
$M…M^b$	8.479	8.833	9.116	8.500

[a] distance between the metal center and the plane generated by the three equatorially coordinated nitrogen atoms (N2-N4)
[b] closest intermolecular distance between two metal centers

In each case, there is deviation from the ideal trigonal angle of 120° in the equatorial plane, and the angles between the axial nitrogen and oxygen atoms are <180°. This bend can be attributed to hydrogen bonding between the water and the sulfonyl oxygen atoms. See Table II-10 for a summary of the relevant distances and angles.

Table II-10 Selected bond lengths (Å) and angles (°) around the inner coordination sphere of **2**, **7-9**.

	2	**7**	**8**	**9**
N1	2.180(2)	2.171(3)	2.207(3)	2.29(3)
N2	2.032(2)	2.043(3)	2.040(3)	2.05(3)
N3	2.033(3)	2.058(3)	2.008(3)	1.99(3)
N4	2.022(2)	2.026(3)	2.002(3)	2.03(3)
N2-M-N3	120.04(10)	116.99(12)	119.38(13)	125.4(11)
N3-M-N4	114.81(10)	116.99(12)	116.33(13)	114.2(13)
N4-M-N2	118.90(10)	118.91(12)	117.75(13)	114.1(12)
N1-M-O7	176.72(9)	174.57(10)	177.20(11)	174.3(11)

II.5.2 DC Magnetic Studies

Static DC measurements were performed on complexes **7-9** from 1.8 – 300 K using a SQUID magnetometer, Figure II.40. Complex **2**, discussed previously in this chapter, is also shown in Figure II.40. The $\chi_m T$ values are all higher than 1.87 emu K mol^{-1}, the ideal value for an S=3/2 system with *g*=2. Complex **7** exhibits a $\chi_m T$ value of 2.77 emu K mol^{-1} at 300 K, which slowly decreases to 2.30 emu K mol^{-1} at 50 K, after which temperature there is a steep decrease to 1.51 emu K mol^{-1} at 2 K. Complex **8** exhibits a $\chi_m T$ value of 2.47 emu K mol^{-1} at 300 K, which slowly decreases to 2.23 emu K mol^{-1} at 50 K, after which there is a steep decrease down to 1.47 emu K mol^{-1} at 2 K. Complex **9** exhibits a $\chi_m T$ value of 2.67 emu K mol^{-1} at 300 K, which slowly decreases to 2.30 emu K mol^{-1} at 50 K and a steep decrease to 1.47 emu K mol^{-1} at 2 K. These deviations from ideality reflect spin-orbit coupling. Each compound exhibits Curie-like behavior until ~30 K, after which $\chi_m T$ decreases as expected due to zero-field splitting.

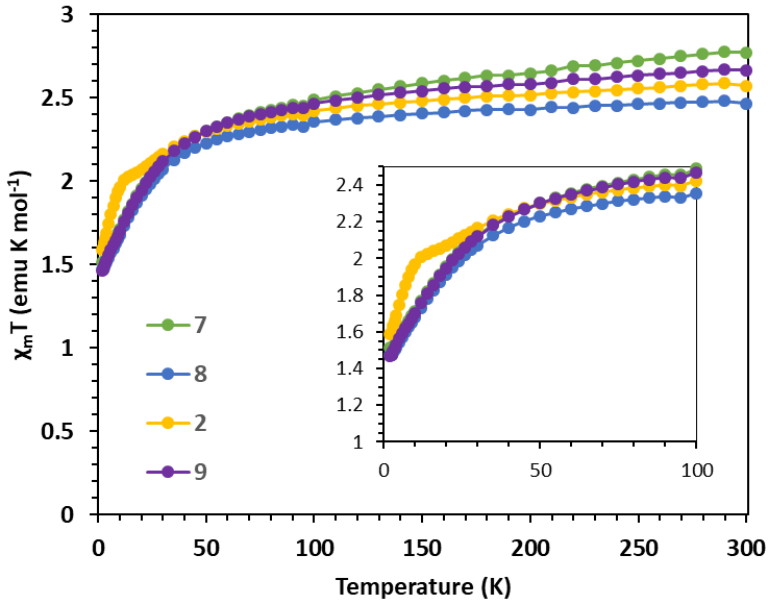

Figure II.40 $\chi_m T$ vs T data for compounds **2, 7-9**, as labelled, under a 1000 Oe DC field. Solid lines are guides for the eye.

The anisotropic nature of these complexes is also supported by the M versus H plots at 1.8 K that do not saturate even up to 7 T. The expected saturation point for each compound is 3 μ_B. Compound **2** reaches a maximum below 2.5 μ_B, Figure II.11, **7** reaches a maximum below 2.5 μ_B at 7 T, Figure II.41, **8** reaches a maximum below 2.5 μ_B, Figure II.42, and compound **9** also reaches a maximum below 2.5 μ_B, Figure II.43. In all cases, the lack of saturation and values well below those expected are indicative of significant anisotropy in all four systems.

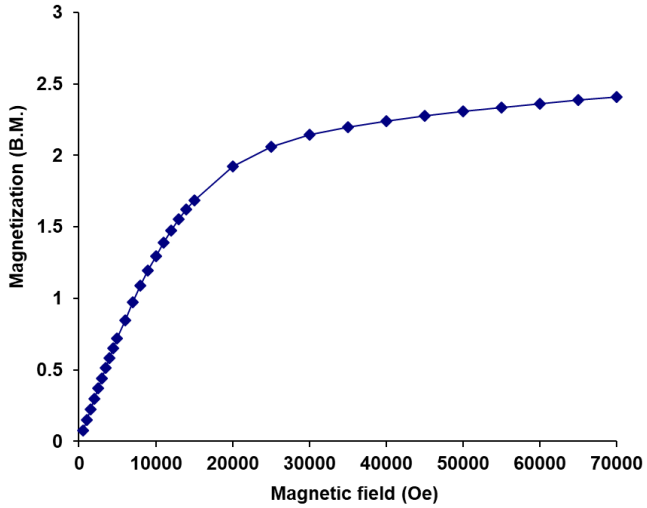

Figure II.41 Magnetization vs field for compound **7**. Solid line is a guide for the eye.

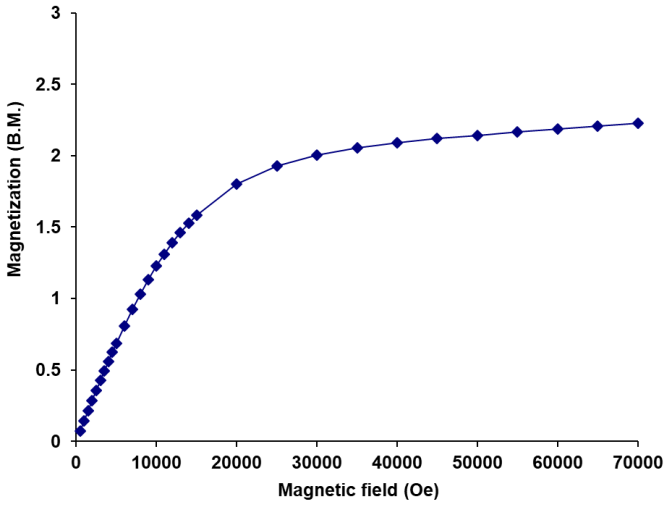

Figure II.42 Magnetization vs field for compound **8**. Solid line is a guide for the eye.

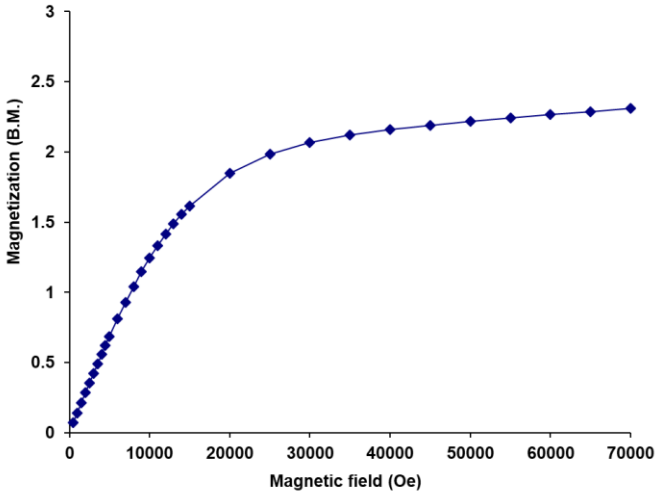

Figure II.43 Magnetization vs field for compound **9**. Solid line is a guide for the eye.

Reduced magnetization data were measured for **1**-**6** between 1.8 and 4 K and fit with the PHI program.[81] The reduced magnetization data for **7** lack superposition of the isofield lines, as is the case with anisotropic contributions. The data were fit with g, D, and E values equal to 2.24, 33 cm^{-1}, and 0.2 cm^{-1}, respectively, Figure II.44. The reduced magnetization data for **8** also exhibit a lack of superposition in the isofield lines. The data were fit with g, D, and E values equal to 2.40, 24 cm^{-1}, and 0.001 cm^{-1}, respectively, Figure II.45. In a similar manner, compound **9** does not show superposition in the isofield lines. The data were fit with g, D, and E values equal to 2.40, 24 cm^{-1}, and 0.001 cm^{-1}, respectively, Figure II.46.

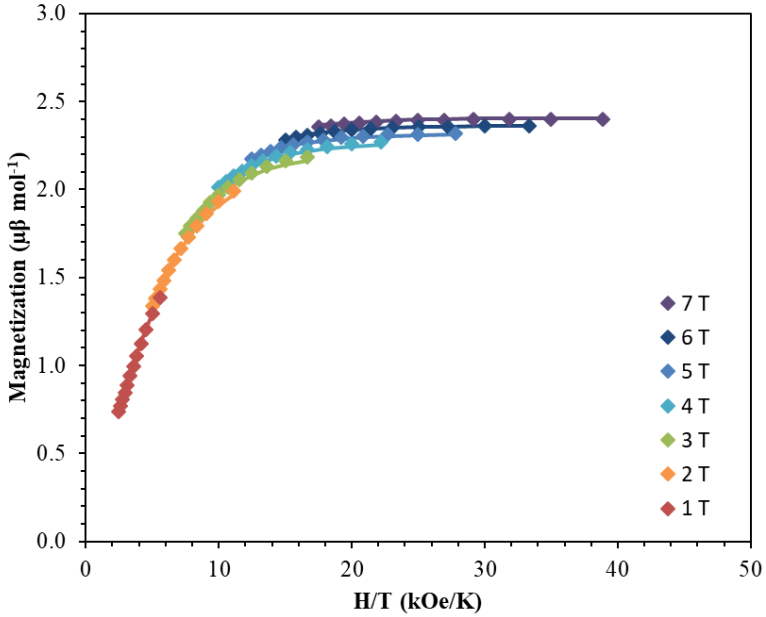

Figure II.44 Reduced magnetization for **7**. Solid lines are fits to the experimental data using the PHI program.

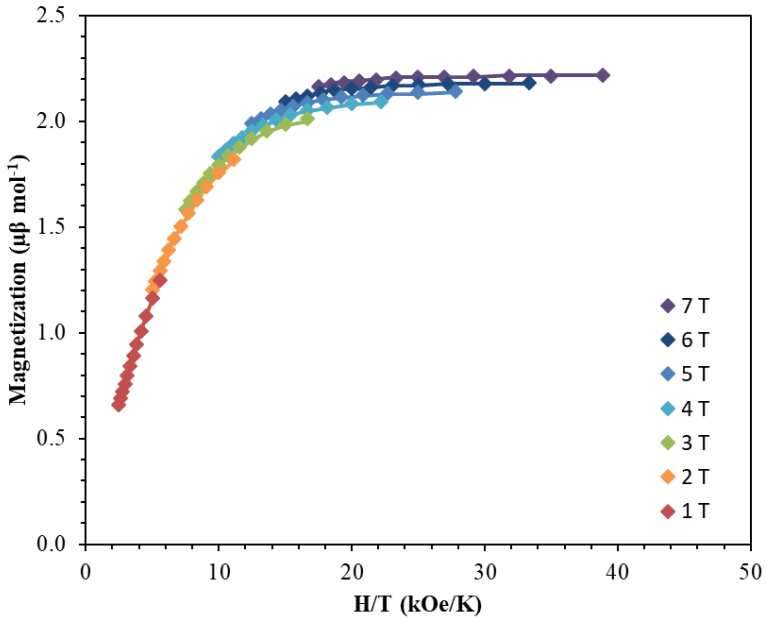

Figure II.45 Reduced magnetization for **8**. Solid lines are fits to the experimental data using the PHI program.

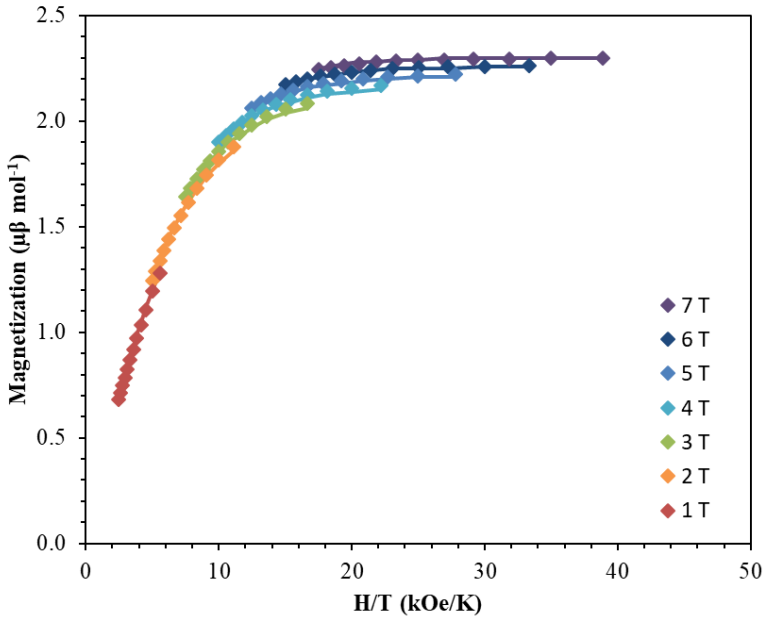

Figure II.46 Reduced magnetization for **9**. Solid lines are fits to the experimental data using the PHI program.

A summary of the g, D, and E values for compounds **2** and **7**-**9** can be found in Table II-11. These results are in good agreement with the predictions in the paper of Ruiz *et al.*[40]. Each complex exhibits a large, positive D value as expected. Complexes **2** and **8** were fit to very similar D values, and **7** has a slightly lower D value. Complex **9** displays the lowest D value in the series. These results indicate a rough correlation between decreasing electron donating abilities and decreasing D values.

Table II-11 Comparison of g, D (cm^{-1}), and E (cm^{-1}) values for compounds **2** and **7**-**9**.

		2	**7**	**8**	**9**
PHI	g	2.40	2.40	2.26	2.29
	D	24	21	24	20
	|E|	0.001	0.08	0.07	0.04

II.5.3 AC Magnetic Studies

Dynamic AC measurements under varying fields were performed on complexes **7-9**. No signal was observed for any of the complexes without an applied DC field. As a result, AC measurements under applied DC fields from 400-2000 Oe were measured, and all three were found to exhibit slow magnetic relaxation. The field used for further studies was chosen as the one with the most obvious maximum in χ" signals at the lowest frequencies.

Compound **7** exhibits the lowest frequency maximum around 70 Hz, **8** displays a frequency maximum at ~650 Hz, and compound **9** displays a frequency maximum at ~860 Hz. Fittings of the Cole-Cole plots for **7-9** were performed to extract U_{eff}, τ, and α parameters based on a modified Debye Function. The linear portion of the resulting Arrhenius plot was fit to extract the barrier (U_{eff}) for each complex.

Complex **7** was measured under an applied DC field of 1200 Oe. A maximum in χ" was observed up to 4.6 K, along with the corresponding decrease in χ'. The low temperature regime is dominated by frequency independent quantum tunneling up to approximately 3.4 K, after which temperature the thermal regime becomes more prevalent. The χ' and χ" plots can be found in Figure II.47.

a)

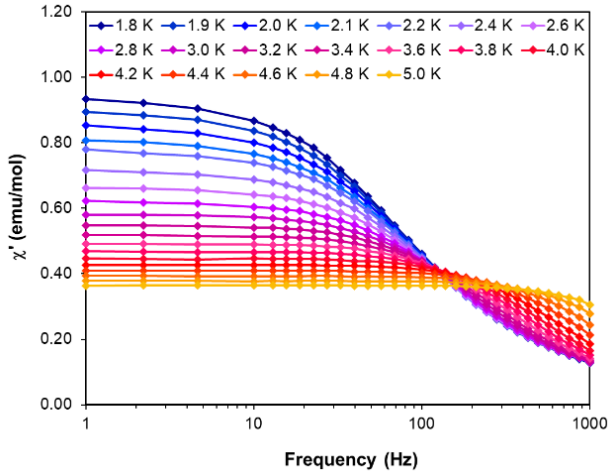

b)

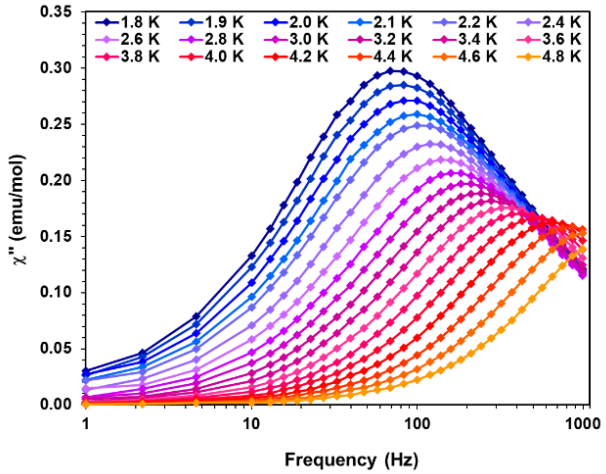

Figure II.47 a) In phase susceptibility (χ') vs Frequency and b) out of phase susceptibility (χ") for **7**. Solid lines are guides for the eye.

The in-phase and out-of-phase susceptibility plots were subsequently converted into Cole-Cole plots and fit using CC-fit,[83] which led to a maximum α value of 0.25, indicating a moderately wide range of relaxations times. A linear fit of the temperatures between 4.0 K and 4.8 K in the Arrhenius plot, Figure II.48, resulted in a barrier of U_{eff}/k_b = 25 K and $\tau_o = 5.5 \times 10^{-7}$ s.

a)

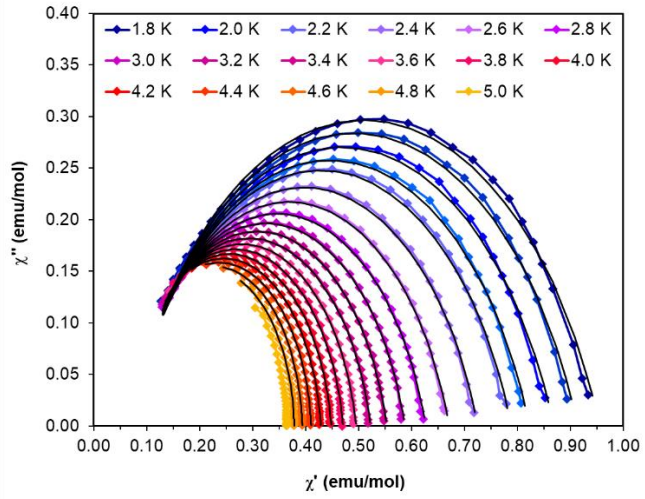

b)

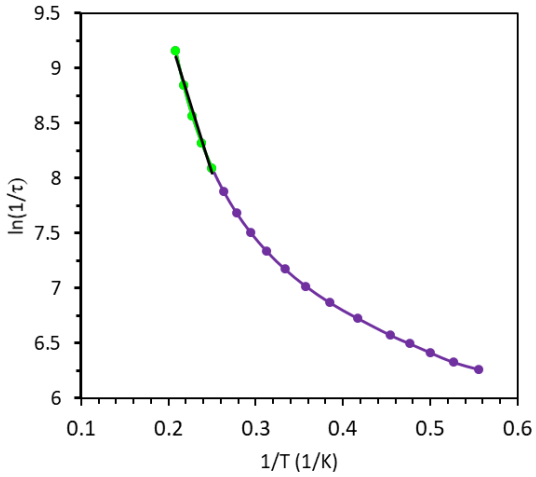

Figure II.48 a) cole-cole plot fit via CC-fit, black lines are fits to the data b) ln(1/τ) vs 1/T for **7**. Green data was fit with the black line shown.

Complex **8** was measured under an applied DC field of 800 Oe. A maximum in χ" was observed up to 2.2 K, along with the corresponding decrease in χ'. A clear maximum is only visible for a few temperatures, and data were collected up to 3.2 K. The χ' and χ" plots can be found in Figure II.49.

a)

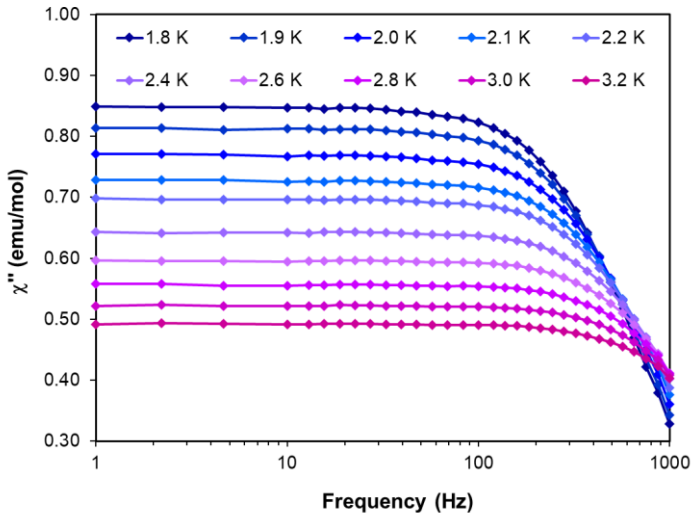

b)

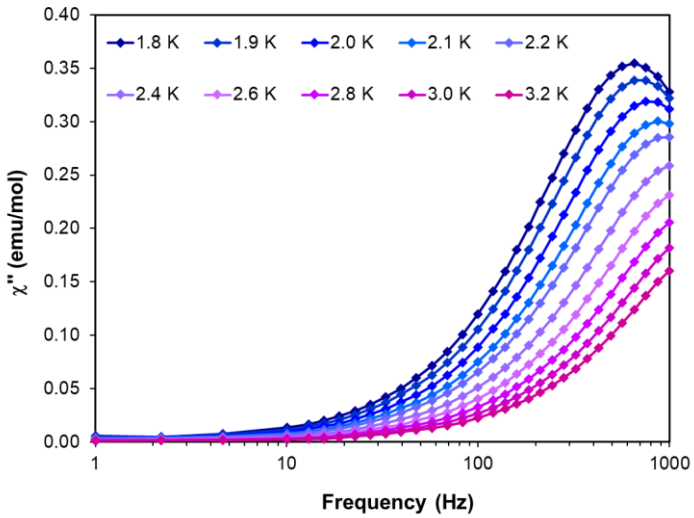

Figure II.49 a) In phase susceptibility (χ') vs Frequency and b) out of phase susceptibility (χ") for **8**. Solid lines are guides for the eye.

The Cole-Cole plot was fit using CC-fit[83] which led to a maximum α value of 0.04, indicating a narrow range of relaxations times. A linear fit of the temperatures between 1.8 K and 2.6 K in the Arrhenius plot, Figure II.50, resulted in a barrier of U_{eff}/k_b = 4.4 K and $\tau_o = 2.25 \times 10^{-5}$ s.

a)

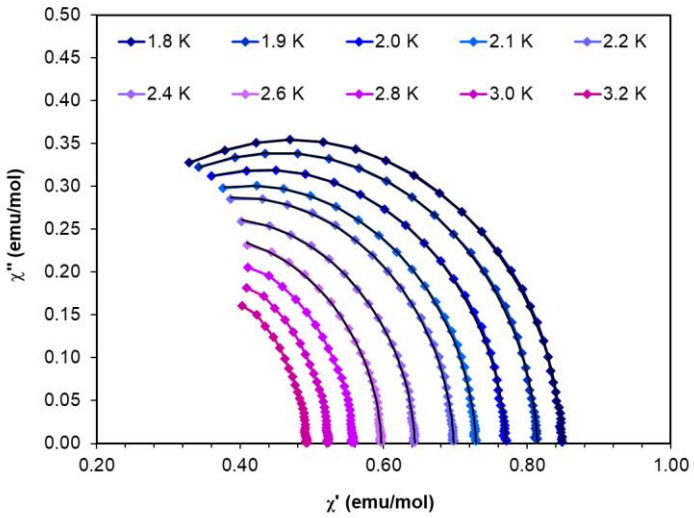

b)

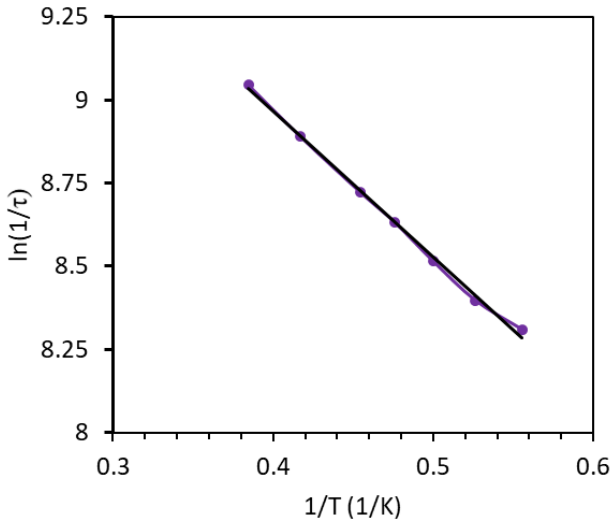

Figure II.50 a) Cole-Cole plot fit via CC-fit, black lines are fits to the data b) ln(1/τ) vs 1/T for **8**. Black line is a linear fit to the data.

Complex **9** was measured under an applied DC field of 1200 Oe. A maximum in χ" was observed up to 1.9 K, along with the corresponding decrease in χ', Figure II.51.

a)

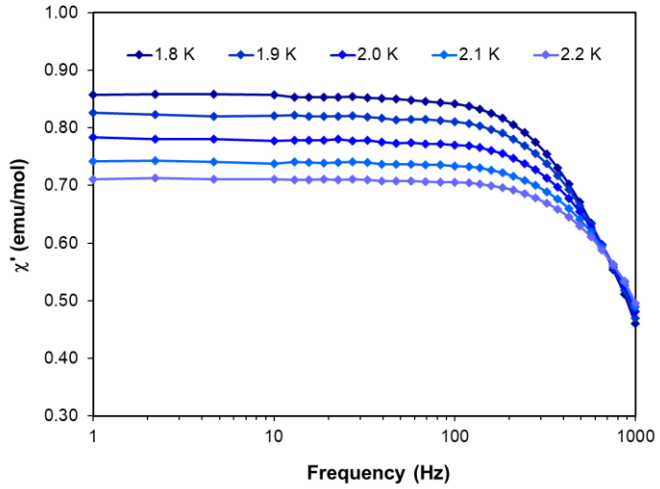

b)

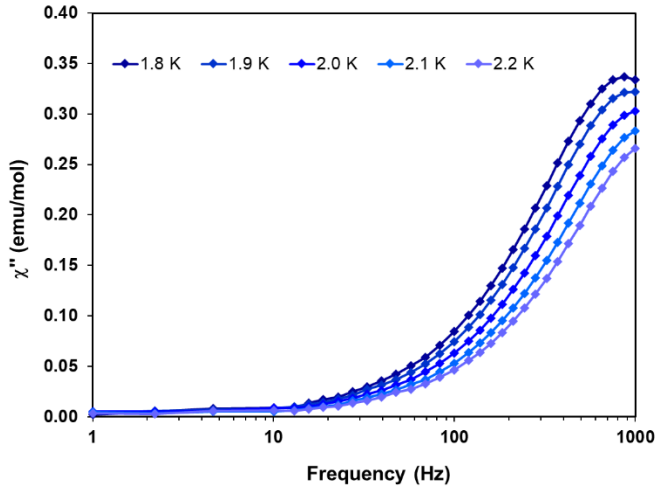

Figure II.51 a) In phase susceptibility (χ') vs Frequency and b) out of phase susceptibility (χ") for **9**. Solid lines are guides for the eye.

The Cole-Cole plot was fit using CC-fit[83] which led to a maximum α value of 0.04, indicating a narrow range of relaxations times. A linear fit of the temperatures between 1.8 K and 2.6 K in the Arrhenius plot, Figure II.52, resulted in a barrier of U_{eff}/k_b = 4.2 K and $\tau_o = 1.67 \times 10^{-5}$ s.

a)

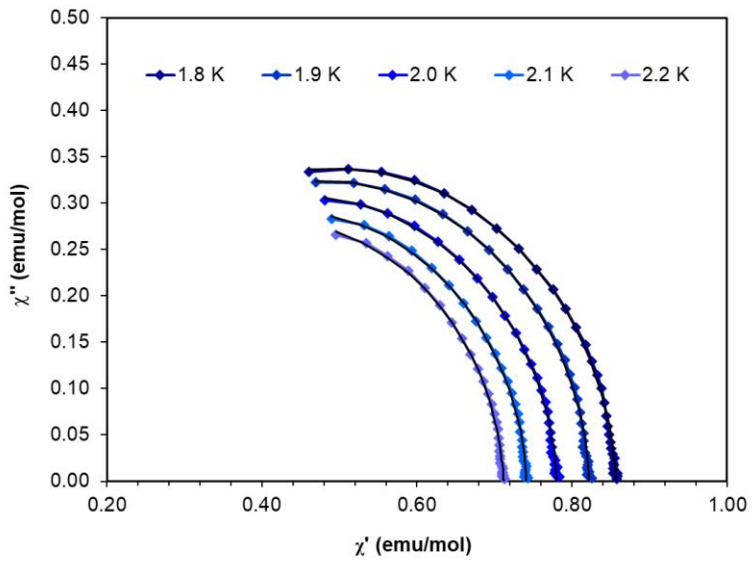

b)

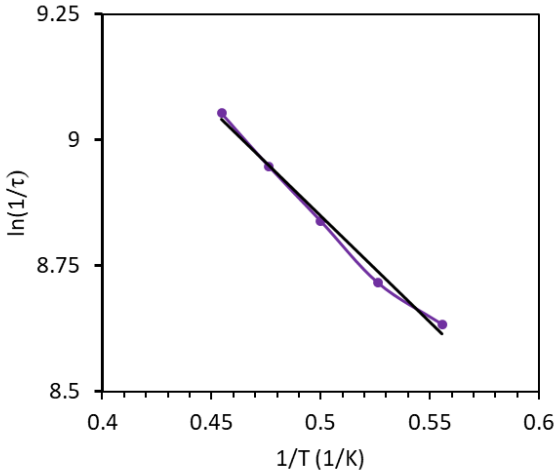

Figure II.52 a) Cole-Cole plot fit via CC-fit, black lines are fits to the data b) ln(1/τ) vs 1/T fpr **9**. Black line is a linear fit to the data.

The barriers for all 3 compounds are lower than expected given the 2|D| energy gaps between the $m_S = 1/2$ and $m_S = 3/2$ microstates, which are 42, 48, and 40 cm^{-1}, for complexes **7**, **8**, and **9**, respectively. These results are attributed to the presence of alternative relaxations such as Raman and quantum tunneling. There is

not sufficient data for compounds **8** and **9** to adequately fit these alternative relaxations.

II.5.4 Magneto-structural Correlations

Comparisons of crystal structures for compounds **7-9** and **2** revealed a general trend that the best performing magnets exhibit the most ideal geometries. These results lend credence to the requirement of strict geometric control for superior magnetic behavior. There does not appear to be a correlating trend between M···M separation and magnetic behavior which is not surprising because all compounds have distances greater than 8 Å, at which dipolar relaxations are expected to be suppressed.[65]

A comparison of the D values and U_{eff} barriers for compounds **7-9** and **2**, Table II-12, reveals that the D values for the complexes appear to generally correlate with electron donating abilities of the substituents, but the barrier height appears to be more dependent upon geometric distortion. A more direct comparison between the two best performing magnets, compounds **2** and **7**, would require computational analysis. $[Co(TPMA)(CH_3CN)](BF_4)_2$ (TPMA = tris(2-pyridylmethyl)amine) is the only other trigonal bipyramidal compound reported to have a positive *D* value, which is equal to 9.9 cm^{-1}.[65] The reported barrier height (U_{eff}) is 22 K. This report is quite similar to the results that were found for these four complexes in terms of the barrier height.

Table II-12 Comparison of D and U_{eff} values for complexes **2** and **7-9**.

	2	**7**	**8**	**9**
D (cm^{-1})	24	21	24	20
U_{eff} (K)	10	25	4.4	4.2

Another series that probed the effect of electron donating and withdrawing substituents on magnetic behavior is the trigonal monopyramidal $[Fe(tpa^{R})]^{-}$ series by Long, *et al*.[25] Theoretical studies on the series found a direct correlation between electron donating ability and the D value, similar to what was observed in this chapter.[26] A similar computational study of these complexes would certainly yield interesting insights into the origin of the magnetic behavior of these complexes.

II.6 Conclusions

In the first half of this chapter, results of the syntheses and characterization of three pairs of complexes in this work underscored the importance of ideal geometries. A general trend of trigonal monopyramidal geometries exhibiting superior SMM behavior as compared to the trigonal bipyramidal geometries was described. The trigonal monopyramidal cobalt and iron complexes exhibit slow magnetic relaxation under applied fields, resulting in barriers of 44 K and 40 K respectively. Coordination of a single water molecule in the open axial site of the trigonal monopyramidal complexes exerts a drastic dampening effects on the D value as well as slow relaxation. Computations reveal that coordination of water rotates the D_{zz} axis away from the C_3 axis of symmetry resulting in a smaller D value. The aquo species $(Me_4N)[Co(MST)(OH_2)]$ still shows slow magnetic relaxation under an applied field, but the barrier is reduced to 9.9 K. Water coordination totally quenches the magnetic behavior in the iron complex, and reduces the D value for nickel to -185 cm^{-1}. The drastic effect of a single coordinated water molecule emphasizes the subtle nature of SMM behavior in mononuclear complexes.

In the second half of this chapter, results of the syntheses and characterization of three trigonal bipyramidal complexes based on the MST ligand with varying electron donating and withdrawing substituents was investigated. This study stresses the importance, not only of strict geometric control, but also fine tuning of ligands via electron donating substituents. The D values of the complexes were found to roughly correlate with the electron donating ability of the phenyl substituents.

The new data reported in this chapter add valuable information to the growing knowledge base of mononuclear transition metal SMMs. In the future, the knowledge gleaned from these two projects can be used to synthesize new SMMs that exhibit magnetic behavior at even higher temperatures. The fundamental principles can be used to build molecules purposely designed to have highly improved magnetic properties.

CHAPTER III

MAGNETIC STUDIES OF PARTIALLY AND FULLY ENCAPSULATED DIVALENT COBALT IONS WITH TRIGONALLY SYMMETRIC LIGANDS

III.1 Introduction

Single molecule magnets were first recognized in 1993, and, since this time, the topic has grown into a major field of study. Gatteschi *et al*. discovered that $Mn_{12}O_{12}(O_2CCH_3)_{16}(H_2O)_4$ (referred to as Mn_{12}) demonstrates magnetic bi-stability similar to what is observed in bulk magnetism.[3, 5] These materials exhibit hysteresis which looks very similar to those of bulk magnets, but which is of a very different origin. The SMM hysteresis arises from a barrier (U) for spin reversal between the m_s microstates from the total spin S of the system. These microstates are non-degenerate due to a negative zero field splitting (ZFS) parameter $-D_z$, and the barrier created by the separation of microstates is equal to $S^2|D|$ and $(S^2-1/4)|D|$ for integer and non-integer spin states, respectively.[17] Over the past 20 years of SMM research, there has been a focus on increasing the spin reversal barrier (U) to higher temperatures for hysteresis to occur. Lately, the focus of the field has been towards increasing the axial zero field splitting parameter D_z rather than the spin value.[40]

Strict control over the geometry of these molecules, and their interactions with each other, are vital to improving the magnetic behavior. The controlled synthesis of mononuclear complexes can subsequently be used in the building block approach to build multinuclear complexes with controlled anisotropy and coupling. However, direct

comparison between a mononuclear and dinuclear complex is often difficult due to significant changes in coordination, geometry, and oxidation state. A symmetric ligand structure that could either coordinate with two metal centers or be forced to coordinate with one metal center would be ideal for such a study. Cryptand-like organic ligands are promising as both ends are identical to each other, and they exhibit high symmetry in the tethers connecting those ends. These types of molecules have been used for the coordination of cations,[91] anions,[92-93] and transition metal ions.[94-97]

In particular, the cryptand-like ligand 6,16,2,5-tribenzena(1,4)-1,4,8,11,14,18,23,27-octaazabicyclo[9.9.9]nonacosaphane (L^1), Figure III.1, was chosen. When considering what would be a good mimic of one-half of this cryptand, the ligand tris(2-(benzylidene)amino)ethyl)amine ($tren^{bn}$), Figure III.1, is a close relation. These ligands are ideal for a comparison between partially and fully encapsulated transition metal centers. Divalent cobalt was chosen as the transition metal to pursue because it has strong anisotropy and compounds exhibiting interesting magnetic behavior have been observed,[18, 43, 63, 65, 98] particularly in trigonal symmetries.[65, 86-87] A direct comparison of these complexes should yield fascinating magnetic results and insights.

For this chapter, the syntheses, structures, and magnetic properties of two mononuclear cobalt complexes, $[Co(tren^{bn})Cl](BPh_4)$ (**1**) and $[Co(tren^{bn})Br](BPh_4)$ (**2**), and two dinuclear cobalt complexes, $[Co_2(L^1)(Cl)](ClO_4)_3$ (**3**) and $[Co_2(L^1)(Br)](ClO_4)_3$ (**4**), were studied and their properties compared.

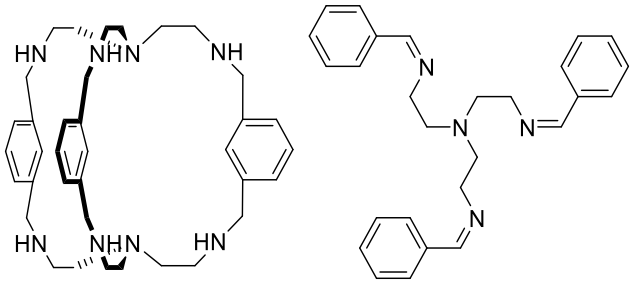

Figure III.1 Schematic drawing of the ligand structures for L^1 (left) and $tren^{bn}$ (right).

III.2 Experimental Methods

III.2.1 Complex Synthesis

The synthesis of **1** and **2** took place in an MBRAUN glovebox under a nitrogen atmosphere. Acetonitrile was degassed, refluxed over molecular sieves, and stored in the drybox over molecular sieves. Diethyl ether was purified using an MBRAUN purification system and stored over 3Å molecular sieves. Dichloromethane (DCM) was dried over P_2O_5 and stored over 3Å molecular sieves. Sodium tetraphenylborate was dried under vacuum at 100°C overnight and stored in the glovebox. Anhydrous $CoCl_2$ and $CoBr_2$ were purchased from Fisher Scientific, and used as received. For **3** and **4**, $Co(ClO_4)_2$, NH_4Cl, and $(n\text{-}Bu)_4NBr$ were purchased commercially, stored in a desiccator, and used as received. Acetonitrile and methanol were purchased from Fisher Scientific, stored under ambient conditions, and used as received. Caution, perchlorate salts are potentially explosive and must be handled with care and in small quantities. $Tren^{bn}$, L^1, **3**, and **4** were synthesized by following literature procedures.[99-100]

[Co(tren^{bn})Cl](BPh$_4$) (1). Tren^{bn} (100 mg, 0.24 mmol) was dissolved in 10 mL of acetonitrile. $CoCl_2$ (58 mg, 0.24 mmol) was added resulting in a dark blue solution. The reagent $NaBPh_4$ was then added and the solution turned bright purple and cloudy. After stirring overnight, the acetonitrile was removed and the residue was dissolved in DCM. After stirring overnight, the resulting cloudy, purple solution was filtered through a fine frit to give a clear, purple solution. Slow diffusion of Et_2O into the filtrate resulted in purple crystals suitable for single crystal X-ray diffraction (148 mg, 74.7% yield).

[Co(tren^{bn})Br](BPh$_4$) (2). Tren^{bn} (100 mg, 0.24 mmol) was dissolved in 10 mL of acetonitrile. $CoBr_2$ (53 mg, 0.24 mmol) was added resulting in a purple solution, followed by $NaBPh_4$ resulting in a dark purple, cloudy solution. After stirring overnight, the acetonitrile was removed and the residue was dissolved in DCM. After stirring overnight, the resulting cloudy, purple solution was filtered through a fine frit resulting in a clear, purple solution. Slow diffusion of Et_2O into the filtrate resulted in purple crystals suitable for single crystal X-ray diffraction (153 mg, 73.6% yield).

[Co$_2$(L^1)(Cl)](ClO$_4$)$_3$ (3). $Co(ClO_4)_2 \cdot 6H_2O$ (122 mg, 0.33 mmol) was dissolved in 5 mL of methanol and 5 mL of acetonitrile. NH_4Cl (8.9 mg, 0.167 mmol) was subsequently added to the solution, followed by L^1 (100 mg, 0.167 mmol) which was added dropwise as a methanolic solution (5 mL). After 4 hours, the resulting purple solid was isolated via filtration and dissolved in CH_3CN. Slow evaporation resulted in purple, x-ray quality single crystals (32 mg, 16% yield).

[Co$_2$(L^1)(Br)](ClO$_4$)$_3$ (3). $Co(ClO_4)_2 \cdot 6H_2O$ (122 mg, 0.33 mmol) was dissolved in 5 mL of methanol and 5 mL of acetonitrile. (*n*-Bu)$_4$NCl (54 mg, 0.167 mmol) was subsequently

added to the solution, followed by dropwise addition of L^1 (100 mg, 0.167 mmol) in methanol (5 mL). After 4 hours, the resulting purple solid was isolated via filtration and dissolved in CH_3CN. Slow evaporation resulted in purple, X-ray quality single crystals (32 mg, 15% yield).

III.2.2 Crystallography

Structural characterization for **1** and **2** was performed using the synchrotron at Argonne National Laboratory. Suitable crystals were mounted on glass fibers using Paratone oil and placed in a cold stream of N_2 for collection at 100 K. Crystals of **3** and **4** were collected on a Bruker QUEST instrument equipped with a Mo Kα source and CCD detector. Suitable crystals were mounted on MiTeGen microloops using Paratone oil and placed in a cold stream of N_2 for collection at 100 K. The collected data for **1**-**4** were integrated within the APEX 2 software suite, as well as SADABS for absorbance corrections.[70] The structures were solved and refined using SHELXT[71] and SHELXL[72], respectively, within the OLEX program.[73] Hydrogen atoms were added in calculated positions. In some cases, reorientations of hydrogen atoms were performed to match visible electron density as well as due to obvious hydrogen bonding interactions.

All non-hydrogen atoms were refined anisotropically. Both **1** and **2** exhibit positional disorder over one of the phenyl group arms in the main cationic molecule in ratios of 57:43 and 63:37, respectively. The use of SIMU and SADI restraints were necessary in order to achieve a reasonable model of the disorder. Additionally, **1** and **2** were run through the program SQUEEZE.[101] Diethyl ether co-crystallizes, disordered over multiple positions in each structure. Attempts to model the solvent molecule were

not successful. The electron counts of 40 and 41 for **1** and **2**, respectively, from the program are very close to the 42 electrons in one diethyl ether molecule. No disorder was visible in the structures for **3** and **4**. Further crystallographic details are listed in Table III-1.

Table III-1 Crystal data and structure refinement for complexes **1-4**.

Identification code	co_trenbn_cl	co_trenbn_br
Empirical formula	$C_{51}H_{50}BClCoN_4$	$C_{51}H_{50}BBrCoN_4$
Formula weight	824.14	868.60
Temperature/K	100	100
Crystal system	monoclinic	monoclinic
Space group	C2/c	C2/c
a/Å	34.5671(15)	34.7669(18)
b/Å	15.0100(7)	15.0215(8)
c/Å	20.2852(9)	20.2934(10)
α/°	90	90
β/°	120.5490(10)	120.6030(10)
γ/°	90	90
Volume/$Å^3$	9064.1(7)	9122.1(8)
Z	8	8
ρcalcg/cm^3	1.208	1.265
μ/mm^{-1}	0.476	0.691
F(000)	3464.0	3608.0
Crystal size/mm^3	0.97 × 0.16 × 0.15	0.56 × 0.098 × 0.065
Radiation	Synchrotron (λ = 0.41328)	Synchrotron(λ = 0.41328)
2Θ range for data collection/°	4.664 to 53.112	2.712 to 26.712
Index ranges	$-43 \le h \le 43$, $-18 \le k \le 18$, $-24 \le l \le 24$	$-38 \le h \le 38$, $-16 \le k \le 16$, $-21 \le l \le 22$
Reflections collected	100023	72745
Independent reflections	9205 [R_{int} = 0.0585, R_{sigma} = 0.0259]	6480 [R_{int} = 0.0636, R_{sigma} = 0.0284]
Data/restraints/parameters	9205/177/578	6480/177/578
Goodness-of-fit on F^2	1.056	1.062
Final R indexes [I>=2σ (I)]	R_1 = 0.0520, wR_2 = 0.1548	R_1 = 0.0426, wR_2 = 0.1196
Final R indexes [all data]	R_1 = 0.0581, wR_2 = 0.1595	R_1 = 0.0483, wR_2 = 0.1231
Largest diff. peak/hole / e $Å^{-3}$	1.45/-0.64	1.00/-0.56

Table III-1 Continued.

Identification code	CoLCl	CoLBr
Empirical formula	$C_{42}H_{67}Cl_4Co_2N_{11}O_{14}$	$C_{42}H_{67}BrCl_3Co_2N_{11}O_{14}$
Formula weight	1209.72	1254.18
Temperature/K	100	120
Crystal system	triclinic	triclinic
Space group	P-1	P-1
a/Å	12.9884(11)	13.0947(3)
b/Å	13.9606(12)	13.9256(3)
c/Å	15.4677(14)	15.5508(3)
α/°	87.470(2)	87.4040(10)
β/°	66.461(2)	65.9870(10)
γ/°	81.663(2)	81.6510(10)
Volume/Å^3	2543.8(4)	2562.54(10)
Z	2	2
ρcalcg/cm^3	1.579	1.625
μ/mm^{-1}	0.938	1.658
F(000)	1260.0	1296.0
Crystal size/mm^3	0.78 × 0.056 × 0.042	0.085 × 0.053 × 0.046
Radiation	MoKα (λ = 0.71073)	MoKα (λ = 0.71073)
2Θ range for data collection/°	4.148 to 55.754	4.212 to 56.612
Index ranges	$-17 \le h \le 17$, $-18 \le k \le 18$, $-20 \le l \le 20$	$-17 \le h \le 17$, $-18 \le k \le 18$, $-20 \le l \le 20$
Reflections collected	118176	130830
Independent reflections	11856 [R_{int} = 0.0510, R_{sigma} = 0.0273]	12713 [R_{int} = 0.0756, R_{sigma} = 0.0327]
Data/restraints/parameters	11856/0/667	12713/0/667
Goodness-of-fit on F$^{2\,c}$	1.041	1.077
Final R indexes [I>=2σ (I)]^{a,b}	R_1 = 0.0385, wR_2 = 0.0819	R_1 = 0.0518, wR_2 = 0.1333
Final R indexes [all data]^{a,b}	R_1 = 0.0522, wR_2 = 0.0875	R_1 = 0.0804, wR_2 = 0.1658
Largest diff. peak/hole / e Å^{-3}	0.90/-0.67	3.12/-1.53

$^a R_1 = \Sigma(||F_o| - |F_c||)/\Sigma|F_o|$. $^b wR_2 = [\Sigma[w(F_o^2 - F_c^2)^2]/\Sigma[w(F_o^2)^2]]^{1/2}$ ^{c}Goodness-of-fit = $[\Sigma[w(F_o^2 - F_c^2)^2]/(n - p)]^{1/2}$, where *n* is the number of reflections and p is the total number of parameters refined.

[Co(tren^{bn})Cl](BPh$_4$) and [Co(tren^{bn})Br](BPh$_4$). The crystal structures for **1** and **2** are very similar, and will be discussed together. Coordination for both complexes involves four nitrogen atoms from the tren^{bn} ligand in the equatorial positions, as well as one axial position. The remaining axial position is filled by chloride or bromide anions for **1** and **2**, respectively, resulting in trigonal bipyramidal geometry for both compounds. The anion tetraphenylborate is present for charge balance. These findings confirm the divalent oxidation state of the cobalt centers. Both complexes crystallize in the monoclinic space group C2/c. The crystal structures for **1** and **2** can be found in Figure III.2 and Figure III.3, respectively.

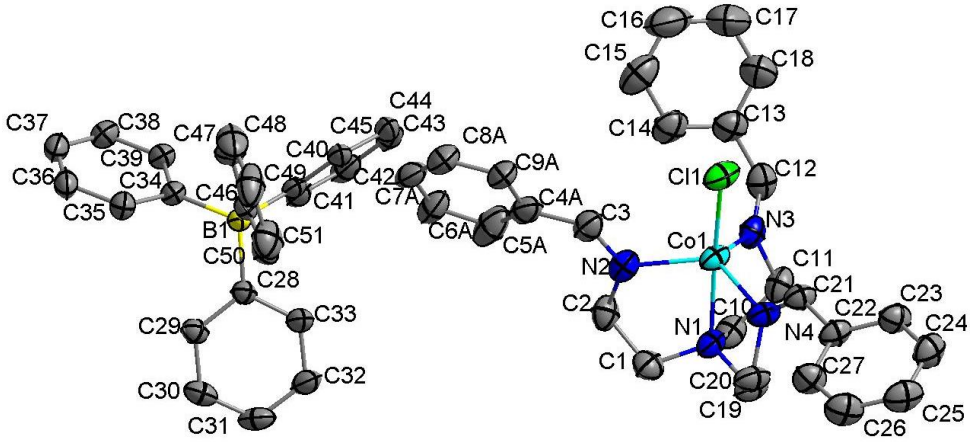

Figure III.2 Crystal structure and atom numbering scheme of [Co(tren^{bn})Cl](BPh$_4$). Hydrogen atoms and half of the disorder were omitted for clarity. Thermal ellipsoids were drawn at the 50% probability level. Colors are as follows: turquoise, Co; blue, N; yellow, B; green, Cl; grey, C.

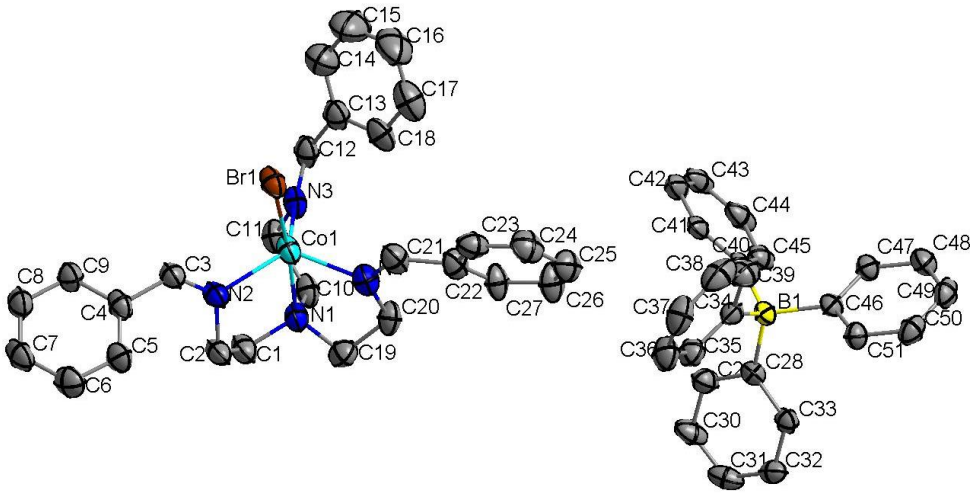

Figure III.3 Crystal structure and atom numbering scheme of [Co(tren^{bn})Br](BPh$_4$). Hydrogen atoms and half of the disorder were omitted for clarity. Thermal ellipsoids were drawn at the 50% probability level. Colors are as follows: turquoise, Co; blue, N; yellow, B; brown, Br; grey, C.

For **1**, the three arms of the ligand coordinate about the cobalt cation with bond angles that vary between 107.80(8)° and 123.01(9)°. In **2**, these angles vary between 108.12(11)° and 123.05(12)°. These distortions from 120° are indicative of a deviation from ideal trigonal geometry. The bond lengths in **1** vary between 2.055(2) Å and 2.114(2) Å. For **2**, the bond lengths varied between 2.046(3) Å and 2.111(3) Å. These variations in length further emphasize the distortion from ideal geometry. The bond angles between the axial nitrogen atom, cobalt ion, and axial halide are 174.65(6)° and 174.06(8)°, for **1** and **2**, respectively. The metal center is out of the plane generated by these three equatorial nitrogen atoms by 0.400 Å and 0.396 Å for **1** and **2**, respectively. The closest intermolecular distance between two of the cobalt centers is 8.608 Å and 8.708 Å for **1** and **2**, respectively.

$[Co_2(L^1)(Cl)](ClO_4)_3$ and $[Co_2(L^1)(Br)](ClO_4)_3$. The crystal structures for **3** and **4** are very similar, and will be discussed together. The complexes are coordinated to four nitrogen atoms from the L^1 ligand in the equatorial positions, as well as one axial position, on both ends of the cage-like structure. The remaining axial position is filled by a bridging chloride or a bridging bromide anion for **3** and **4**, respectively, resulting in trigonal bipyramidal geometry for the cobalt centers. Three perchlorate anions, as well as three acetonitrile and two water molecules, are also present in the crystals. Both complexes crystallize in the triclinic space group $P\bar{1}$. The crystal structures for **3** and **4** can be found in Figure III.4 and Figure III.5, respectively.

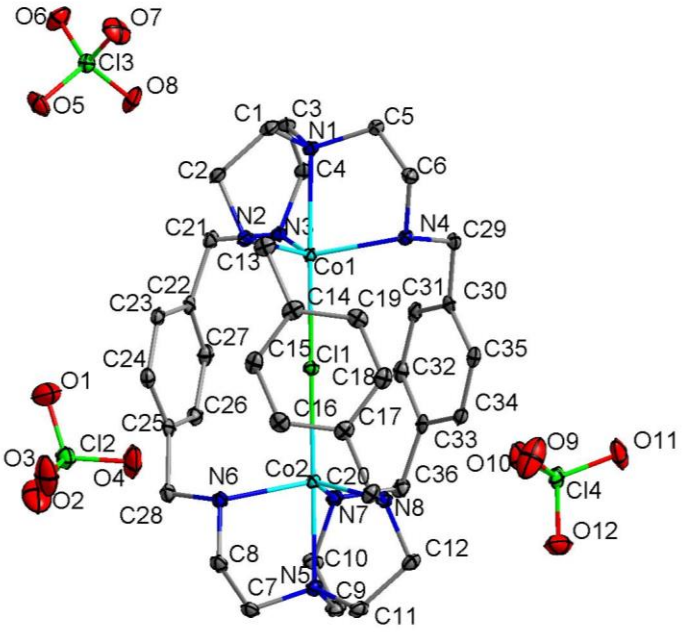

Figure III.4 Crystal structure and atom numbering scheme of $[Co_2(L^1)(Cl)](ClO_4)_3$. Hydrogen atoms and solvent molecules were omitted for clarity. Thermal ellipsoids were drawn at the 50% probability level. Colors are as follows: turquoise, Co; blue, N; green, Cl; red, O; grey, C.

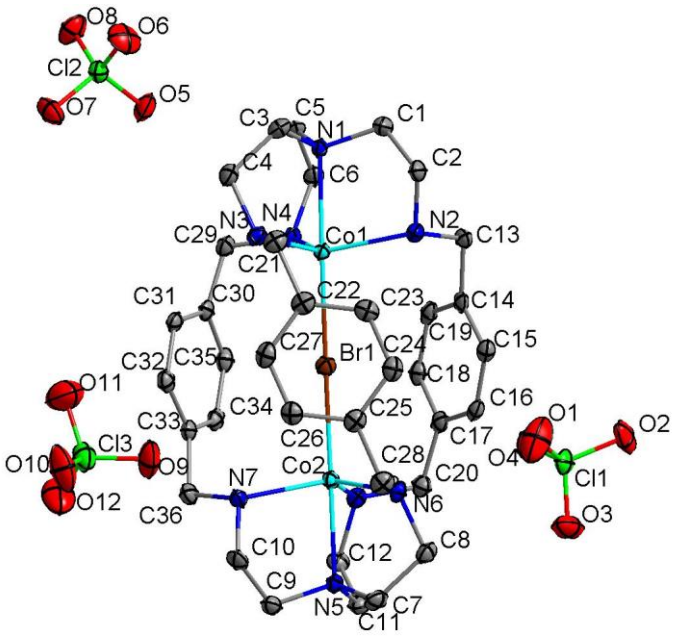

Figure III.5 Crystal structure and atom numbering scheme of $[Co_2(L^1)(Br)](ClO_4)_3$. Hydrogen atoms and solvent molecules were omitted for clarity. Thermal ellipsoids were drawn at the 50% probability level. Colors are as follows: turquoise, Co; blue, N; green, Cl; brown, Br; red, O; grey, C.

For compound **3**, the three arms of the ligand coordinate to the cobalt cations with bond angles that vary between 116.24(7)° and 117.05(7)° on one end and 116.09(7)° and 117.80(7)° on the other end. In **2**, these angles vary between 116.74(13)° and 117.83(13)° on one end and 116.75(13)° and 118.15(12)° on the opposite end. These deviations from 120° indicate a distorted trigonal geometry for each metal center. The bond distances in **1** vary between 2.1175(18) Å and 2.1284(17) Å on one end, and 2.1160(18) Å and 2.1295(18) Å on the opposite end. For **2**, the bond lengths varied between 2.114(3) Å and 2.124(3) Å on one end, and 2.115(3) Å and 2.133(3) Å on the other. These variations further emphasize the distortion from ideal geometry. The bond angles between the axial nitrogen atom, cobalt ion, and axial halide in **3** are 178.86(5)° and 178.18(5)° on each end.

The angle between the two cobalt cations and the bridging halide is 178.83(3)°. The bond angles between the axial nitrogen atom, cobalt ion, and axial halide in **4** are 179.26(8)° and 178.24(8)° on each end. The angle between the two cobalt cations and the bridging halide is 178.43(2)°. The metal center is above the plane generated by these three equatorial nitrogen atoms by 0.382 Å and 0.389 Å on each end of **3**. In **4**, these distances are 0.354 Å and 0.350 Å.

III.2.3 Magnetic Measurements

Magnetic data were collected on a Quantum Design MPMS-3 SQUID from 1.8-300 K with DC fields from 0-7 T. Compounds **1-4** were collected in plastic bags. Diamagnetic corrections were applied for the bags using pre-calibration, and diamagnetic contribution from the compounds were calculated based on Pascal's constants.[74]

III.3 Results and Discussion

III.3.1 Crystallographic Details

Reported herein are the four compounds: $[Co(tren^{bn})Cl](BPh_4)$ (**1**), $[Co(tren^{bn})Br](BPh_4)$ (**2**), $[Co_2(L^1)(Cl)](ClO_4)_3$ (**3**), and $[Co_2(L^1)(Br)](ClO_4)_3$ (**4**). Compounds **1** and **2** were synthesized with CoX_2 (X=Cl,Br), the ligand $tren^{bn}$, and $NaBPh_4$ in acetonitrile. Crystals were obtained by slow diffusion of diethyl ether into dichloromethane (DCM) solutions. Compounds **3** and **4** were synthesized from $Co(ClO_4)_2$, L^1, and NH_4Cl (for **3**) or $N(n\text{-bu})_4Br$ (for **4**) in a 50:50 mixture of methanol and acetonitrile. Crystals were obtained by slow evaporation. Complexes **1** and **2** crystallize in the monoclinic space group C2/c, and complexes **3** and **4** crystallize in triclinic $P\bar{1}$. The structures of **3** and **4** were previously reported using

slow diffusion of diethyl ether as the crystallization method rather than slow evaporation.[102] The structures of **1** and **3** are shown in Figure III.6. The blue polyhedra emphasize the trigonal bipyramidal geometries in each complex.

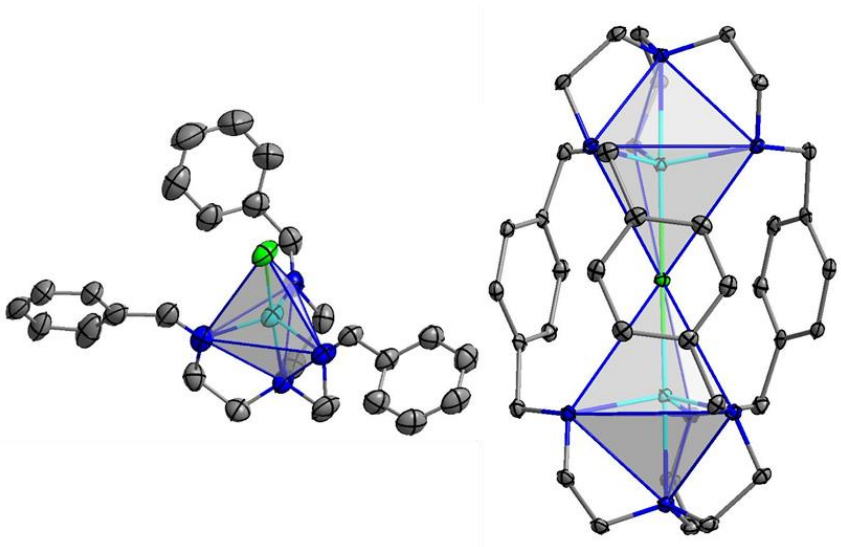

Figure III.6 Crystal structure for **1** and **3** as representative examples. All hydrogen atoms and co-crystallizing anions and solvent have been omitted for clarity. Colors are as follows: turquoise, Co; blue, N; green, Cl; grey, C. Blue polyhedra were generated around the cobalt ions.

The geometries of the complexes were confirmed using the SHAPE program[79-80] which compares the experimental metrical parameters to the perfect geometry, with 0 indicating a perfect match to that geometry. In all cases, trigonal bipyramidal is the best geometry to describe the coordination of **1-4,** Table III-2. Complex **1** is closer to an ideal trigonal bipyramidal geometry than complex **2**. For **3** and **4**, **3** is slightly closer to an ideal geometry, but they are quite similar to each other.

Additionally, while there is some variation, both cobalt ions in each cage exhibit similar values, indicating similar amounts of distortion on each side of the cage.

Table III-2 Shape measurements for compounds **1**-**4**. For **3** and **4**, t and b represent the top and bottom of each cage-like structure. Abbreviations are as follows: PP, pentagon; vOC, vacant octahedron; TBPY, trigonal bipyramid; SPY, square pyramid; JTBPY, Johnson trigonal bipyramid.

	PP	**vOC**	**TBPY**	**SPY**	**JTBPY**
1	33.275	6.555	1.732	5.214	2.929
2	33.431	6.791	2.203	5.546	2.825
3_t	37.147	8.050	1.541	6.660	2.452
3_b	36.567	8.017	1.499	6.539	2.445
4_t	37.152	8.041	1.588	6.730	2.335
4_b	36.573	8.049	1.549	6.589	2.329

In each structure, the metal center is above the equatorial plane generated by the three coordinating nitrogen atoms, with **4** exhibiting the least distortion with a Co-N_{plane} distance of 0.350 Å. A comparison of the mononuclear complexes to the dinuclear compounds reveals that the cobalt ions in the latter complexes are closer to in plane than those in the mononuclear complexes. The intermolecular distances in the mononuclear complexes are ~0.6 Å closer than those in the dinuclear complexes. See Table III-3 for a summary of these measurements for all compounds.

Table III-3 Selected intermolecular and intramolecular distances (Å) of **1**-**4**.

	1	**2**	**3_t**	**3_b**	**4_t**	**4-b**
$N_3…M^a$	0.400	0.396	0.382	0.389	0.354	0.350
$M…M^b$	8.608	8.708	9.270	9.270	9.272	9.272

[a] distance between the metal center and the plane generated by the three equatorially coordinated nitrogen atoms (N2-N4)

[b] closest intermolecular distance between cobalt ions in two different molecules

The bond lengths are longer upon comparison of **1** vs **3** and **2** vs **4**, with **3** and **4** being longer in each case. In each case, there is deviation from the ideal trigonal angle of 120° in the equatorial plane, and the angles between the axial nitrogen and halide atoms are <180°. In **3** and **4**, the angle between the two cobalt centers and the halide atom is slightly less than 180°. See Table III-4 for a summary of the relevant distances and angles.

Table III-4 Selected bond lengths (Å) and angles (°) around the inner coordination sphere of **1-4**. Nitrogen atoms labelled per molecule or end of the cage structure, X=Cl/Br.

	1	**2**	**3_t**	**3_b**	**4_t**	**4-b**
N1/N5	2.2469(19)	2.241(3)	2.2801(18)	2.2766(18)	2.259(3)	2.262(3)
N2/N6	2.055(2)	2.081(3)	2.1175(18)	2.1196(18)	2.124(3)	2.133(3)
N3/N7	2.114(2)	2.111(3)	2.1215(17)	2.1160(18)	2.114(3)	2.116(3)
N4/N8	2.0862(19)	2.046(3)	2.1284(17)	2.1295(18)	2.119(3)	2.115(3)
X	2.2818(7)	2.4349(6)	2.4241(6)	2.4196(6)	2.4970(6)	2.4922(6)
N2/6-M-N3/7	107.80(8)	118.10(12)	116.24(7)	116.09(7)	117.23(13)	117.11(12)
N3/7-M-N4/8	118.26(8)	108.12(11)	117.05(7)	117.80(7)	116.74(13)	116.75(13)
N4/8-M-N2/6	123.01(9)	123.05(12)	116.84(7)	116.60(7)	117.83(13)	118.15(12)
N1/5-M-X	174.65(6)	174.06(8)	178.86(5)	178.18(5)	179.26(8)	178.24(8)
Co1-X-Co2			178.83(3)		178.43(2)	

III.3.2 DC Magnetic Studies

Static DC measurements were performed on complexes **1-4** from 1.8 – 300 K using a SQUID magnetometer. The χ_mT vs T plots for **1** and **2** are visualized in Figure III.7. The χ_mT values are all higher than 1.87 emu K mol^{-1}, the ideal value for an S=3/2 system with *g*=2. Complex **1** exhibits a χ_mT value of 2.27 emu K mol^{-1} at 300 K, which slowly decreases to 2.09 emu K mol^{-1} at 50 K, after which there is a steep decrease down to 1.39 emu K mol^{-1} at 2 K. Complex **2** exhibits a χ_mT value of 2.54 emu K mol^{-1} at 300 K, which slowly decreases to 2.38 emu K mol^{-1} at 50 K, after which there is a steep decrease to 1.50 emu K mol^{-1} at 2 K. These deviations from ideality reflect spin-orbit coupling. Each

compound exhibits near Curie-like behavior until ~50 K, after which $\chi_m T$ decreases as expected due to zero-field splitting.

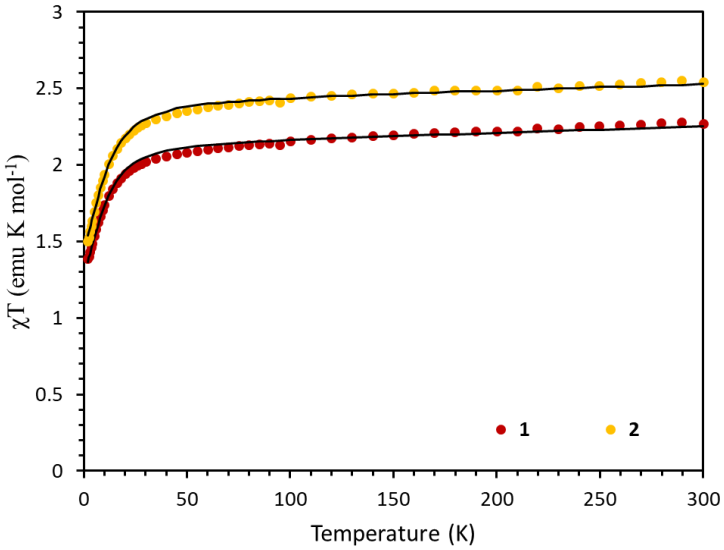

Figure III.7 $\chi_m T$ vs T data for compounds **1** and **2**, as labelled, under a 1000 Oe DC field. Solid lines are fits to the data using the program PHI.

The $\chi_m T$ vs T plots for **3** and **4** (Figure III.8) indicate that the $\chi_m T$ value at 300 K for **3** is 3.74 emu K mol^{-1}, which is equal to the spin-only value for two non-interacting S=3/2 ions with *g*=2. Compound **4** is lower than this value at 3.46 emu K mol^{-1}. In both cases, $\chi_m T$ rapidly decreases to 0.12 emu K mol^{-1} and 0.04 emu K mol^{-1} for **3** and **4**, respectively, which is consistent with antiferromagnetic coupling. In a fully coupled system, this would result in a non-magnetic ground state. Interestingly, for **3**, an increase in $\chi_m T$ occurs below 14 K, where $\chi_m T$ increases from 0.18 emu K mol^{-1} to 0.31 emu K mol^{-1} at 7 K, after which a steep decrease is observed. This increase is absent in **4**.

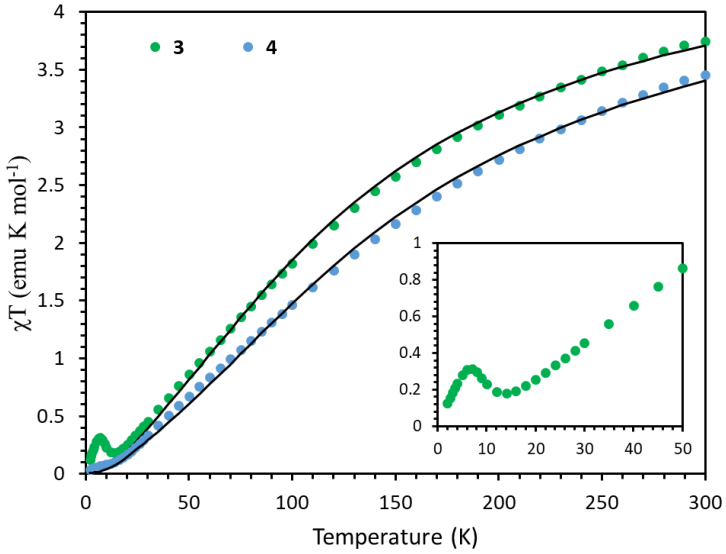

Figure III.8 $\chi_m T$ vs T data for compounds **3** and **4**, as labelled, under a 1000 Oe DC field. Solid lines are fits to the data using the program PHI.

The anisotropic nature of **1** and **2** is supported by the M versus H plots at 1.8 K that do not saturate, even up to 7 T. The expected saturation point for each compound is 3 μ_B, a value which neither of the compounds reach. Compound **1** shows a maximum below 2.5 μ_B, Figure III.9. Compound **2** reaches a maximum equal to 2.5 μ_B at 7 T, Figure III.10.

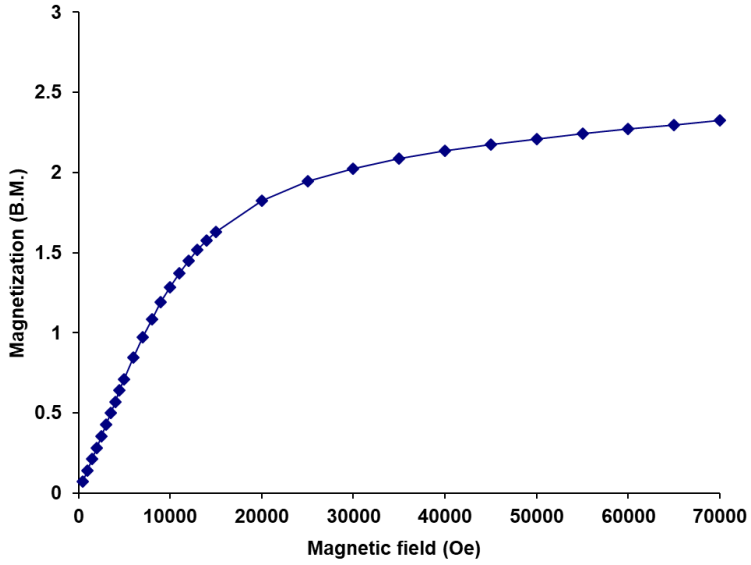

Figure III.9 Magnetization vs field for compound **1**. Solid line is a guide for the eye.

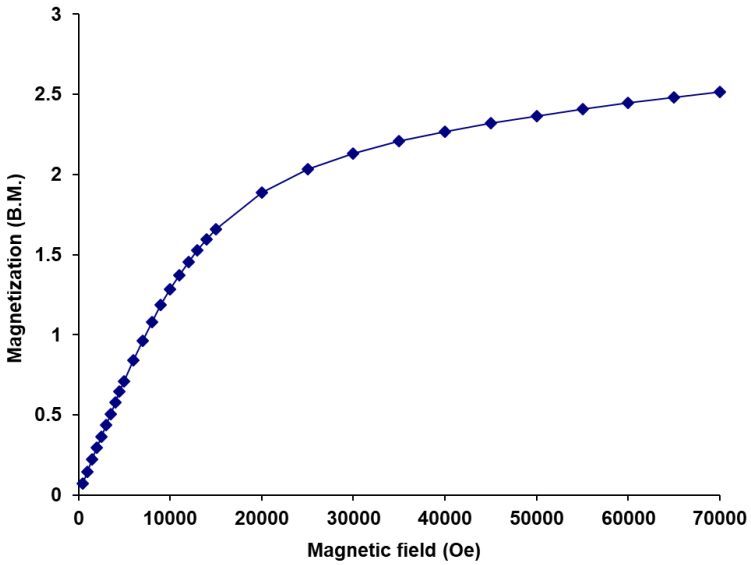

Figure III.10 Magnetization vs field for compound **2**. Solid line is a guide for the eye.

For compounds **3** and **4**, the maximum in magnetization should be very low, corresponding to antiferromagnetic coupling at 1.8 K. For **3**, the maximum is below 0.1 μ_B at 7 T, indicating nearly full antiferromagnetic coupling at low temperatures, Figure III.11. Compound **4** reaches a maximum slightly above 0.1 μ_B, also indicating nearly full antiferromagnetic coupling at low temperatures, Figure III.12.

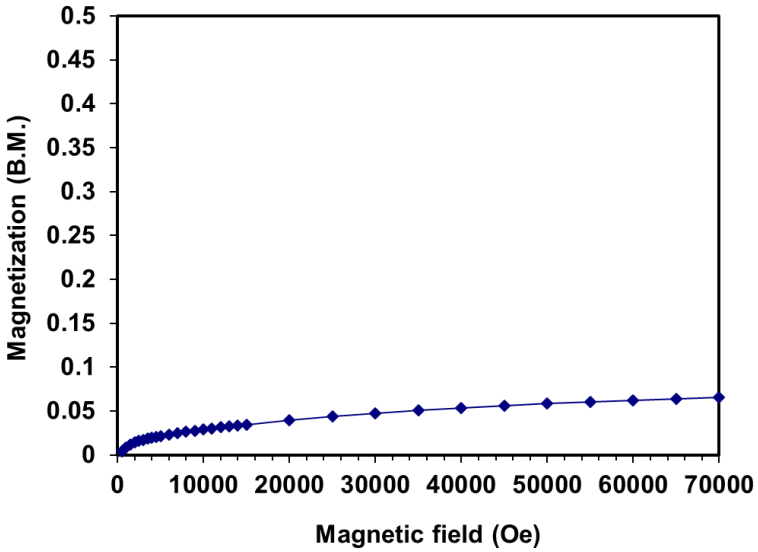

Figure III.11 Magnetization vs field for compound **3**. Solid line is a guide for the eye.

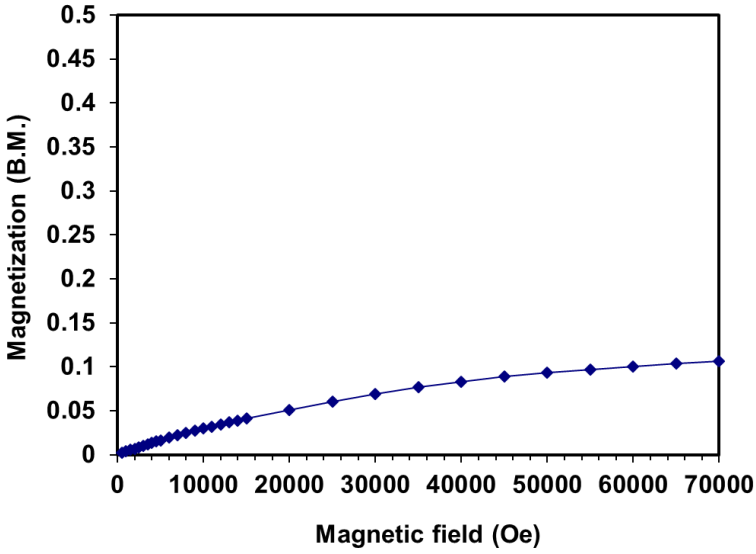

Figure III.12 Magnetization vs field for compound **4**. Solid line is a guide for the eye.

In order to determine experimental g_{iso}, *D*, and *E* values for **1** and **2**, χT and reduced magnetization plots were simultaneously fit using PHI.[81] The fits to the susceptibility plots are provided in Figure III.7. The reduced magnetization for compound **1** shows a lack of superposition in the isofield lines as expected for an anisotropic Co(II) system. The data were fit with g, D, and E values equal to 2.13, 12.21 cm^{-1}, and 0.16 cm^{-1}, respectively, Figure III.13. The reduced magnetization for compound **2** also shows a lack of superposition in the isofield lines, indicative of anisotropy. The data were fit with g, D, and E values equal to 2.26, 13.2 cm^{-1}, and 0.07 cm^{-1}, respectively, Figure III.14.

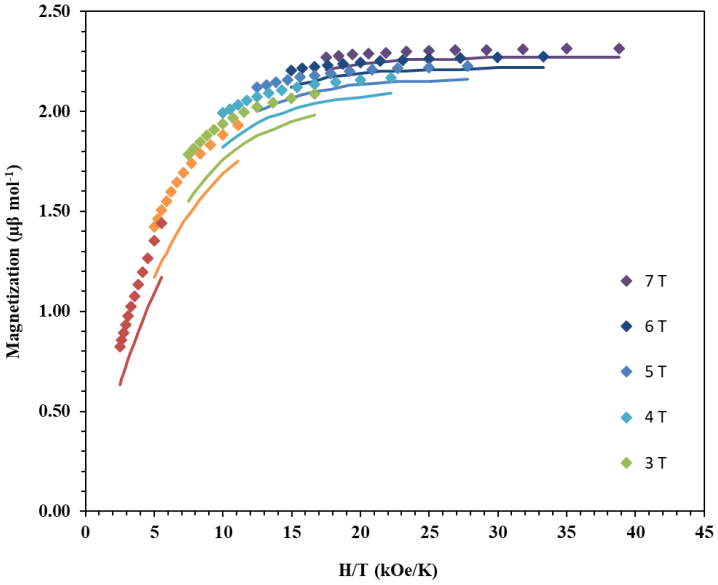

Figure III.13 Reduced magnetization for **1**. Solid lines are fits to the experimental data using the PHI program.

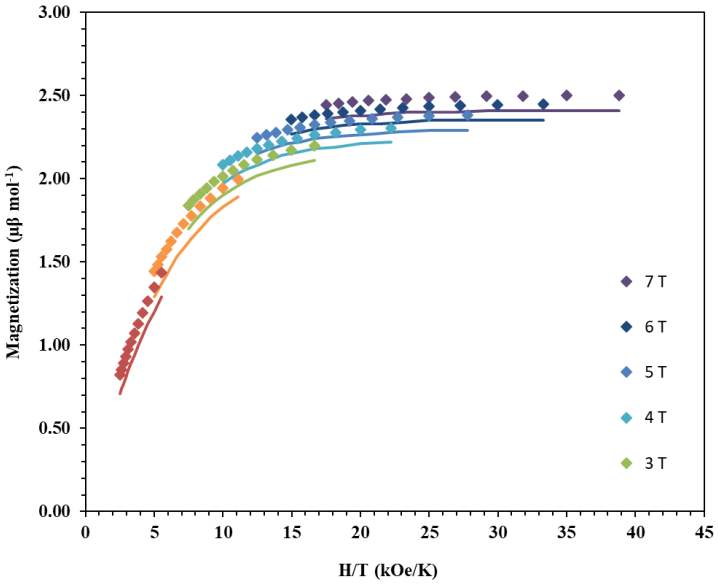

Figure III.14 Reduced magnetization for **2**. Solid lines are fits to the experimental data using the PHI program.

Reduced magnetization were also collected for **3** and **4**. As expected for the antiferromagnetically coupled systems, the magnetization values are low, Figure III.15. For this reason, only $\chi_m T$ was fit using PHI to extract g, D, and J values to evaluate the anisotropy of the cobalt centers, as well as the strength of the coupling between the two metal centers, Figure III.8. To avoid over parameterization, the g and D values for each cobalt center were assumed to be equal. The sign of D could not be determined based on the experimental fits to $\chi_m T$, with both positive and negative D yielding similar results, and so the |D| is reported for **3** and **4**. In the case of **3**, only the temperature range between 300 K and 18 K was fit due to the peak in $\chi_m T$ at low temperatures. This resulted in g, |D|, and J values of 2.31, 16.02 cm^{-1}, and -21.21 cm^{-1} respectively. For **4**, the total temperature range between 300 K and 2 K was fit. This resulted in g, |D|, and J values of 2.28, 26.1 cm^{-1}, and -25.29 cm^{-1} respectively.

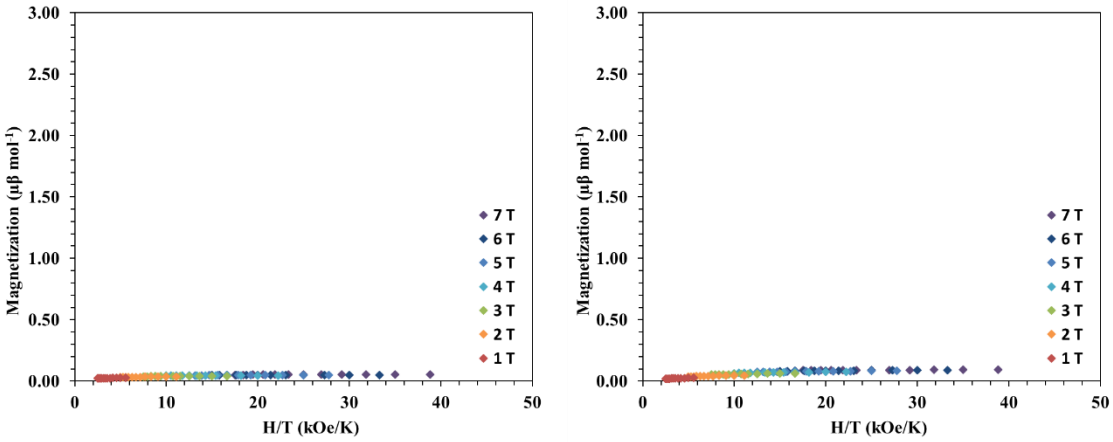

Figure III.15 Reduced magnetization at 1.8 K for **3** (left) and **4** (right).

Upon comparison to the predictions made by Ruiz et al.[40], **1** and **2** strongly agree. Both **1** and **2** exhibit relatively large, positive D values based on the data fits. Compound **2** has a slightly larger D value as expected due to the coordination of a heavier halide. A direct comparison of **3** and **4** is difficult due to the issue in assigning the sign of D. Both positive and negative D values have been observed in literature for trigonal bipyramidal Co(II) complexes, so an assumption cannot be made on literature precedence either.[65, 98, 100, 103] The g, D, E, and J values for **1-4** are summarized in Table III-5.

Table III-5 Experimental values of g, D, E, and J for **1-4** based on PHI fittings.

	1	**2**	**3**	**4**
g	2.13	2.26	2.31	2.28
D (cm^{-1})	12.21	13.2	16.02	26.1
E (cm^{-1})	0.16	0.07		
J (cm^{-1})			-21.21	-25.29

III.3.3 AC Magnetic Studies

Compounds **1-4** were also measured under an AC field to probe the magnetic properties using DC fields from 0 Oe to 2000 Oe. Compound **1** exhibits only the beginning of an out-of-phase signal under applied DC fields up to 2000 Oe, Figure III.16. Compound **2** exhibits slightly better magnetic behavior, with a peak visible under a 2000 Oe DC field at high frequencies, Figure III.17.

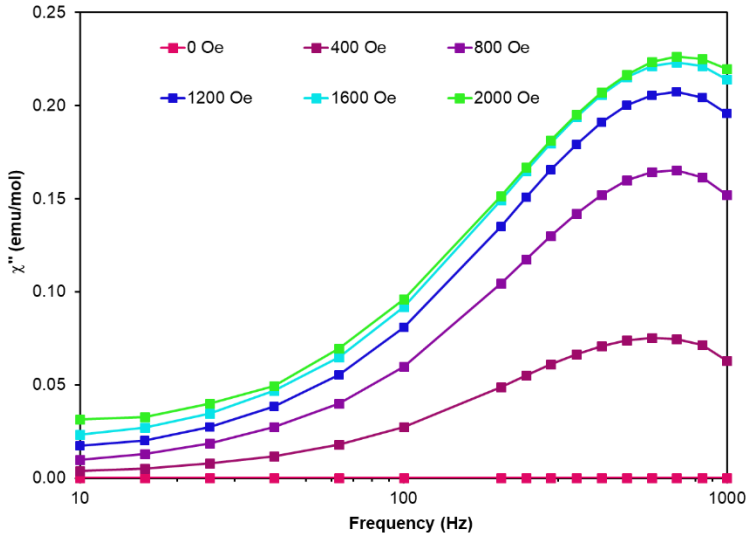

Figure III.16 Out-of-phase susceptibility for compound **1** under applied DC fields from 0 Oe to 2000 Oe, as labelled.

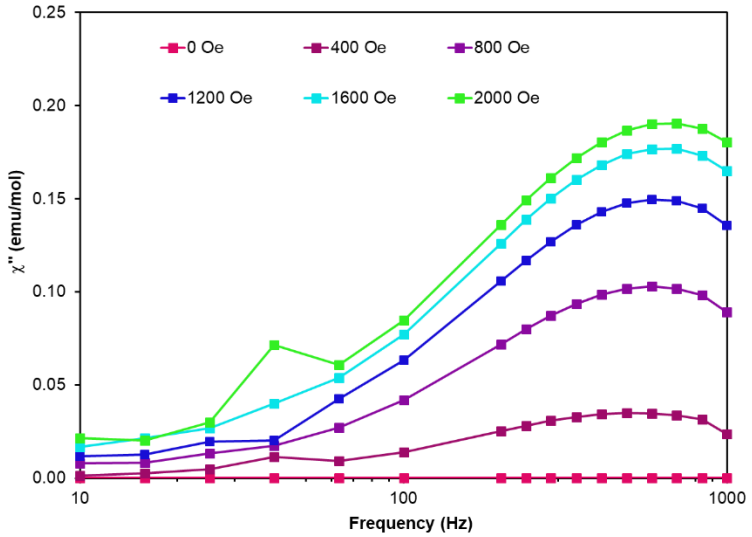

Figure III.17 Out-of-phase susceptibility for compound **2** under applied DC fields from 0 Oe to 2000 Oe, as labelled.

Complex **2** was measured under an applied DC field of 2000 Oe. A maximum in χ" was observed up to 2.2 K, along with the corresponding decrease in χ'. The χ' and χ" plots are provided in Figure III.18.

a)

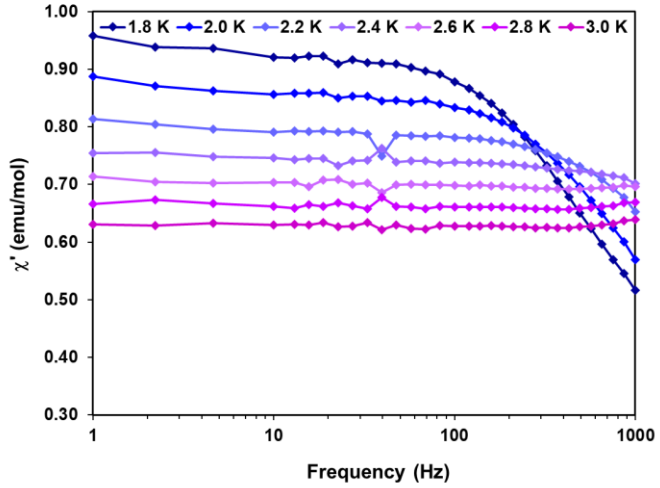

b)

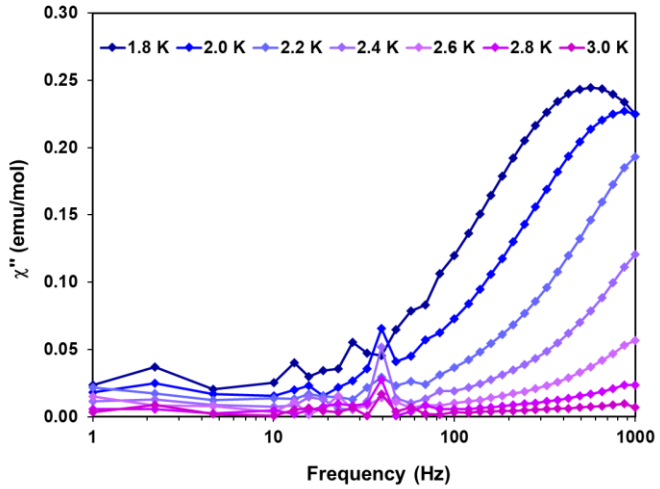

Figure III.18 a) In-phase susceptibility (χ') vs Frequency and b) out-of-phase susceptibility (χ") for **2** under an applied DC field of 2000 Oe. Solid lines are guides for the eye.

The in-phase and out-of-phase susceptibility plots were converted into a Cole-Cole plot. It was subsequently fit using CC-fit[83] which led to a maximum α value of 0.17, indicating a relatively narrow range of relaxations times. The resulting Arrhenius plot was fit with a linear fit line resulting in a barrier of U_{eff}/k_b = 6.7 K and τ_o = 1.20 x 10^{-8} s, Figure III.19.

a)

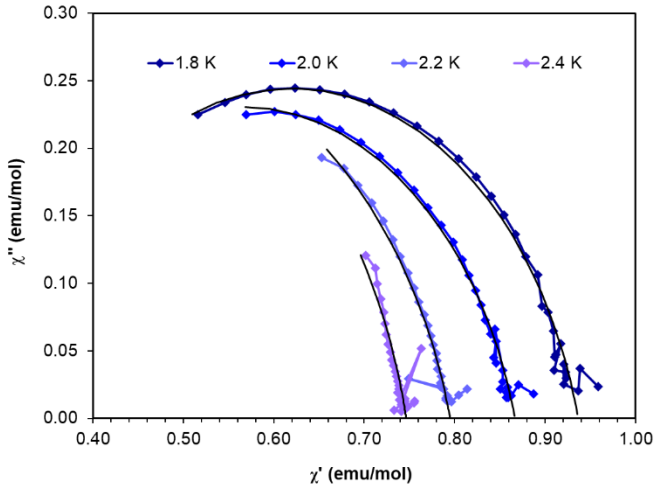

b)

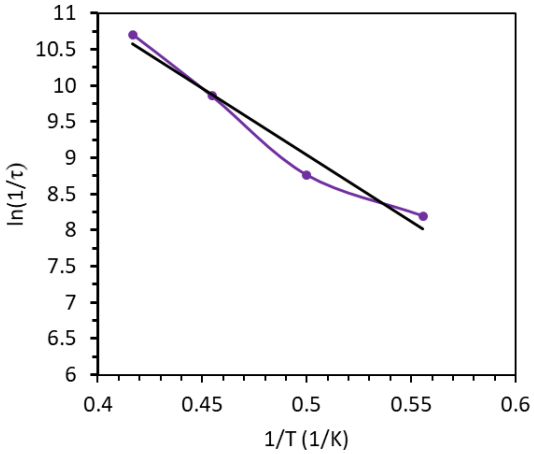

Figure III.19 a) Cole-Cole plot fit via CC-fit and b) ln(τ) vs 1/T fit with a linear regression. Black lines are fits to the data.

The magnetic behavior for **3** and **4** was also investigated. Compound **3** exhibits an out-of-phase signal under a zero applied DC field. However, the in-phase susceptibility also exhibited a similar shaped signal, Figure III.20. This shape of the in-phase data indicates that the spin blocking that is being observed cannot be attributed to SMM behavior.

a)

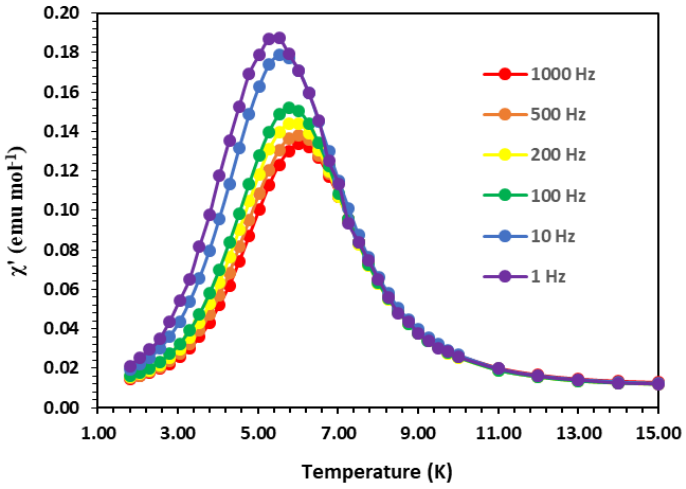

b)

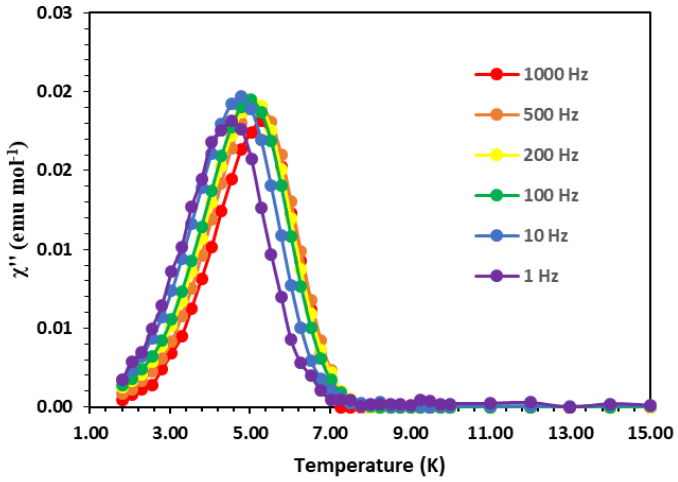

Figure III.20 a) In-phase and b) out-of-phase susceptibility for **3** under 0 applied DC field at the frequencies indicated.

The maximum peaks in both graphs start close to the same temperature at which there was a maximum in the low temperature regime in the $\chi_m T$ vs T plots, indicative of a change in the interaction between molecules. In this vein, the Mydosh parameter was calculated according to the equation $X = \Delta T/(T_f * \Delta(\log_{10} \upsilon))$.[104-105] This resulted in a value of 0.045 and 0.055 for χ' and χ", respectively. These values are an order of magnitude smaller than what is usually observed in SMM behavior. They are in the range observed for complexes that behave as glassy magnets.[104-105] Additional confirmation comes from χ" being approximately 10% of χ'.[104-105] In order to further assess the glassy magnetic behavior, the field cooled (FC) and zero field cooled (ZFC) magnetic susceptibilities were investigated. Cooling for the FC data took place under a DC field of 10,000 Oe. Strong irreversibility in the susceptibility is observed, indicated by the significant divergence at approximately 5 K, Figure III.21. This behavior is expected for, and evidence towards, the blocking of the spins in random orientations, resulting in the glassy magnetic bheavior.[105-106]

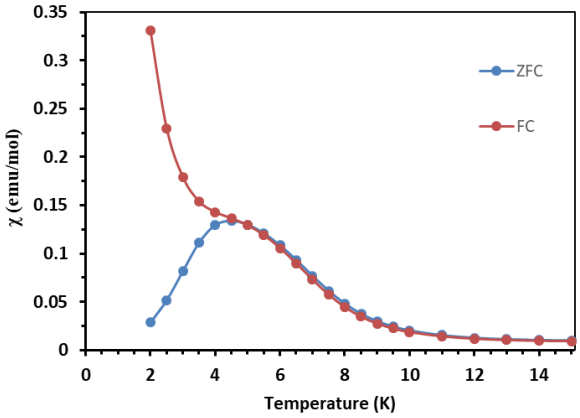

Figure III.21 Susceptibility for **3** from 2 K to 15 K under field cooled (FC) and zero field cooled (ZFC) conditions.

The out-of-phase susceptibility in **4** was measured to probe for any similar glassy magnet behavior. The in-phase and out-of-phase susceptibility data were measured under applied DC fields from 0-2000 Oe at 1.8 K and 5 K, Figure III.22. No signal was observed at either temperature. Correspondingly, there is no divergence in the FC and ZFC data, Figure III.23.

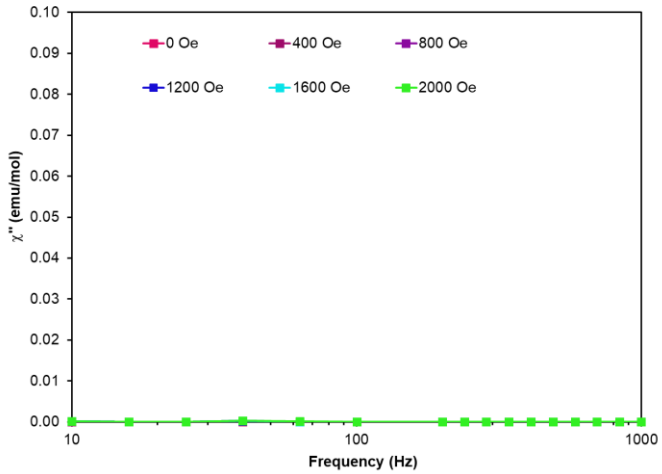

Figure III.22 Out-of-phase susceptibility for **4** at 5 K under applied DC fields from 0 Oe to 2000 Oe, as labelled.

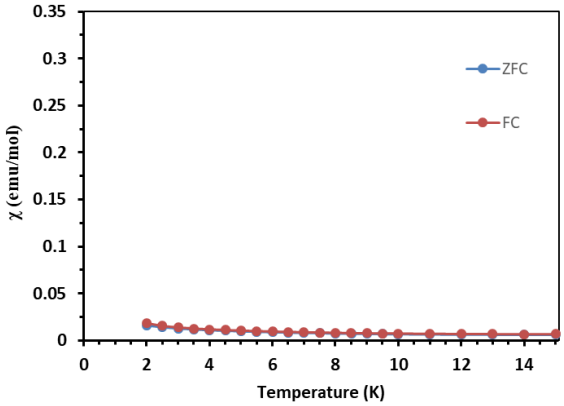

Figure III.23 Susceptibility from 2 K to 15 K for **4** under field cooled (FC) and zero field cooled (ZFC) conditions.

III.3.4 Magneto-Structural Correlations

Comparisons of the crystal structures for the mononuclear complexes **1** and **2** and the dinuclear complexes **3** and **4** indicate that the geometry about each ion could be described as trigonal bipyramidal. Compounds **3** and **4** exhibit geometries closer to ideal than their mononuclear analogues. When comparing the chloride containing molecules with the bromide derivatives, the chloride complexes, **1** and **3**, are closer to ideal geometry than their bromide analogues. The intermolecular distances are longer in **3** and **4** by approximately 0.6 Å.

For both pairs of complexes, the D value for the bromide containing complexes is larger than the D value for the chloride containing complexes. This is expected due to the heavy atom effect of the bromide ion, and has been observed in literature.[107-112] Additionally, the D values for **3** and **4** are larger than those for **1** and **3**. This correlates with the SHAPE values that were observed for the complexes. Based on these observations, the full cage appears to help stabilize the low coordination sphere around each cobalt ion, resulting in a more ideal geometry and higher D values.

The out-of-phase susceptibility data also correlate with the observed D values for **1** and **2**. Although neither exhibits SMM behavior in the absence of a DC field, compound **2** exhibits slow relaxation at slightly higher temperatures than **1**, which directly correlates with geometric trends, as well as with the D values. Both complexes have barriers significantly under the maximum value based on the 2|D| energy gaps between the spin microstates, which would give U=24.4 cm^{-1} and 26.4 cm^{-1} for **1** and **2**, respectively. This

is likely due to significant quantum tunneling effects due to the deviation from an ideal trigonal bipyramidal geometry.

Both **3** and **4** exhibit significant antiferromagnetic coupling between the two metal centers through the halide bridge, with strongest coupling observed for **4**. This is predicted due to the larger and more diffuse orbitals of the Br atom compared to the Cl atom.[100] Trends in the magnetic coupling between similar cage-like compounds have been studied by Murugesu, *et al.*[100] Their cages differ only in coordination to the bridging phenyl group, which takes place in the 1,3 positions rather than the 1,4 positions. The authors observe an inverse relationship between coupling strength and the distance between the two metal centers; the shorter the distance, the stronger the coupling. Interestingly, the same trend is not observed in complexes **3** and **4**. While **4** has a longer intermetallic bond distance of 4.989 Å, as compared to 4.844 Å in **3**, it also exhibits stronger coupling. The authors also reported no out-of-phase susceptibility for each of their complexes, even the chloride analogue to the one presented herein.

Recently, the out-of-phase susceptibility for two complexes employing the same cage-like ligand as the one in this chapter have been reported. In this case, coordination of only one cobalt center with an azide ligand in the axial position resulted in slow magnetic relaxation under an applied DC field of 500 Oe.[103] When the cage is fully occupied with two cobalt centers, antiferromagnetic coupling is observed, but no out-of-phase signal. It would be interesting to perform a similar study with chloride and bromide in the axial position. Particularly in the case of **3**, it would lend insight into the origin of the glassy magnetic behavior, and whether it is dependent upon the antiferromagnetic coupling.

Additionally, computational studies of all four complexes would lend further evidence towards the sign and magnitude of the D values in **1**-**4**, as well as the J values for **3** and **4**.

III.4 Conclusions

In this chapter, the syntheses of four complexes was reported, along with their structural and magnetic characterization. A direct comparison between two pairs of molecules, one mononuclear and the other dinuclear, was made. The nitrogen donor ligands that were used were either partially encapsulated or fully encapsulated the divalent cobalt ions, with chloride or bromide in the open axial site.

Both mononuclear complexes exhibited slow magnetic relaxation under an applied field, with the heavier halide bromide resulting in improved magnetic behavior. Both of the dinuclear complexes exhibited strong antiferromagnetic coupling, with the bromide ion engendering stronger coupling between the two cobalt centers. The chloride containing dinuclear complex exhibited glassy magnetic behavior up to 6 K. In comparison, no out-of-phase signal was observed for the bromide analogue.

Together, these results yield fascinating insights into the magnetic behavior of four closely related complexes. The need for strict geometric control, as well as the advantage of heavier atoms in SMM behavior were verified. Computational studies would yield more information about how the orbitals in each complex contribute to the vastly different magnetic behavior. Future studies also include partial coordination of the cage-like structures with only one cobalt ion, as well alternative bridging ligands which restrict coupling between the metal centers.

CHAPTER IV

MAGNETIC RELAXATION DYNAMICS OF 3D TRANSITION METAL MOLECULES USING A TI(IV) FRAGMENT AS AN INORGANIC BLOCKING LIGAND

IV.1 Introduction

Recently, great strides have been made in increasing the temperature at which hysteresis is observed for single molecule magnets (SMMs). With the current record of 80 K, these molecules are becoming feasible for real application in technologies such as data storage and quantum computing.[6, 48, 54, 56-57] Single molecule magnets exhibit hysteresis, of a different origin than bulk magnets due to the presence of a thermal barrier between the spin microstates $+m_s$ and $-m_s$ of the total Spin ground state S. In 3d metal complexes, this thermal barrier is defined as $U=|D|S^2$ for integer systems and $U=|D|(S^2-1/4)$ for non-integer systems. Research has focused on maximizing *D*, the axial zero field splitting parameter. Initially, attempts were made to increase the barrier by synthesizing high spin systems. However, experimental and computational results have revealed that increasing spin is not the most effective method to increase the barrier.[16, 58]

While lanthanide based SMMs have held the record for many years now, 3d transition metal based SMMs have remained important as they have been found to exhibit barriers close to those achieved by lanthanide systems, and have been vital to understanding the various relaxation mechanisms present in SMMs. Orbach relaxation of the spins up and over the barrier is the ideal relaxation process, but Raman and quantum

tunneling processes also occur which serve to undercut the barrier and lower the operating temperature of the magnets.[17] Geometric control over the symmetry around the 3d metal center has come to the forefront as a way to increase barrier height in the complexes. For example, the record temperatures for both cobalt and iron systems come from linear systems; $[K(crypt\text{-}222)][Fe^{I}(C(TMS)_3)_2]$ and $[(sIPr)Co^{II}NDmp]$ (Dmp = 2,6-dimesitylphenyl) exhibit barriers of 226 cm^{-1} and 413 cm^{-1} respectively.[43, 60]

One of the problems observed in mononuclear SMMs is relaxation of the spins via interaction between two molecules, i.e. dipolar interactions. This is often observed in both lanthanide and 3d metal mononuclear systems. A few methods have been used to control geometry and prevent dipolar interactions between molecules: solid state dilution, bulky ligands, and multinuclear systems with diamagnetic metal centers surrounding the paramagnetic metal center. Solid state dilution commonly uses Zn(II) for 3d metal systems and Y(III) for lanthanide metal systems. Dilution with an isomorphic complex employing a diamagnetic metal, while effective, cannot be universally applied to every system. Sometimes it is not possible to isolate an identical structure with the diamagnetic ion, particularly with zinc.

In the case of bulky ligands, those with trigonal symmetry have been pursued due to their ability to limit quantum tunneling mechanisms.[18, 24-25, 64-65, 86-87, 113-114] It is also advantageous for this ligand to help control coordination in the remaining open positions for the metal center. Finally, it is ideal for the ligand to be bulky enough to help separate the paramagnetic metal centers from one another. One such ligand that has been used is the scorpionate trispyrazolylborate (Tp) ligand and its derivatives, employed in the

synthesis of polynuclear and mononuclear complexes exhibiting SMM behavior.[115-122]

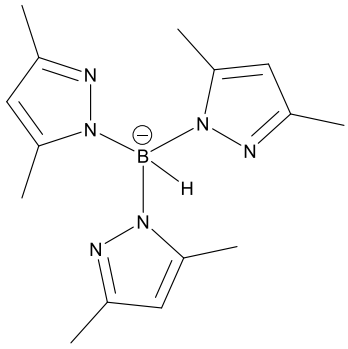

Figure IV.1 Schematic of the Tp* anion used in the synthesis of the four compounds described herein.

Trivalent cobalt in an octahedral geometry has been employed several times to functionally act as a diluting agent in multinuclear complexes with Mn^{III} and Co^{II} SMMs.[107, 123-124] No other metals in a diamagnetic ground state have been used in this manner to the best of our knowledge. The goal was to synthesize complexes that would take advantage of both ligand and diamagnetic metal dilution effects. To this end, the recently reported complexes (TEA)[Tp*$TiCl_3$] and (TEA)[Tp*$Ti(CN)_3$][125], which used the methylated derivative of the Tp ligand, tris(3,5-dimethyl-1-pyrazolyl)borate, were employed, Figure IV.1. The premise is that if the titanium in these complexes is oxidized to the tetravalent ion, it would become diamagnetic and could subsequently be used as novel bulky inorganic ligand.

Herein, the report of the successful synthesis of air stable, trinuclear complexes containing Tp*Ti^{IV} as a capping group around divalent manganese, iron, cobalt, and nickel is described. Acetate and oxo bridges act as the connection between the metal centers,

resulting in the compounds [$(Tp^*Ti)_2(\mu\text{-}O_2)(\mu\text{-}OAc)_4Mn$], [$(Tp^*Ti)_2(\mu\text{-}O_2)(\mu\text{-}OAc)_4Ni$], [$(Tp^*Ti)_2(\mu\text{-}O_2)(\mu\text{-}OAc)_4Ni$], and[$(Tp^*Ti)_2(\mu\text{-}O_2)(\mu\text{-}OAc)_4Ni$].

IV.2 Experimental Methods

IV.2.1 Complex Synthesis

Acetonitrile was degassed, refluxed over molecular sieves, and stored in an MBRAUN glovebox over molecular sieves. Anhydrous DMF was purchased and stored over molecular sieves. (TEA)[$Tp^*Ti(CN)_3$] was synthesized according to literature procedure[125] and stored in an MBRAUN drybox under nitrogen. All other chemicals were purchased from commercial sources and used as received.

[$(Tp^*Ti)_2(\mu\text{-}O)_2(\mu\text{-}OAc)_4Mn$]•4$CH_3CN$ (1). $Mn(OAc)_2$•4H_2O (44 mg, 0.18 mmol) was dissolved in DMF (20 mL) under ambient conditions. (TEA)[$Tp^*Ti(CN)_3$] (100 mg, 0.18 mmol) was dissolved in CH_3CN (20 mL) under an N_2 atmosphere. The (TEA)[$Tp^*Ti(CN)_3$] solution was brought out of the glovebox and immediately poured into the $Mn(OAc)_2$ solution resulting in a color change from pale yellow to lime green to dark yellow over the course of 8 hours. After sitting for 24 hours, yellow, X-ray quality crystals of **1** were isolated (59 mg, 28% yield).

[$(Tp^*Ti)_2(\mu\text{-}O)_2(\mu\text{-}OAc)_4Fe$]•4$CH_3CN$ (2). $Fe(OAc)_2$ (31.4 mg, 0.18 mmol) was suspended in DMF (20 mL) and (TEA)[$Tp^*Ti(CN)_3$] (100 mg, 0.18 mmol) was dissolved in CH_3CN (20 mL) under an N_2 atmosphere. Both solutions were brought out of the glovebox and the (TEA)[$Tp^*Ti(CN)_3$]was immediately poured into the $Fe(OAc)_2$ suspension resulting in a color change from orange to red to dark green over the course of 24 hours. Dark blue-green, X-ray quality crystals of **2** were isolated (79 mg, 37% yield).

[(Tp*Ti)$_2$(μ-O)$_2$(μ-OAc)$_4$Co]•4CH$_3$CN (3). Co(OAc)$_2$•4H$_2$O (48 mg, 0.19 mmol) was dissolved in DMF (20 mL) under ambient conditions. (TEA)[Tp*Ti(CN)$_3$] (105 mg, 0.19 mmol) was dissolved in CH$_3$CN (20 mL) under an N$_2$ atmosphere. The (TEA)[Tp*Ti(CN)$_3$] solution was brought out of the glovebox and immediately poured into the Co(OAc)$_2$ solution resulting in a color change from purple to dark green over the course of 8 hours. After sitting for 24 hours, yellow-orange, X-ray quality crystals of **3** were isolated (72 mg, 32% yield).

[(Tp*Ti)$_2$(μ-O)$_2$(μ-OAc)$_4$Ni]•4CH$_3$CN (4). Ni(OAc)$_2$•4H$_2$O (40 mg, 0.14 mmol) was dissolved in DMF (20 mL) under ambient conditions. (TEA)[Tp*Ti(CN)$_3$] (80 mg, 0.14 mmol) was dissolved in CH$_3$CN (20 mL) under an N$_2$ atmosphere. The (TEA)[Tp*Ti(CN)$_3$] solution was brought out of the glovebox and immediately poured into the Ni(OAc)$_2$ solution resulting in a color change to pale yellow. After sitting for 24 hours, pale yellow x-ray quality crystals of **4** were isolated (54 mg, 25% yield).

IV.2.2 Crystallography

Structural characterization of **1-4** was performed using a Bruker QUEST instrument equipped with a Mo Kα source and CCD detector. Once the single crystals were selected, they were mounted on the instrument using paratone oil and a MiTeGen microloop. Collection took place under a cold stream of nitrogen at 100 K. The frames were integrated using the Apex2 software, and the absorbance was corrected using SADABS integrated in Apex2.[70] The structure was solved using SHELXT[71] and refined using SHELXL[72] with the OLEX 2 program.[73] All atoms were refined anisotropically, with the exception of hydrogen atoms which were placed in calculated positions.

Compounds **1** and **2** were solved as twins. Compound **1** was solved using the twin law (-1, 0, 0, 0, -1, 0, 0.987, 0, 1) with a minor component of 17.14(8) percent. Compound **2** was solved using the twin law (-1, 0, 0, 0, -1, 0, 0.995, 0, 1) with the minor component present at 31.45(10) percent. Both twin laws were found using the PLATON program.[126] All four compounds have four molecules of acetonitrile co-crystallized with the compound. Crystallographic and refinement details can be found in Table IV-1.

Table IV-1 Crystal data and structure refinement for Ti_2M complexes.

Identification code	Ti2Mn	Ti2Fe
Empirical formula	$C_{46}H_{68}B_2MnN_{16}O_{10}Ti_2$	$C_{46}H_{68}B_2FeN_{16}O_{10}Ti_2$
Formula weight	1177.52	1178.43
Temperature/K	100	100
Crystal system	monoclinic	Monoclinic
Space group	$P2_1/n$	$P2_1/n$
a/Å	19.2441(11)	19.1509(6)
b/Å	15.7449(9)	15.7078(5)
c/Å	21.4998(12)	21.5380(7)
α/°	90	90
β/°	116.2190(10)	116.2570(10)
γ/°	90	90
Volume/Å^3	5844.1(6)	5810.5(3)
Z	4	4
ρ_{calc}g/cm^3	1.338	1.347
μ/mm^{-1}	0.545	0.581
F(000)	2460.0	2464.0
Crystal size/mm^3	0.153 × 0.125 × 0.059	0.111 × 0.105 × 0.031
Radiation	MoKα (λ = 0.71073)	MoKα (λ = 0.71073)
2Θ range for data collection/°	4.234 to 50.308	4.254 to 50.248
Index ranges	-22 ≤ h ≤ 22, -18 ≤ k ≤ 18, -25 ≤ l ≤ 25	-22 ≤ h ≤ 22, -18 ≤ k ≤ 18, -25 ≤ l ≤ 25
Reflections collected	128162	127847
Independent reflections	10532 [R_{int} = 0.0482, R_{sigma} = 0.0197]	10538 [R_{int} = 0.0748, R_{sigma} = 0.0290]
Data/restraints/parameters	10532/0/715	10538/0/709
Goodness-of-fit on F$^{2\,c}$	1.121	1.107
Final R indexes [I>=2σ (I)]^{a,b}	R_1 = 0.0460, wR_2 = 0.1105	R_1 = 0.0464, wR_2 = 0.1052
Final R indexes [all data]^{a,b}	R_1 = 0.0517, wR_2 = 0.1151	R_1 = 0.0574, wR_2 = 0.1118
Largest diff. peak/hole / e Å^{-3}	0.63/-0.72	0.98/-0.72

Table IV-1 Continued.

Identification code	Ti2Co	Ti2Ni
Empirical formula	$C_{46}H_{68}B_2CoN_{16}O_{10}Ti_2$	$C_{46}H_{68}B_2N_{16}NiO_{10}Ti_2$
Formula weight	1181.51	1181.29
Temperature/K	110	100
Crystal system	monoclinic	monoclinic
Space group	$P2_1/n$	$P2_1/n$
a/Å	19.1158(7)	19.0749(8)
b/Å	15.6992(6)	15.6645(7)
c/Å	21.4240(8)	21.3475(9)
α/°	90	90
β/°	115.4670(10)	115.2880(10)
γ/°	90	90
Volume/Å^3	5804.7(4)	5767.4(4)
Z	4	4
ρ_{calc}g/cm^3	1.352	1.360
μ/mm^{-1}	0.617	0.660
F(000)	2468.0	2472.0
Crystal size/mm^3	0.13 × 0.12 × 0.047	0.131 × 0.128 × 0.052
Radiation	MoKα (λ = 0.71073)	MoKα (λ = 0.71073)
2Θ range for data collection/°	4.584 to 50.904	4.588 to 50.232
Index ranges	-23 ≤ h ≤ 23, -18 ≤ k ≤ 18, -25 ≤ l ≤ 25	-22 ≤ h ≤ 22, -18 ≤ k ≤ 18, -25 ≤ l ≤ 25
Reflections collected	132663	128873
Independent reflections	10694 [R_{int} = 0.0831, R_{sigma} = 0.0319]	10271 [R_{int} = 0.1168, R_{sigma} = 0.0430]
Data/restraints/parameters	10694/0/714	10271/0/714
Goodness-of-fit on F$^{2\,c}$	1.109	1.073
Final R indexes [I>=2σ (I)]^{a,b}	R_1 = 0.0498, wR_2 = 0.1073	R_1 = 0.0458, wR_2 = 0.0874
Final R indexes [all data]^{a,b}	R_1 = 0.0680, wR_2 = 0.1149	R_1 = 0.0725, wR_2 = 0.0966
Largest diff. peak/hole / e Å^{-3}	0.63/-0.58	0.40/-0.39

$^a R_1 = \Sigma(||F_o| - |F_c||)/\Sigma|F_o|$. $^b wR_2 = [\Sigma[w(F_o^2 - F_c^2)^2]/\Sigma[w(F_o^2)^2]]^{1/2}$ ^{c}Goodness-of-fit = $[\Sigma[w(F_o^2 - F_c^2)^2]/(n - p)]^{1/2}$, where *n* is the number of reflections and p is the total number of parameters refined.

[(Tp*Ti)$_2$(μ-O)$_2$(μ-OAc)$_4$Mn]•4CH$_3$CN. The Mn ion is coordinated to four acetate bridging ligands and two oxo-bridging ligands; there are also four interstitial acetonitrile molecules. The total charge of the compound is neutral, with Ti^{IV} and Mn^{II} oxidation states. The compound crystallizes in the monoclinic space group $P2_1/n$. The molecular unit is depicted in Figure IV.2. Coordination of the equatorial plane in the octahedron around the Mn^{II} center is a result of the acetate ligands, and the axial positions are filled by the oxo-bridges. The angles between the acetate ligands varies between 88.80(10)° and 91.68(10)°. The angle between O1 and O6 is 175.49(9)°. These deviations from 90° and 180° for the equatorial and axial atoms, respectively, are indicative of distortion away from an ideal octahedral geometry. The bond lengths vary between 2.171(3) Å and 2.180(2) Å in the equatorial positions and 2.114(2) Å to 2.116(2) Å in the axial positions, which indicates an axial compression. The closest intermolecular distance between two of the manganese centers is 10.641 Å.

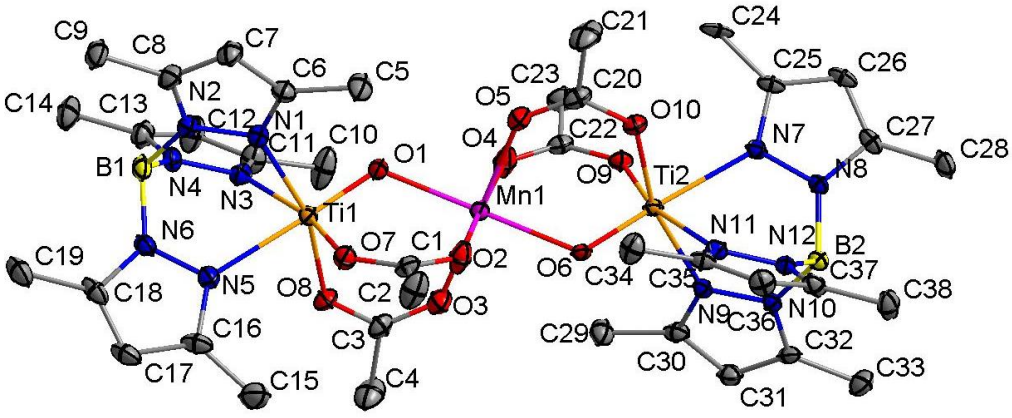

Figure IV.2 Crystal structure and atom numbering scheme of the [(Tp*Ti)$_2$(μ-O)$_2$(μ-OAc)$_4$Mn]. The acetonitrile molecules and hydrogen atoms were omitted for clarity. Thermal ellipsoids were drawn at the 50% probability level. Colors are as follows: purple, Mn; orange, Ti; blue, N; yellow, B; red, O; grey, C.

[(Tp*Ti)$_2$(μ-O)$_2$(μ-OAc)$_4$Fe]•4CH$_3$CN. Coordination and crystallization of this molecule is identical to **1**. The molecular structure is provided in Figure IV.3. The angles between the acetate ligands varies between 87.86(11)° and 92.38(10)°. The angle between O1 and O6 is 177.00(10)°. These deviations from 90° and 180° for the equatorial and axial angles, respectively, are indicative of distortion away from an ideal octahedral geometry. The bond lengths vary between 2.127(3) Å and 2.132(3) Å in the equatorial positions and equals 2.036(2) Å for the axial positions, in accord with an axial compression. The closest intermolecular distance between two of the iron centers is 10.734 Å.

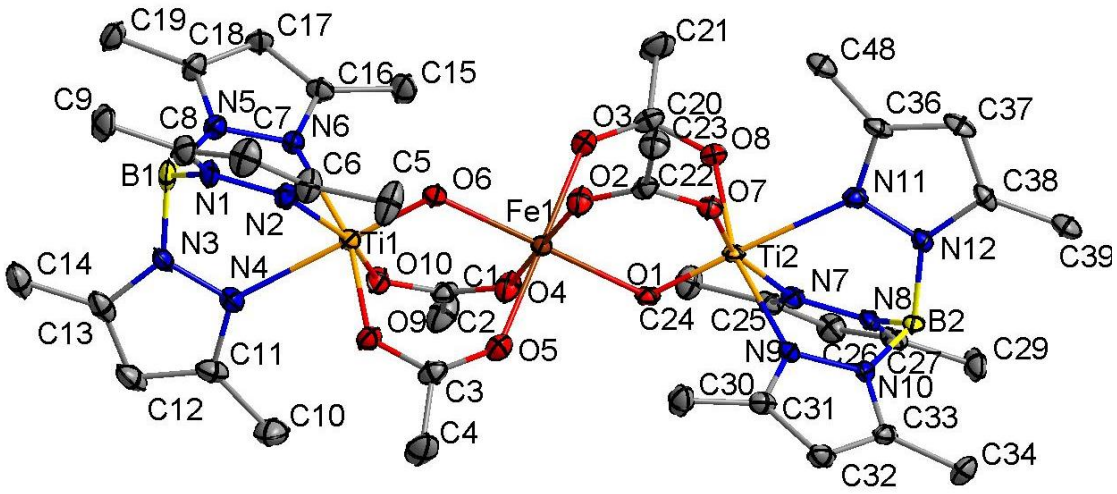

Figure IV.3 Crystal structure and atom numbering scheme of the [(Tp*Ti)$_2$(μ-O)$_2$(μ-OAc)$_4$Fe]. The acetonitrile molecules and hydrogen atoms were omitted for clarity. Thermal ellipsoids were drawn at the 50% probability level. Colors are as follows: brown, Fe; orange, Ti; blue, N; yellow, B; red, O; grey, C.

[(Tp*Ti)$_2$(μ-O)$_2$(μ-OAc)$_4$Co]•4CH$_3$CN. Coordination and crystallization of this molecule is identical to **1**. The molecular structure is provided in Figure IV.4. The angles between the acetate ligands varies between 88.18(10)° and 92.50(10)°. The angle between O1 and O6 is 178.05(9)°. These deviations from 90° and 180° are indicative of distortion away from an ideal octahedral geometry. The bond lengths vary between 2.084(2) Å and 2.100(2) Å in the equatorial positions and between 2.037(2) Å and 2.040(2) Å for the axial positions, which indicates axial compression. The closest intermolecular distance between two of the cobalt centers is 10.754 Å.

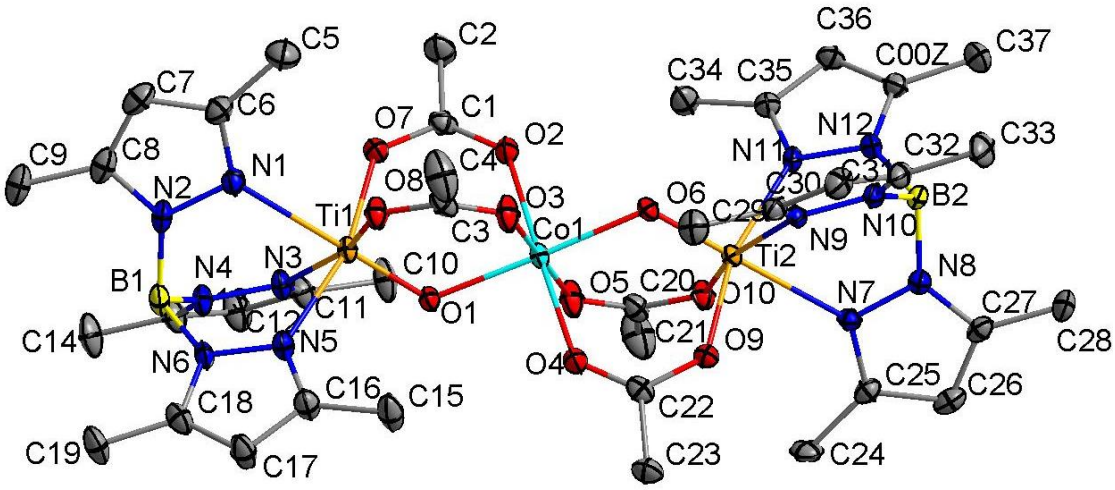

Figure IV.4 Crystal structure and atom numbering scheme of the [(Tp*Ti)$_2$(μ-O)$_2$(μ-OAc)$_4$Co]. The acetonitrile molecules and hydrogen atoms were omitted for clarity. Thermal ellipsoids were drawn at the 50% probability level. Colors are as follows: turquoise, Co; orange, Ti; blue, N; yellow, B; red, O; grey, C.

[(Tp*Ti)$_2$(μ-O)$_2$(μ-OAc)$_4$Ni]•4CH$_3$CN. Coordination and crystallization of this molecule is identical to **1**. The molecular structure is provided in Figure IV.5. The angles between the acetate ligands varies between 87.77(9)° and 92.90(8)°. The angle between O1 and O6 is 178.40(8)°. The bond lengths vary between 2.039(2) Å and 2.056(2) Å in the equatorial positions and between 2.0186(18) Å and 2.0232(18) Å. These distances and angles indicate distortion and axial compression of the octahedral geometry. The closest intermolecular distance between two of the nickel centers is 10.692 Å.

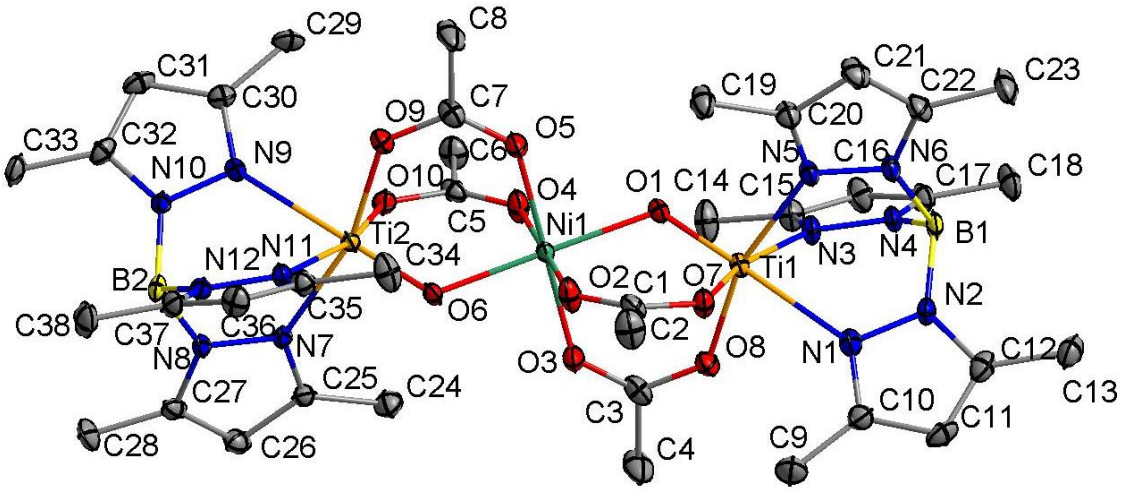

Figure IV.5 Crystal structure and atom numbering scheme of the [(Tp*Ti)$_2$(μ-O)$_2$(μ-OAc)$_4$Ni]. The acetonitrile molecules and hydrogen atoms were omitted for clarity. Thermal ellipsoids were drawn at the 50% probability level. Colors are as follows: green, Ni; orange, Ti; blue, N; yellow, B; red, O; grey, C.

IV.2.3 Magnetic Measurements

Magnetic data were collected on a Quantum Design MPMS-3 SQUID from 1.8-300 K with DC fields from 0-7 T. Compounds **1-4** were collected in plastic bags. Diamagnetic corrections were applied for the bags based on a prior calibration, and diamagnetic contribution from the compounds were calculated based on Pascal's constants.[74]

IV.2.4 Computational Details

Ab initio calculations were performed to compute the ZFS (*D*) of Mn^{II}, Fe^{II}, Co^{II}, and Ni^{II} ions in **1**−**4** using ORCA 3.0 suite of programs.[127] We employed the BP86 functional along with scalar relativistic ZORA Hamiltonians and ZORA-def2-TZVP basis sets for the metal ions and the first coordination sphere, and def2-SVP for the rest of the atoms. The RI approximation with secondary TZV/J Columbic fitting basis sets were used along with increased integration grids (Grid 5 in ORCA convention). The tight SCF convergence was used throughout the calculations ($1x10^{-8}$ Eh). The SOC contributions in the *ab initio* framework were obtained using second-order perturbation theory as well as by employing the effective Hamiltonian approach, which enables calculations of all matrix elements to be made of the anisotropic spin Hamiltonian from the *ab initio* energies and wave functions numerically. Here the state average-CASSCF (Complete Active Space Self-Consistent Field) method was employed to compute the ZFS. The active space is comprised of five active electrons in five active d-orbitals (d^5 system; CAS (5,5)) for the Mn^{II} ion, six active electrons in five active d-orbitals (d^6 system; CAS (6,5)) for the Fe^{II} ion, seven active electrons in five active d-orbitals (d^7 system; CAS (7,5)) for the Co^{II} ion,

and eight active electrons in five active d-orbitals (d^8 system; CAS (8,5)) for the Ni^{II} ion. With this active space, all of 1 sextet for the Mn^{II} ion, 5 quintet and 45 triplet states for the Fe^{II} ion, 10 quartet and 40 doublet states for Co^{II} the ion, and 10 triplet and 15 singlet states for the Ni^{II} ion were calculated in the configuration interaction procedure. [76]

$$\hat{H}_{so} = \sum_i \xi_i \left(\hat{l}_{Zi}.\hat{s}_{Zi} + \frac{1}{2} (\hat{l}_{+i}.\hat{s}_{-i} + \hat{l}_{-i}.\hat{s}_{+i}) \right)$$

The sign and the magnitude of *D* values are rationalized using the spin−orbit operator, given in the equation above. When a spin-allowed excitation of a β-electron occurs between orbitals with same $|\pm m_l|$ levels, the $\sum_i \hat{l}_{Zi}.\hat{s}_{Zi}$ operator couples those orbitals and leads to a negative *D* value. Conversely, when such an excitation occurs between orbitals with different $|\pm m_l|$ levels, the $\frac{1}{2}\sum_i (\hat{l}_{+i}.\hat{s}_{-i} + \hat{l}_{-i}.\hat{s}_{+i})$ operator couples those orbitals and leads to a positive *D* value. [40, 98]

IV.3 Results and Discussion

IV.3.1 Crystallographic Details

The compounds $[(Tp^*Ti)_2(\mu\text{-}O_2)(\mu\text{-}OAc)_4Mn]\bullet 4CH_3CN$ (**1**), $[(Tp^*Ti)_2(\mu\text{-}O_2)(\mu\text{-}OAc)_4Fe]\bullet 4CH_3CN$ (**2**), $[(Tp^*Ti)_2(\mu\text{-}O_2)(\mu\text{-}OAc)_4Co]\bullet 4CH_3CN$ (**3**), and $[(Tp^*Ti)_2(\mu\text{-}O_2)(\mu\text{-}OAc)_4Ni]\bullet 4CH_3CN$ (**4**) were synthesized via reaction between the relevant $M(OAc)_2$ salt and $(TEA)[Tp^*Ti(CN)_3]$ in a 1:1 mixture of dimethylformamide (DMF) and acetonitrile. After standing for 24 hours, square block crystals were isolated. Single crystal X-ray crystallographic studies revealed that all four compounds crystallize in the space group monoclinic $P2_1/n$. The central atom is in the divalent oxidation state with octahedral coordination, and the titanium metal centers are in the tetravalent oxidation state with

trigonal octahedral coordination, Figure IV.6. The cyanide ligands have hydrolyzed, and are not present in the final product.

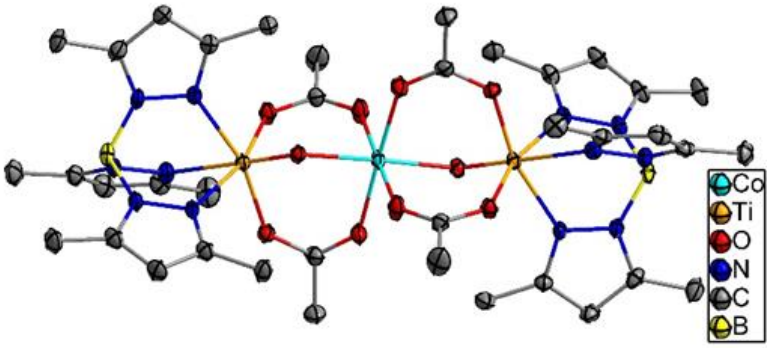

Figure IV.6 Crystal structure of compound **3** as a representative example of all four complexes. Hydrogen atoms and acetonitrile molecules were omitted for clarity. Colors are as labelled.

Coordination around each Ti^{IV} metal center consists of one Tp* ligand, an oxo-bridge, and one half of two acetate bridges. The titanium core is out of plane from the equatorially coordinated atoms towards the central 3d metal. The central core is defined by the pertinent 3d metal atom, two oxo-bridges, and four acetate bridges. In each case, the octahedral geometry is axially compressed. Tables Table IV-2 and Table IV-3 contain a summary of relevant bond distances and angles, respectively, around the divalent metal centers for compounds **1**-**4**.

Table IV-2 M...O bond distances (Å) for compounds **1-4**.

	O1	O2	O3	O4	O5	O6
1	2.116(2)	2.176(2)	2.171(3)	2.180(2)	2.178(3)	2.114(2)
2	2.036(2)	2.130(3)	2.132(3)	2.124(3)	2.131(3)	2.036(2)
3	2.040(2)	2.098(2)	2.084(2)	2.100(2)	2.086(2)	2.037(2)
4	2.0232(18)	2.050(2)	2.039(2)	2.056(2)	2.041(2)	2.0189(18)

Table IV-3 Selected bond angles (°) around M in compounds **1-4**.

	O1 – M – O6	O2 – M – O3	O3 – M – O4	O4 – M – O5	O5 – M – O2
1	175.49(9)	91.68(10)	90.72(10)	88.80(10)	88.82(10)
2	177.00(10)	89.61(10)	87.86(11)	92.38(10)	90.16(10)
3	178.08(9)	92.50(10)	88.96(9)	90.36(10)	88.18(10)
4	178.40(8)	92.90(8)	88.66(8)	90.67(8)	87.77(9)

The SHAPE program[80] was used to analyze how close the geometry is to perfectly octahedral (0 is no distortion). The results are summarized in Table IV-4, where the values range from **1** as the most distorted compound at 0.091, and **3** as the least distorted at 0.045. The other possible geometries for a six coordinate compound were also investigated to confirm octahedral as the geometry.

Table IV-4 SHAPE values for compounds **1-4**. Geometry abbreviations are as follows: HP, Hexagon; PPY, Pentagonal bipyramid; OC, octahedral; TPR, trigonal prism; JPPY Johnson pentagonal pyramid.

	HP	PPY	OC	TPR	JPPY
1	32.24	28.75	0.091	15.54	32.06
2	32.46	28.82	0.084	15.76	32.06
3	32.36	29.00	0.045	15.83	32.45
4	31.41	28.69	0.061	15.87	32.15

The distance between the divalent metal centers in each molecule was measured to observe how effective the inorganic blocking ligand was at separating the paramagnetic metal centers from each other. These values are listed in Table IV-5 and range from compound **1** with the closest distance of 10.641 Å to compound **3** with the longest distance of 10.754 Å. These distances are longer than the typical distance of 8 Å at which dipolar interaction should be suppressed.[65]

Table IV-5 M…M distances (Å) for the divalent metal centers in compounds **1-4**.

	1	**2**	**3**	**4**
M…M Distance	10.641	10.734	10.754	10.692

IV.3.2 DC Magnetic Studies

Static DC magnetic studies were performed on compounds **1-4** from 300 – 2 K under fields of 0 – 7 T. The χT data for complexes **1-4** from 300 – 2 K can be found in Figure IV.7. Compound **1** exhibits Curie paramagnetic behavior with χT ranging from 4.36 emu K mol^{-1} at 300 K to 4.03 emu K mol^{-1} at 2K. This is very close to the expected χT value of 4.375 emu K mol^{-1} for an S=5/2 system with g=2. Compound **2** shows a linear decrease of χT from 4.37 emu K mol^{-1} at 300 K to approximately 3.17 emu K mol^{-1} at 20 K, with a steeper decrease occurring down to 2.56 emu K mol^{-1} at 2 K. Compound **3** exhibits a χT of 3.00 emu K mol^{-1} at 300 K with only a slight decrease down to 2.85 emu K mol^{-1} at 140 K, and then a steeper decrease in χT down to 1.96 emu K mol^{-1} at 2 K. Compound **4** behaves like a Curie paramagnet with a χT of 1.16 emu K mol^{-1} from 300 K to approximately 15 K, which is expected for a S=1 system with g=1.14. After 15 K, a

sharp decrease occurs down to a χT of 0.87 emu K mol^{-1} at 2 K which can be attributed to zero-field splitting and spin-orbit coupling.

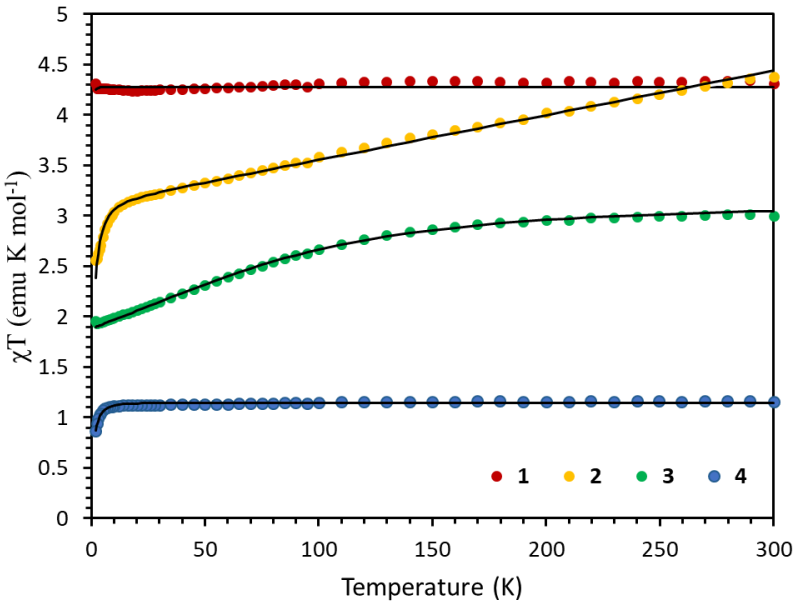

Figure IV.7 χT vs T plots for complexes **1-4**, as labelled. Black lines are fits to the data using the program PHI.

The isotropic nature of complex **1** is supported by the M versus H plot at 1.8 K which saturates by 7 T. The expected saturation point is 5 μ_B, and the experimentally observed saturation point of 4 μ_B is just below that, Figure IV.8. The anisotropic nature of complexes **2-4** is also supported by the M versus H plots at 1.8 K that do not saturate even up to 7 T. The expected saturation point for compound **2** is 4 μ_B. The graph does not saturate and reaches a maximum of 3.12 μ_B at 7 T, Figure IV.9.

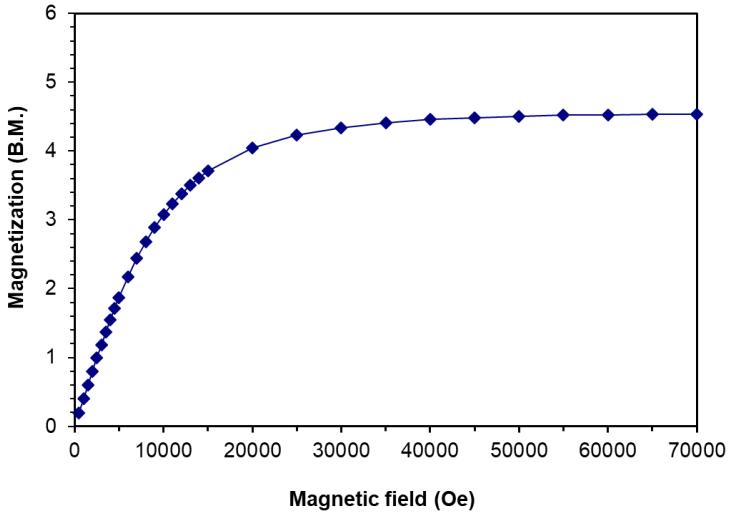

Figure IV.8 Magnetization vs field for compound **1**. Solid line is a guide for the eye.

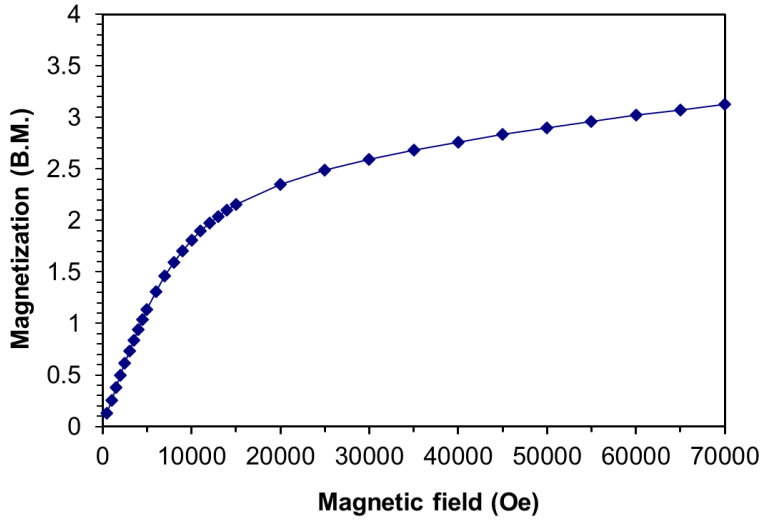

Figure IV.9 Magnetization vs field for compound **2**. Solid line is a guide for the eye.

The expected saturation point for compound **3** is 3 μ_B. The graph does not saturate and reaches a maximum of 2.17 μ_B at 7 T, Figure IV.10. The expected saturation point for compound **4** is 2 μ_B. The graph does not saturate and reaches a maximum of 1.94 μ_B at 7 T, Figure IV.11.

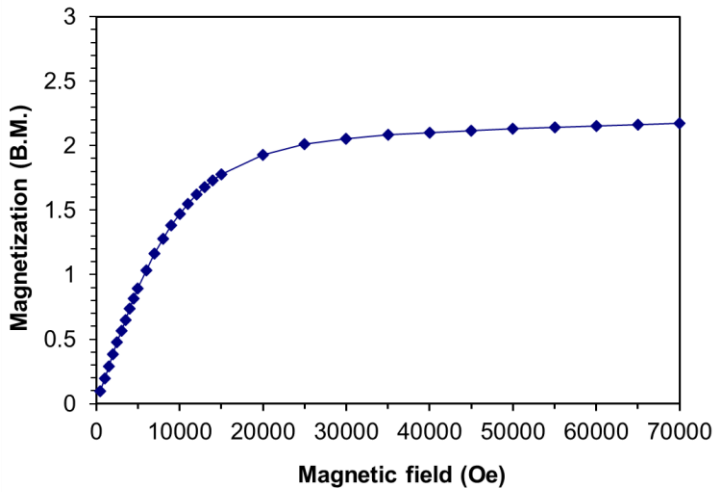

Figure IV.10 Magnetization vs field for compound **3**. Solid line is a guide for the eye.

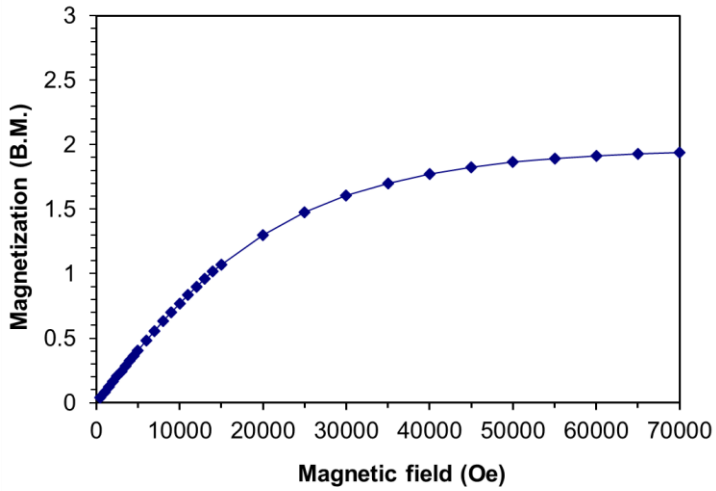

Figure IV.11 Magnetization vs field for compound **4**. Solid line is a guide for the eye.

In order to determine experimental g_{iso}, *D*, and *E* values, χT and reduced magnetization plots were simultaneously fit using PHI.[81] The fits to the susceptibility plots can be found in Figure IV.7. The reduced magnetization data for compound **1** show a superposition of the isofield lines as expected for the isotropic Mn(II) system. The data were fit with g, D, and E values equal to 1.98, -0.04 cm^{-1}, and 0.0002 cm^{-1}, respectively, Figure IV.12. The reduced magnetization data for compound **2** show a lack of superposition in the isofield lines, indicative of anisotropy. The data were fit with g, D, and E values equal to 2.04, 2.49 cm^{-1}, and 0.59 cm^{-1}, respectively, Figure IV.13.

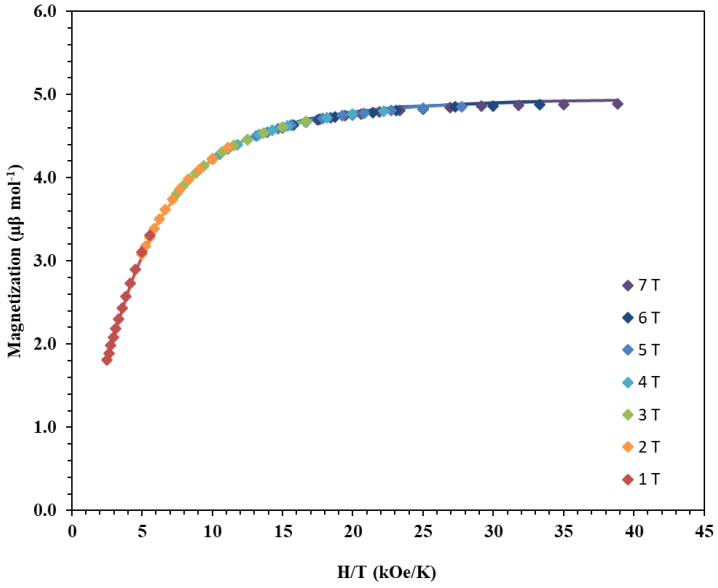

Figure IV.12 Reduced magnetization for **1**. Solid lines are fits to the experimental data using the PHI program.

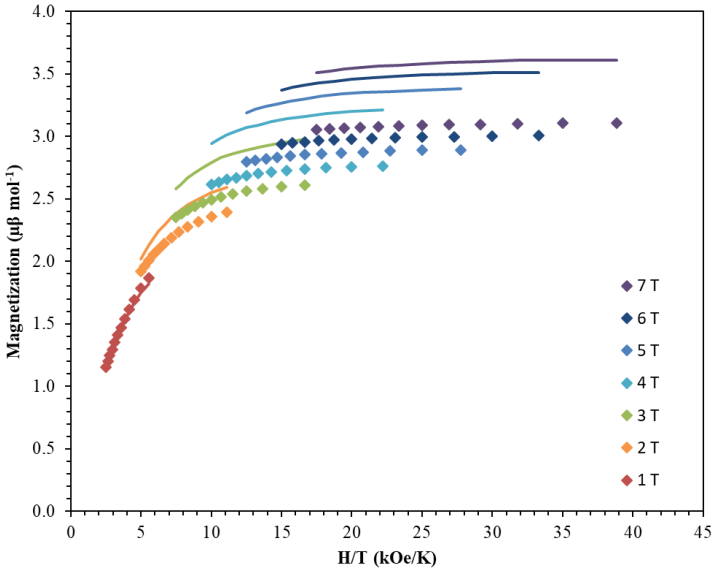

Figure IV.13 Reduced magnetization for **2**. Solid lines are fits to the experimental data using the PHI program.

The reduced magnetization data for compound **3** show a lack of superposition of the isofield lines, indicative of anisotropy. The data were fit with g, D, and E values equal to 2.58, 85.1 cm^{-1}, and 27.95 cm^{-1}, respectively, Figure IV.14. The reduced magnetization data for compound **4** show a lack of superposition in the isofield lines, indicative of anisotropy. The data were fit with g, D, and E values equal to 2.14, -5.1 cm^{-1}, and 0.080 cm^{-1}, respectively, Figure IV.15.

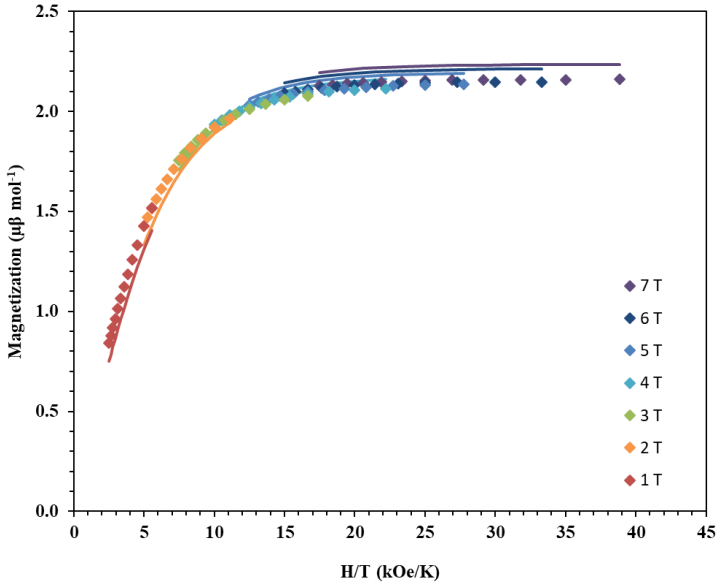

Figure IV.14 Reduced magnetization for **3**. Solid lines are fits to the experimental data using the PHI program.

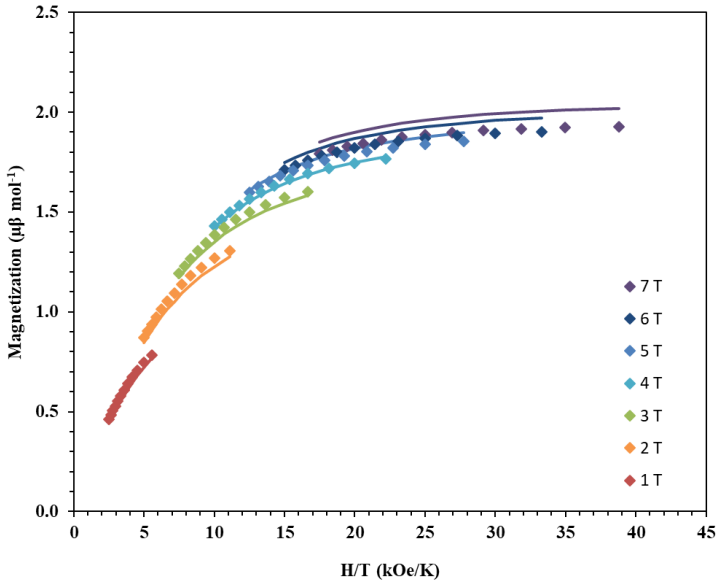

Figure IV.15 Reduced magnetization for **4**. Solid lines are fits to the experimental data using the PHI program.

If one compares these results to the predictions in the paper of Ruiz *et al.*[40], they are largely in good agreement. Compound **1** is very nearly isotropic as expected for a high spin, S=5/2 system. Slight distortions in the octahedral geometry resulted in a D value just below 0. A d^6 compound is predicted to have a large positive or negative D value, but the experimental value for **2** is small and positive. A d^7 compound is predicted to have a large positive or negative D value. The experimental results for **3** agree, with a large, positive D value based on the data fits. A d^8 compound is predicted to have a small positive or negative D value. The experimental results for **4** are in agreement, with a small, negative D value observed from the data fits.

Ab initio CASSCF calculations were carried out essentially to probe the origin and sign of the observed D values of metal ions in **1**-**4**. Computed g_x, g_y and g_z values, along with the transition energies of the first four excited states and their contributions to the *D* value for **1** – **4** are tabulated in Table IV-6. Though the Mn^{II} ion in **1** is isotropic in nature, calculations were performed to obtain the orbital splitting diagram of the ion. Calculations yielded a very small *D* value with a g value of 2.0, both of which support the isotropic nature for an octahedral Mn^{II} ion. The crystal field splitting for **1** can be found in Figure IV.16.

Table IV-6 CASSCF computed g_x, g_y and g_z values, transition energies (cm^{-1}) and contributions to *D* value from the first four excited states for **1 – 4**.

Complex	g_x, g_y, g_z	Excited state	Energy	*D* Contribution
1	2.00, 2.00, 2.00	First	23286.0	-0.31
		Second	23373.1	-0.3
		Third	23750.8	0.56
		Fourth	25993.2	0.0
2	2.09, 2.13, 2.14	First	6809.6	3.7
		Second	6981.3	2.2
		Third	7607.8	-4.1
		Fourth	9886.6	0.002
3	1.21, 1.75, 3.17	First	20.4	68.1
		Second	698.7	34.1
		Third	6222.6	0.9
		Fourth	6404.9	6.9
4	2.31, 2.32, 2.33	First	1289.4	-61.1
		Second	1372.3	29.8
		Third	7068.1	29.5
		Fourth	11858.0	0.01

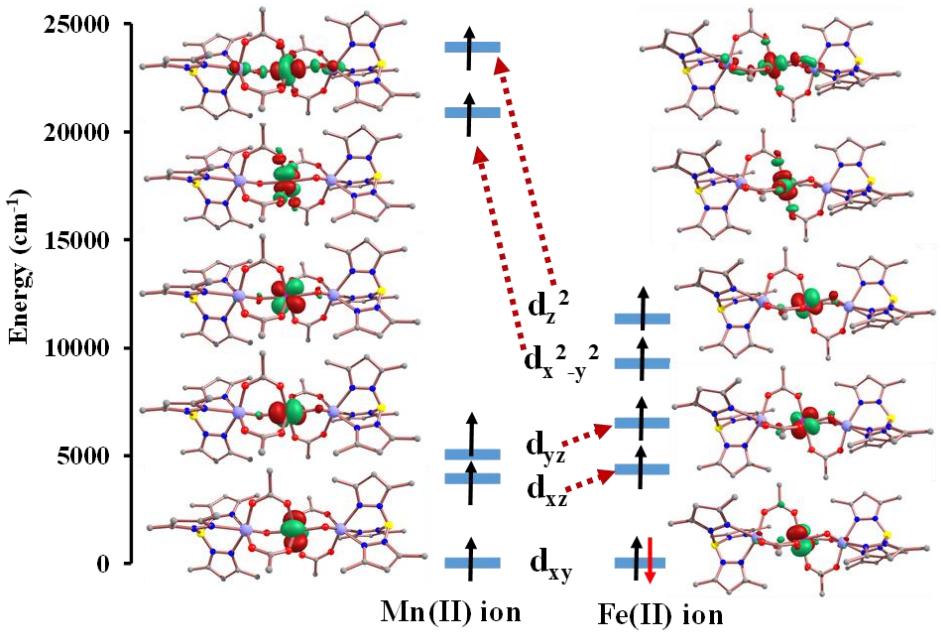

Figure IV.16 CASSCF computed crystal field splitting for **1** (left) and **2** (right). Red arrows indicate the labels for each orbital. Spin-up (black) and spin-down (red) arrows represent α and β electrons.

The CASSCF computed crystal splitting of the d orbitals for the Fe^{II} ion in **2** is shown in Figure IV.16. The results signify that the first transition of a β electron occurs between orbitals with different $|\pm m_l|$ levels, d_{xy} and d_{xz}, which leads to a positive *D* value.[40, 98, 128] This transition requires a relatively large energy (~1300 cm^{-1}), which causes a small positive D value (+3.7 cm^{-1}). The second transition occurs between d_{xy} and d_{yz} orbitals, further increasing the positive D value total. A comparatively large, negative contribution (–4.1 cm^{-1}) from the third transition subsequently reduces the total *D* value to the very small value of 1.03 cm^{-1}.

The d-orbital splitting for the Co^{II} ion in complex **3** and the Ni^{II} ion in complex **4** are shown in Figure IV.17. In **3**, the spin-free, first excitation occurs between the d_{yz} and d_{xz} orbitals, and the second excitation occurs between the d_{yz} and $d_{x^2-y^2}/d_{z^2}$ levels (different $|\pm m_l|$ values). Both excitations cause large, positive contributions to the *D* value (68.1 and 34.1 cm^{-1}). This is due to the very low-lying excited states (~20 and ~700 cm^{-1}). The third and fourth excitations also cause a positive contribution on *D*, resulting an overall large, positive *D* value for complex **3**. For **4**, the CASSCF methods predict that the first spin-free excitation occurs between the d_{xy} and $d_{x^2-y^2}$ orbitals (same $|\pm m_l|$ value), with a small required energy, which leads to a large negative D value.[129] The second excitation also happens with a small required energy, but arises between the d_{xy} and d_{z^2} orbitals (different $|\pm m_l|$ values), which leads to a large, positive D value. This large, positive D value from the second transition tremendously reduces the overall negative D value to -1.74 cm^{-1}.

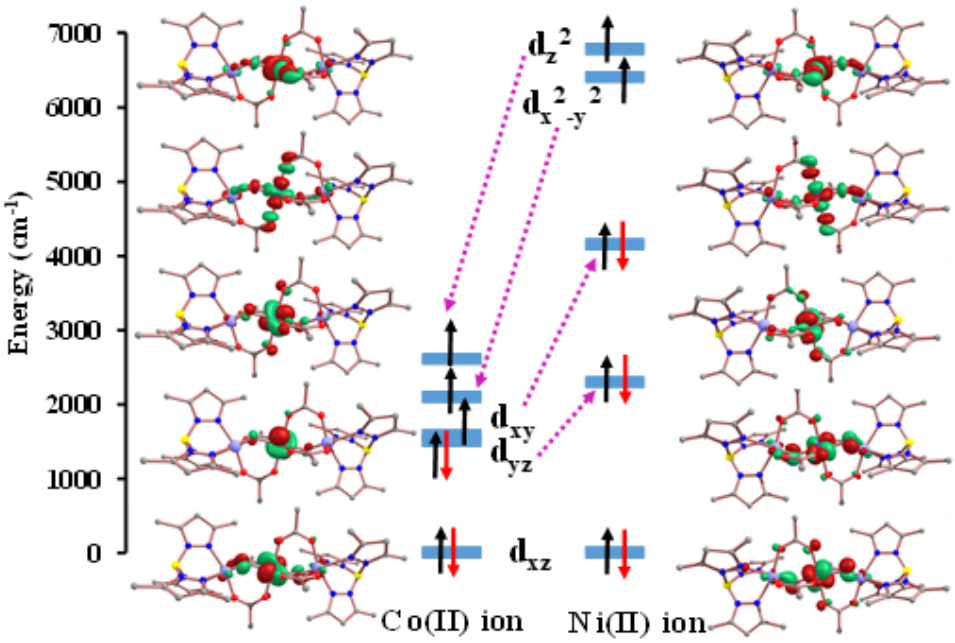

Figure IV.17 CASSCF computed crystal field splitting for **3** (left) and **4** (right). Purple arrows indicate the labels for each orbital. Spin-up (black) and spin-down (red) arrows represent α and β electrons.

These computational results were then compared back to the experimental data that were fit with PHI. The results are summarized in Table IV-7. These CASSCF computed D values of -0.02, 1.03, 123.9 and -1.74 cm^{-1} are in good agreement with the experimental *D* values of -0.04, 2.5, 85.1 and -5.1 cm^{-1} for **1**, **2**, **3** and **4**, respectively.

Table IV-7 Experimentally fitted and CASSCF calculated g, D (cm^{-1}), and E (cm^{-1}) values for complexes **1-4**.

		1	**2**	**3**	**4**
EXP	g	1.98	2.04	2.58	2.14
	D	-0.04	2.49	85.1	-5.1
	E	0.0002	0.59	27.95	0.080
CASSCF	g	2	2.12	2.04	2.32
	D	-0.02	1.1	123.9	-1.75
	E	0.002	0.154	33.45	0.0875

IV.3.3 AC Magnetic Studies

Compounds **2-4** were also measured under an AC field to probe the dynamic magnetic properties using DC fields from 0 Oe to 3500 Oe. Compound **2** exhibits only the beginning of an out-of-phase signal under applied DC fields up to 2000 Oe, Figure IV.18. Compound **4** did not exhibit any signal up to 2000 Oe DC fields, Figure IV.19.

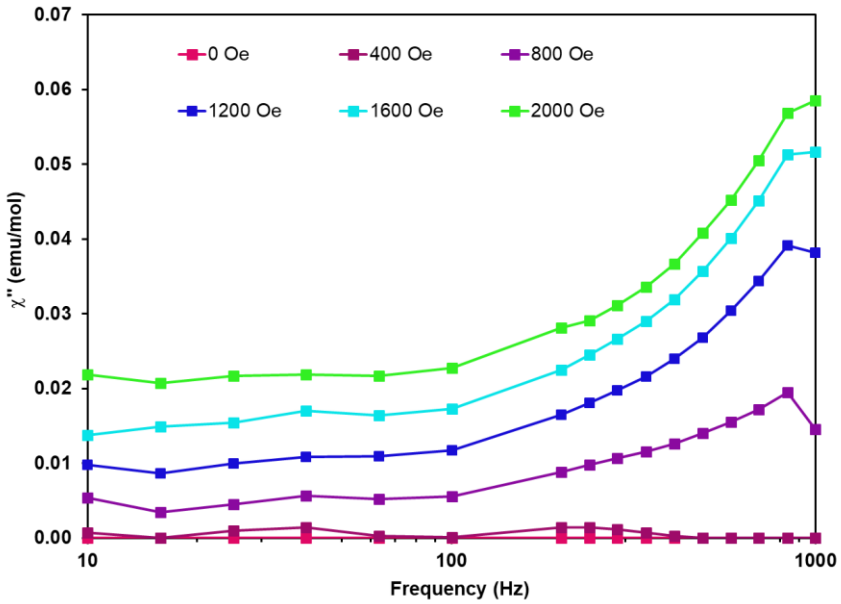

Figure IV.18 Out-of-phase susceptibility for compound **2** under applied DC fields from 0 Oe to 2000 Oe, as labelled.

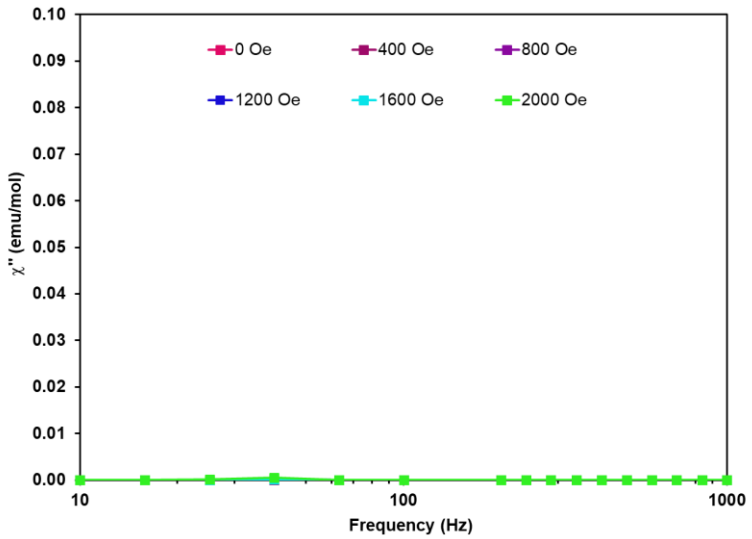

Figure IV.19 Out-of-phase susceptibility for compound **4** under applied DC fields from 0 Oe to 2000 Oe, as labelled.

Compound **3** exhibits slow magnetic relaxation under applied DC fields. This compound was measured at 1.8, 2.5, and 4 K under DC fields from 0 – 10,000 Oe to identify the fields at which to collect data, as shown in Figure IV.20, Figure IV.21, and Figure IV.22, respectively. Based on these measurements from 0-10,000 Oe, the fields 375, 1000, 2000, and 3500 Oe were selected to observe the field dependent relaxations which appeared to be present.

The Cole-Cole plots for each compound at a particular field were subsequently fit using CC-fit.[83] The resulting Arrhenius plot was fit according to the equation:

$$\tau^{-1} = \tau_{QTM}^{-1} + AT + CT^{n} + \tau_{0}^{-1} exp\left(-\frac{U_{eff}}{k_B T}\right)$$

In order to avoid over parameterization, A was assumed to be equal to 0.

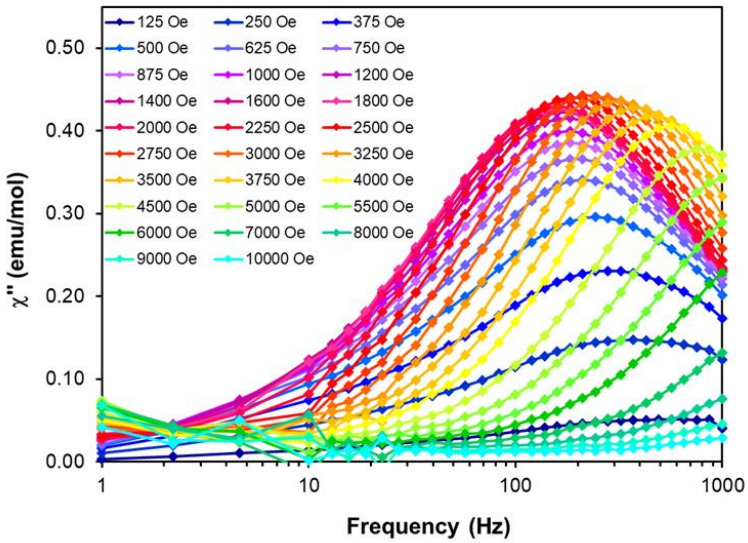

Figure IV.20 Out-of-phase susceptibility for **3** at 1.8 K under DC fields ranging from 125 Oe to 10000 Oe. Solid lines are guides for the eye.

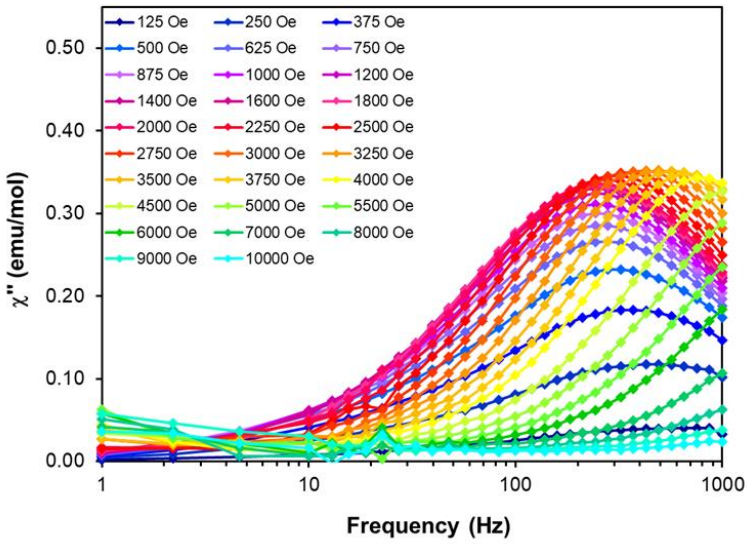

Figure IV.21 Out-of-phase susceptibility for **3** at 2.5 K under DC fields ranging from 125 Oe to 10000 Oe. Solid lines are guides for the eye.

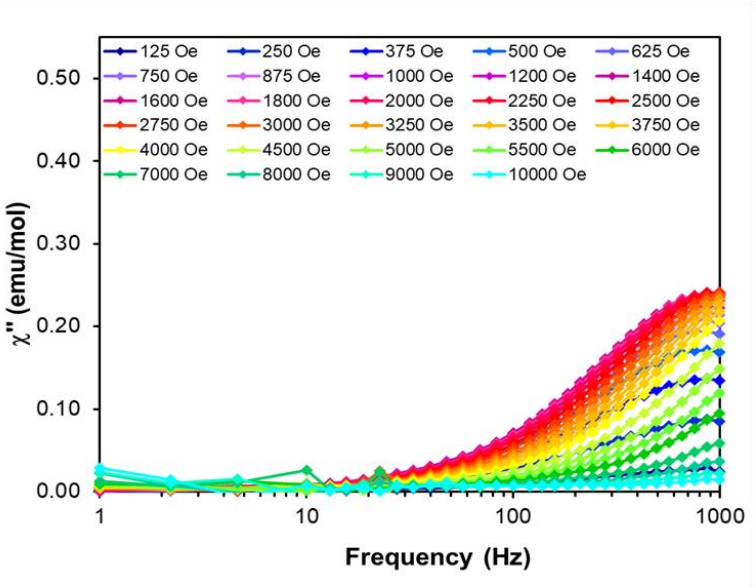

Figure IV.22 Out-of-phase susceptibility for **3** at 4 K under DC fields ranging from 125 Oe to 10000 Oe. Solid lines are guides for the eye.

Under a DC field of 375 Oe, quantum tunneling dominates as the major form of relaxation. A maximum peak around 322 Hz decreases in amplitude, indicative of quantum tunneling, until about 3.4 K, and then a temperature dependent shift in frequency is observed. The in-phase and out-of-phase plots can be found in Figure IV.23.

a)

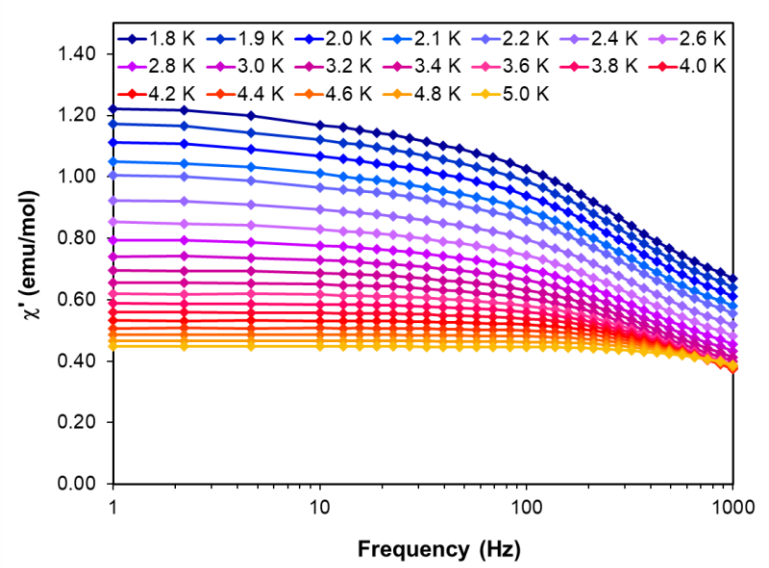

b)

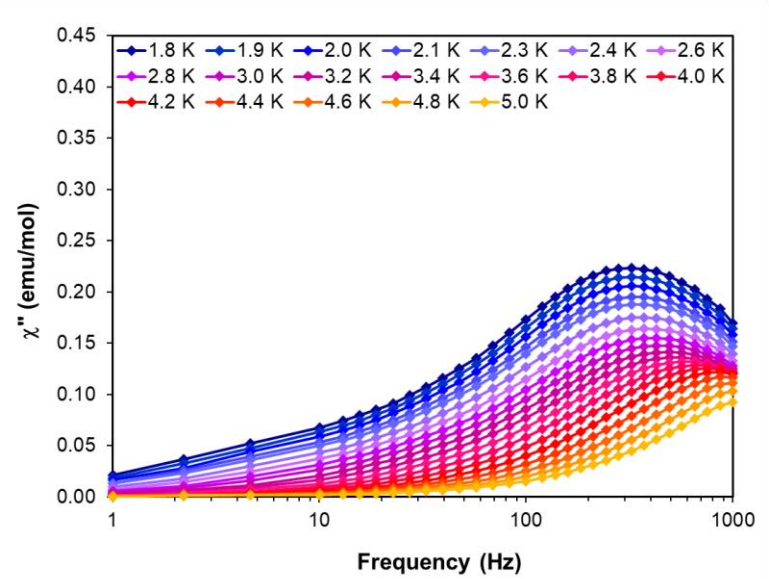

Figure IV.23 a) In-phase susceptibility (χ') vs Frequency and b) out-of-phase susceptibility (χ") for **3** under an applied DC field of 375 Oe. Solid lines are guides for the eye.

The in phase and out of phase susceptibility plots were subsequently converted into Cole-Cole plots. These were subsequently fit using CC-fit[83] which led to a maximum

α value of 0.30, indicating a relatively wide range of relaxations times. The fit of all temperatures in the Arrhenius plot, Figure IV.24, resulted in a barrier of U_{eff}/k_b = 6.7 K and τ_o = 1.3 x 10^{-4} s. Extracted Raman parameters of C = 0.026 s^{-1} and n = 7.9 are in agreement with the expected range for a Kramers ion.[84] The τ^{-1} value for quantum tunneling was fit to 0.0005 s.

a)

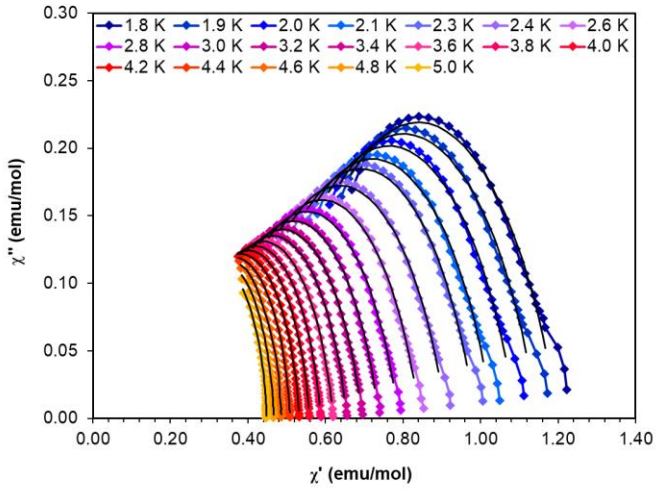

b)

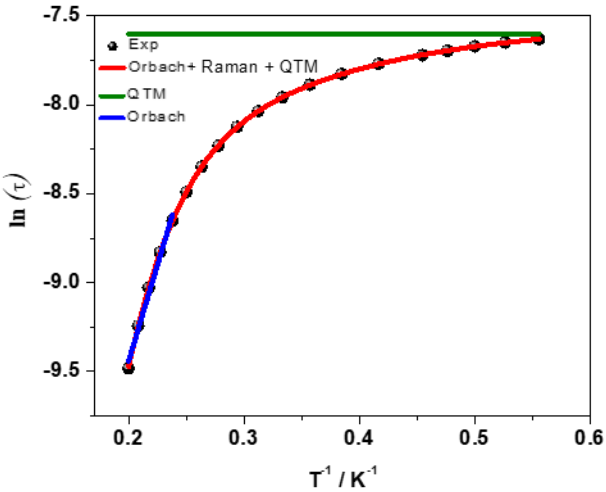

Figure IV.24 a) Cole-Cole plot fit via CC-fit, black lines are fits to the data b) ln(τ) vs 1/T, black dots are experimental data and colored lines are fits as labelled.

Under a DC field of 1000 Oe, quantum tunneling dominates as the major form of relaxation. A maximum peak around 159 Hz decreases in amplitude, indicative of quantum tunneling, until about 3.0 K, after which a temperature dependent shift in frequency is observed. The in-phase and out-of-phase plots can be found in Figure IV.25.

a)

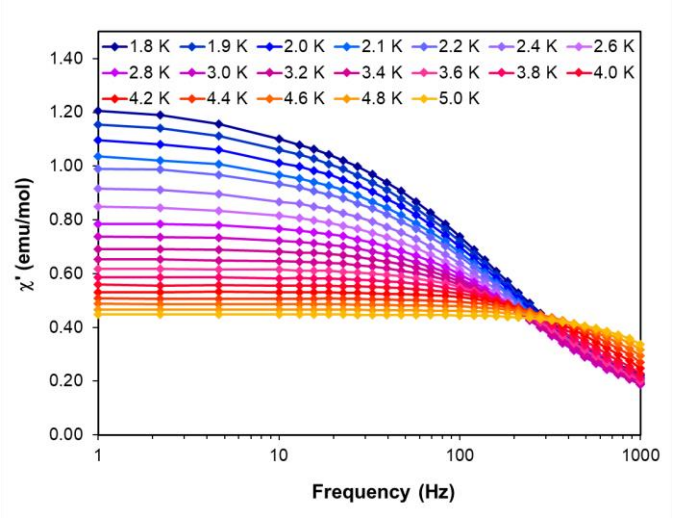

b)

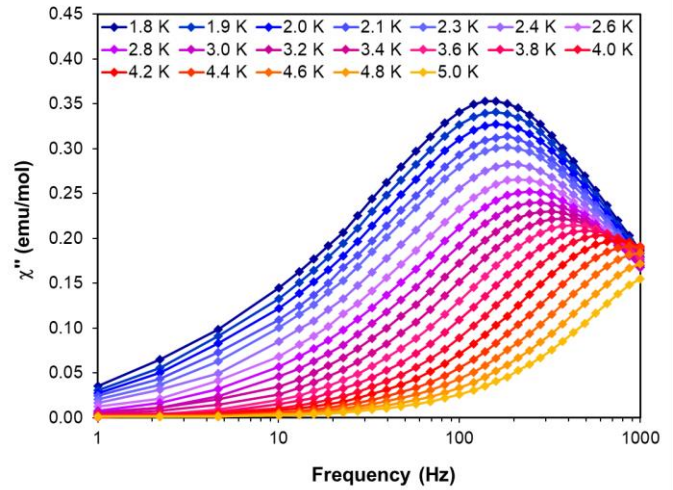

Figure IV.25 a) In-phase susceptibility (χ') vs Frequency and b) out-of-phase susceptibility (χ") for **3** under an applied DC field of 1000 Oe. Solid lines are guides for the eye.

The resulting Cole-Cole plot was fit using CC-fit[83] which led to a maximum α value of 0.30, indicating a relatively wide range of relaxations times. The fit of all temperatures in the Arrhenius plot, Figure IV.26, resulted in a barrier of U_{eff}/k_b = 10.0 K and τ_o = 4.5 x 10^{-5} s. Raman parameters of C = 0.042 s^{-1} and n = 7.4 are in agreement with the expected range for a Kramers ion.[84] The τ^{-1} value for quantum tunneling was fit to 0.001 s.

a)

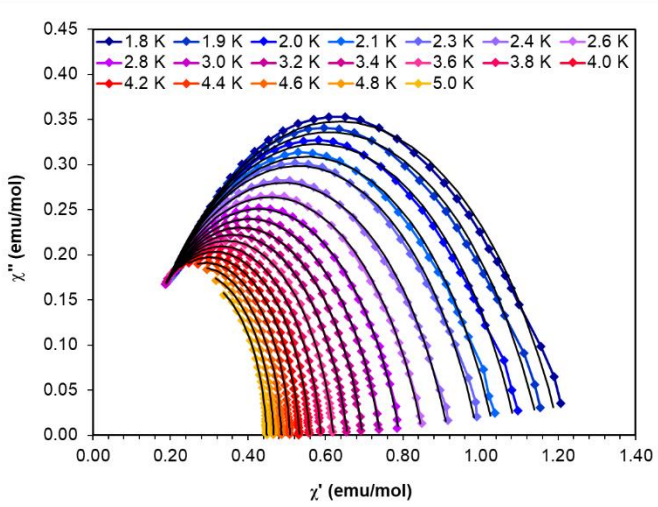

b)

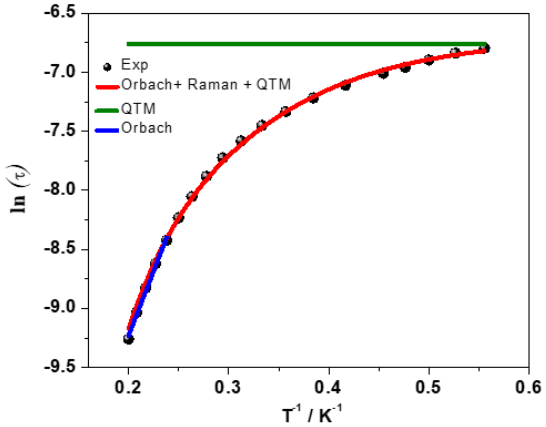

Figure IV.26 a) Cole-Cole plot fit via CC-fit, black lines are fits to the data b) ln(τ) vs 1/T, black dots are experimental data and colored lines are fits as labelled.

Under a DC field of 2000 Oe, quantum tunneling dominates as the major form of relaxation. A maximum peak around 159 Hz exhibits a temperature dependent shift in frequency which increases as the temperature increases. The in-phase and out-of-phase plots can be found in Figure IV.27.

a)

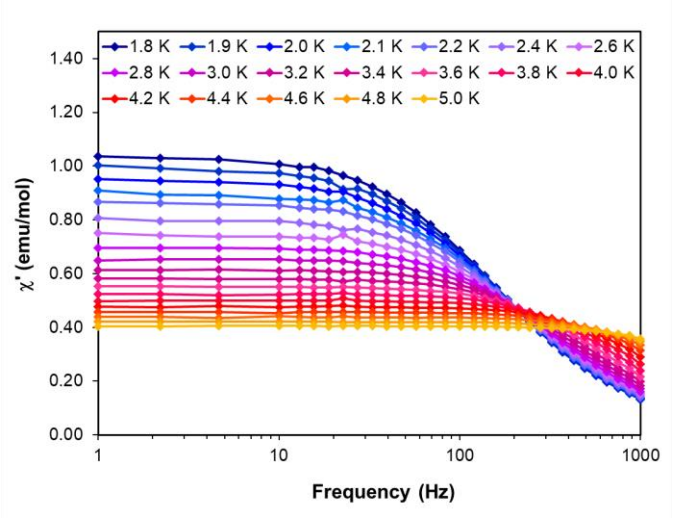

b)

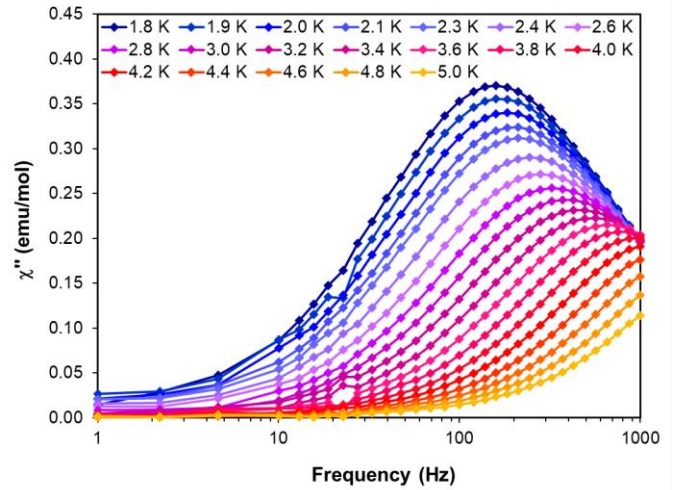

Figure IV.27 a) In-phase susceptibility (χ') vs Frequency and b) out-of-phase susceptibility (χ") for **3** under an applied DC field of 2000 Oe. Solid lines are guides for the eye.

The resulting Cole-Cole plot was fit using CC-fit[83] which led to a maximum α value of 0.20, indicating a moderate range of relaxations times. The fit of all temperatures in the Arrhenius plot, Figure IV.28, resulted in a barrier of U_{eff}/k_b = 14.4 K and τ_o = 1.7 x 10^{-5} s. Raman parameters of C = 0.045 s^{-1} and n = 9 are in agreement with the expected range for a Kramers ion.[84] The τ^{-1} value for quantum tunneling was fit to 0.001 s.

a)

b)

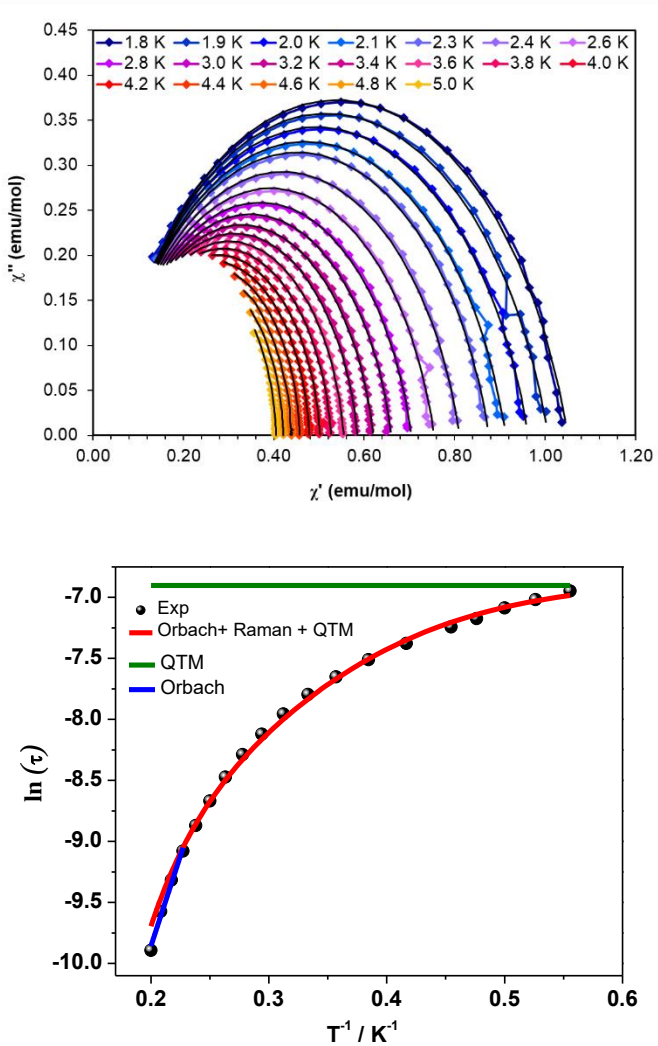

Figure IV.28 a) Cole-Cole plot fit via CC-fit, black lines are fits to the data b) ln(τ) vs 1/T, black dots are experimental data and colored lines are fits as labelled.

Under a DC field of 3500 Oe, a thermal relaxation appears to be the major form of relaxation. A maximum peak around 211 Hz decreases in amplitude and exhibits a temperature dependent shift in frequency over all measured temperatures. The in-phase and out-of-phase plots can be found in Figure IV.29.

a)

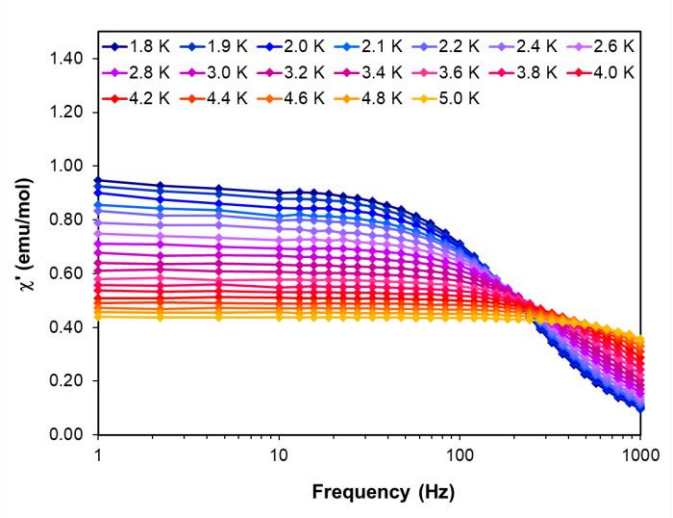

b)

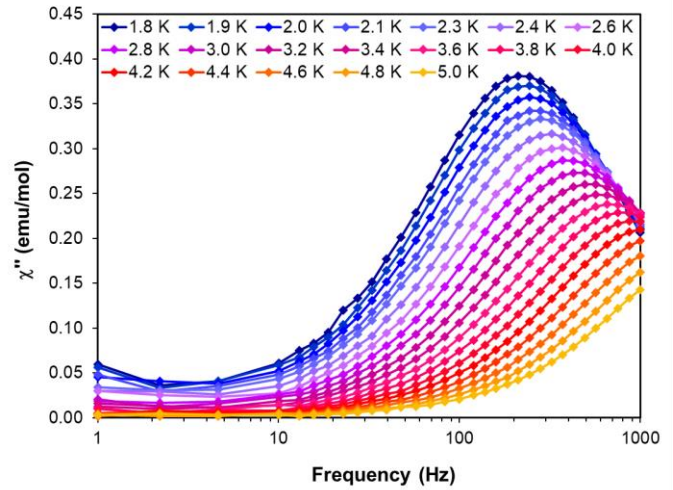

Figure IV.29 a) In-phase susceptibility (χ') vs Frequency and b) out-of-phase susceptibility (χ") for **3** under an applied DC field of 3500 Oe. Solid lines are guides for the eye.

The resulting Cole-Cole plot was fit using CC-fit[83] which led to a maximum α value of 0.12, indicating a narrow range of relaxations times. The fit of all temperatures in the Arrhenius plot, Figure IV.30, resulted in a barrier of U_{eff}/k_b = 6.8 K and τ_o = 6.2 x 10^{-5} s. Raman parameters of C = 0.033 s^{-1} and n = 7.8 are in agreement with the expected range for a Kramers ion.[84] The τ^{-1} value for quantum tunneling was fit to 0.001 s.

a)

b)

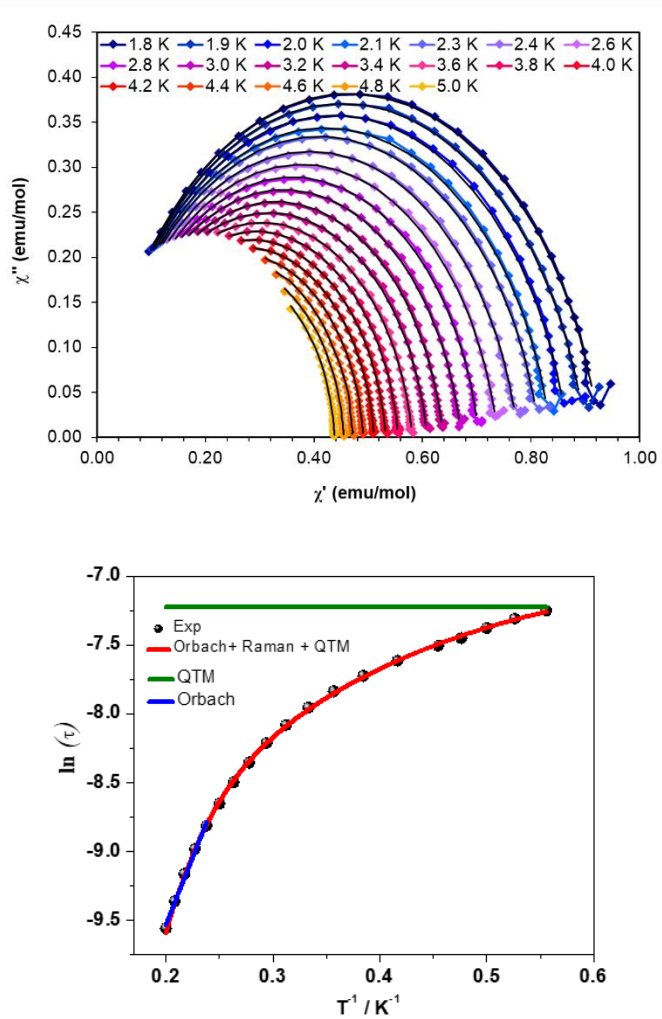

Figure IV.30 a) Cole-Cole plot fit via CC-fit, black lines are fits to the data b) ln(τ) vs 1/T, black dots are experimental data and colored lines are fits as labelled.

The barrier of complex **3** is lower across all applied DC fields than expected given the 2|D| energy gap between the m_S = 1/2 and m_S = 3/2 microstates, which would give U=2|D|=170.2 cm^{-1}. For the sake of comparison, a summary of the relaxation values for **3** at each field can be found in Table IV-8. The U_{eff} barrier increases with increasing field for the first three fields studied. At 3500 Oe, the barrier decreases back down nearly to the same value as 375 Oe. The α values decrease as the field increases, which is expected when stronger fields are applied. This supports the suppression of quantum tunneling due to applied field, which can be seen in the out-of-phase plots, where temperature dependent shifts change from less than half the data at 375 Oe to describing the full set of data at 3500 Oe. Raman relaxation is prominent at all four fields.

Table IV-8 Values for Orbach, Raman, and quantum tunneling relaxations for compound **3** under the applied fields indicated.

	U_{eff}/k_b (K)	τ_o (s)	τ^{-1}_{QTM} (s)	C (s^{-1} K^{-n})	n
3 – 375 Oe	6.7	1.3 x 10^{-4}	0.0005	0.026	7.9
3 – 1000 Oe	10.0	4.5 x 10^{-5}	0.001	0.042	7.4
3 – 2000 Oe	14.4	1.7 x 10^{-5}	0.001	0.045	9
3 – 3500 Oe	6.8	6.2 x 10^{-5}	0.001	0.033	7.8

IV.3.4 Structural, Magnetic, and Computational Correlations

Detailed crystallographic, computational, and magnetic studies were undertaken in order to understand the magnetism of complexes employing the new Ti(IV) inorganic blocking ligand. As the Co(II) complex was the only one to exhibit slow magnetic

relaxation, computations were performed to explore the reason behind this observed behavior.

All four of the compounds crystallize in the same space group. Each one exhibits octahedral geometry which is axially compressed. As expected, this results in splitting of the e_g orbitals, with d_{z^2} highest in energy for all four complexes, followed by the $d_{x^2-y^2}$ orbital. The differences in the remaining complexes comes from the splitting of the t_{2g} orbitals. In compounds **1** and **2**, the d_{xz} and d_{yz} orbitals are higher in energy than the d_{xy} orbital. However, in the case of compounds **3** and **4**, the d_{xy} orbital is higher in energy than the d_{xz} and d_{yz} orbitals. As previously stated, the resulting D values are generally consistent with predictions.

The observed results in for the experimentally and computationally derived D values can also be correlated with SHAPE values. Compound **3** is the least distorted, and is also the only one to exhibit slow magnetic relaxation. Compound **1** is the most distorted, which explains the deviation away from a purely isotropic system that was observed. Compound **2** is the second most distorted. This relatively large distortion partially explains why a smaller D value was observed than expected. This is supported by the computational results which show high energy excitations, resulting in small D values. The mix of positive and negative D values from the first four excitations further reduces that D value. Compound **4** is the second least distorted, and the experimentally and computationally derived D values are close to what is predicted.

The positive D value of **3** is consistent with the majority of large coordination number Co(II) SMMs that have been reported, which also exhibit easy plane anisotropy. To date, only two isostructural, octahedral compounds have been reported that exhibit negative D values.[130] There are no reported octahedral Fe(II) SMMs which have been reported, to the best of our knowledge. Compound **2** is consistent with these results. There is one reported octahedral, Ni(II) SMM which has a small D value of -13 cm^{-1}.[131] This compound is one of only two reported Ni(II) SMMs. Though this compound also exhibits an axially compressed octahedron about the metal center, the sign of D is opposite of that for **4**. Predictions have been made about Ni(II) ions, in which axial compression should result in negative D values, whereas equatorial compression should result in positive D values.[132] At first, compound **4** appears to contradict these predictions. However, upon computational exploration of the first four excited states, it can be seen that the first excitation indeed results in a large, negative D value. The second and third excitations contribute large, and positive D values, resulting in an overall small, positive D value. This highlights the importance of the effects of higher order excitations on the overall D value of a given complex.

As Ti(IV) is proposed as a new blocking ligand, it is prudent to compare these results to those of other SMMs employing the use of inorganic blocking ligands. Octahedral Co(III) is the only other 3d metal which has been employed as an inorganic blocking ligand.[17, 23] Three complexes have been reported employing octahedral, low spin Co(III) as a diamagnetic blocking ligand.[123, 130] Each exhibits

a large, negative D value. Two of these complexes are octahedral, and the third is trigonal prismatic. The closest intermolecular cobalt distances for these complexes are 7.635, 8.355, and 12.661 Å. The same distance in **3** of 10.754 falls short of one of these examples, but is longer than the other two. This presents Ti(IV) with Tp* as a viable choice for diamagnetic dilutions.

Ti(IV) as a diamagnetic blocking ligand has distinct advantages over the current options of Co(III) as an inorganic blocking ligand and Zn(II) complexes as dilution agents. It can be difficult to isolate isostructural Zn(II) complexes, which can limit its ability in dilutions. It can also be difficult to be exact when performing dilutions with a small amount of paramagnetic material. When a diamagnetic blocking ligand is employed, the uncertainty in the structure and measurements is reduced. In terms of Co(III) as an inorganic blocking ligand, it is only viable in the low-spin state with a triply degenerate ground state. This severely limits the potential ligands and coordination environments which can be pursued. Ti(IV) will remain diamagnetic no matter the geometry as it is d^0. This greatly increases the versatility of coordination with the Ti(IV) ion, as well as coordination of the ion to the relevant paramagnetic metal center. This is quite advantageous given the strong correlation between geometry and magnetic behavior for SMMs. Although the SMM behavior observed in **3** is not extraordinary, it does exemplify the opportunities which lie in this new type of ligand in the magnetic community.

IV.4 Conclusions

In this chapter, the results of the syntheses and characterization of four new complexes presented Ti(IV) as a new inorganic blocking ligand for SMMs. One compound was found to exhibit slow magnetic relaxation under an applied field. The Tp^*Ti^{IV} blocking ligand was found to be effective at separating the paramagnetic ions from one another, with intermolecular distances consistently greater than 10 Å.

Although the magnetic data are not record bearing, these complexes serve as a solid proof of principle for the use of Ti(IV) as an inorganic blocking ligand. In the future, directed focus on different ligands to alter the geometry about the paramagnetic centers would be promising to pursue. Given the d^0 electron count of Ti(IV), it will be particularly versatile in this venture.

CHAPTER V

SLOW MAGNETIC DYNAMICS IN A FAMILY OF MONONUCLEAR LANTHANIDE COMPLEXES EXHIBITING THE RARE CUBIC COORDINATION GEOMETRY*

V.1 Introduction

Bistable molecular species that retain their magnetization below a characteristic blocking temperature in the absence of a magnetic field and exhibit magnetic hysteresis loops reminiscent of the diagnostic property of classical magnets are classified as Single Molecule Magnets (SMMs).[133-134] Slow magnetic relaxation of SMMs originates from an appreciable ground state spin value combined with significant uniaxial magnetic anisotropy ($-D_z$) which can lead to large energy barriers (U_{eff}) to the reversal of magnetization and high blocking temperatures (T_B).[134] Experimental detection of the relaxation process is the observation of temperature and frequency dependence of the in-phase (χ') and the out-of-phase (χ'') components of the AC magnetic susceptibility.[133-134]

Lanthanide complexes have proven to be ideal candidates for SMM behavior due to the fact that most of the rare earth ions, especially Dy^{III} and Tb^{III}, possess remarkably large single-ion anisotropies as compared to other paramagnetic ions of the periodic table.[49, 135-137] A variety of polynuclear and mononuclear 4*f* metal SMMs have been

* Parts of this chapter reproduced with permission from "Slow magnetic dynamics in a family of mononuclear lanthanide complexes exhibiting the rare cubic coordination geometry" Alexandropoulos, D. I.; Schulte, K. A.; Vignesh, K. R.; Dunbar, K. R. *Chem. Commun.* **2018**, *54* (72), 10136-10139. Reproduced by permission of the Royal Society of Chemistry.

reported[49, 135-137] since the first example in 2003[45, 138-139]. Recently, a highly successful trend in this area of research has been to maximize the axial magnetic anisotropy of individual metal ions by choosing appropriate ligands to affect the strength and the symmetry of the crystal field in low-coordinate systems or highly symmetric coordination environments.[140-141] The former strategy has produced remarkable results, particularly in the case of the highly sterically congested compound $[(Cp^{ttt})_2Dy][B(C_6F_5)_4]$ (Cp^{ttt}=1,2,4-tri(*tert*-butyl) cyclopentadienide), which exhibits magnetic hysteresis up to 60 K.[54, 142]

Lanthanide ions, however, usually prefer much higher coordination numbers than the aforementioned case, including 8-coordinate species. The most common geometries for 8-coordinate Ln complexes are bicapped trigonal prismatic (C_{2v}), triangular dodecahedral (D_{2d}), and square antiprismatic (D_{4d}) architectures. The latter symmetry is ubiquitous in the field of rare earth SMMs, with an impressive number of bis(phthalocyanine) complexes displaying some of the highest reported energy barriers to date.[45, 138-139] Although the square antiprismatic geometry is the most prevalent coordination geometry for 4*f* metal ions with eight donor ligands, higher symmetries remain very rare and are largely unexplored vis-à-vis their magnetic properties. In higher symmetries the crystal field parameters responsible for the transverse anisotropy can be minimized and thus the SMM properties can be improved.

To this end, the high-yield syntheses, structures, and magnetic properties of a new family of isostructural mononuclear complexes $[Co^{III}(Tp)_2]_{1.3}[M(NO_3)_2(dbm)_2](NO_3)_{0.3}$ (M = Tb (**1**), Dy (**2**), Er (**3**), and Y (**4**)) were studied. The ligands are the oxygen donor ligands 1,3-diphenyl-1,3-propanedionate (dbm) and nitrate.

V.2 Experimental Methods

V.2.1 Complex Synthesis

All syntheses were performed under ambient conditions. $Co(dbm)_2$[143] and KTp[144] were synthesized according to published procedures. All other chemicals were commercially available and used as received.

Synthesis of $[Co^{III}(Tp)_2]_{1.3}[Tb(NO_3)_2(dbm)_2](NO_3)_{0.3}$ (1). To a colorless solution of KTp (12.6 mg, 0.05 mmol) in MeCN (7.5 mL) was added solid $Co(dbm)_2$ (25.2 mg, 0.05 mmol) followed by stirring for 5 min. The reagent $Tb(NO_3)_3{\cdot}5H_2O$ (21.7 mg, 0.05 mmol) was then added and the resulting dark orange solution was stirred for a further 15 min. The solution was subsequently filtered, and left to stand undisturbed for crystallization. Slow evaporation of the solvent gave diffraction quality crystals of **1** after 1 week which were collected by filtration, washed with hexanes (3 x 5 mL), and dried in air. Yield is 65% (45.69 mg). Anal. Calc. for $C_{54}H_{48.67}N_{18.33}B_{2.67}O_{11}Co_{1.33}Tb$ **(1)**: C, 46.44; H, 3.51; N, 18.38 %. Found: C, 46.55; H, 3.57; N, 18.28 %. Selected ATR data (Nujol mull, cm^{-1}): 1589 (w), 1541 (w), 1516 (w), 1305 (s), 1221 (m), 1117 (m), 1073 (m), 1053 (m), 800 (w), 771 (m), 721 (s), 681 (m), 617 (w), 511 (w).

Synthesis of $[Co^{III}(Tp)_2]_{1.3}[Dy(NO_3)_2(dbm)_2](NO_3)_{0.3}$ (2). This complex was prepared in the same manner as complex **1** but using $Dy(NO_3)_3{\cdot}6H_2O$ (22.8 mg, 0.05 mmol) in place of $Tb(NO_3)_3{\cdot}5H_2O$. After 1 week, diffraction quality crystals of **2** had appeared; these were collected by filtration and washed with Hexanes (3 x 5 mL); the yield is 55% (38.50 mg). Anal. Calc. for $C_{54}H_{48.67}N_{18.33}B_{2.67}O_{11}Co_{1.33}Dy$ **(2)**: C, 46.32; H, 3.50; N, 18.34 %. Found: C, 46.23; H, 3.37; N, 18.21 %. Selected ATR data (Nujol mull, cm^{-1}): 1589 (m), 1542 (m),

1516 (w), 1323 (m), 1220 (m), 1118 (m), 1073 (m), 1053 (m), 772 (m), 745 (s), 721 (s), 682 (m), 619 (w), 509 (w).

Synthesis of $[Co^{III}(Tp)_2]_{1.3}[Er(NO_3)_2(dbm)_2](NO_3)_{0.3}$ (3). This complex was prepared in the same manner as complex **1** but using $Er(NO_3)_3{\cdot}5H_2O$ (22.1 mg, 0.05 mmol) in place of $Tb(NO_3)_3{\cdot}5H_2O$. After 1 week, diffraction quality crystals of **3** had appeared; these were collected by filtration and washed with hexanes (3 x 5 mL); the yield is 60% (42.14 mg). Anal. Calc. for $C_{54}H_{48.67}N_{18.33}B_{2.67}O_{11}Co_{1.33}Er$ **(3)**: C, 46.17; H, 3.49; N, 18.27 %. Found: C, 46.28; H, 3.57; N, 18.19 %. Selected ATR data (Nujol mull, cm^{-1}): 1587 (w), 1540 (w), 1516 (w), 1305 (m), 1221 (m), 1117 (m), 1075 (m), 1053 (m), 774 (m), 742 (m), 722 (m), 681 (w), 620 (w).

Synthesis of $[Co^{III}(Tp)_2]_{1.3}[Y(NO_3)_2(dbm)_2](NO_3)_{0.3}$ (4). This complex was prepared in the same manner as complex **1** but using $Y(NO_3)_3{\cdot}6H_2O$ (21.7 mg, 0.05 mmol) in place of $Tb(NO_3)_3{\cdot}5H_2O$. After 1 week, diffraction quality crystals of **4** had appeared which were collected by filtration and washed with hexanes (3 x 5 mL); the yield is 50% (33.16 mg). Anal. Calc. for $C_{54}H_{48.67}N_{18.33}B_{2.67}O_{11}Co_{1.33}Y$ **(4)**: C, 48.89; H, 3.70; N, 19.35 %. Found: C, 49.01; H, 3.59; N, 19.27 %. Selected ATR data (Nujol mull, cm^{-1}): 1590 (m), 1543 (s), 1516 (m), 1306 (m), 1221 (m), 1117 (m), 1072 (m), 1053 (m), 938 (m), 800 (w), 771 (m), 744 (s), 721 (s), 681 (m), 659 (w), 617 (w), 514 (w).

V.2.2 Crystallography

Structural characterization of the complexes was performed on single crystals at the APS housed in the Argonne National Laboratory. X-ray data were collected using a synchrotron source with a wavelength of 0.41328 Å and a Pilatus 1M (CdTe) pixel array detector. Crystals suitable for diffraction were affixed to glass fibers using Paratone oil. Collection was performed at 100 K under a N_2 cold stream. The frames were integrated using the Apex II software program with a pre-existing mask supplied before collection.[145] A multiscan absorption correction was performed using SADABS within the APEX II software suite. The structures were solved with SHELXT[146] and refined with SHELXL-2014[147] within the OLEX program.[73] Dispersion corrections calculated in PLATON were applied to all structures for each element according to the wavelength of collection.[148] All hydrogen atoms were placed in calculated positions. All non-hydrogen atoms were finished with anisotropic refinement.

The structures for $[Co^{III}(Tp)_2]_{1.3}[Tb(NO_3)_2(dbm)_2](NO_3)_{0.3}$, $[Co^{III}(Tp)_2]_{1.3}[Dy(NO_3)_2(dbm)_2](NO_3)_{0.3}$, $[Co^{III}(Tp)_2]_{1.3}[Er(NO_3)_2(dbm)_2](NO_3)_{0.3}$, and $[Co^{III}(Tp)_2]_{1.3}[Y(NO_3)_2(dbm)_2](NO_3)_{0.3}$ were all refined in the cubic space group *I*23 as an inversion twin with minor components of 0.49, 0.42, 0.45, and 0.47 for the Tb, Dy, Er, and Y complexes respectively. The higher symmetry space group $Im\bar{3}$ was investigated, but the additional mirror plane symmetry does not allow for torsion in the bidentate ligands coordinated to the lanthanide metal centers. In order to obtain a more accurate model of these ligands, the structure was refined as an inversion twin in the lower symmetry space group.

Each of the structures was run through the program SQUEEZE.[101] The electron density accounts for the remaining 1/3 of a nitrate anion needed to charge balance the compound as well as co-crystallizing acetonitrile molecules. Attempts were made to try and model the disorder but were not successful. The electron density, after accounting for the nitrate anion, results in 5.3, 4.3, 5.1, and 4.4 acetonitrile molecules in the Tb, Dy, Er, and Y complexes, respectively.

There is a small amount of disorder in the lanthanide metal centers and directly coordinated atoms. Modeling this disorder did not significantly improve the refinement. The Cambridge Crystallographic Database Centre numbers for each complex are: 1847190 for $[Co^{III}(Tp)_2]_{1.3}[Tb(NO_3)_2(dbm)_2](NO_3)_{0.3}$, 1847187 for $[Co^{III}(Tp)_2]_{1.3}[Dy(NO_3)_2(dbm)_2](NO_3)_{0.3}$, 1847188 for $[Co^{III}(Tp)_2]_{1.3}[Er(NO_3)_2(dbm)_2](NO_3)_{0.3}$, and 1847189 for $[Co^{III}(Tp)_2]_{1.3}[Y(NO_3)_2(dbm)_2](NO_3)_{0.3}$. Unit cell parameters, structure solution and refinement details for all complexes are summarized in Table V-1. The programs used for molecular graphics were MERCURY[149] and Diamond.[150]

Powder diffraction data was collected on all four complexes to confirm bulk purity of samples prior to magnetic measurements. Simulated powder patterns were generated using the program Mercury based on the structures from single crystal diffraction experiments.

Table V-1 Crystal data and structural refinement parameters for compounds **1-4**. Reproduced by permission from Alexandropoulos, D. I.; Schulte, K. A.; Vignesh, K. R.; Dunbar, K. R. *Chem. Commun.* **2018**, *54* (72), 10136-10139.

Complex	**1**	**2**
Empirical formula	$C_{54}H_{48.67}B_{2.67}Co_{1.33}N_{18}O_{10}Tb$	$C_{54}H_{48.67}B_{2.67}Co_{1.33}N_{18}O_{10}Dy$
Formula weight	1376.08	1379.67
Temperature/K	100.0	100.0
Crystal system	cubic	cubic
Space group	I23	I23
a/Å	20.9135(4)	20.9059(3)
b/Å	20.9135(4)	20.9059(3)
c/Å	20.9135(4)	20.9059(3)
α/°	90	90
β/°	90	90
γ/°	90	90
Volume/Å^3	9147.0(5)	9137.1(4)
Z	6	6
ρ_{calc}g/cm^3	1.499	1.504
μ/mm^{-1}	0.396	0.397
F(000)	4158.0	4164.0
Crystal size/mm^3	0.94 × 0.121 × 0.113	0.143 × 0.13 × 0.071
Radiation	Synchrotron (λ = 0.41328)	Synchrotron (λ = 0.41328)
2Θ range for data collection/°	2.774 to 30.706	2.774 to 40.22
Index ranges	$-18 \le h \le 18$ $0 \le k \le 18$ $2 \le l \le 26$	$-24 \le h \le 24$ $0 \le k \le 24$ $2 \le l \le 34$
Reflections collected	3381	7378
Independent reflections	3381 R_{int} = 0.0442 R_{sigma} = 0.0105	7378 R_{int} = 0.0392 R_{sigma} = 0.0116
Data/restraints/ parameters	3381 / 0 / 200	7378 / 0 / 200
Goodness-of-fit on F^2	1.147	1.076
Final R^{a,b} indexes [I>=2σ (I)]	R_1 = 0.0334 wR_2 = 0.0810	R_1 = 0.0469 wR_2 = 0.1192
Final R^{a,b} indexes [all data]	R_1 = 0.0337 wR_2 = 0.0813	R_1 = 0.0505 wR_2 = 0.1217
Largest diff. peak /hole / e Å^{-3}	0.40 / -1.36	1.64 / -3.50

Table V-1 Continued.

Complex	**3**	**4**
Empirical formula	$C_{54}H_{48.67}B_{2.67}Co_{1.33}N_{18}O_{10}Er$	$C_{54}H_{48.67}B_{2.67}Co_{1.33}N_{18}O_{10}Y$
Formula weight	1384.44	1306.08
Temperature/K	100.0	100.0
Crystal system	cubic	cubic
Space group	I23	I23
a/Å	20.9076(4)	20.9091(4)
b/Å	20.9076(4)	20.9091(4)
c/Å	20.9076(4)	20.9091(4)
α/°	90	90
β/°	90	90
γ/°	90	90
Volume/Å^3	9139.3(5)	9141.3(5)
Z	6	6
ρ_{calc}g/cm^3	1.509	1.424
μ/mm^{-1}	0.434	0.338
F(000)	4176.0	4002.0
Crystal size/mm^3	0.255 × 0.242 × 0.214	0.97 × 0.105 × 0.102
Radiation	Synchrotron (λ = 0.41328)	Synchrotron (λ = 0.41328)
2Θ range for data collection/°	2.774 to 40.356	2.774 to 35.354
Index ranges	$-24 \le h \le 24$ $0 \le k \le 24$ $2 \le l \le 34$	$-21 \le h \le 21$ $0 \le k \le 21$ $2 \le l \le 30$
Reflections collected	7435	5076
Independent reflections	7435 R_{int} = 0.0431 R_{sigma} = 0.0120	5076 R_{int} = 0.0413 R_{sigma} = 0.0117
Data/restraints/ parameters	7435 / 0 / 200	5076 / 0 / 200
Goodness-of-fit on F^2	1.064	1.063
Final R^{a,b} indexes [I>=2σ (I)]	R_1 = 0.0454 wR_2 = 0.1191	R_1 = 0.0330 wR_2 = 0.0890
Final R^{a,b} indexes [all data]	R_1 = 0.0474 wR_2 = 0.1208	R_1 = 0.0348 wR_2 = 0.0901
Largest diff. peak /hole / e Å^{-3}	1.70 / -3.76	0.37 / -1.25

[a] $R_1 = \Sigma(||F_o| - |F_c||)/\Sigma|F_o|$. [b] $wR_2 = [\Sigma[w(F_o^2 - F_c^2)^2]/\Sigma[w(F_o^2)^2]]^{1/2}$, $w = 1/[\sigma^2(F_o^2) + (ap)^2 + bp]$, where $p = [\max(F_o^2, 0) + 2F_c^2]/3$.

$[Co^{III}(Tp)_2]_{1.3}[Tb(NO_3)_2(dbm)_2](NO_3)_{0.3}$ The coordination of lanthanide containing anion in this salt involves two nitrate ligands and two dbm ligands. The cobalt containing cation in this salt is coordinated to two Tp* ligands. Both the terbium and cobalt metal ions are in the trivalent oxidation state. The compound crystallizes in the cubic space group I23. The crystal structure and powder pattern of the compound can be found in Figure V.1 and Figure V.2, respectively.

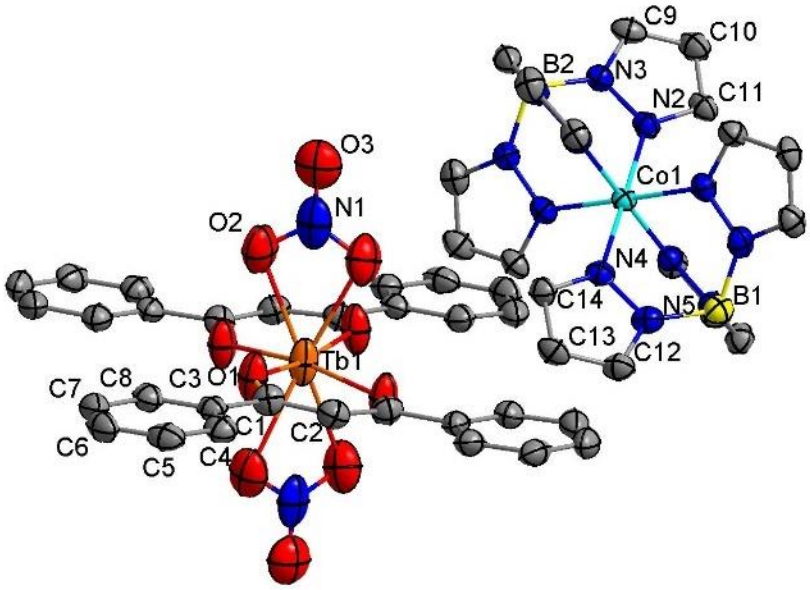

Figure V.1 Crystal structure of $[Co^{III}(Tp)_2]_{1.3}[Tb(NO_3)_2(dbm)_2](NO_3)_{0.3}$. Hydrogen atoms were omitted for clarity. Thermal ellipsoids were drawn at the 50% probability level. Colors are as follows: Colors are as follows: orange, Tb; turquoise, Co; blue, N; yellow, B; red, O; grey, C.

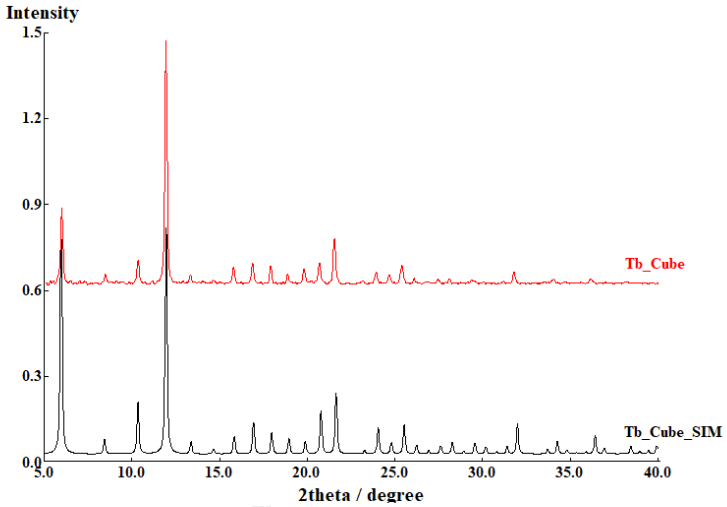

Figure V.2 Powder pattern for $[Co^{III}(Tp)_2]_{1.3}[Tb(NO_3)_2(dbm)_2](NO_3)_{0.3}$. Reproduced by permission from Alexandropoulos, D. I.; Schulte, K. A.; Vignesh, K. R.; Dunbar, K. R. *Chem. Commun.* **2018**, *54* (72), 10136-10139.

$[Co^{III}(Tp)_2]_{1.3}[Dy(NO_3)_2(dbm)_2](NO_3)_{0.3}$ This compound is isostructural with **1.** It can be described similarly, with dysprosium as the lanthanide cation. The crystal structure and powder pattern of the compound can be found in Figure V.3 and Figure V.4, respectively.

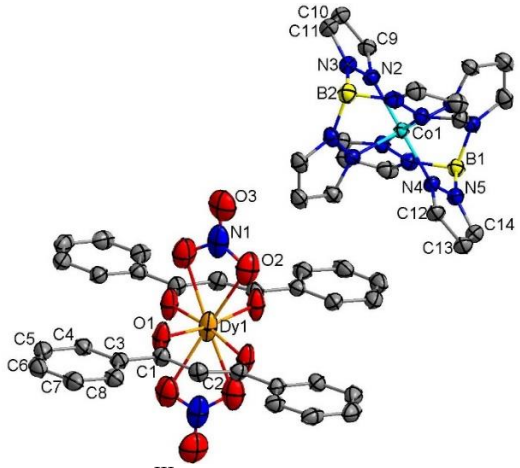

Figure V.3 Crystal structure of $[Co^{III}(Tp)_2]_{1.3}[Dy(NO_3)_2(dbm)_2](NO_3)_{0.3}$. Hydrogen atoms were omitted for clarity. Thermal ellipsoids were drawn at the 50% probability level. Colors are as follows: Colors are as follows: orange, Dy; turquoise, Co; blue, N; yellow, B; red, O; grey, C.

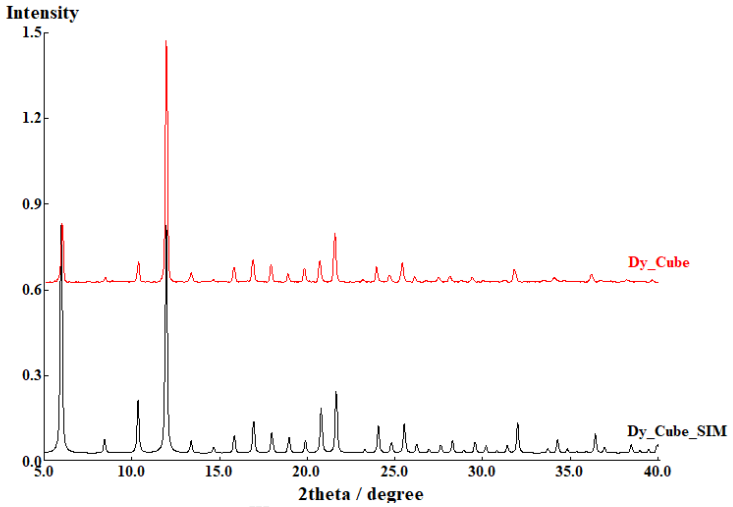

Figure V.4 Powder pattern for $[Co^{III}(Tp)_2]_{1.3}[Dy(NO_3)_2(dbm)_2](NO_3)_{0.3}$. Reproduced by permission from Alexandropoulos, D. I.; Schulte, K. A.; Vignesh, K. R.; Dunbar, K. R. *Chem. Commun.* **2018**, *54* (72), 10136-10139.

$[Co^{III}(Tp)_2]_{1.3}[Er(NO_3)_2(dbm)_2](NO_3)_{0.3}$ This compound is isostructural with **1.** It can be described similarly, with erbium as the lanthanide cation. The crystal structure and powder pattern of the compound can be found in Figure V.5 and Figure V.6, respectively.

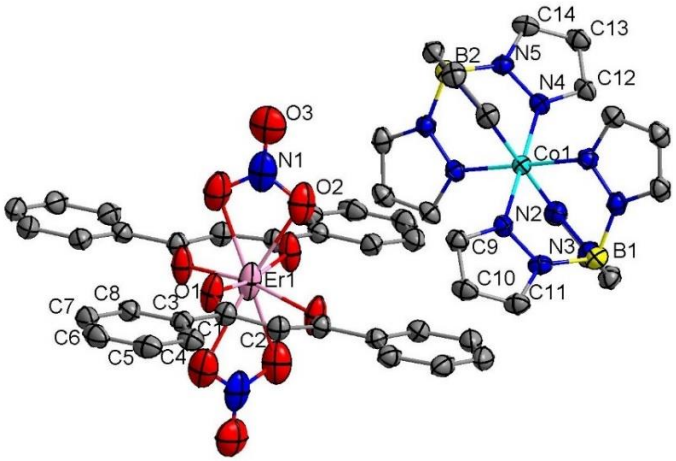

Figure V.5 Crystal structure of $[Co^{III}(Tp)_2]_{1.3}[Er(NO_3)_2(dbm)_2](NO_3)_{0.3}$. Hydrogen atoms were omitted for clarity. Thermal ellipsoids were drawn at the 50% probability level. Colors are as follows: Colors are as follows: pink, Er; turquoise, Co; blue, N; yellow, B; red, O; grey, C.

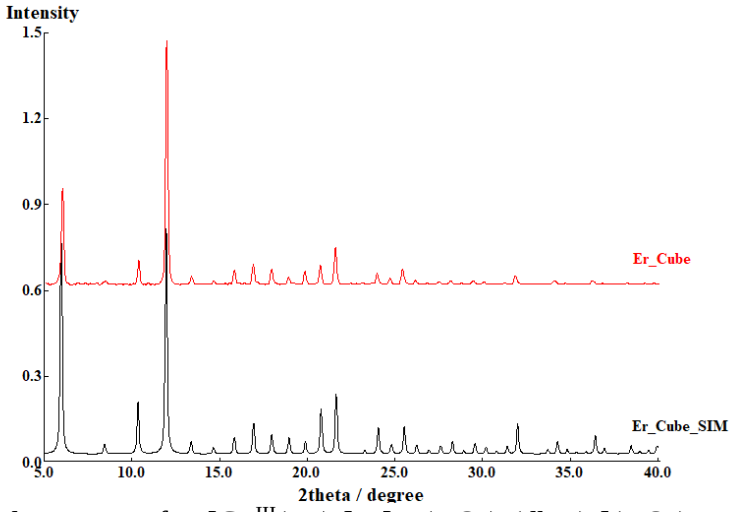

Figure V.6 Powder pattern for $[Co^{III}(Tp)_2]_{1.3}[Er(NO_3)_2(dbm)_2](NO_3)_{0.3}$. Reproduced by permission from Alexandropoulos, D. I.; Schulte, K. A.; Vignesh, K. R.; Dunbar, K. R. *Chem. Commun.* **2018**, *54* (72), 10136-10139.

$[Co^{III}(Tp)_2]_{1.3}[Y(NO_3)_2(dbm)_2](NO_3)_{0.3}$ This compound is isostructural with **1.** It can be described similarly, with yttrium as the lanthanide cation. The crystal structure and powder pattern of the compound are provided in Figure V.7 and Figure V.8, respectively.

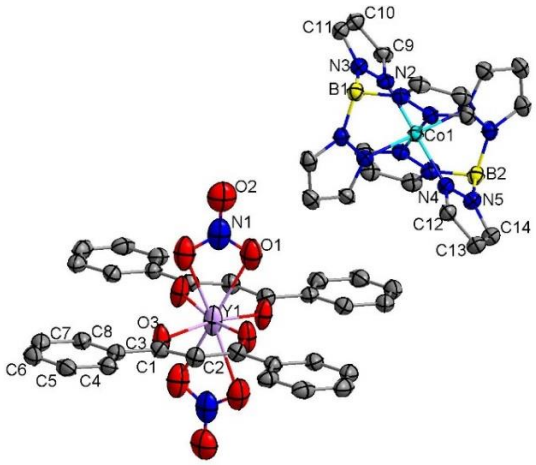

Figure V.7 Crystal structure of $[Co^{III}(Tp)_2]_{1.3}[Y(NO_3)_2(dbm)_2](NO_3)_{0.3}$. Hydrogen atoms were omitted for clarity. Thermal ellipsoids were drawn at the 50% probability level. Colors are as follows: Colors are as follows: pink, Er; turquoise, Co; blue, N; yellow, B; red, O; grey, C.

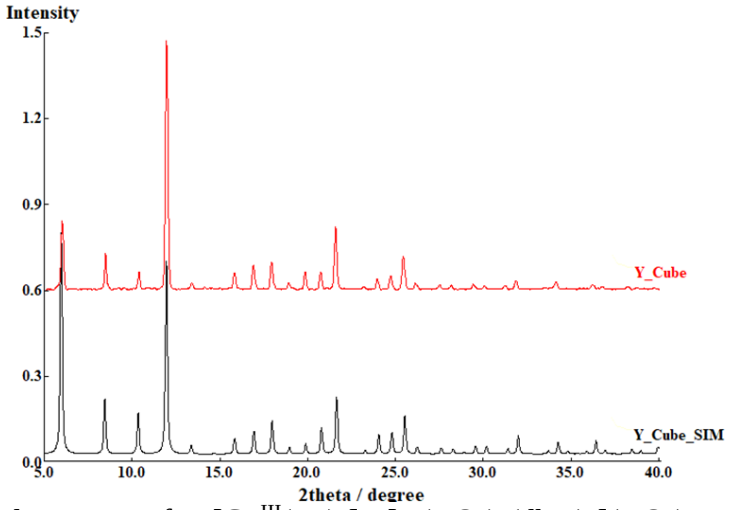

Figure V.8 Powder pattern for $[Co^{III}(Tp)_2]_{1.3}[Y(NO_3)_2(dbm)_2](NO_3)_{0.3}$. Reproduced by permission from Alexandropoulos, D. I.; Schulte, K. A.; Vignesh, K. R.; Dunbar, K. R. *Chem. Commun.* **2018**, *54* (72), 10136-10139.

V.2.3 Magnetic Measurements

Magnetic data were collected on a Quantum Design MPMS-3 SQUID from 1.8-300 K with DC fields from 0-7 T. Compounds **1-4** were collected in plastic bags. Diamagnetic corrections were applied for the bags based on a previous calibration. The diamagnetic contribution from the compounds were calculated based on Pascal's constants.[74]

V.2.4 Computational Details

Using MOLCAS 8.0,[151] *ab initio* calculations were performed for the Dy^{III} ion using the crystal structures of **2** to rationalize the observed SMM behavior. Relativistic effects are taken into account on the basis of the Douglas−Kroll Hamiltonian.[152] The spin-free eigen states are achieved by the Complete Active Space Self-Consistent Field (CASSCF) method.[153] The basis sets were taken from the ANORCC library for the calculations.[154]

We employed the [ANO-RCC... 8s7p5d3f2g1h.] basis set for Dy^{III} atoms, the [ANO-RCC...3s2p.] basis set for C atoms, the [ANO-RCC...2s.] basis set for H atoms, the [ANO-RCC...3s2p1d.] basis set for N atoms, and the [ANO-RCC...3s2p1d.] basis set for O atoms. In the first step, a guessorb calculation was run using a Seward module to create the starting guess orbitals. Nine electrons across seven 4f orbitals of the Dy^{III} ion were included. Then using these guess orbitals, the active space was chosen based on the number of active electrons in the number of active orbitals and carried out the SA-CASSCF calculations. The Configuration Interaction (CI) procedure was computed for the Dy^{III} ion and considered twenty-one sextet excited states in the calculations to compute the anisotropy. After computing these excited states, the RASSI-SO[155] module was used to calculate the spin-orbit (SO) coupled states. Moreover, these computed SO states were considered in the SINGLE_ANISO[156] program to compute the *g*-tensors. The *g*-tensors for the Kramers doublets of Dy^{3+} were computed based on the pseudospin S = ½ formalism.[156] Crystal-field (CF) parameters were extracted using the SINGLE_ANISO code, as implemented in MOLCAS 8.0.

V.3 Results and Discussion

V.3.1 Crystallographic Details

Reactions of $Co(dbm)_2$, $M(NO_3)_3{\cdot}xH_2O$ (M = Tb^{III}, Dy^{III}, Er^{III}, and Y^{III}), and KTp in a 1 : 1 : 1 molar ratio in MeCN produced pale-yellow/orange crystals of $[Co^{III}(Tp)_2]_{1.3}[M(NO_3)_2(dbm)_2](NO_3)_{0.3}$ (M = Tb (**1**), Dy (**2**), Er (**3**) and Y (**4**)) (yields >50%). After slow evaporation over the course of 1 week, orange crystals were isolated. Single crystal x-ray crystallographic studies revealed that all four compounds crystallize

in the space group Cubic I23. The lanthanide ions are in the trivalent oxidation state with cubic coordination, and the cobalt metal centers are in the trivalent oxidation state with octahedral coordination. The formulae of **1-4** are based on metric parameters, charge-balance considerations, and bond valence sum (BVS) calculations on the Co atom. The dbm ligand was selected as one of the chelating ligands since β-diketonate complexes have been successfully used in the design of mononuclear Ln SMMs.[157-158] The diamagnetic $[Co^{III}(Tp)_2]^+$ cation (Tp = tris(pyrazolyl)borate) was generated *in situ* and imposes high crystallographic symmetry and helps to impart greater intermolecular separation between molecules than smaller cations. In these compounds, the eight-coordinate lanthanide ions are in a cubic geometry. These results constitute rare examples in which lanthanide ions exhibit a distorted O_h local symmetry in a LnO_8 coordination environment;[159-160] the only other related example is $[Dy(ntbi)_2]\cdot 3Cl$ [ntbi = tris(benzimidazol-2-ylmethyl)amine] with a LnN_8 core.[161]

In view of the structural similarities of **1-4**, only the structure of **2** will be described as a representative example. The asymmetric unit features one quarter of the $[Dy(NO_3)_2(dbm)_2]^-$ anion, with the remainder related through two C_2 axes. There is also one-third of a $[Co(Tp)_2]^+$ cation, lying on a C_3 axis, and one-third of a disordered nitrate ion in the asymmetric unit. In **2**, the 8-coordinate Dy^{III} ion is surrounded only by oxygen donor atoms with four coordination sites being occupied by two trans chelating nitrates and the remaining four positions being filled by the O atoms of two chelating dbm ligands, Figure V.9. The anion of **2** crystallizes with a $[Co(Tp)_2]^+$ cation.

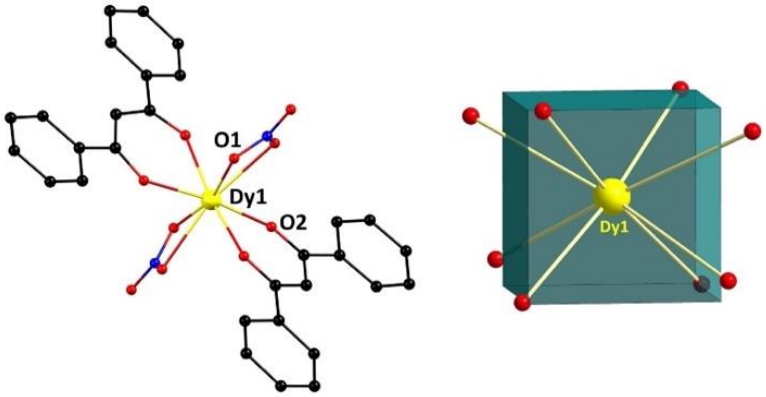

Figure V.9 (left) Crystal structure of anion **2** and (right) cubic geometry of Dy1 in the structure of **2**. Points connected by the black lines define the vertices of the ideal polyhedron. H atoms were omitted for the sake of clarity. Color scheme: Dy, yellow; N, blue; O, red; C, black. Reproduced by permission from Alexandropoulos, D. I.; Schulte, K. A.; Vignesh, K. R.; Dunbar, K. R. *Chem. Commun.* **2018**, *54* (72), 10136-10139.

Charge considerations require a formal Co^{III} description for the cation in **2**, which is further supported by the Co-N bond distances (all <1.933(2) Å) which clearly indicate a low-spin Co^{III} ion. The assignment of the Co oxidation state is confirmed by BVS calculations, Table V-2. The crystal packing of **2** reveals well-isolated $[Dy(NO_3)_2(dbm)_2]^-$ moieties with $[Co(Tp)_2]^+$ cations inserted in between, Figure V.10. The closest intermolecular Dy···Dy contact is 10.453(2) Å.

Table V-2 Bond valence sum (BVS)[c] calculations for Co atoms in **1-4**. Reproduced by permission from Alexandropoulos, D. I.; Schulte, K. A.; Vignesh, K. R.; Dunbar, K. R. *Chem. Commun.* **2018**, *54* (72), 10136-10139.

Compound	1	2	3	4
Co^{II}	3.43	3.47	3.46	3.46
Co^{III}	<u>3.17</u>	<u>3.20</u>	<u>3.19</u>	<u>3.19</u>

[c] The underlined value is the one closest to the charge for which it was calculated. The oxidation state is the nearest whole number to the underlined value.

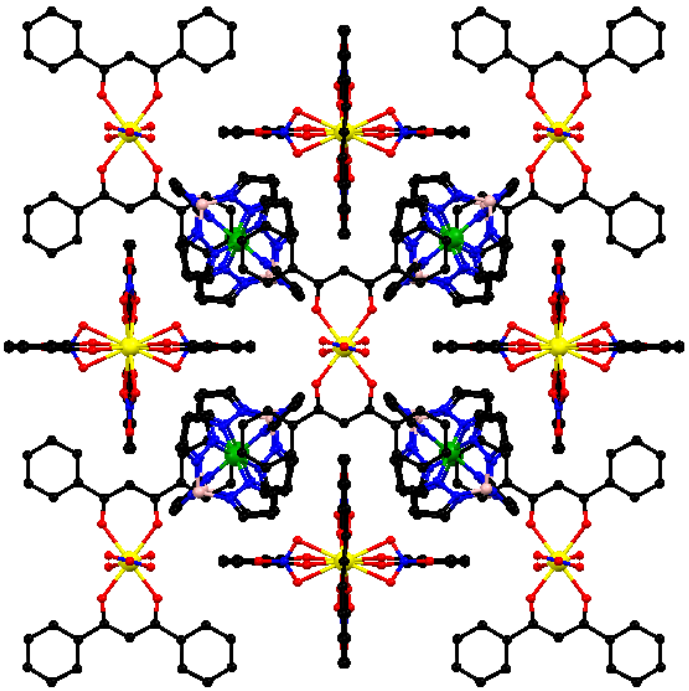

Figure V.10 Packing diagram of **2** along α axis. Hydrogen atoms are omitted for the sake of clarity. Reproduced by permission from Alexandropoulos, D. I.; Schulte, K. A.; Vignesh, K. R.; Dunbar, K. R. *Chem. Commun.* **2018**, *54* (72), 10136-10139.

SHAPE[79] calculations were performed for the Dy1 atom and revealed that it adopts a geometry closest to cubic (CShM: 3.08). The SHAPE results for all four complexes can be found in Table V-3. The two O_4-planes are defined by O1 and O2 atoms with the Dy^{III} ion being centered between the O_4-planes ($d_{Dy\text{-}O4}$ = 1.190(2) Å). The CShM value is large, implying a distorted coordination environment which is further supported by the fact that the Dy-O distances are not equal (2.273(2) Å for Dy-O1 and 2.500(1) Å for Dy-O2), indicating deviations from the ideal symmetry.

Table V-3 Shape measures of the 8-coordinate lanthanide coordination polyhedra. The values in boldface indicate the closest polyhedron according to the Continuous Shape Measures. Reproduced by permission from Alexandropoulos, D. I.; Schulte, K. A.; Vignesh, K. R.; Dunbar, K. R. *Chem. Commun.* **2018**, *54* (72), 10136-10139.

Polyhedron[d]	**1**	**2**	**3**	**4**
OP-8	31.30	31.80	31.00	31.48
HPY-8	26.19	26.23	26.28	26.27
HBPY-8	7.88	7.78	8.18	7.96
CU-8	**3.26**	**3.07**	**3.60**	**3.37**
SAPR-8	6.83	6.97	5.83	6.34
TDD-8	5.97	6.02	5.29	5.61
JGBF-8	11.07	11.22	10.81	10.93
JETBPY-8	22.39	22.29	22.66	22.45
JBTPR-8	7.15	7.31	6.17	6.65
BTPR-8	7.05	7.23	6.06	6.56
JSD-8	8.18	8.38	7.10	7.61
TT-8	4.18	3.99	4.51	4.29
ETBPY-8	20.68	20.67	20.91	20.75

[d] Abbreviations: OP-8, octagon; HPY-8, heptagonal pyramid; HBPY-8, hexagonal bipyramid; CU-8, cube; SAPR-8, square antiprism; TDD-8, triangular dodecahedron; JGBF-8, Johnson gyrobifastigium; JETBPY-8, Johnson elongated triangular bipyramid; JBTPR-8, Johnson biaugmented trigonal prism; BTPR-8, biaugmented trigonal prism; JSD-8, Johnson snub diphenoid; TT-8, triakis tetrahedron; ETBPY-8, elongated trigonal bipyramid.

In order to evaluate the symmetry of the inner coordination sphere around the lanthanide ion in **2**, several key geometrical parameters were evaluated, Figure V.11. Firstly, the angle between the four-fold axis and the Ln-O bond direction (compression angle, θ) that describes the axial distortion of the coordination environment was examined. A value of $\theta = 54.74°$ corresponds to an ideal non-distorted cubic environment while smaller or wider angles reflect axial elongation and compression, respectively. [136, 160, 162-163] In **2**, θ was calculated to be 59.59° (average value), revealing axial compression.

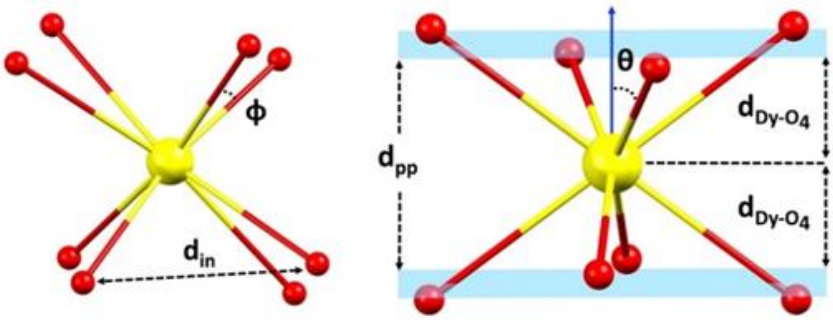

Figure V.11 Key geometrical parameters analyzed for the coordination environment of Dy in **2**; see the text for details. Reproduced by permission from Alexandropoulos, D. I.; Schulte, K. A.; Vignesh, K. R.; Dunbar, K. R. *Chem. Commun.* **2018**, *54* (72), 10136-10139.

Also, the ratio between the interplanar distance d_{pp} = 2.381(1) Å, between the upper and lower O_4-planes, and the shortest O-O distance in the O_4-plane, d_{in} = 2.905(2) Å, indicates axial compression.[136, 160, 162-163] The d_{in} value is similar to those reported for the axially compressed Ln polyoxometallate complexes LnPOM (2.785-2.964). Another crucial parameter for the determination of the symmetry of the lanthanide coordination geometry is the skew or twist angle, φ, defined as the angle between the diagonals of the two different O_4-planes. A value of φ = 0 is expected for an ideal square prismatic or cubic symmetry while a value of φ = 45° describes a non-distorted square antiprismatic geometry.[136, 160, 162-163] In **2**, φ angle gave an average of 10.22° (calculated as the torsion angle between all different O_4-planes). This value is lower than those reported for the square antiprismatic Ln phthalocyanine $LnPc_2$ (34.4-45)[136] and Ln polyoxometalate LnPOM (39.1-46.9)[160] complexes, suggesting that while the geometry of the Dy ion is very distorted, it is best described as cubic rather than as square antiprismatic. See Table V-4 to find these values for complexes **1**, **3**, and **4**.

Table V-4 Key geometrical parameters analyzed for the coordination environment of 8-coordinate lanthanide ions in **1, 3,** and **4**. Reproduced by permission from Alexandropoulos, D. I.; Schulte, K. A.; Vignesh, K. R.; Dunbar, K. R. *Chem. Commun.* **2018**, *54* (72), 10136-10139.

Compound[e]	**1**	**3**	**4**
d_{M-O1} / Å	2.280(1)	2.253(2)	2.259(1)
d_{M-O2} / Å	2.499(2)	2.461(1)	2.478(1)
$d_{M-Oplane}$ / Å	1.183(2)	1.184(2)	1.188(2)
d_{pp} / Å	2.367(2)	2.368(2)	2.375(2)
d_{in} / Å	2.908(2)	2.862(1)	2.876(1)
φ / °	13.46	16.49	14.93
θ / °	59.84	59.36	59.40

[e] Abbreviations: d_{M-O1} and d_{M-O2}, metal-oxygen distances; $d_{M-Oplane}$, distance between the metal ion and the O_4-plane; d_{pp}, distance between the upper and lower O_4-planes; d_{in}, the shortest O-O distance in the O_4-plane; φ, skew or twist angle, angle between the diagonals of the two different O_4-planes (average value); θ, compression angle, angle between the four-fold axis and the M-O bond direction.

V.3.2 DC Magnetic Studies

The static direct current (DC) magnetic properties of **1-4** were measured from 2 to 300 K in a 1000 Oe applied field, Figure V.12. The data for the diamagnetic complex **4** further support a trivalent oxidation state for the cobalt ion and confirm that the observed paramagnetic behavior of **1-3** arises exclusively from the 4*f* Ln^{III} ions. The experimental $\chi_M T$ values at 300 K for complexes **1-3** (11.63 cm^3 K mol^{-1} for **1**, 14.13 cm^3 K mol^{-1} for **2**, and 11.37 cm^3 K mol^{-1} for **3**) are in good agreement with the theoretical values (11.82 cm^3 K mol^{-1} for **1**, 14.17 cm^3 K mol^{-1} for **2**, and 11.48 cm^3 K mol^{-1} for **3**) expected for a single Tb^{III} ($^7F_6$, $S = 3$, $L = 3$, $g = 3/2$), Dy^{III} ($^6H_{15/2}$, $S = 5/2$, $L = 5$, $g = 4/3$), or Er^{III} ($^4I_{15/2}$, $S = 3/2$, $L = 6$, $g = 6/5$) ion.[46] Complexes **1-3** exhibit similar behavior, with $\chi_M T$ decreasing slightly from 300 K to reach a value of 10.90 cm^3 K mol^{-1} for **1**, 13.44 cm^3 K mol^{-1} for **2**,

and 9.98 cm^3 K mol^{-1} for **3** at 100 K. Below these temperatures, $\chi_M T$ decreases more rapidly to a minimum value of 8.84 cm^3 K mol^{-1} for **1**, 12.22 cm^3 K mol^{-1} for **2**, and 5.68 cm^3 K mol^{-1} for **3** at 2.0 K. This steeper decrease observed below 100 K can mainly be attributed to the presence of magnetic anisotropy and/or depopulation of the excited Stark sublevels of the Ln^{III} ions rather than to the presence of intermolecular interactions (average Ln-Ln distance ~10.455(1) Å).

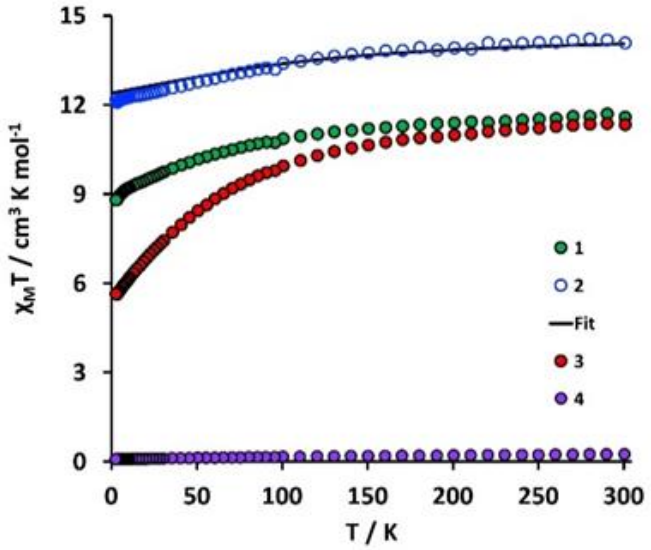

Figure V.12 Temperature dependence of $\chi_M T$ for **1-4.** Black solid line is the *ab initio* calculated data for **2.** Reproduced by permission from Alexandropoulos, D. I.; Schulte, K. A.; Vignesh, K. R.; Dunbar, K. R. *Chem. Commun.* **2018**, *54* (72), 10136-10139.

This conclusion is further supported by the lack of saturation in the M vs H plots for complexes **1-3**, Figure V.13. **1** and **2** reach a maximum value below 6 μ_B, and **3** reaches a maximum below 5 μ_B. These results are in accord with the reduced magnetization data for **1-3**, in which all the isofield lines are non-superimposed, Figure V.14, Figure V.15, and Figure V.16 for **1-3**, respectively.

a)

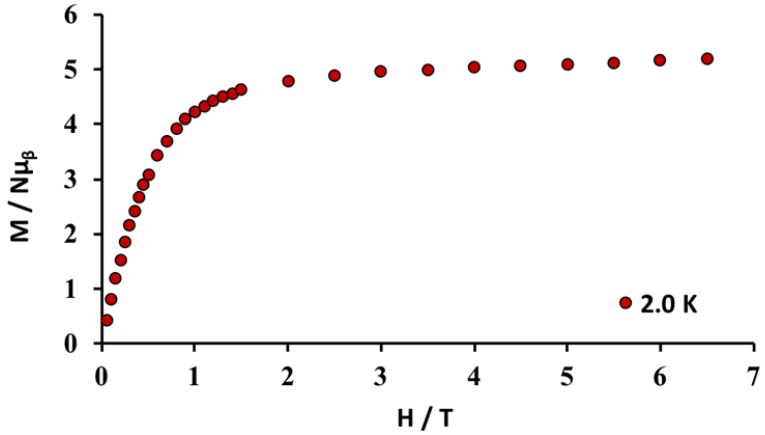

b)

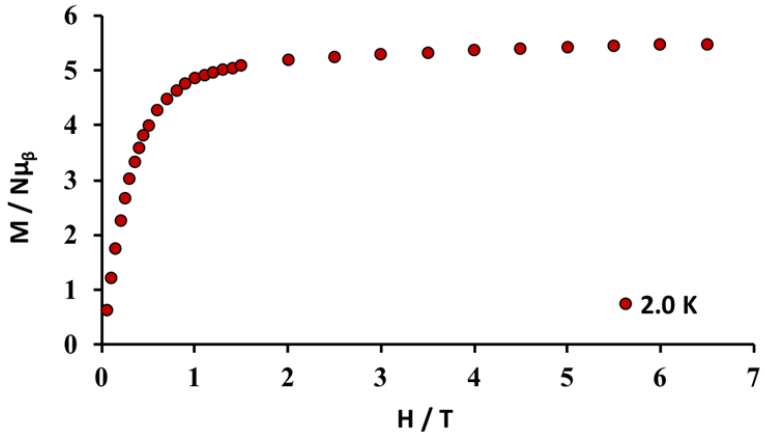

c)

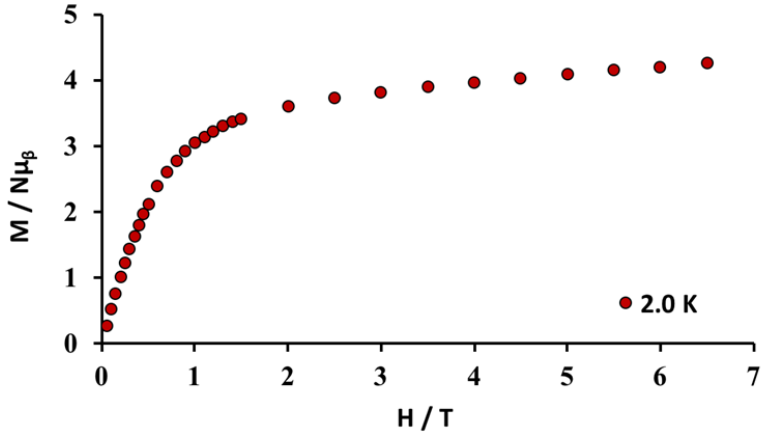

Figure V.13 Magnetization vs Field for compounds a) **1**, b) **2**, and c) **3**. Reproduced by permission from Alexandropoulos, D. I.; Schulte, K. A.; Vignesh, K. R.; Dunbar, K. R. *Chem. Commun.* **2018**, *54* (72), 10136-10139.

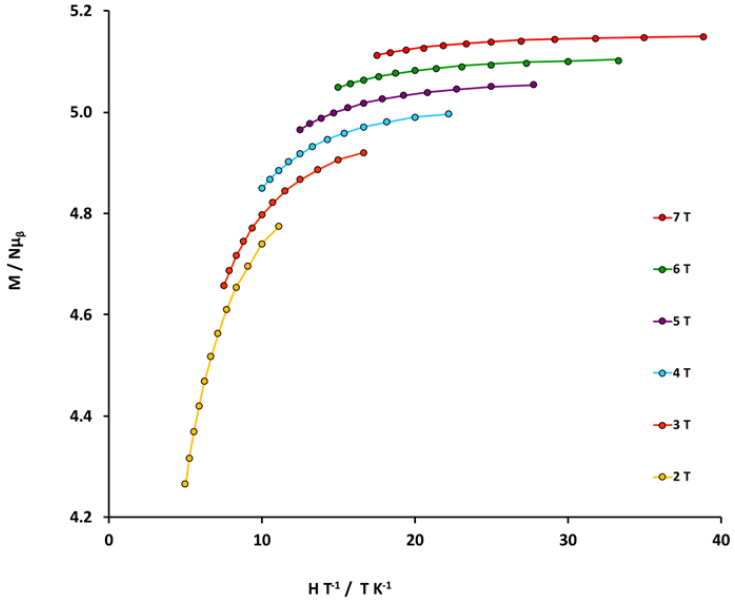

Figure V.14 Plot of reduced magnetization ($M/N\mu_B$) vs. HT^{-1} for compound **1** at applied fields of 2–7 T and in the 2–5 K temperature range. Solid lines are guides for the eye. Reproduced by permission from Alexandropoulos, D. I.; Schulte, K. A.; Vignesh, K. R.; Dunbar, K. R. *Chem. Commun.* **2018**, *54* (72), 10136-10139.

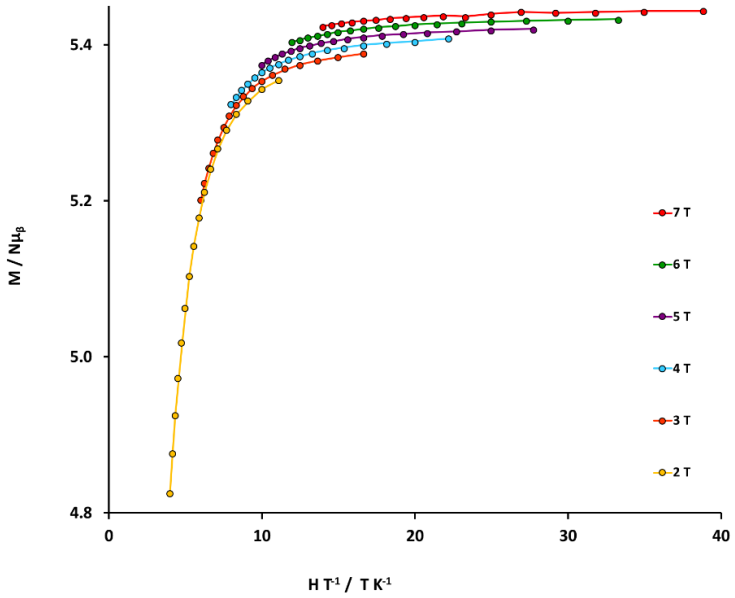

Figure V.15 Plot of reduced magnetization ($M/N\mu_B$) vs. HT^{-1} for compound **2** at applied fields of 2–7 T and in the 2–5 K temperature range. Solid lines are guides for the eye. Reproduced by permission from Alexandropoulos, D. I.; Schulte, K. A.; Vignesh, K. R.; Dunbar, K. R. *Chem. Commun.* **2018**, *54* (72), 10136-10139.

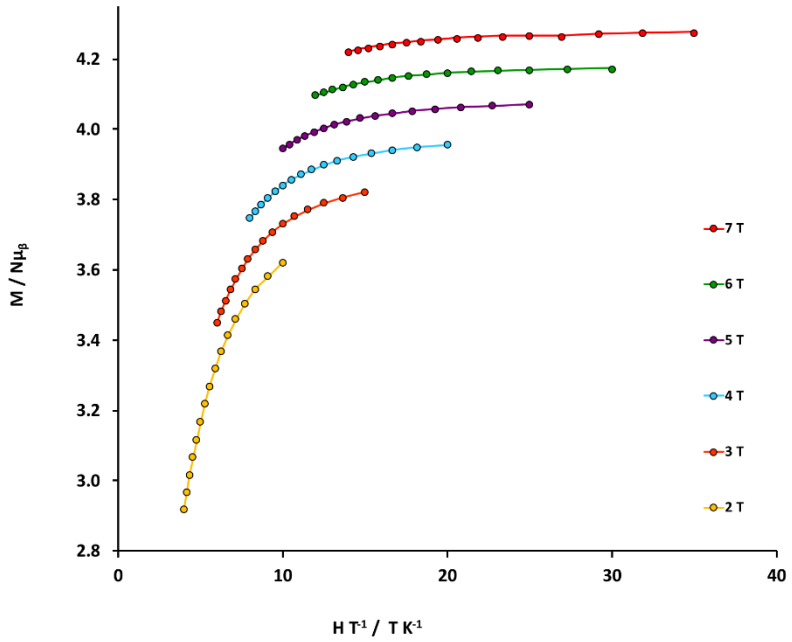

Figure V.16 Plot of reduced magnetization ($M/N\mu_B$) vs. HT^{-1} for compound **3** at applied fields of 2–7 T and in the 2–5 K temperature range. Solid lines are guides for the eye. Reproduced by permission from Alexandropoulos, D. I.; Schulte, K. A.; Vignesh, K. R.; Dunbar, K. R. *Chem. Commun.* **2018**, *54* (72), 10136-10139.

V.3.3 AC Magnetic Studies

Alternating current (*ac*) magnetic susceptibility measurements were also performed in order to probe the magnetic dynamics of **1**-**3**. Complex **1** only exhibited quantum tunneling of magnetization, Figure V.17. Complex **3** showed only the beginnings of an out-of-phase signal even under applied DC fields up to 2000 Oe, Figure V.18. As such, further magnetic characterization of either of these complexes could not be performed.

a)

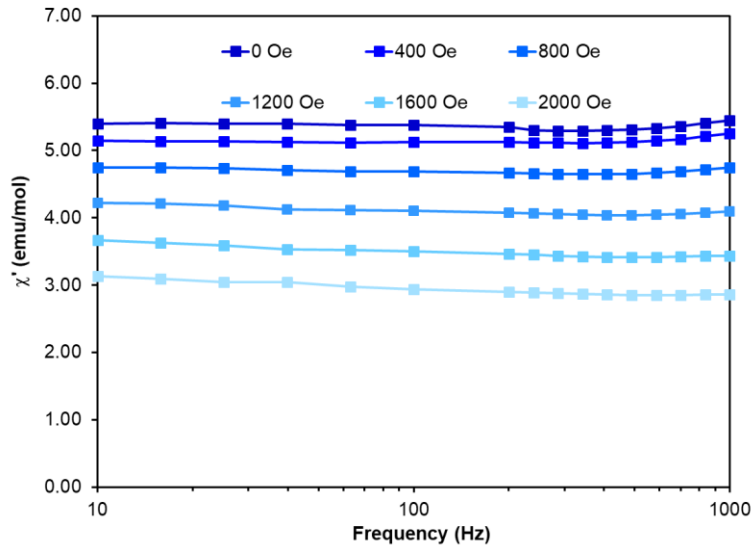

b)

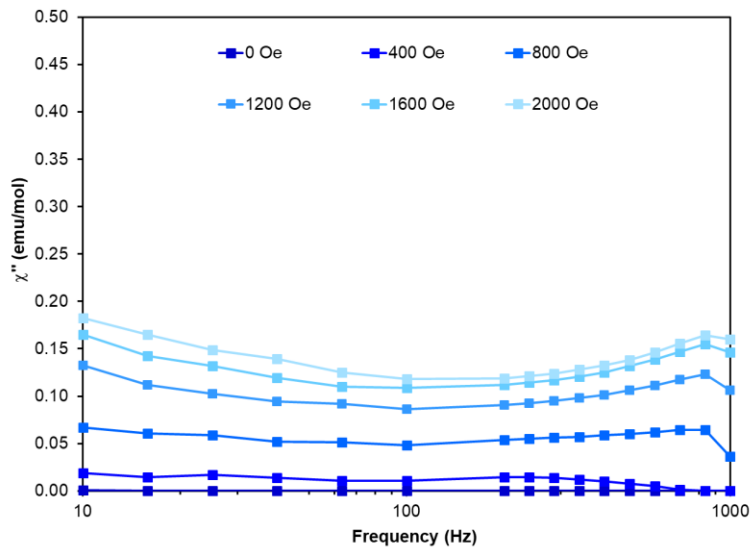

Figure V.17 a) In-phase and b) out-of-phase susceptibility for compound **1** at applied DC fields from 0-2000 Oe, as labelled. Adapted by permission from Alexandropoulos, D. I.; Schulte, K. A.; Vignesh, K. R.; Dunbar, K. R. *Chem. Commun.* **2018**, *54* (72), 10136-10139.

a)

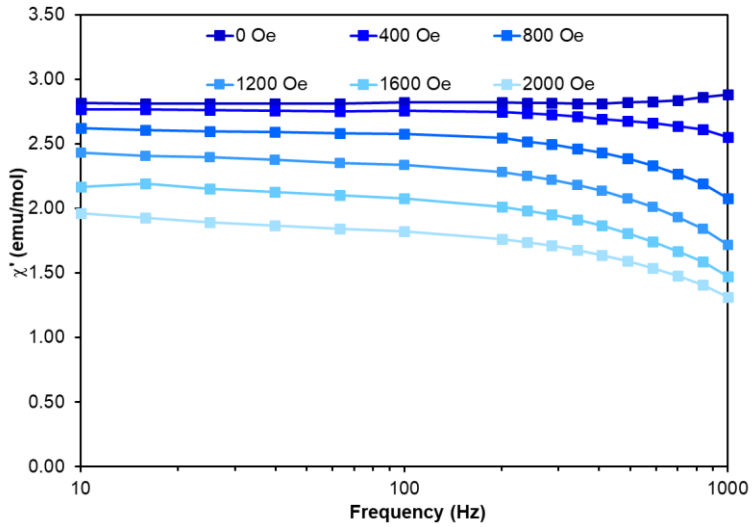

b)

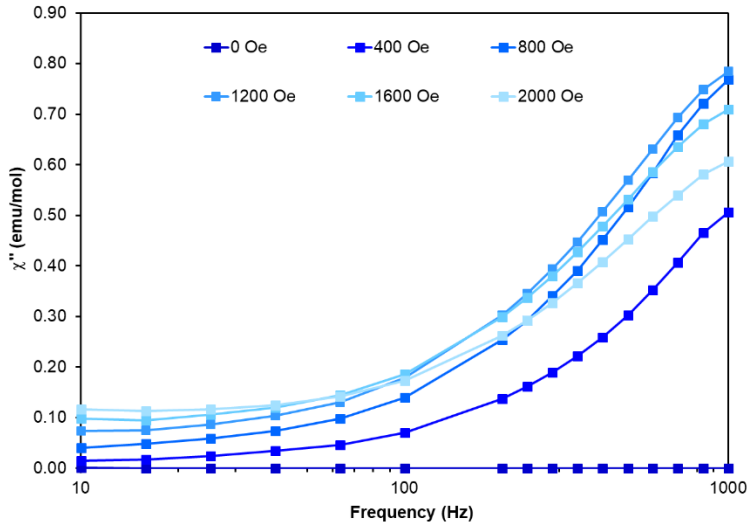

Figure V.18 a) In-phase and b) out-of-phase susceptibility for compound **3** at applied DC fields from 0-2000 Oe, as labelled. Adapted by permission from Alexandropoulos, D. I.; Schulte, K. A.; Vignesh, K. R.; Dunbar, K. R. *Chem. Commun.* **2018**, *54* (72), 10136-10139.

Only complex **2** exhibits in-phase (χ′) and out-of-phase (χ″) AC susceptibility signals that are frequency and temperature dependent in the absence of an applied DC field. No peak maxima of the χ″ signals were observed in the frequency range of 1-1000 Hz from 2 to 19 K, indicating significant quantum tunneling of the magnetization (QTM), Figure V.19.

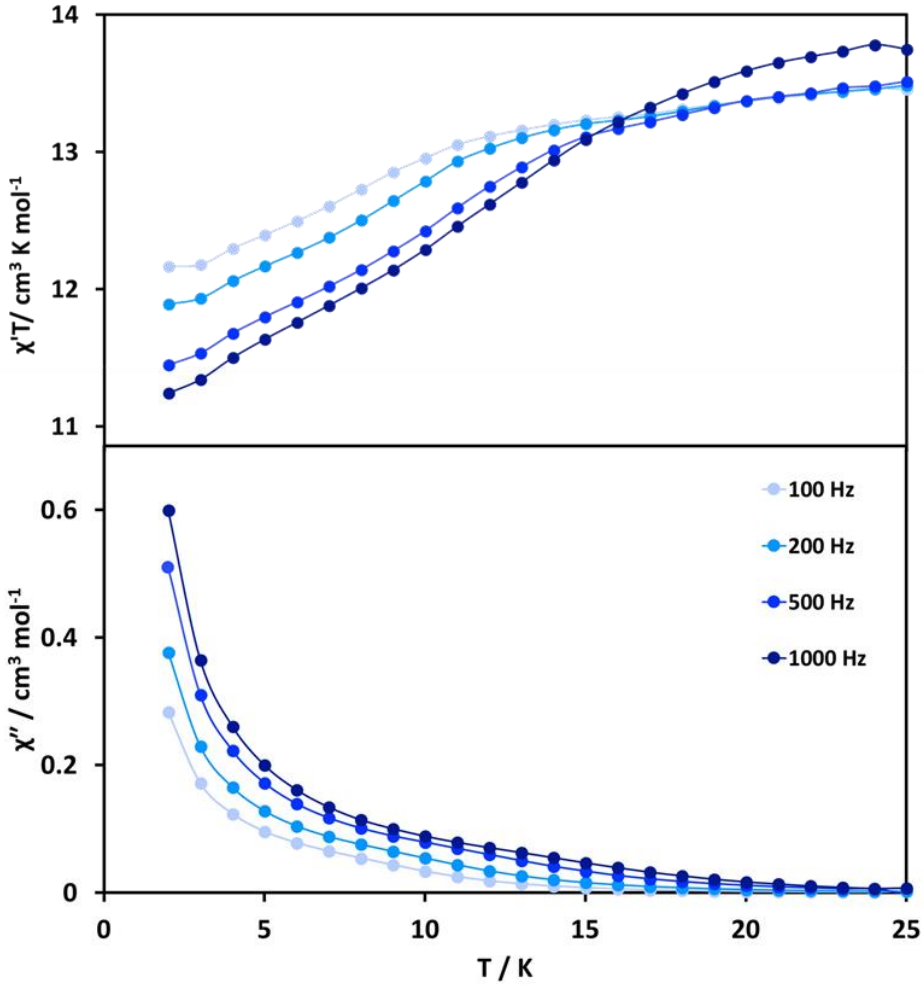

Figure V.19 Temperature dependence of the in-phase χ′T product (top) and out-of-phase χ′′ (bottom) ac susceptibility signals of **2** in a 2.0 G field oscillating at the indicated frequencies. Reproduced by permission from Alexandropoulos, D. I.; Schulte, K. A.; Vignesh, K. R.; Dunbar, K. R. *Chem. Commun.* **2018**, *54* (72), 10136-10139.

Such QTM behavior can be suppressed by the application of a small DC field. To this end, AC susceptibility measurements at various static fields (0 – 2000 Oe) were performed, and the DC field of 200 Oe was chosen as the optimum field at which a well-resolved maximum in χ'' is visible at 10 K, Figure V.20.

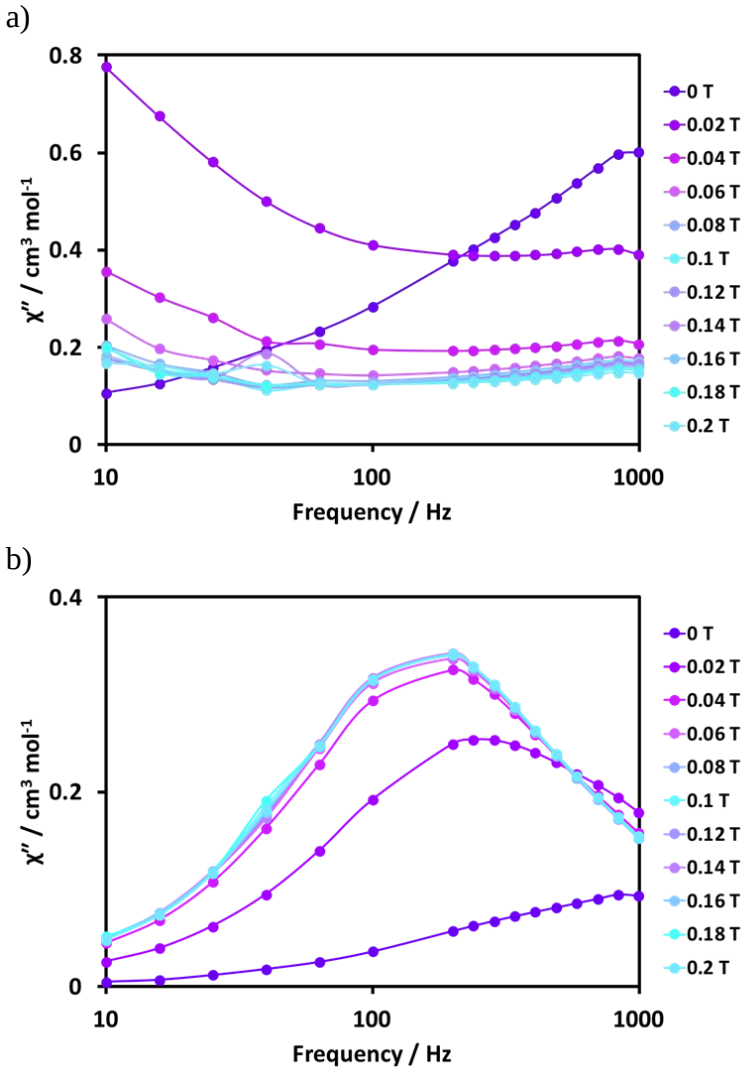

Figure V.20 Out-of-phase susceptibility for compound **2** at various DC fields from 0-0.2 T at a) 1.8 K and b) 10 K. Solid lines are guides for the eye. Reproduced by permission from Alexandropoulos, D. I.; Schulte, K. A.; Vignesh, K. R.; Dunbar, K. R. *Chem. Commun.* **2018**, *54* (72), 10136-10139.

In-phase and out-of-phase susceptibility data were subsequently collected on **2** under a 200 Oe DC field. The presence of peaks that shift to lower frequency as the temperature decreases is indicative of slow magnetic relaxation. At low temperatures, a distinct tail appears at high frequencies, suggesting a second relaxation process.

a)

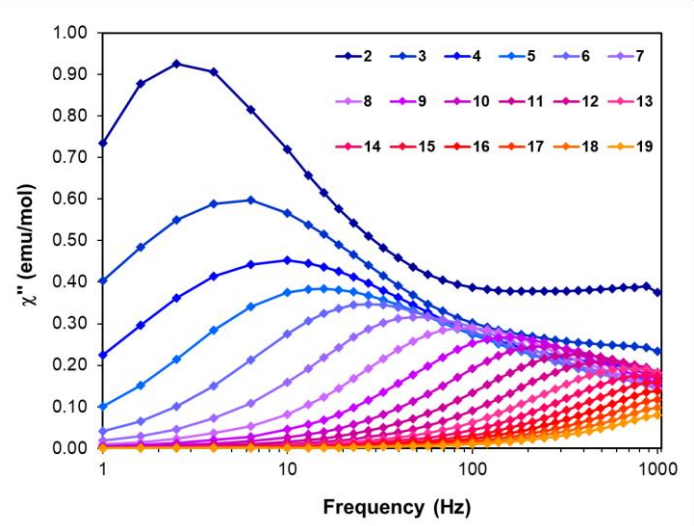

b)

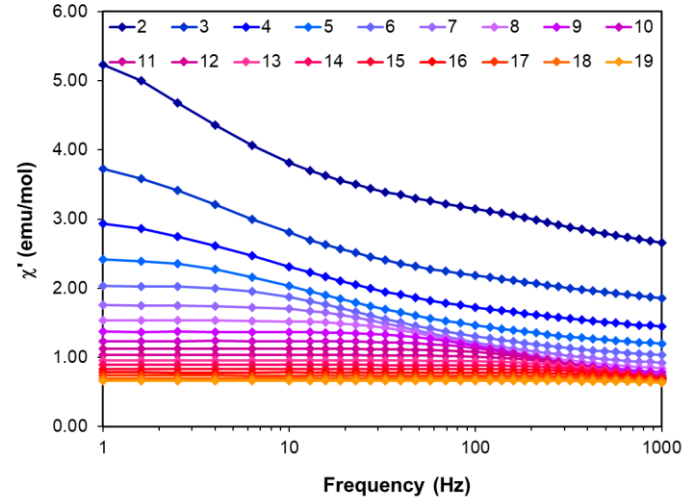

Figure V.21 a) In-phase and b) out-of-phase susceptibility for **2** under a 200 Oe DC field. Adapted by permission from Alexandropoulos, D. I.; Schulte, K. A.; Vignesh, K. R.; Dunbar, K. R. *Chem. Commun.* **2018**, *54* (72), 10136-10139.

As a result, the experimental data between 2-19 K were fit using a generalized Debye model in CC-fit to extract τ and α parameters with two relaxation processes being considered, Figure V.22.[164] U_{eff} and τ_0 values could not be obtained for the second thermally activated relaxation process since QTM, although reduced to some extent, still dominates the low-temperature regime. The relaxation times from fitting the main, lower frequency relaxation were plotted as ln(τ) vs. 1/T. To extract an effective energy barrier, and to quantify the Raman process which usually dictates the intermediate regime in the ln(τ) vs. 1/T plot, the data between 2 to 19 K were analyzed by the following equation[165]:

$$\tau^{-1} = \tau_{QTM}^{-1} + CT^{n} + \tau_0^{-1}\exp\left(-\frac{U_{eff}}{k_B T}\right)$$

where τ_{QTM}^{-1}, CT^n, and $\tau_0^{-1}\exp(-U_{eff}/k_BT)$ represent QTM, Raman, and Orbach relaxation processes, respectively. A U_{eff}/k_BT of 95.7 K and a pre-exponential factor $\tau_0 = 1.9 \times 10^{-8}$ s were extracted at high-temperatures, while the τ_{QTM}^{-1} parameter was obtained as 0.07 s at low-temperatures.[166] Additionally, the following Raman components were extracted: n = 2.79 and C = 0.98 s^{-1} $K^{-2.79}$.

a)

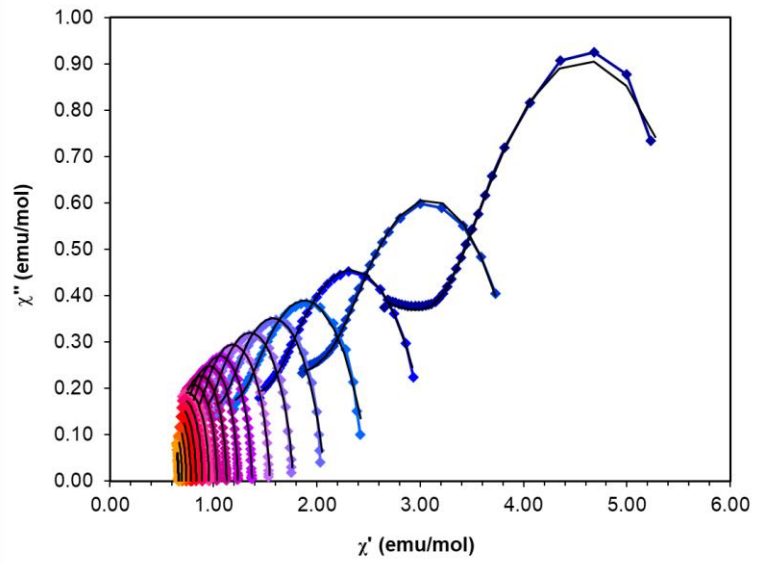

b)

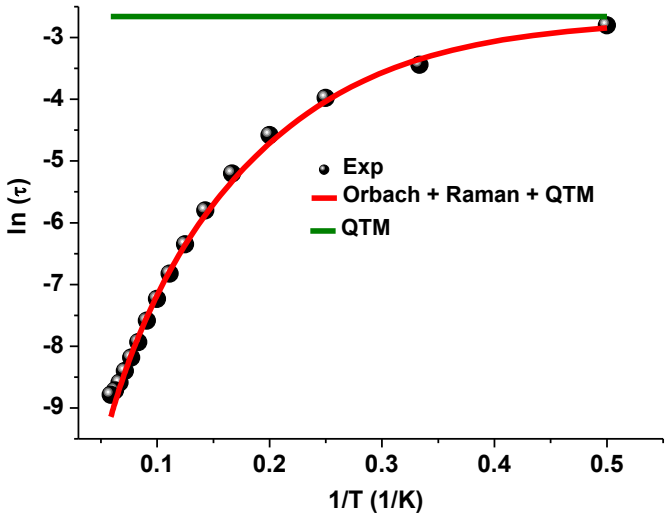

Figure V.22 a) Cole-cole plot for **2** and b) resulting Arrhenius plot. Solid black lines are the fits to the cole-cole plot using CC-fit. Black dots are the experimental data from that fit. Red and green lines are fit lines, as labelled. Adapted by permission from Alexandropoulos, D. I.; Schulte, K. A.; Vignesh, K. R.; Dunbar, K. R. *Chem. Commun.* **2018**, *54* (72), 10136-10139.

Given the small required field to suppress quantum tunneling, hysteresis measurements were also undertaken at 1.8 K. No hysteresis behavior was observed for **2**, including butterfly-type hysteresis, Figure V.23.

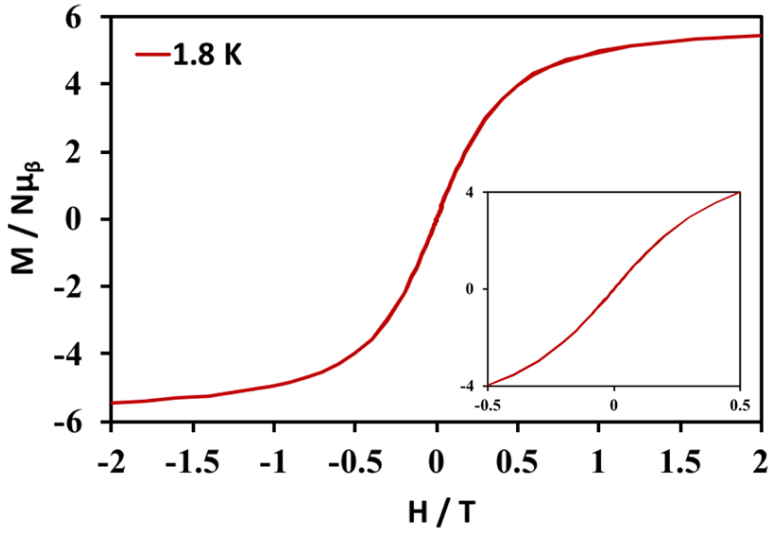

Figure V.23 Magnetization (M) vs. applied dc field (H) measurements for a microcrystalline sample of **2** at 1.8 K. Reproduced by permission from Alexandropoulos, D. I.; Schulte, K. A.; Vignesh, K. R.; Dunbar, K. R. *Chem. Commun.* **2018**, *54* (72), 10136-10139.

To further understand the observed magnetic behavior of **2**, CASSCF/RASSI/SINGLE_ANISO *ab initio* calculations were performed using MOLCAS 8.0. These calculations revealed that the ground state Kramers doublet (KD) of the Dy^{III} ion has small transverse components (g_x, g_y), with the g_z value reaching close to the expected value (20) for a pure Ising $|m_J = \pm 15/2>$multiplet, Table V-5.

These results indicate a small QTM value for the ground state KD and indicate that magnetic relaxation can occur through higher excited states. The transverse components

are enhanced in excited states. Indeed, the second excited KD has larger transverse components, as compared to the first, suggesting that relaxation of magnetization via these KDs is more favorable. This conclusion is in good agreement with the experimental data where an extremely small DC field is required to achieve SMM behavior. The correlation between the *ab initio* computed and the experimental magnetic susceptibility data of **2,** Figure V.12**,** lends confidence to the extracted parameters.

Table V-5 *Ab Initio* Computed Eight Low-lying Kramers Doublet Energies (cm^{-1}) and g-tensors of each Kramers Doublets in **2**. Reproduced by permission from Alexandropoulos, D. I.; Schulte, K. A.; Vignesh, K. R.; Dunbar, K. R. *Chem. Commun.* **2018**, *54* (72), 10136-10139.

KDs	Energy (cm^{-1})	g_x, g_y and g_z
1	0.0	0.0202 0.0237 19.7199
2	234.9	0.0459 0.1109 15.4744
3	317.6	1.8979 2.0641 12.2892
4	457.0	1.7856 4.3905 9.4439
5	572.6	0.1305 1.2204 17.9329
6	609.6	8.1826 8.0311 0.0825
7	716.1	3.5694 4.1807 12.2314
8	886.1	0.3676 0.6645 18.3199

The computed energy barrier was extracted by constructing the magnetic relaxation mechanisms, Figure V.24. In **2**, the ground state axial nature is well reflected in the negligible transversal moment matrix elements relevant to small QTM process (0.0073 μ_B). This is further supported by the wave function analysis where the ground KD is mostly made up of the $m_J = \pm 15/2 >$ state with small contributions from the $m_J = \pm 13/2 >$ state. Notably, the enhanced transverse first excited KD anisotropy components are supported by considerable transversal moment matrix elements within the first excited state doublets, corresponding to the Thermally Assisted-QTM (TA-QTM) process (0.026 μ_B). Additionally, magnetic moment matrix elements related to spin-phonon transitions (Orbach and Raman; green and purple arrows in Figure V.24) between ground and higher excited states (i.e. 1.7/0.02 μ_B) is not sufficient to promote relaxation via the first excited KD.

On the other hand, the first excited KD transverse anisotropy is witnessed by enhanced mixed character i.e. combination of $m_J = \pm 13/2 >$ and $m_J = \pm 9/2 >$ states. Additionally, the second KD possesses small g_x and g_y components, with a g_z value of approximately 16 indicating the presence of strong axial nature, even in the first excited energy level. This finding, in conjunction with the small angle between the ground and first excited KDs (0.01°), stimulates relaxation via second excited KDs.[167] The large transverse components ($g_x = 1.89$, $g_y = 2.06$) in the second excited KDs enable fast TA-QTM (0.66 μ_B) between these states. This delineates U_{cal} as 317.6 cm^{-1} (457 K) which is highly overestimated compared to the experimentally determined energy barrier of 95.7 K. This situation is perhaps due to the exclusion of intermolecular and hyperfine

interactions in the calculation and the possibility of a non-Orbach relaxation mechanism.[168]

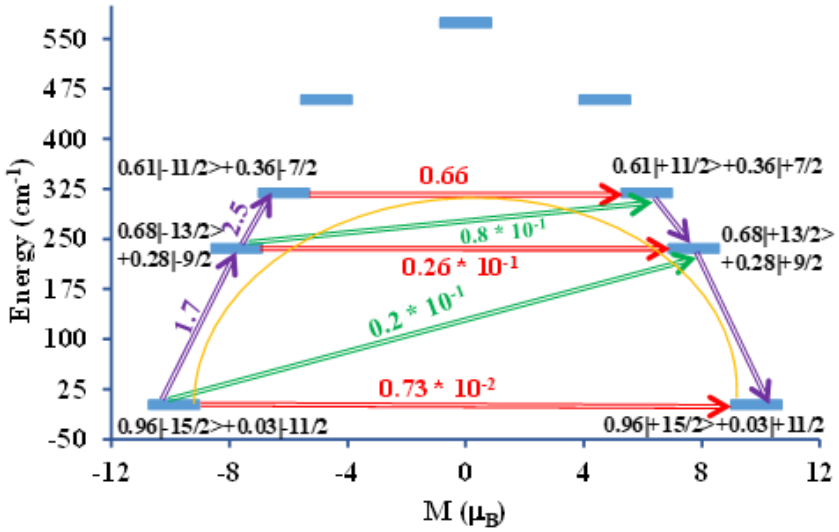

Figure V.24 Magnetization blocking barrier for **2**. Thick blue lines indicate Kramers doublets (KDs) as a function of the computed magnetic moment. Green/purple double-dashed arrows show possible pathways through Orbach/Raman relaxations. Double-dashed red arrows represent QTM/TA-QTM between the connecting pairs. The numbers at each arrow are absolute values for the corresponding matrix element of the transition magnetic moment. The yellow curve shows the most feasible magnetic relaxation pathway. Reproduced by permission from Alexandropoulos, D. I.; Schulte, K. A.; Vignesh, K. R.; Dunbar, K. R. *Chem. Commun.* **2018**, *54* (72), 10136-10139.

V.4 Conclusions

A new family of 8-coordinate, mononuclear lanthanide complexes in which the metal ions are in a very rare cubic coordination geometry has been isolated. The presence of significant distortions in **1**-**3**, as revealed by the structural analysis, breaks the ideal O_h symmetry of the inner coordination sphere. As a result, slow relaxation of the magnetization at low temperatures was only observed for complex **2** under an applied field

of 200 Oe. Fitting of the data, considering all the possible relaxation pathways, gave an energy barrier U_{eff} = 95.7 K with $\tau_0 = 1.9 \times 10^{-8}$ s for the thermal relaxation. *Ab initio* calculations support the SMM behavior of **2**, but overestimate the energy barrier. Work in progress includes substitution of the nitrate ions by other chelating ligands, such as beta diketonates and sterically enhanced dbm derivates, in order to probe how deviations from the cubic symmetry affect the crystal field splitting of the lanthanide ion and the magnetic properties of the compounds.

CHAPTER VI

CONCLUSIONS AND FUTURE OUTLOOK

To date, one of the biggest challenges in the field of single molecule magnets has been to increase the operating temperature above liquid nitrogen temperatures (77 K) or above. This goal has recently been achieved, but it is imperative that we understand the mechanisms that are operative in leading to magnetic relaxation, and to work on increasing the air and thermal stability of the magnets as extremely air sensitive molecules are not practical for use in devices. The work presented herein focused on these two goals, with the aim of building on the current foundation of knowledge to design ideal magnets with controlled relaxation in the future.

In Chapter II, two series of molecules were presented exploring the effects of changes in geometry and the effect of electron donating and withdrawing substituents on slow magnetic relaxation. In the first half of the chapter, a series of trigonal monopyramidal complexes were synthesized employing a tetradentate, nitrogen based donor which coordinated with divalent iron, cobalt, and nickel. When water was added to these complexes, coordination of a water molecule in the axial position took place, resulting in trigonal bipyramidal complexes. It was found that the trigonal monopyramidal complexes universally had more ideal geometries, resulting in larger D values, and better magnetic behavior. Computational and experimental analysis revealed that coordination of the water molecule tilted the D_{zz} axis off of the C_3 symmetry axis, which in turn lead too poorer magnetic behavior.

In the second series of compounds in the chapter, the substituents decorating the tetradentate ligand were modified to varying electron donating and withdrawing groups. The D values of the complexes were found to roughly directly correlate with the electron donating ability of the phenyl substituents, which resulted in large changes in U_{eff}. Together, these results showcase the drastic effect that a small change in the coordination environment can have on magnetic behavior, as well as that trigonal monopyramidal geometry can lead to near record D values.

In Chapter III, the magnetic behavior of four complexes were explored to probe the effect of partial and full encapsulation of divalent cobalt ions by nitrogen donor ligands. The mononuclear complexes showcased that slow magnetic relaxation improves with coordination of heavier halide atoms in the axial position, with the bromide containing complex exhibiting a higher barrier than the chloride containing complex. After generating a fully encapsulating cage by joining two ligands together through a phenyl bridge, antiferromagnetic coupling took place between two cobalt ions via the halide bridge connecting them. The chloride containing structure exhibited glassy magnet behavior up to 6 K, but such behavior was absent in the bromide analogue. Together, these molecules represent a rich exploration of magnetism, with small changes resulting in huge changes in the magnetic behavior.

In Chapter IV, tetravalent titanium was presented as a new option for solid state dilution of magnetic molecules. In particular, a scorpionate ligand coordinated to Ti(IV), combined with divalent manganese, iron, cobalt, or nickel, resulted in trinuclear structures with octahedral geometry about the paramagnetic metal center. The inorganic blocking

ligands were effective at separating the metal centers from each other, with the closest metal-metal distance of 10.641 Å. Only the cobalt complex displayed slow magnetic relaxation, with an applied DC field being required to suppress quantum tunneling. These complexes introduce Ti(IV) as an effective inorganic ligand, and open the door for exploration of this new dilution method in both transition metal and lanthanide based single molecule magnets.

In Chapter V, the first lanthanide based single molecule magnet in a cubic geometry was presented. A series of lanthanide complexes were synthesized employing bidentate, oxygen donor ligands. A diamagnetic, cobalt(III) containing counter-cation was generated in-situ to further dilute the paramagnetic metal centers. Significant distortions in the geometry about the Dy(III) center are present which led to the need for a small applied DC field in order to observe slow magnetic relaxation behavior. By reducing these distortions, air-stable, lanthanide single molecule magnets should be possible to design.

Given the progress that has been made on single molecule magnet behavior to date, the overall goal to use these molecules in applications such as data storage and quantum computing is becoming more feasible. For this to be possible, however, single molecule magnets must be deposited onto a surface. Given the sensitivity of most of the SMM molecules under investigation, deposition onto a surface can have strong effects on the magnetic behavior, or even complete degradation of the compound. One method to accomplish this is through incorporation into metal-organic frameworks (MOFs). Examples of this have resulted in improved thermal stability and isolation due to the framework.[169-173] Another method is direct deposition onto a surface. Using this technique,

it has been reported that in some cases the magnetic behavior is retained, as is the case for $Mn_{12}OAc$ on a carbon nanotube, where as in other cases it is suppressed, as is the case for $TbPc_2$ on a cobalt surface.[174-177] Very recently, another alternative was studied wherein an SMM was deposited onto a gold nanoparticle.[178] The authors utilize a chiral magnetic molecule, $[Mn_9O_4(Me\text{-}sao)_6(L)_3(MeO)_3(MeOH)_3]Cl$ ($Me\text{-}saoH_2$ = methylsalicylaldoxime, HL = lipoic acid), and demonstrate retention of both its magnetic and optical properties upon deposition. Another technique that has recently been reported is direct bonding of a single molecule magnet to a metal oxide surface through the ligand on the SMM.[179] Therein the authors were still able to observe hysteresis after coordination, indicating that this method is another viable option. This area of the field is growing, and is certainly vital to the future realization of SMM containing devices.

REFERENCES

1. Sung, H. W. F.; Rudowicz, C. *J. Magn. Magn. Mater.* **2003,** *260* (1), 250-260.

2. Spaldin, N. A., *Magnetic Materials: Fundamentals and Applications*. 2 ed.; Cambridge University Press: Cambridge, 2010.

3. Lis, T. *Acta Crystallogr. Sect. B* **1980,** *36* (9), 2042-2046.

4. Caneschi, A.; Gatteschi, D.; Sessoli, R.; Barra, A. L.; Brunel, L. C.; Guillot, M. *J. Am. Chem. Soc.* **1991,** *113* (15), 5873-5874.

5. Sessoli, R.; Gatteschi, D.; Caneschi, A.; Novak, M. A. *Nature* **1993,** *365* (6442), 141-143.

6. Bogani, L.; Wernsdorfer, W. *Nat. Mater.* **2008,** *7*, 179.

7. Sessoli, R.; Tsai, H. L.; Schake, A. R.; Wang, S.; Vincent, J. B.; Folting, K.; Gatteschi, D.; Christou, G.; Hendrickson, D. N. *J. Am. Chem. Soc.* **1993,** *115* (5), 1804-1816.

8. Friedman, J. R.; Sarachik, M. P.; Tejada, J.; Ziolo, R. *Phys. Rev. Lett.* **1996,** *76* (20), 3830-3833.

9. Feltham, H. L. C.; Brooker, S. *Coord. Chem. Rev.* **2014,** *276*, 1-33.

10. Christou, G. *Polyhedron* **2005,** *24* (16), 2065-2075.

11. Sun, Z.; N. Hendrickson, D.; Sun, Z.; M. Grant, C.; L. Castro, S.; Christou, G. *Chem. Commun.* **1998,** (6), 721-722.

12. Tasiopoulos, A. J.; Vinslava, A.; Wernsdorfer, W.; Abboud, K. A.; Christou, G. *Angew. Chem. Int. Ed.* **2004,** *43* (16), 2117-2121.

13. Aubin, S. M. J.; Wemple, M. W.; Adams, D. M.; Tsai, H.-L.; Christou, G.; Hendrickson, D. N. *J. Am. Chem. Soc.* **1996,** *118* (33), 7746-7754.

14. Ako, A. M.; Hewitt, I. J.; Mereacre, V.; Clérac, R.; Wernsdorfer, W.; Anson, C. E.; Powell, A. K. *Angew. Chem.* **2006,** *118* (30), 5048-5051.

15. Wang, X.-Y.; Prosvirin, A. V.; Dunbar, K. R. *Angew. Chem. Int. Ed.* **2010,** *49* (30), 5081-5084.

16. Waldmann, O. *Inorg. Chem.* **2007,** *46* (24), 10035-10037.

17. Frost, J. M.; Harriman, K. L. M.; Murugesu, M. *Chem. Sci.* **2016,** *7* (4), 2470-2491.

18. Pinkowicz, D.; Birk, F. J.; Magott, M.; Schulte, K.; Dunbar, K. R. *Chem. Eur. J.* **2017,** *23* (15), 3548-3552.

19. Henderson, J. J.; Koo, C.; Feng, P. L.; del Barco, E.; Hill, S.; Tupitsyn, I. S.; Stamp, P. C. E.; Hendrickson, D. N. *Phys. Rev. Lett.* **2009,** *103* (1), 017202.

20. Glaser, T.; Hoeke, V.; Gieb, K.; Schnack, J.; Schröder, C.; Müller, P. *Coord. Chem. Rev.* **2015,** *289-290*, 261-278.

21. Gatteschi, D.; Sessoli, R. *Angew. Chem. Int. Ed.* **2003,** *42* (3), 268-297.

22. Craig, G. A.; Murrie, M. *Chem. Soc. Rev.* **2015,** *44* (8), 2135-2147.

23. Min, F.; Ming-Liang, T. *Chem. Eur. J.* **2018,** *24* (30), 7574-7594.

24. Freedman, D. E.; Harman, W. H.; Harris, T. D.; Long, G. J.; Chang, C. J.; Long, J. R. *J. Am. Chem. Soc.* **2010,** *132* (4), 1224-1225.

25. Harman, W. H.; Harris, T. D.; Freedman, D. E.; Fong, H.; Chang, A.; Rinehart, J. D.; Ozarowski, A.; Sougrati, M. T.; Grandjean, F.; Long, G. J.; Long, J. R.; Chang, C. J. *J. Am. Chem. Soc.* **2010,** *132* (51), 18115-18126.

26. Atanasov, M.; Ganyushin, D.; Pantazis, D. A.; Sivalingam, K.; Neese, F. *Inorg. Chem.* **2011,** *50* (16), 7460-7477.

27. Zadrozny, J. M.; Liu, J.; Piro, N. A.; Chang, C. J.; Hill, S.; Long, J. R. *Chem. Commun.* **2012,** *48* (33), 3927-3929.

28. Vallejo, J.; Castro, I.; Ruiz-García, R.; Cano, J.; Julve, M.; Lloret, F.; De Munno, G.; Wernsdorfer, W.; Pardo, E. *J. Am. Chem. Soc.* **2012,** *134* (38), 15704-15707.

29. Rajnák, C.; Titiš, J.; Fuhr, O.; Ruben, M.; Boča, R. *Inorg. Chem.* **2014,** *53* (16), 8200-8202.

30. Huang, W.; Liu, T.; Wu, D.; Cheng, J.; Ouyang, Z. W.; Duan, C. *Dalton Trans.* **2013,** *42* (43), 15326-15331.

31. Herchel, R.; Váhovská, L.; Potočňák, I.; Trávníček, Z. *Inorg. Chem.* **2014,** *53* (12), 5896-5898.

32. Wu, D.; Zhang, X.; Huang, P.; Huang, W.; Ruan, M.; Ouyang, Z. W. *Inorg. Chem.* **2013,** *52* (19), 10976-10982.

33. Colacio, E.; Ruiz, J.; Ruiz, E.; Cremades, E.; Krzystek, J.; Carretta, S.; Cano, J.; Guidi, T.; Wernsdorfer, W.; Brechin, E. K. *Angew. Chem. Int. Ed.* **2013,** *52* (35), 9130-9134.

34. Gómez-Coca, S.; Urtizberea, A.; Cremades, E.; Alonso, P. J.; Camón, A.; Ruiz, E.; Luis, F. *Nat. Commun.* **2014,** *5*, 4300.

35. Habib, F.; Korobkov, I.; Murugesu, M. *Dalton Trans.* **2015,** *44* (14), 6368-6373.

36. Jiang, S.-D.; Maganas, D.; Levesanos, N.; Ferentinos, E.; Haas, S.; Thirunavukkuarasu, K.; Krzystek, J.; Dressel, M.; Bogani, L.; Neese, F.; Kyritsis, P. *J. Am. Chem. Soc.* **2015,** *137* (40), 12923-12928.

37. Feng, X.; Liu, J.-L.; Pedersen, K. S.; Nehrkorn, J.; Schnegg, A.; Holldack, K.; Bendix, J.; Sigrist, M.; Mutka, H.; Samohvalov, D.; Aguilà, D.; Tong, M.-L.; Long, J. R.; Clérac, R. *Chem. Commun.* **2016,** *52* (87), 12905-12908.

38. Pedersen, K. S.; Sigrist, M.; Sørensen, M. A.; Barra, A.-L.; Weyhermüller, T.; Piligkos, S.; Thuesen, C. A.; Vinum, M. G.; Mutka, H.; Weihe, H.; Clérac, R.; Bendix, J. *Angew. Chem. Int. Ed.* **2014,** *53* (5), 1351-1354.

39. Pedersen, K. S.; Sigrist, M.; Sørensen, M. A.; Barra, A.-L.; Weyhermüller, T.; Piligkos, S.; Thuesen, C. A.; Vinum, M. G.; Mutka, H.; Weihe, H.; Clérac, R.; Bendix, J. *Angew. Chem.* **2014,** *126* (5), 1375-1378.

40. Gomez-Coca, S.; Cremades, E.; Aliaga-Alcalde, N.; Ruiz, E. *J. Am. Chem. Soc.* **2013,** *135* (18), 7010-7018.

41. Zadrozny, J. M.; Long, J. R. *J. Am. Chem. Soc.* **2011,** *133* (51), 20732-20734.

42. Zadrozny, J. M.; Xiao, D. J.; Atanasov, M.; Long, G. J.; Grandjean, F.; Neese, F.; Long, J. R. *Nat Chem* **2013,** *5* (7), 577-581.

43. Yao, X.-N.; Du, J.-Z.; Zhang, Y.-Q.; Leng, X.-B.; Yang, M.-W.; Jiang, S.-D.; Wang, Z.-X.; Ouyang, Z.-W.; Deng, L.; Wang, B.-W.; Gao, S. *J. Am. Chem. Soc.* **2017,** *139* (1), 373-380.

44. Bunting, P. C.; Atanasov, M.; Damgaard-Møller, E.; Perfetti, M.; Crassee, I.; Orlita, M.; Overgaard, J.; van Slageren, J.; Neese, F.; Long, J. R. *Science* **2018**, 362 (6421), DOI: 10.1126/science.aat7319.

45. Ishikawa, N.; Sugita, M.; Ishikawa, T.; Koshihara, S.-y.; Kaizu, Y. *J. Am. Chem. Soc.* **2003,** *125* (29), 8694-8695.

46. Benelli, C.; Gatteschi, D. *Chem. Rev.* **2002,** *102* (6), 2369-2388.

47. Tang, J.; Zhang, J., *Lanthanide Single Molecule Magnets*. 1 ed.; Springer-Verlag Berlin Heidelberg: 2015; p 211.

48. Guo, F. S.; Day, B. M.; Chen, Y. C.; Tong, M. L.; Mansikkamäki, A.; Layfield, R. A. *Angew. Chem. Int. Ed.* **2017,** *56* (38), 11445-11449.

49. Rinehart, J. D.; Long, J. R. *Chem. Sci.* **2011,** *2* (11), 2078-2085.

50. Rinehart, J. D.; Fang, M.; Evans, W. J.; Long, J. R. *J. Am. Chem. Soc.* **2011,** *133* (36), 14236-14239.

51. Liu, J.-L.; Chen, Y.-C.; Zheng, Y.-Z.; Lin, W.-Q.; Ungur, L.; Wernsdorfer, W.; Chibotaru, L. F.; Tong, M.-L. *Chem. Sci.* **2013,** *4* (8), 3310-3316.

52. Chen, Y.-C.; Liu, J.-L.; Ungur, L.; Liu, J.; Li, Q.-W.; Wang, L.-F.; Ni, Z.-P.; Chibotaru, L. F.; Chen, X.-M.; Tong, M.-L. *J. Am. Chem. Soc.* **2016,** *138* (8), 2829-2837.

53. Liu, J.; Chen, Y.-C.; Liu, J.-L.; Vieru, V.; Ungur, L.; Jia, J.-H.; Chibotaru, L. F.; Lan, Y.; Wernsdorfer, W.; Gao, S.; Chen, X.-M.; Tong, M.-L. *J. Am. Chem. Soc.* **2016,** *138*(16), 5441-5450.

54. Goodwin, C. A. P.; Ortu, F.; Reta, D.; Chilton, N. F.; Mills, D. P. *Nature* **2017,** *548*, 439.

55. Guo, F.-S.; Day, B. M.; Chen, Y.-C.; Tong, M.-L.; Mansikkamäki, A.; Layfield, R. A. *Science* **2018**, *362*, 1400-1403.

56. Awschalom, D. D.; Flatte, M. E.; Samarth, N. *Scientific American* **2002,** *286* (6), 67-73.

57. Mannini, M.; Pineider, F.; Sainctavit, P.; Danieli, C.; Otero, E.; Sciancalepore, C.; Talarico, A. M.; Arrio, M.-A.; Cornia, A.; Gatteschi, D.; Sessoli, R. *Nat. Mater.* **2009,** *8*, 194.

58. Ruiz, E.; Cirera, J.; Cano, J.; Alvarez, S.; Loose, C.; Kortus, J. *Chem. Commun.* **2008,** (1), 52-54.

59. Zadrozny, J. M.; Atanasov, M.; Bryan, A. M.; Lin, C.-Y.; Rekken, B. D.; Power, P. P.; Neese, F.; Long, J. R. *Chem. Sci.* **2013,** *4* (1), 125-138.

60. Zadrozny, J. M.; Xiao, D. J.; Atanasov, M.; Long, G. J.; Grandjean, F.; Neese, F.; Long, J. R. *Nat. Chem.* **2013,** *5*, 577.

61. Kazin, P. E.; Zykin, M. A.; Trusov, L. A.; Eliseev, A. A.; Magdysyuk, O. V.; Dinnebier, R. E.; Kremer, R. K.; Felser, C.; Jansen, M. *Chem. Commun.* **2017,** *53* (39), 5416-5419.

62. Kazin, P. E.; Zykin, M. A.; Schnelle, W.; Zubavichus, Y. V.; Babeshkin, K. A.; Tafeenko, V. A.; Felser, C.; Jansen, M. *Inorg. Chem.* **2017,** *56* (3), 1232-1240.

63. Rechkemmer, Y.; Breitgoff, F. D.; van der Meer, M.; Atanasov, M.; Hakl, M.; Orlita, M.; Neugebauer, P.; Neese, F.; Sarkar, B.; van Slageren, J. *Nat. Commun.* **2016,** *7*, 10467.

64. Marriott, K. E. R.; Bhaskaran, L.; Wilson, C.; Medarde, M.; Ochsenbein, S. T.; Hill, S.; Murrie, M. *Chem. Sci.* **2015,** *6* (12), 6823-6828.

65. Woods, T. J.; Ballesteros-Rivas, M. F.; Gómez-Coca, S.; Ruiz, E.; Dunbar, K. R. *J. Am. Chem. Soc.* **2016,** *138* (50), 16407-16416.

66. Lacy, D. C.; Park, Y. J.; Ziller, J. W.; Yano, J.; Borovik, A. S. *J. Am. Chem. Soc.* **2012,** *134* (42), 17526-17535.

67. Park, Y. J.; Cook, S. A.; Sickerman, N. S.; Sano, Y.; Ziller, J. W.; Borovik, A. S. *Chem. Sci.* **2013,** *4* (2), 717-726.

68. Cook, S. A.; Ziller, J. W.; Borovik, A. S. *Inorg. Chem.* **2014,** *53* (20), 11029-11035.

69. Lau, N.; Ziller, J. W.; Borovik, A. S. *Polyhedron* **2015,** *85*, 777-782.

70. *APEX2*, v2013.10-0; Bruker AXS: Madison, WI, 2013.

71. Sheldrick, G. *Acta Crystallographica Section A* **2015,** *71* (1), 3-8.

72. Sheldrick, G. *Acta Crystallographica Section A* **2008,** *64* (1), 112-122.

73. Dolomanov, O. V.; Bourhis, L. J.; Gildea, R. J.; Howard, J. A. K.; Puschmann, H. *J. Appl. Crystallogr.* **2009,** *42* (2), 339-341.

74. Bain, G. A.; Berry, J. F. *J. Chem. Ed.* **2008,** *85* (4), 532.

75. Neese, F. *WIREs Comput. Mol. Sci.* **2011,** *2* (1), 73-78.

76. Weigend, F.; Ahlrichs, R. *PCCP* **2005,** *7* (18), 3297-3305.

77. Angeli, C.; Cimiraglia, R.; Malrieu, J.-P. *Chem. Phys. Lett.* **2001,** *350* (3), 297-305.

78. Angeli, C.; Cimiraglia, R.; Malrieu, J.-P. *J. Chem. Phys.* **2002,** *117* (20), 9138-9153.

79. Alvarez, S.; Alemany, P.; Casanova, D.; Cirera, J.; Llunell, M.; Avnir, D. *Coord. Chem. Rev.* **2005,** *249* (17), 1693-1708.

80. *Shape*, 2.0; Universitat de Barcelona: Barcelona, Spain, 2010.

81. Chilton, N. F.; Anderson, R. P.; Turner, L. D.; Soncini, A.; Murray, K. S. *J. Comput. Chem.* **2013,** *34* (13), 1164-1175.

82. Kumar, S. S.; Tulika, G.; Prashi, B.; Gopalan, R. *Chem. Eur. J.* **2014,** *20* (33), 10305-10313.

83. Chilton, N. *CC-FIT*, Manchester, U.K., 2014.

84. Abragam, A.; Bleaney, B., *Electron Paramagnetic Resonance of Transition Ions*. University Press: Oxford, 1970.

85. Miklovic, J.; Valigura, D.; Boca, R.; Titis, J. *Dalton Trans.* **2015,** *44* (28), 12484-12487.

86. Pinero Cruz, D. M.; Woodruff, D. N.; Jeon, I.-R.; Bhowmick, I.; Secu, M.; Hillard, E. A.; Dechambenoit, P.; Clerac, R. *New J. Chem.* **2014,** *38* (8), 3443-3448.

87. Ruamps, R.; Batchelor, L. J.; Guillot, R.; Zakhia, G.; Barra, A.-L.; Wernsdorfer, W.; Guihery, N.; Mallah, T. *Chem. Sci.* **2014,** *5* (9), 3418-3424.

88. Bendix, J.; Brorson, M.; Schaffer, C. E. *Inorg. Chem.* **1993,** *32* (13), 2838-2849.

89. Gruden-Pavlović, M.; Perić, M.; Zlatar, M.; García-Fernández, P. *Chem. Sci.* **2014,** *5* (4), 1453-1462.

90. Craig, G. A.; Sarkar, A.; Woodall, C. H.; Hay, M. A.; Marriott, K. E. R.; Kamenev, K. V.; Moggach, S. A.; Brechin, E. K.; Parsons, S.; Rajaraman, G.; Murrie, M. *Chem. Sci.* **2018,** *9* (6), 1551-1559.

91. Rodriguz-Ubis, J.-C.; Alpha, B.; Plancherel, D.; Lehn, J.-M. *Helv. Chim. Acta* **1984,** *67* (8), 2264-2269.

92. Ravikumar, I.; Lakshminarayanan, P. S.; Suresh, E.; Ghosh, P. *Inorg. Chem.* **2008,** *47* (18), 7992-7999.

93. Farrell, D.; Gloe, K.; Gloe, K.; Goretzki, G.; McKee, V.; Nelson, J.; Nieuwenhuyzen, M.; Pal, I.; Stephan, H.; Town, R. M.; Wichmann, K. *Dalton Trans.* **2003,** (10), 1961-1968.

94. Drew, M. G. B.; Marrs, D.; Hunter, J.; Nelson, J. *J. Chem. Soc., Dalton Trans.* **1992,** (1), 11-18.

95. Anthony Deeney, F.; J. Harding, C.; G. Morgan, G.; McKee, V.; Nelson, J.; J. Teat, S.; Clegg, W. *J. Chem. Soc., Dalton Trans.* **1998,** *11*, 1837-1844.

96. Escuer, A.; J. Harding, C.; Dussart, Y.; Nelson, J.; McKee, V.; Vicente, R. *J. Chem. Soc., Dalton Trans.* **1999,** *2*, 223-228.

97. Bond, A. D.; Derossi, S.; Harding, C. J.; McInnes, E. J. L.; McKee, V.; McKenzie, C. J.; Nelson, J.; Wolowska, J. *Dalton Trans.* **2005,** *14*, 2403-2409.

98. Schulte, K. A.; Vignesh, K. R.; Dunbar, K. R. *Chem. Sci.* **2018,** *9*, 9018-9026.

99. Woollard-Shore, J. G.; Holland, J. P.; Jones, M. W.; Dilworth, J. R. *Dalton Trans.* **2010,** *39* (6), 1576-1585.

100. Caballero-Jimenez, J.; Habib, F.; Ramirez-Rosales, D.; Grande-Aztatzi, R.; Merino, G.; Korobkov, I.; Singh, M. K.; Rajaraman, G.; Reyes-Ortega, Y.; Murugesu, M. *Dalton Trans.* **2015,** *44* (18), 8649-8659.

101. Spek, A. *Acta Cryst. C* **2015,** *71* (1), 9-18.

102. Chen, J.-M.; Zhuang, X.-M.; Yang, L.-Z.; Jiang, L.; Feng, X.-L.; Lu, T.-B. *Inorg. Chem.* **2008,** *47* (8), 3158-3165.

103. El-Khatib, F.; Cahier, B.; Shao, F.; López-Jordà, M.; Guillot, R.; Rivière, E.; Hafez, H.; Saad, Z.; Girerd, J.-J.; Guihéry, N.; Mallah, T. *Inorg. Chem.* **2017,** *56* (8), 4601-4608.

104. Mydosh, J. A., *Spin glasses : an experimental introduction*. Taylor & Francis: London 1993.

105. Balanda, M. *Acta Phys. Pol., A* **2013,** *124* (6), 964-976.

106. Pejaković, D. A.; Manson, J. L.; Miller, J. S.; Epstein, A. J. *Phys. Rev. Lett.* **2000,** *85* (9), 1994-1997.

107. Chandrasekhar, V.; Dey, A.; Mota, A. J.; Colacio, E. *Inorg. Chem.* **2013,** *52* (8), 4554-4561.

108. Saber, M. R.; Dunbar, K. R. *Chem. Commun.* **2014,** *50* (82), 12266-12269.

109. Zadrozny, J. M.; Telser, J.; Long, J. R. *Polyhedron* **2013,** *64*, 209-217.

110. Shao, D.; Shi, L.; Zhang, S.-L.; Zhao, X.-H.; Wu, D.-Q.; Wei, X.-Q.; Wang, X.-Y. *Cryst. Eng. Comm.* **2016,** *18* (22), 4150-4157.

111. Mondal, A. K.; Mondal, A.; Dey, B.; Konar, S. *Inorg. Chem.* **2018,** *57* (16), 9999-10008.

112. Shao, D.; Zhang, S.-L.; Shi, L.; Zhang, Y.-Q.; Wang, X.-Y. *Inorg. Chem.* **2016,** *55* (21), 10859-10869.

113. Feng, X.; Hwang, S. J.; Liu, J.-L.; Chen, Y.-C.; Tong, M.-L.; Nocera, D. G. *J. Am. Chem. Soc.* **2017,** *139* (46), 16474-16477.

114. Lin, P.-H.; Smythe, N. C.; Gorelsky, S. I.; Maguire, S.; Henson, N. J.; Korobkov, I.; Scott, B. L.; Gordon, J. C.; Baker, R. T.; Murugesu, M. *J. Am. Chem. Soc.* **2011,** *133* (40), 15806-15809.

115. Zhang, Y.-Z.; Mallik, U. P.; Rath, N. P.; Clérac, R.; Holmes, S. M. *Inorg. Chem.* **2011,** *50* (21), 10537-10539.

116. Li, D.; Clérac, R.; Parkin, S.; Wang, G.; Yee, G. T.; Holmes, S. M. *Inorg. Chem.* **2006,** *45* (14), 5251-5253.

117. Wang, C.-F.; Zuo, J.-L.; Bartlett, B. M.; Song, Y.; Long, J. R.; You, X.-Z. *J. Am. Chem. Soc.* **2006,** *128* (22), 7162-7163.

118. Zhang, Y.-Z.; Mallik, U. P.; Clérac, R.; Rath, N. P.; Holmes, S. M. *Chem. Commun.* **2011,** *47* (25), 7194-7196.

119. Li, D.; Parkin, S.; Wang, G.; Yee, G. T.; Clérac, R.; Wernsdorfer, W.; Holmes, S. M. *J. Am. Chem. Soc.* **2006,** *128* (13), 4214-4215.

120. Zhang, Y.; Mallik, U. P.; Rath, N.; Yee, G. T.; Clérac, R.; Holmes, S. M. *Chem. Commun.* **2010,** *46* (27), 4953-4955.

121. Jiang, L.; Choi, H. J.; Feng, X.-L.; Lu, T.-B.; Long, J. R. *Inorg. Chem.* **2007,** *46* (6), 2181-2186.

122. Wang, C.-F.; Gu, Z.-G.; Lu, X.-M.; Zuo, J.-L.; You, X.-Z. *Inorg. Chem.* **2008,** *47* (18), 7957-7959.

123. Zhu, Y.-Y.; Cui, C.; Zhang, Y.-Q.; Jia, J.-H.; Guo, X.; Gao, C.; Qian, K.; Jiang, S.-D.; Wang, B.-W.; Wang, Z.-M.; Gao, S. *Chem. Sci.* **2013,** *4* (4), 1802-1806.

124. Alexandru, M.-G.; Visinescu, D.; Marino, N.; de Munno, G.; Lloret, F.; Julve, M. *RSC Advances* **2015,** *5* (116), 95410-95420.

125. Brown, A.; Saber, M.; Van den Heuvel, W.; Schulte, K.; Soncini, A.; Dunbar, K. R. *Inorg. Chem.* **2017,** *56* (3), 1031-1035.

126. Spek, A. *J. Appl. Crystallogr.* **2003,** *36* (1), 7-13.

127. Neese, F. *Wiley Interdisciplinary Reviews: Computational Molecular Science* **2012,** *2* (1), 73-78.

128. Singh, S. K.; Vignesh, K. R.; Archana, V.; Rajaraman, G. *Dalton Trans.* **2016,** *45* (19), 8201-8214.

129. Singh, S. K., Gupta, T., Padku P., Rajaraman G. *Chem. Eur. J.* **2014,** *20* (33), 10305-10313.

130. Manna, S.; Bhunia, A.; Mistri, S.; Vallejo, J.; Zangrando, E.; Puschmann, H.; Cano, J.; Manna, S. C. *Eur. J. Inorg. Chem.* **2017,** *2017* (19), 2585-2594.

131. Miklovič, J.; Valigura, D.; Boča, R.; Titiš, J. *Dalton Trans.* **2015,** *44* (28), 12484-12487.

132. Titiš, J.; Boča, R. *Inorg. Chem.* **2010,** *49* (9), 3971-3973.

133. Christou, G.; Gatteschi, D.; Hendrickson, D. N.; Sessoli, R. *MRS Bulletin* **2000,** *25* (11), 66-71.

134. Bagai, R.; Christou, G. *Chem. Soc. Rev.* **2009,** *38* (4), 1011-1026.

135. Sessoli, R.; Powell, A. K. *Coord. Chem. Rev.* **2009,** *253* (19–20), 2328-2341.

136. Sorace, L.; Benelli, C.; Gatteschi, D. *Chem. Soc. Rev.* **2011,** *40* (6), 3092-3104.

137. Woodruff, D. N.; Winpenny, R. E. P.; Layfield, R. A. *Chem. Rev.* **2013,** *113* (7), 5110-5148.

138. Ishikawa, N.; Sugita, M.; Wernsdorfer, W. *Angew. Chem. Int. Ed.* **2005,** *44* (19), 2931-2935.

139. Branzoli, F.; Carretta, P.; Filibian, M.; Zoppellaro, G.; Graf, M. J.; Galan-Mascaros, J. R.; Fuhr, O.; Brink, S.; Ruben, M. *J. Am. Chem. Soc.* **2009,** *131* (12), 4387-4396.

140. Ungur, L.; Chibotaru, L. F. *Phys. Chem. Chem. Phys.* **2011,** *13* (45), 20086-20090.

141. Chilton, N. F.; Collison, D.; McInnes, E. J. L.; Winpenny, R. E. P.; Soncini, A. *Nat. Commun.* **2013,** *4*, 2551.

142. Guo, F.-S.; Day, B. M.; Chen, Y.-C.; Tong, M.-L.; Mansikkamäki, A.; Layfield, R. A. *Angew. Chem. Int. Ed.* **2017,** *56* (38), 11445-11449.

143. Soldatov Dmitriy, V.; Ripmeester John, A. *Chem. Eur. J.* **2001,** *7* (14), 2979-2994.

144. Trofimenko, S.; Long, J. R.; Nappier, T.; Shore, S. G., Poly(1-pyrazolyl)borates, Their Transition-Metal Complexes, and Pyrazaboles. In *Inorganic Syntheses*, John Wiley & Sons, Inc.: 1970; pp 99-109.

145. Bruker-AXS *APEX3*, 2014.11-0; Bruker AXS: Madison, WI, 2015.

146. Sheldrick, G. M. *Acta Crystallogr. Sect. A, Found. and Adv.* **2015,** *71*, 3-8.

147. Sheldrick, G. M. *Acta crystallogr. Sect. C, Struc. Chem.* **2015,** *C71* (Pt 1), 3-8.

148. Spek, A. *Acta Crystallographica Section D* **2009,** *65* (2), 148-155.

149. Macrae, C. F.; Edgington, P. R.; McCabe, P.; Pidcock, E.; Shields, G. P.; Taylor, R.; Towler, M.; van de Streek, J. *J. Appl. Crystallogr.* **2006,** *39* (3), 453-457.

150. Pennington, W. *J. Appl. Crystallogr.* **1999,** *32* (5), 1028-1029.

151. Aquilante, F.; Autschbach, J.; Carlson, R. K.; Chibotaru, L. F.; Delcey, M. G.; Vico, L. D.; Galván, I. F.; Ferré, N.; Frutos, L. M.; Gagliardi, L.; Garavelli, M.; Giussani, A.; Hoyer, C. E.; Manni, G. L.; Lischka, H.; Ma, D.; Malmqvist, P. Å.; Müller,

T.; Nenov, A.; Olivucci, M.; Pedersen, T. B.; Peng, D.; Plasser, F.; Pritchard, B.; Reiher, M.; Rivalta, I.; Schapiro, I.; Segarra-Martí, J.; Stenrup, M.; Truhlar, D. G.; Ungur, L.; Valentini, A.; Vancoillie, S.; Veryazov, V.; Vysotskiy, V. P.; Weingart, O.; Zapata, F.; Lindh, R. *J. Comput. Chem.* **2016,** *37*, 506-541.

152. Hess, B. A.; Marian, C. M.; Wahlgren, U.; Gropen, O. *Chem. Phys. Lett.* **1996,** *251* (5–6), 365-371.

153. Roos, B. O.; Malmqvist, P.-A. *Phys. Chem. Chem. Phys.* **2004,** *6* (11), 2919-2927.

154. Roos, B. O.; Lindh, R.; Malmqvist, P.-A.; Veryazov, V.; Widmark, P.-O.; Borin, A. C. *J. Phys. Chem. A* **2008,** *112* (45), 11431-11435.

155. Malmqvist, P. A.; Roos, B. O.; Schimmelpfennig, B. *Chem. Phys. Lett.* **2002,** *357* (3-4), 230-240.

156. Chibotaru, L. F.; Ungur, L. *J. Chem. Phys.* **2012,** *137* (6), 064112-22.

157. Jiang, S. D.; Wang, B. W.; Su, G.; Wang, Z. M.; Gao, S. *Angew. Chem. Int. Ed.* **2010,** *49* (41), 7448-7451.

158. Li, X. L.; Chen, C. L.; Gao, Y. L.; Liu, C. M.; Feng, X. L.; Gui, Y. H.; Fang, S. M. *Chem. Eur. J.* **2012,** *18* (46), 14632-14637.

159. Barsukova, M.; Izarova Natalya , V.; Biboum Rosa, N.; Keita, B.; Nadjo, L.; Ramachandran, V.; Dalal Naresh , S.; Antonova Nadya , S.; Carbó Jorge , J.; Poblet Josep , M.; Kortz, U. *Chem. Eur. J.* **2010,** *16* (30), 9076-9085.

160. Baldoví, J. J.; Cardona-Serra, S.; Clemente-Juan, J. M.; Coronado, E.; Gaita-Ariño, A.; Palii, A. *Inorg. Chem.* **2012,** *51* (22), 12565-12574.

161. Goswami, S.; Biswas, S.; Tomar, K.; Konar, S. *Eur. J. Inorg. Chem.* **2016,** *2016* (17), 2774-2782.

162. Koike, N.; Uekusa, H.; Ohashi, Y.; Harnoode, C.; Kitamura, F.; Ohsaka, T.; Tokuda, K. *Inorg. Chem.* **1996,** *35* (20), 5798-5804.

163. Sorensen, M. A.; Weihe, H.; Vinum, M. G.; Mortensen, J. S.; Doerrer, L. H.; Bendix, J. *Chem. Sci.* **2017,** *8* (5), 3566-3575.

164. Chilton, N. F. *CC-fit model*, The Univesity of Manchester.

165. Meihaus, K. R.; Minasian, S. G.; Lukens, W. W.; Kozimor, S. A.; Shuh, D. K.; Tyliszczak, T.; Long, J. R. *J. Am. Chem. Soc.* **2014,** *136* (16), 6056-6068.

166. Brown, A. J.; Pinkowicz, D.; Saber, M. R.; Dunbar, K. R. *Angew. Chem. Int. Ed.* **2015,** *54* (20), 5864-5868.

167. Pugh, T.; Tuna, F.; Ungur, L.; Collison, D.; McInnes, E. J. L.; Chibotaru, L. F.; Layfield, R. A. *Nat. Commun.* **2015,** *6*, 7492.

168. Vignesh, K. R.; Langley, S. K.; Murray, K. S.; Rajaraman, G. *Inorg. Chem.* **2017,** *56* (5), 2518-2532.

169. Aulakh, D.; Pyser, J. B.; Zhang, X.; Yakovenko, A. A.; Dunbar, K. R.; Wriedt, M. *J. Am. Chem. Soc.* **2015,** *137* (29), 9254-9257.

170. Mínguez Espallargas, G.; Coronado, E. *Chem. Soc. Rev.* **2018,** *47* (2), 533-557.

171. Baldoví, J. J.; Coronado, E.; Gaita-Ariño, A.; Gamer, C.; Giménez-Marqués, M.; Mínguez Espallargas, G. *Chem. Eur. J.* **2014,** *20* (34), 10695-10702.

172. Oyarzabal, I.; Fernández, B.; Cepeda, J.; Gómez-Ruiz, S.; Calahorro, A. J.; Seco, J. M.; Rodríguez-Diéguez, A. *CrystEngComm* **2016,** *18* (17), 3055-3063.

173. Chen, Q.; Li, J.; Meng, Y.-S.; Sun, H.-L.; Zhang, Y.-Q.; Sun, J.-L.; Gao, S. *Inorg. Chem.* **2016,** *55* (16), 7980-7987.

174. Gonidec, M.; Biagi, R.; Corradini, V.; Moro, F.; De Renzi, V.; del Pennino, U.; Summa, D.; Muccioli, L.; Zannoni, C.; Amabilino, D. B.; Veciana, J. *J. Am. Chem. Soc.* **2011,** *133* (17), 6603-6612.

175. Vincent, R.; Klyatskaya, S.; Ruben, M.; Wernsdorfer, W.; Balestro, F. *Nature* **2012,** *488*, 357.

176. del Carmen Giménez-López, M.; Moro, F.; La Torre, A.; Gómez-García, C. J.; Brown, P. D.; van Slageren, J.; Khlobystov, A. N. *Nat. Commun.* **2011,** *2*, 407.

177. Malavolti, L.; Poggini, L.; Margheriti, L.; Chiappe, D.; Graziosi, P.; Cortigiani, B.; Lanzilotto, V.; de Mongeot, F. B.; Ohresser, P.; Otero, E.; Choueikani, F.; Sainctavit, P.; Bergenti, I.; Dediu, V. A.; Mannini, M.; Sessoli, R. *Chem. Commun.* **2013,** *49* (98), 11506-11508.

178. Mitcov, D.; Pedersen, A. H.; Ceccato, M.; Gelardi, R. M.; Hassenkam, T.; Konstantatos, A.; Reinholdt, A.; Sørensen, M. A.; Thulstrup, P. W.; Vinum, M. G.;

Wilhelm, F.; Rogalev, A.; Wernsdorfer, W.; Brechin, E. K.; Piligkos, S. *Chem. Sci.* **2019**, DOI: 10.1039/C8SC04917C.

179. Campbell, V. E.; Tonelli, M.; Cimatti, I.; Moussy, J.-B.; Tortech, L.; Dappe, Y. J.; Rivière, E.; Guillot, R.; Delprat, S.; Mattana, R.; Seneor, P.; Ohresser, P.; Choueikani, F.; Otero, E.; Koprowiak, F.; Chilkuri, V. G.; Suaud, N.; Guihéry, N.; Galtayries, A.; Miserque, F.; Arrio, M.-A.; Sainctavit, P.; Mallah, T. *Nat. Commun.* **2016,** *7*, 13646.